Analytical Microscopy of Corroded Zirconium Alloys



Thomas Aarholt

Wolfson College

University of Oxford

A thesis submitted for the degree of

Doctor of Philosophy

Michaelmas 2018

Acknowledgements

I'd like to express my sincere gratitude to my supervisors, Professors Chris R. M. Grovenor and Sergio Lozano-Perez. Their knowledge and advice has been incredibly helpful throughout my project. Sergio's teaching and long chats with Chris have been brilliant. They have been both been excellent supervisors, and I have been very lucky to have been part of their research groups.

I am very thankful to Jing Hu, Judith Dohr and Martina Meisnar. At times it felt like the four of us could take on the world if necessary.

I'm very grateful to the electron microscopy technical support group (TSG) for their invaluable help over the years of research at Oxford. Their ability to repair equipment and keep it going is remarkable.

The MUZIC consortium has been an enormous source of excitement, and the biannual meetings all over Europe have provided me with healthy discussion and learning. Meeting young and senior researchers who work in similar fields to myself has been a source of inspiration to keep going, and the numerous debates on the corrosion of zirconium has been extremely fruitful. I am very grateful to the time spent with the MUZIC group, particularly to Westinghouse Electric Company for sponsoring my DPhil.

I am most appreciative to Dr Haibo Jiang and Dr Kexue Li for help with the acquisition of depth profiles on the NanoSIMS. Their work is acknowledged in the relevant chapter.

I am enormously grateful to Wolfson College for its hospitality and in particular to Wolfson College Boat Club. I have fantastic memories from rowing and have built great relationships with my fellow rowers.

I am very grateful to Anna. Her love for me has kept me going when the going got tough, and without her I'm pretty sure this thesis would not have happened.

Finally, I am eternally grateful to my parents. They put the spark of curiosity in me, and have always been there for me.

Contents

List of Abbreviations **xiii**

1 Preface **1**
1.1 Motivation . . . 1
1.1.1 The MUZIC collaboration . . . 1
1.2 Conventions . . . 2

2 Literature Review **5**
2.1 Introduction . . . 6
2.2 Zirconium and zirconium alloys . . . 6
2.2.1 Physical properties . . . 7
2.2.2 Zirconium in the nuclear industry . . . 8
2.3 Zirconium alloys . . . 9
2.3.1 The Zircaloy family . . . 11
2.3.2 The Zr-Nb alloys . . . 11
2.3.3 ZIRLO . . . 14
2.4 Oxidation . . . 14
2.4.1 Transition . . . 15
2.4.2 Zirconia . . . 17
2.4.3 Oxidation kinetics . . . 18
2.4.4 Pre-transition . . . 21
2.4.5 Post-transition . . . 22
2.4.6 Transition mechanism . . . 24
2.4.7 Mechanical breakdown of the oxide . . . 25
2.4.8 Oxide phase transformation . . . 26
2.4.9 Dissolution of the alloying elements in the oxide . . . 27
2.4.10 Suboxide phase at the metal-oxide interface . . . 28
2.5 Hydrogen pickup . . . 30
2.5.1 Delayed hydride cracking . . . 32
2.5.2 Hydrogen content in the oxide . . . 33
2.5.3 Hydrogen pickup mechanisms . . . 33
2.5.4 Effect of alloying elements on hydrogen pickup . . . 39
2.6 Effect of sample preparation . . . 49
2.7 Summary . . . 50

3 Experimental techniques and methodology 51
3.1 Electron interactions with matter . . . 52
3.2 Scanning electron microscopy . . . 52
3.2.1 SEM instruments used in this project . . . 54
3.3 Focused ion beam - sample preparation . . . 56
3.3.1 Ion interactions with matter . . . 56
3.3.2 TEM sample preparation . . . 57
3.4 Transmission electron microscopy . . . 61
3.5 Energy-dispersive X-ray spectroscopy . . . 63
3.5.1 EDS use in my project . . . 64
3.6 Electron energy loss spectroscopy . . . 65
3.6.1 Multiple linear least squares fitting . . . 72
3.6.2 Suboxide EELS analysis . . . 73
3.7 HyperSpy EELS analysis software package . . . 75
3.8 Secondary ion mass spectrometry . . . 75
3.8.1 Diffusion profiles . . . 77
3.9 Materials . . . 78

4 The corrosion of ZIRLO 81
4.1 Introduction . . . 82
4.2 Oxidation characterisation . . . 84
4.2.1 The inaccuracy of 'pre'- and 'post'-transition descriptions . . . 84
4.2.2 3D-FIB Sectioning . . . 84
4.3 ZIRLO samples . . . 86
4.3.1 Oxide structure . . . 86
4.3.2 3-day pre-transition ZIRLO . . . 87
4.3.3 45-day pre-transition ZIRLO . . . 90
4.3.4 135-day post-transition ZIRLO . . . 91
4.3.5 225-day post-transition ZIRLO . . . 96
4.4 EELS analysis on ZIRLO . . . 103
4.4.1 Low-loss EELS . . . 103
4.4.2 Core-loss EELS of the metal-oxide interface . . . 115
4.4.3 3-day ZIRLO . . . 119
4.4.4 45-day ZIRLO . . . 121
4.4.5 Necessity of EDS for SPP imaging . . . 125
4.4.6 SPP oxidation state . . . 125
4.5 Discussion . . . 130
4.5.1 3D-FIB sectioning . . . 130
4.5.2 EELS fine structure and plasmon analysis . . . 131

4.5.3 Dissolution of Fe in SPPs . . . 132
4.5.4 The effect of cracks . . . 134
4.5.5 Porosity near the metal-oxide interface . . . 136
4.5.6 Corrosion resistance and oxygen-saturated region . . . 138
4.5.7 Suboxide . . . 139
4.6 Summary . . . 141

5 The corrosion of Zircaloy-4 **145**
5.1 Oxidation of Zircaloy-4 . . . 146
5.2 Oxidation characterisation . . . 148
5.2.1 3-day pre-transition Zircaloy-4 . . . 148
5.2.2 45-day pre-transition Zircaloy-4 . . . 152
5.2.3 105-day post-transition Zircaloy-4 . . . 160
5.3 Low-loss EELS analysis of Zircaloy-4 . . . 163
5.3.1 Plasmon peaks comparison to ZIRLO . . . 165
5.3.2 Combined suboxide and oxygen-saturated metal region . . . 165
5.4 Discussion . . . 166
5.4.1 The inaccuracy of "pre"- and "post"-transition descriptions . 166
5.4.2 Oxide microstructure comparison with ZIRLO . . . 168
5.4.3 Combined suboxide and oxygen-saturated metal region . . . 171
5.4.4 Hydride formation in thin foils . . . 175
5.4.5 Why does the sawtooth oxide form its shape? . . . 176
5.4.6 The influence of alloying elements on the corrosion of zirconium alloys . . . 177
5.5 Summary of results and discussion . . . 180
5.5.1 Similarities . . . 182
5.5.2 Differences . . . 182

6 Hydrogen pickup **185**
6.1 Introduction . . . 186
6.2 Materials . . . 186
6.3 Results . . . 188
6.3.1 A note on sample-preparation . . . 188
6.3.2 Typical NanoSIMS results . . . 189
6.3.3 Using the SE image to identify the oxide . . . 192
6.3.4 Proving that the deuterium signal is not from natural H_2O . 194
6.3.5 Hydrocarbon contamination from resin . . . 195
6.4 Overview of alloys . . . 197
6.4.1 125-day pre-transition ZIRLO . . . 197
6.4.2 225-day post-transition ZIRLO . . . 200

6.4.3 225-day pre-transition Zr-1Nb . . . 200
6.4.4 585-day post-transition Zr-1Nb . . . 203
6.4.5 Hydrides compared between STEM and NanoSIMS . . . 203
6.5 High-resolution oxide analysis . . . 205
6.5.1 Peak of hydrogen in first part of the oxide . . . 205
6.5.2 Pre-transition 125-day ZIRLO . . . 206
6.5.3 Pre-transition 225-day Zr-1Nb . . . 208
6.5.4 Pre-transition 61-days Zircaloy-4 . . . 208
6.5.5 Post-transition 225-day ZIRLO . . . 210
6.5.6 Post-transition 585-day Zr-1Nb . . . 213
6.5.7 Barrier to hydrogen in oxide . . . 214
6.5.8 SEM imaging of post-SIMS areas . . . 215
6.5.9 Deuterium hot-spots in the oxide . . . 217
6.5.10 FEGSEM and EDS of hot-spot . . . 219
6.5.11 Deuterides in the metal . . . 220
6.6 Discussion . . . 223
6.6.1 Comparison of alloys and impact of alloying additions on hydrogen pickup . . . 223
6.6.2 Oxide barrier to hydrogen ingress . . . 225
6.6.3 Hydrogen hot-spots in the oxide . . . 226
6.7 Summary . . . 227

7 Depth profiling 231
7.1 Introduction . . . 231
7.2 Results . . . 235
7.2.1 One-dimensional depth profiles . . . 235
7.2.2 Three-dimensional depth profiles . . . 238
7.3 Discussion . . . 245
7.3.1 Hydrogen pathways through the metal-oxide interface . . . 245
7.3.2 Diffusion profiles . . . 247
7.3.3 Hydrogen uptake hypothesis and relation to oxidation mechanism . . . 252
7.4 Summary . . . 253

8 Summary and suggestions for future work 255
8.1 Oxide microstructure and oxidation behaviour . . . 255
8.2 EELS results . . . 256
8.3 Hydrogen pickup results . . . 258
8.4 Future work . . . 260

9 Removal of cosmic rays in EELS spectrum images **263**
9.1 Cosmic rays 263

10 HyperSpy scripting notebook **269**
10.1 Load and decompose the data using my own decomposition-interface 269
10.2 Fit Core loss EELS with Zr L edges, white lines and the O K edge. 279

References **283**

Publications

Part of the work in this thesis has been or will be published in the following publications:

Journal articles

Hu, J., Setiadinata, B., Aarholt, T., Garner, A., Partezana, J., Bagot, P., Lozano-Perez, S., Preuss, M., Moody, M. and Grovenor, C. High-resolution characterization of Zr nuclear fuel cladding alloys, In Zirconium in the nuclear industry: Eighteenth international symposium, American Society of Testing Materials, 2016.

Hu, J., Setiadinata, B., Aarholt, T., Bagot, P., Moody, M., Grovenor, C.,Ni, N., High-resolution characterization of corrosion and hydrogen pickup of Zr cladding alloys, TopFuel, 2015.

de la Pena et al. F., Electron Microscopy (Big and Small) Data Analysis With the Open Source Software Package HyperSpy, Microsc. Microanal. 23 (Suppl 1), 2017.

Conference poster presentations

Aarholt, T., Moore, K., Frankel, P., Lozano-Perez, S., Grovenor, C. R. M., NanoSIMS and FESEM analysis of deuterated ZIRLO and Zr-1%Nb nuclear fuel cladding alloys, In 18th International Microscopy Congress, Prague, Czech Republic, September 2014.

Aarholt, T., Moore, K., Frankel, P., Lozano-Perez, S., Grovenor, C. R. M., NanoSIMS and TEM analysis of deuterated ZIRLO and Zr-1%Nb nuclear fuel cladding alloys, In International Microscopy of Oxidation, University of Nottingham, UK, April 2013.

Publications currently in preparation

Aarholt, T., Hu, J., Lozano-Perez, S., Grovenor, C. R. M. (2016) Independent Component Analysis on high-energy-resolution low loss EELS of oxidised zirconium alloys, 2017 (unpublished).

Aarholt, T., Li, K., Jiang, H., Moore, K., Lozano-Perez, S., Grovenor, C. R. M., Direct observation of deuterium in ZIRLO oxides by NanoSIMS analysis, 2017 (unpublished).

Li, K., Aarholt, T., Liu, J., Lozano-Perez, S., Grovenor, C. R. M., 3D-characterization of deuterium distributions in oxidised Zircaloy-4 using high-resolution SIMS 2017 (unpublished).

List of Abbreviations

AS . . . . . NanoSIMS aperture

APT . . . . . Atom probe tomography

BCC . . . . . Body-centred cubic

BF . . . . . Bright field

BSS . . . . . Blind source separation

BWR . . . . . Boiling water reactor

CCD . . . . . Charge-coupled device

D1 . . . . . NanoSIMS aperture

DF . . . . . Dark field

DFT . . . . . Density functional theory.

DHC . . . . . Delayed hydride cracking.

EDS . . . . . Energy-dispersive X-ray spectroscopy

EELS . . . . . Electron energy loss spectroscopy

EFTEM . . . . Energy-filtered TEM

ES . . . . . NanoSIMS aperture

FEG . . . . . Field-emission gun

FEGSEM . . . Field-emission gun scanning electron microscope

FIB . . . . . Focused ion beam

FIBSEM . . . Focused ion beam scanning electron microscope

FWHM . . . . Full width at half maximum

GIS . . . . . Gas-injection system

GOS . . . . . Generalised oscillator strength

HAADF . . . . High-angle annular dark field

HCP . . . . . Hexagonal close-packed

HPUF . . . . . Hydrogen pickup-fraction

IHPUF . . . . Instantaneous HPUF

ICA . . . . . Independent component analysis

LOCA . . . . . Loss-of-coolant accident

MLLS . . . . . Multiple linear least squares

NanoSIMS . . Cameca nanoscale secondary ion mass spectrometry instrument

PCA . . . . . Principal component analysis

PWR . . . . . Pressurised water reactor

ROI . . . . . Region-of-interest

SE . . . . . Secondary electrons

SEM . . . . . Scanning electron microscope

SI . . . . . Secondary ion

SI . . . . . Spectrum image

SIMS . . . . . Secondary ion mass spectrometry

SPP . . . . . Second phase particle

STEM . . . . . Scanning transmission electron microscope

TEM . . . . . Transmission electron microscope

TM . . . . . Trademark

ZLP . . . . . Zero-loss peak

SEM . . . . . Scanning electron microscope

SE . . . . . Secondary electron

1 Preface

Contents

1.1 Motivation 1
1.1.1 The MUZIC collaboration 1
1.2 Conventions 2

1.1 Motivation

1.1.1 The MUZIC collaboration

MUZIC-2, or “Mechanistic Understanding in Zirconium Corrosion 2” was a collaboration between Westinghouse, Rolls-Royce, Électricité de France (EDF), University of Oxford, University of Manchester, Imperial College London, Chalmers University and Pennsylvania State University. The programme began in 2012 and ended in 2016, and supported many researchers and doctoral students - including myself - on their work on zirconium. Its focus was on the mechanisms of hydrogen pickup of non-irradiated zirconium cladding alloys. The precursor to MUZIC-2 was MUZIC-1, which focused on the oxidation alone, rather than hydrogen pickup. As a result, many experiments done during the MUZIC-2 program were built upon the discoveries from MUZIC-1. At the time of writing, MUZIC-3 has begun, and builds on the results of MUZIC-1 and 2 to study "hot" samples, zirconium that

has been irradiated in reactor. As will become apparent, considering either the oxidation or hydrogen pickup alone will not be enough to understand the corrosion of zirconium alloys, and whilst we have made huge progress into understanding the nature of zirconium oxidation, there is still much left to learn.

After an amount of time in autoclave or in-reactor, the corrosion rate of zirconium alloys accelerates. During this time, the oxide grows rapidly and the weight gain of the alloy increases, before the corrosion rate slows and the oxide grows at a slower rate. This breakdown of protective oxide is termed "transition", and is a process that repeats periodically as a function of time.

Figure 1.1 shows the weight gain until first transition during oxidation in water of a large range of materials in an autoclave at 360 °C. The oxidation and weight gain measurements were done by Westinghouse for the MUZIC-2 programme, and the alloys made available for this project. The composition of these alloys varies by only a few percent, yet we see a large difference in their corrosion resistance. Understanding the mechanism of corrosion is crucial to producing alloys that offer better corrosion resistance.

Another way of looking at the alloys is to compare what they look like just before transition. Corrosion-resistant alloys tend to have a very slow corrosion rate just before transition, as seen in figure 1.2. Here I have calculated the slope of the weight gain curve just before transition, and plotted the days until transition against it, for a myriad of alloys that have been part of the MUZIC programme. As can be seen, there is a tendency for alloys with a steep slope to hit transition early.

1.2 Conventions

As most of my work has been with oxidised zirconium in cross-section I have made a natural decision in terms of convention. For the TEM section, whenever I present an image of the oxide-metal interface, one can, unless otherwise labelled, expect to find the oxide at the top of the image, and the metal on the bottom. For the NanoSIMS section the oxide will be on the left and the metal on the right as they will often be compared with line profiles drawn in the same direction.

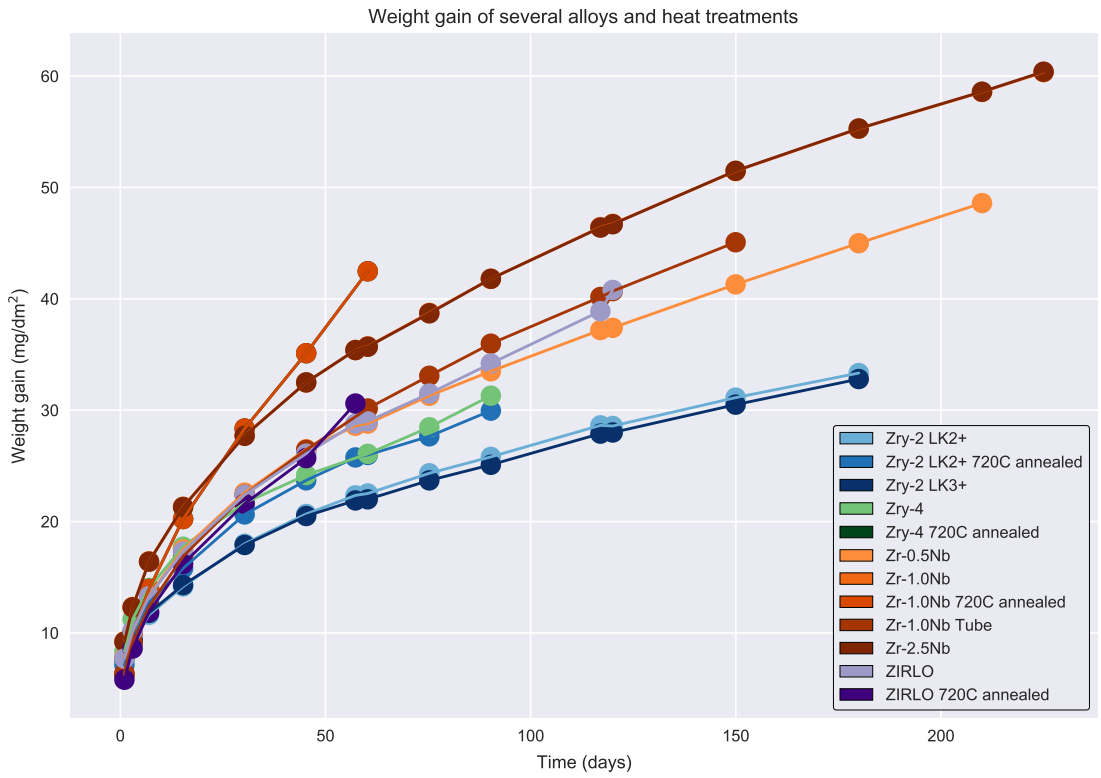


Figure 1.1: Weight gain during oxidation at 360 °C until first transition. The alloys labelled "annealed" describe alloys that were exposed to a higher-temperature anneal for 24 hours at 720 °C

In some cases (SEM, FIB and STEM) the signal is easily rotatable before acquisition to order the image, whilst in others (TEM and NanoSIMS) the orientation of the sample is fixed relative to the detector. Where practical, these results have been rotated to be of most convenience to the reader, whilst in others (for instance where the orientation is 45° to the image frames) the result is simply labelled.

The automatically set contrast and brightness values on images that come straight out of the microscope are often not ideal for emphasising the features that are interesting. Therefore, images will by necessity have been modified (contrast and brightness) to emphasise contrast between grains or other features. In cases where further image processing has taken place it is mentioned in the figure caption.

Finally, due to software text encoding limitations, labels designating the micron length scale are sometimes converted to "um", rather than "µm".

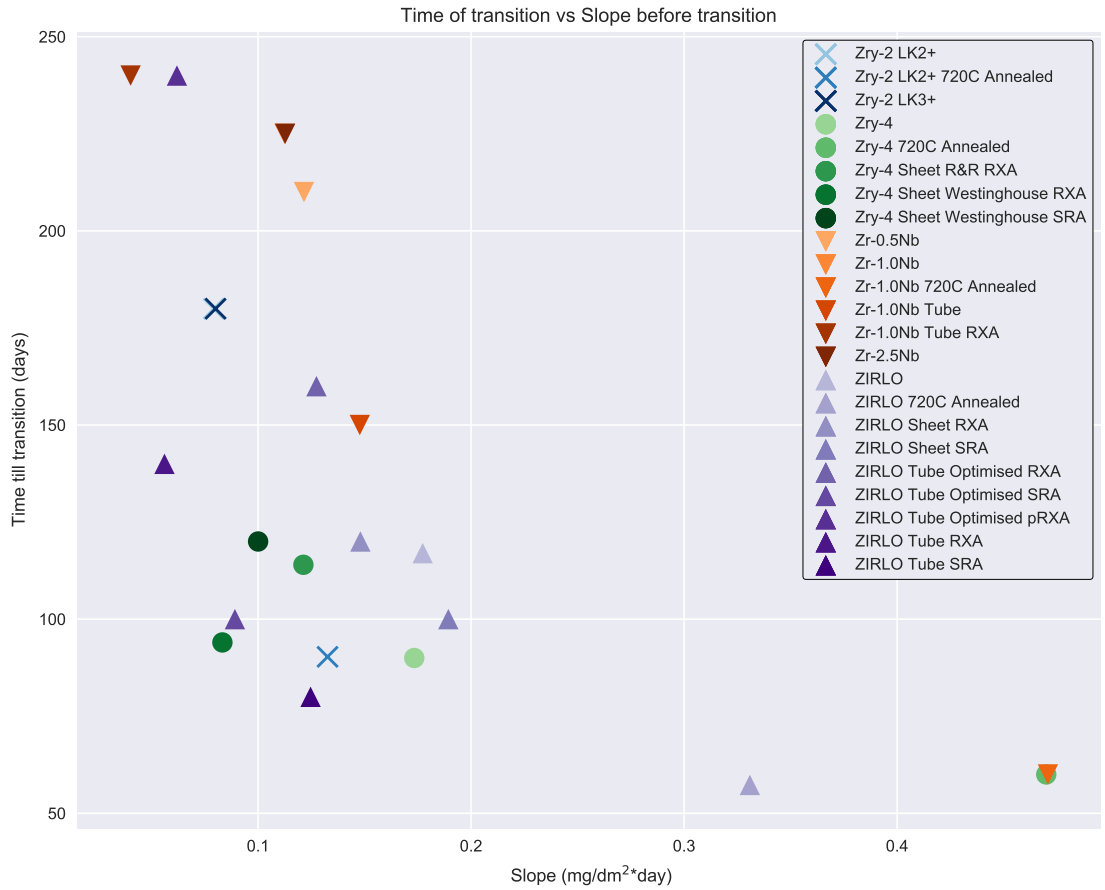


Figure 1.2: The time until transition against the final gradient of the oxidation curve for alloys oxidised at 360 °C

2

Literature Review

Contents

2.1 Introduction 6
2.2 Zirconium and zirconium alloys 6
2.2.1 Physical properties 7
2.2.2 Zirconium in the nuclear industry 8
2.3 Zirconium alloys 9
2.3.1 The Zircaloy family 11
2.3.2 The Zr-Nb alloys 11
2.3.3 ZIRLO 14
2.4 Oxidation 14
2.4.1 Transition 15
2.4.2 Zirconia 17
2.4.3 Oxidation kinetics 18
2.4.4 Pre-transition 21
2.4.5 Post-transition 22
2.4.6 Transition mechanism 24
2.4.7 Mechanical breakdown of the oxide 25
2.4.8 Oxide phase transformation 26
2.4.9 Dissolution of the alloying elements in the oxide 27
2.4.10 Suboxide phase at the metal-oxide interface 28
2.5 Hydrogen pickup 30
2.5.1 Delayed hydride cracking 32
2.5.2 Hydrogen content in the oxide 33
2.5.3 Hydrogen pickup mechanisms 33
2.5.4 Effect of alloying elements on hydrogen pickup 39
2.6 Effect of sample preparation 49
2.7 Summary 50

2.1 Introduction

This review will present an introduction to the relevant literature on the topic of zirconium alloys as cladding material in the nuclear industry. The focus of this work is to understand the corrosion and hydrogen pick-up mechanisms of modern zirconium alloys used for cladding purposes in light water reactors.

First an introduction to the physical properties of zirconium and a short history of its relevance to the nuclear industry is given. Then an overview of the current alloys in industry and research is presented, with focus on their corrosion properties and how they differ. A detailed discussion on the corrosion of zirconium and its alloys is then given, before moving on to the hydrogen pick-up mechanisms and properties. Finally, a short discussion on the effect of sample preparation is given.

2.2 Zirconium and zirconium alloys

Since the 1950s the development of zirconium fuel cladding has led to the creation of a myriad of zirconium alloys. These alloys were developed through empirical means, by mixing elements and testing them, and whilst much effort has been spent trying to understand the underlying processes behind their strengths and weaknesses, the mechanisms behind their corrosion resistance has remained a mystery.

Zirconium as an element was first discovered as zirconia in Sri Lanka by Martin Heinrich Klaproth in 1789. However, it was first isolated into zirconium metal in 1824 by Jöns Jacob Berzelius. Zirconium was not found to have particularly interesting properties for a long time. It would take a hundred years, until 1925, before its distinguished properties began to appear, with the refining of zirconium into zirconium sponge and further into “crystal bar”, which became the name for high purity, ductile zirconium metal [1].

Zirconium was first used as a “getter” in vacuum tubes, but it was also recognised that its corrosion resistance would be desirable in surgery, chemical equipment,

electrical parts and even jewellery and tableware, cost and supply permitting [2]. However, it is the low neutron cross-section of zirconium that has led to the writing of this thesis.

Today, several commercial alloys exist, each one optimised for specific conditions. In the U.S. and Europe, Zircaloy-2 was developed to be used in boiling water reactors. Later on, Zircaloy-4 was created by Westinghouse for the higher temperature and pressure conditions of pressurised water reactors. In Canada and Russia, zirconium alloys with niobium as a major component were developed instead. With improved corrosion- and creep-resistance ZIRLO, and later on, "Optimized ZIRLO", were developed as a successor to Zircaloy-4, the latter of which was first put into operation in a Spanish reactor in 2000, although in the USA they were first used in-reactor in 2008 [3]. Zirconium alloys for nuclear applications remain very much an important topic of research.

2.2.1 Physical properties

As the 40th element in the periodic table, zirconium is a transition metal with a relative atomic mass of 91.22. Its sister elements are titanium and hafnium, which behave very similarly except for those properties for which the nucleus becomes important [2]. Its density is $6.511\,\mathrm{g\,cm^{-3}}$, placing it roughly somewhere between titanium and iron. As a nuclear cladding material, the most important advantage over other metals is zirconium's low neutron absorption cross-section of 0.18 barn [2].

Pure zirconium metal has two allotropes. It can either exist in the hexagonal close packed (HCP) alpha-phase or the body-centred cubic (BCC) beta-phase, according to the phase diagram in figure 2.1 [4]. At room temperature, and up to 862 °C, the pure metal is in the HCP α-phase. As nuclear reactors, even at the fuel, do not exceed a temperature of 862 °C [5], the bulk metal generally exists in the HCP structure. It will be seen though that internal stresses, especially at the metal-oxide interface may affect the material phase, which can have a significant effect on its properties.

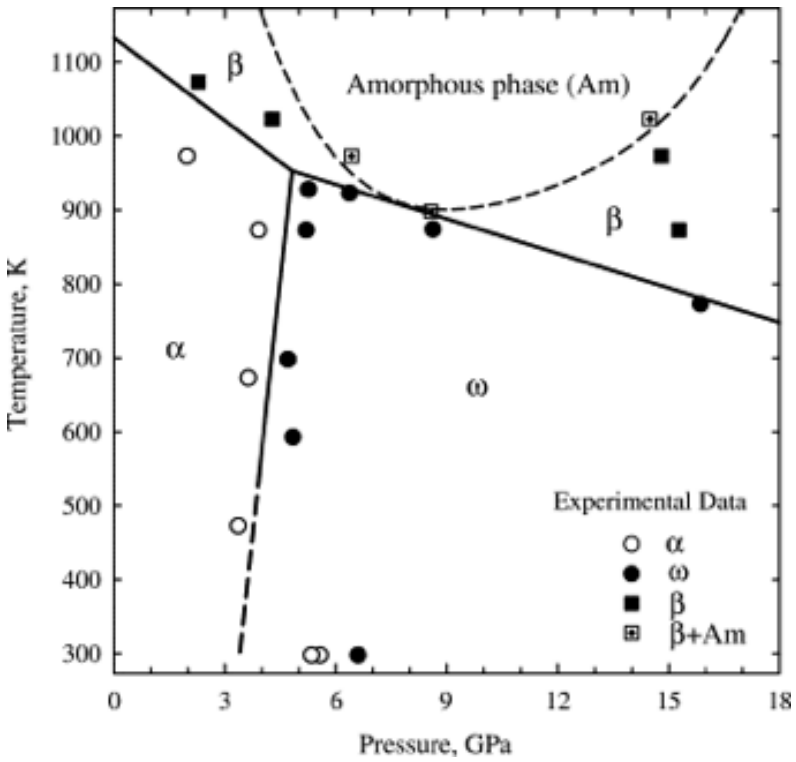


Figure 2.1: The pressure-temperature phase diagram of zirconium [4]

At very high pressure zirconium can transform to a hexagonal omega-phase, as seen on the phase diagram in figure 2.1. In the reactors with highest pressure, pressurised water reactors (PWR), the pressure is of the order of 100 bar, or 0.01 GPa, which is far from the required pressure for transformation.

The HCP alpha-phase lattice parameters a and c are 0.323 nm and 0.514 nm respectively, giving it a constrained unit cell with an axial ratio of 1.591. This compares the ideal close-packed hexagonal ratio of 1.633, which controls many of the mechanical properties, as the energy of the different kinds of dislocations in the hexagonal lattice depend on this ratio [6].

2.2.2 Zirconium in the nuclear industry

Zirconium possesses a combination of properties that makes it uniquely suited for use as cladding material in nuclear reactors. The required material properties for cladding materials in water-cooled reactors are the following [7, 8]:

- 1. Low neutron capture cross-section to prevent material damage and prevent the cladding from moderating the fission reaction by absorbing neutrons.
- 2. Good corrosion resistance against the aqueous atmosphere to prevent leakage of nuclear fuel.
- 3. Adequate strength and ductility to support the structure under high stress and thermal gradient.

Other materials were considered as well: beryllium, magnesium and aluminium were all candidates for cladding materials, and even stainless steels have been used. In the end, for most commercial reactors zirconium was chosen for a combination of satisfactory and safe manufacturing techniques, mechanical properties as well as abundant supply of zirconium ore, an increasingly low price, and its aforementioned exceptionally low neutron absorption cross-section [2].

It was in the early 1950s [9, 10] especially in water-cooled reactors, that zirconium was selected for both cladding purposes and as a material for other structural fuel assembly components. The temperature in these reactors is $300 \pm 50\,^{\circ}\mathrm{C}$ [11], where the corrosion resistance of zirconium is excellent.

The corrosion resistance of pure zirconium was found to be improved by adding up to 5% of different metals to create an alloy. These small amounts of additional elements significantly change the kinetics of oxidation and hydrogen pickup. The most common added metals are tin, niobium, chromium, iron and nickel. However, due to the number of different types of alloys and varying processing steps over the years, it is difficult to quantify the exact effect of the various alloying elements. An attempt is made in the next sections.

2.3 Zirconium alloys

Over the past 60 years there have been two primary binary alloys used in the nuclear industry. The United States and most of Europe have used the zirconium-tin system whilst the USSR/Russia and Canada used the zirconium-niobium system. The

Alloys	Sn / wt. %	Fe / wt. %	Cr / wt. %	Ni / wt. %	Nb / wt. %	O / wt. %
Zircaloy-2	1.2 - 1.7	0.07 - 0.2	0.05 - 0.15	0.03 - 0.08	-	*
Zircaloy-4	1.2 - 1.7	0.18 - 0.24	0.07 - 0.13	-	-	*
ZIRLO	0.9 - 1.2	0.1	-	-	0.9 - 1.13	0.09 - 0.15
Zr-1Nb (M5)	-	0.015 - 0.06	-	-	0.8 - 1.2	*
Zr-1Nb (E110)	-	0.006 - 0.012	-	-	0.95 - 1.05	≤ 0.1
Zr-2.5Nb	-	≤ 0.15	≤ 0.02	≤ 0.007	2.4 - 2.8	0.09 - 0.13

Table 2.1: Composition of standard zirconium alloys. Oxygen content in all alloys ranges from 1100 to 1400 ppm [14–16].

zirconium-tin system became significant with the introduction of the Zircaloy in the 1960s [12, 13].

Of these systems, many variations of alloys have been developed over the past 60 years, most notably the Zircaloy-2, Zircaloy-4, ZIRLO and Zr-Nb alloys. The low solubility of the alloying elements in zirconium means that most alloys are quite dilute. The most common compositions can be seen in table 2.1. The specific effect of adding each alloying element is discussed in a later section.

According to Lustman [2] and Schwope [17], the large possible selection of alloying elements can be divided into five groups. The important alloying elements in zirconium alloys today and relevant corrosion species have been emphasised in bold:

- Alpha-stabilisers (alloying elements that raise the alpha – beta transition temperature): Al, **O**, **Sn**, **N**, B.
- Beta-stabilisers (lower the alpha – beta temperature): **Nb**, Ta, Th, U.
- Eutectic and eutectoid: Ag, Be, Co, **Cr**, Cu, **Fe**, **H**, Mn, Mo, **Ni**, V, W.
- Miscellaneous: C, Ge, Si, Pd.
- Complete solid solubility: Hf, Ti.

There was an early belief that adding alloying elements would increase the plasticity of the oxide, therefore allowing greater oxide thickness before transition [18]. However, other models suggest that adding the elements increases the conductivity of the oxide [19] or enhances anion vacancy populations and increases oxygen migration [20]. Because they have low solubility in Zr metal, most of these trace

additions are found in small second phase particles (SPPs) of a variety of different structures and compositions [21–23].

2.3.1 The Zircaloy family

Tin was initially added to zirconium, creating Zircaloy-1, to counteract nitrogen impurities, which were present in zirconium sponge and found to cause rapid corrosion and spalling of the oxide scales [2, 24]. However, it became apparent that only ≈1% tin, compared to the added 2.5% tin was needed to fully counteract the detrimental effect produced by nitrogen. The remaining alloy elements proved valuable for corrosion resistance, and are described in section 2.5.4. This lower-tin Zircaloy became known as Zircaloy-2.

Of the Zircaloy variations, it is Zircaloy-2 and Zircaloy-4 that are particularly of commercial importance. Except for hydrogen pickup, Zircaloy-4 exhibits essentially the same properties as Zircaloy-2. Zircaloy-2 demonstrates three times the hydrogen pickup of Zircaloy-4. This high hydrogen absorption, resulting in precipitation of ZrH_2, causes embrittlement [25]. Compositionally, Zircaloy-4 is almost identical to Zircaloy-2, but without nickel, and is used in pressurised water reactors (PWRs) because of its better resistance to hydrogen pickup, as there is a higher concentration of hydrogen present in these reactors [26]. Figure 2.2 shows an example of the Zircaloy-4 cladding tubes studied in this project, before and after corrosion.

For all the Zircaloys, tin has only been found in solid solution, and does not form precipitates in the matrix. For lower temperatures (T<600 °C) iron and chromium are present in precipitates in the form of SPPs ranging in sizes from 10 nm to 1000 nm. The structure, size and composition of these SPPs is found to be linked to the alloy's corrosion behaviour [27].

2.3.2 The Zr-Nb alloys

The primary alternative zirconium alloy to the Zircaloys has been binary zirconium niobium. The Zr-Nb alloys include the Canadian Zr-0.5Nb, Zr-1Nb and Zr-2.5Nb (where the number before Nb refers to weight-percent of niobium in the zirconium



Figure 2.2: Examples of several unoxidised (far left) and oxidised zirconium cladding tubes used in this project

matrix), but also the Russian E100, E125, E635 and the French M5 alloys (where the numbers are for identification purposes only). These alloys have no tin content, differ mainly in their niobium content, and slightly in their composition of other alloying elements.

Researchers from Atomic Energy of Canada Limited [28–30] demonstrated that Zr-2.5Nb corrosion was not accelerated by radiation and did not undergo a transition, as Zircaloy-2 did. The lack of transition was attributed by Cox et al. [31, 32] to Zr-2.5Nb always having an impervious protective oxide that maintained a constant-thickness protective film.

M5 is one of the latest Nb-based alloys and is still in development. It has a chemical composition very similar to the other Zr-1Nb alloys, and exhibits very slow corrosion kinetics, and also very low hydrogen-pickup, with and without irradiation [33]. As seen in figure 2.3, the maximum oxide thickness as a function of burnup (or time in reactor) is significantly lower for M5 than for Zircaloy-4. Figure 2.4 shows how the hydrogen-pickup content of M5 is also lower. The same was shown for the materials corroded in an autoclave without radiation.

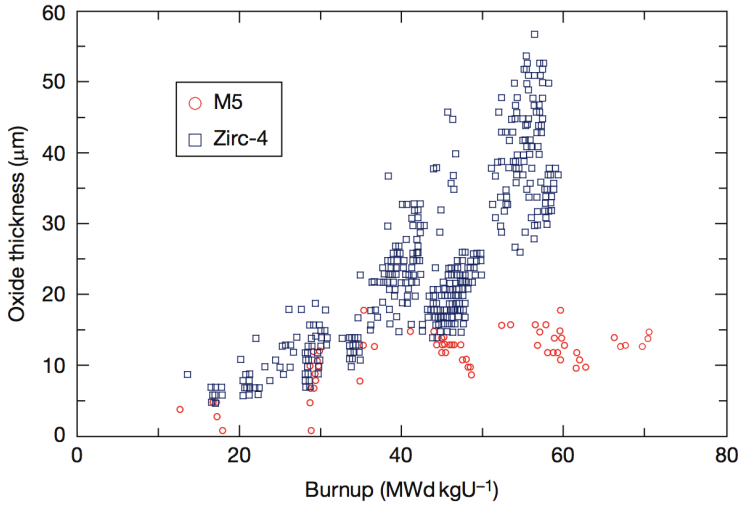


Figure 2.3: Peak oxide layer thickness as a function of burnup for Zircaloy-4 and Zr-1Nb (M5) [33].

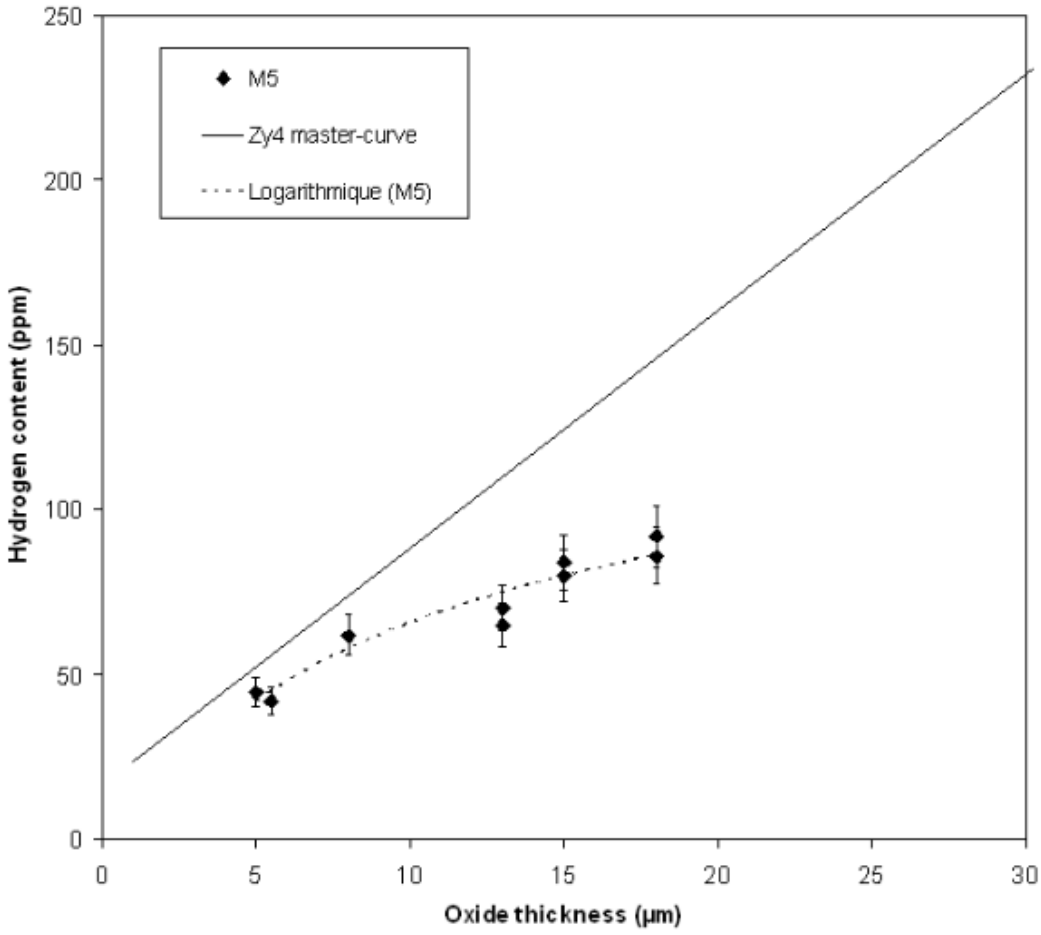


Figure 2.4: Comparison of the hydrogen content of Zircaloy-4 (solid black line) and M5 (scattered) as a function of oxide thickness [33].

2.3.3 ZIRLO

ZIRLO (Zirconium Low Oxidation) is an intermediate between the Zircaloys and the Zr-Nb alloys, containing significant concentrations of both Sn and Nb. In the late 1960s information feedback from plants indicated excellent corrosion resistance by Zircaloy-4 in PWRs. In contrast, test reactor data appeared to give very conflicting results, often indicating orders of magnitude higher corrosion rates [10]. This set in motion research for better zirconium alloys. ZIRLO was first referred to by name in 1992, but has only fairly recently become a commercial alloy. It was developed as a successor to Zircaloy-4 by Westinghouse Electric Company, with improved corrosion- and creep-resistance. Optimized ZIRLO was developed as the successor to ZIRLO, again improving corrosion resistance [3], by reducing tin content.

2.4 Oxidation

The aqueous corrosion of zirconium is mainly related to the oxidation of zirconium by oxygen in the coolant, either dissolved or produced by radiolysis of H_2O. Oxygen has a small solubility in the metal, but once the concentration of oxygen exceeds the solubility limit zirconia, ZrO_2 is formed on the surface, according to equation 2.1.

$$Zr + O_2 \rightarrow ZrO_2 \tag{2.1}$$

As zirconium readily oxidises in air, any component that has been exposed to the atmosphere will have a thin oxide film on the surface, approximately 2 nm to 5 nm thick. This air-formed oxide can be relatively problematic for microanalysis, as will be seen later in the energy-dispersive X-ray and electron energy loss spectroscopy sections of Chapters 4 and 5. The oxide acts as a protective barrier against further oxidation, especially in air, and to a degree in water. Much evidence exists to suggest that the aqueous oxidation of zirconium occurs through the ingress of oxygen ions through the oxide layer, either through the bulk oxide, or along grain boundaries [34–36]. For aqueous corrosion, oxidation happens according to equation 2.2.

$$Zr + 2\,H_2O \rightarrow ZrO_2 + 4\,H \tag{2.2}$$

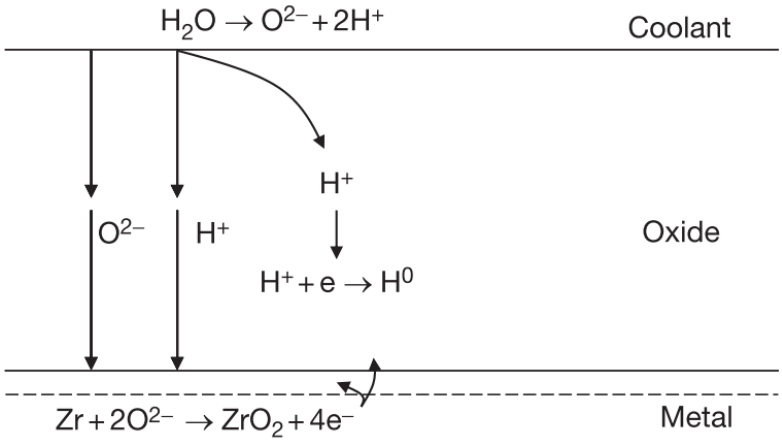


Figure 2.5: Schematic presentation of the corrosion of the zirconium alloys [37].

The ingress of oxygen ions is shown in figure 2.5. As the oxidation rate slows down as the oxide thickness increases, it has been argued that the rate controlling step in the oxidation process is either the diffusion of oxygen in through the oxide film [37, 38], or the diffusion of electrons out through the oxide film. In order to maintain neutrality of charge, these processes are necessarily coupled. Transport of electrons through the oxide is difficult - the ceramic oxide is an insulator, although doping of the oxide has been suggested as a possibility for increasing conductivity [39].

2.4.1 Transition

Generally for metals, a film of oxide becomes a barrier to further oxidation growth, as it prevents the oxidation species access to fresh metal. For zirconium this holds true initially, as the rate of oxidation slows down, labelled as "pre-transition" in figure 2.12.

However, after a condition-dependent time at this slow oxidation rate, the rate accelerates significantly, and the alloy acts as if there was almost no barrier to oxidation at all. This is called the transition point. A new layer of oxide forms, and the previous behaviour repeats, temporarily slowing down further oxide growth. As a result of this, the alloy undergoes cyclic oxidation. This cyclic oxidation has been shown to be remarkably regular, upwards of 17 transitions as shown in figure 2.6.

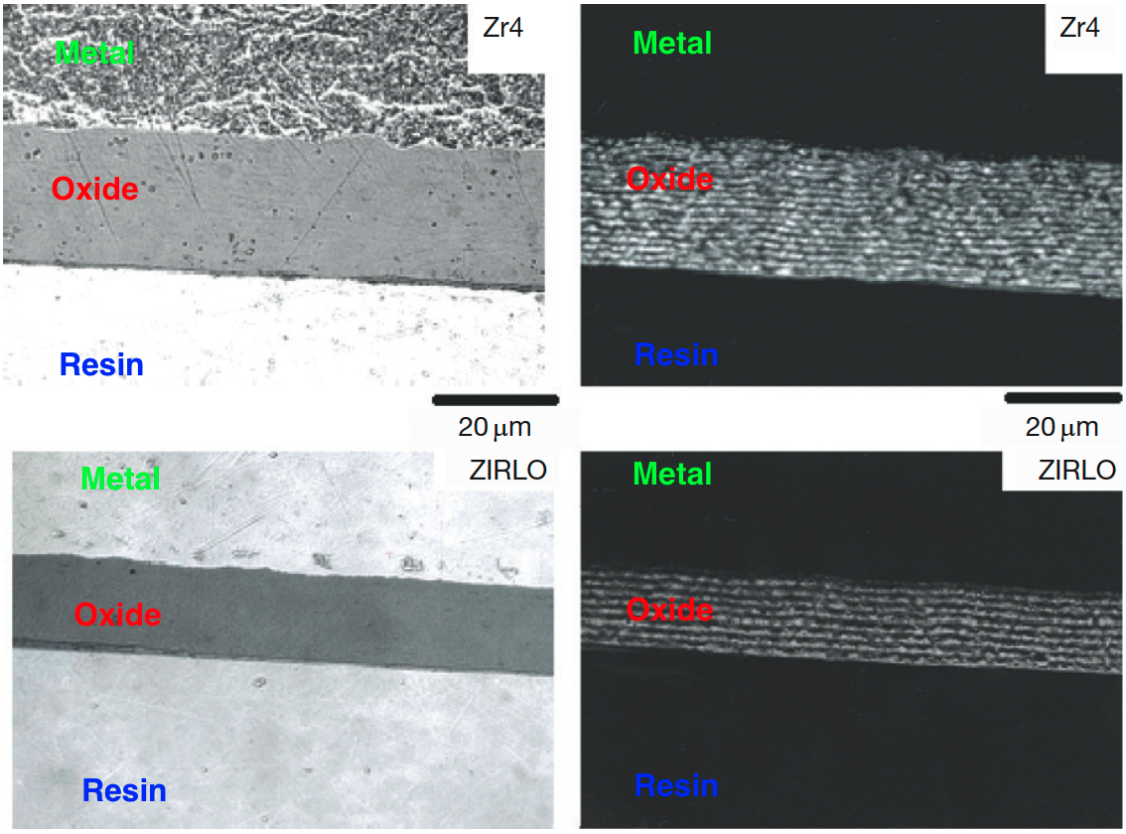


Figure 2.6: Optical micrographs of oxide layers formed in (top) Zircaloy-4 and in (bottom) ZIRLO^{TM}, in reflected (left) and transmitted light (right) [40].

Zirconium metal in contact with oxygen in air at room temperature will spontaneously oxidise to form a thin layer on the surface of the metal. The oxygen reacts according to equation 2.1. Zirconia protects the metal from further corrosion in air, but in the hot, high-pressure aqueous conditions of the reactor, the oxygen somehow bypasses the protective oxide and further corrodes the metal, shown in a typical optical micrograph in figure 2.7. Here the oxide has grown to about 20 µm. The equation for aqueous corrosion is given in equation 2.2. This is the type of corrosion that will be referred to in later discussion. During this aqueous corrosion, atomic hydrogen is released, of which some is absorbed into the metal, some in the oxide, but most is released into the coolant. This is further discussed in Chapter 6.

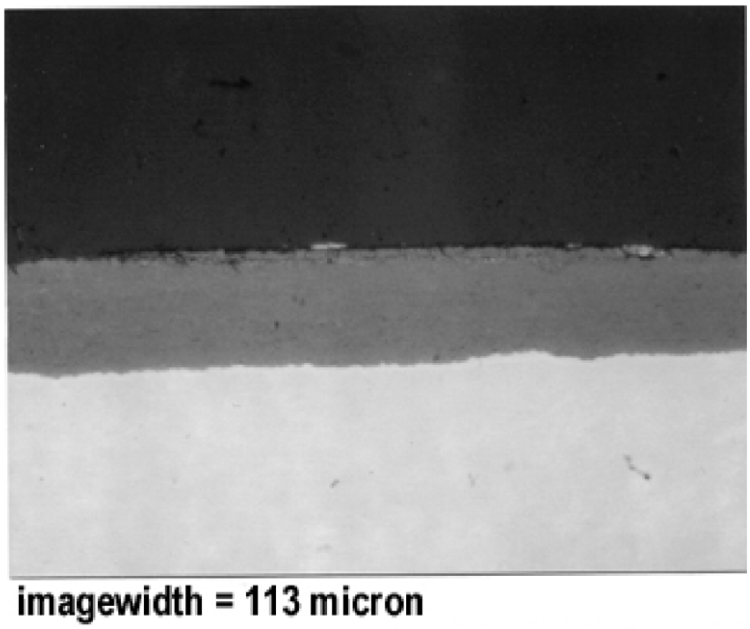


Figure 2.7: Typical optical micrograph of the oxide grown on Zircaloy-2 [41]. The metal is the light grey section lowest on the image and the oxide in the middle.

2.4.2 Zirconia

Zirconia has a relative atomic mass of $123.22\,\mathrm{g\,mol^{-1}}$ and a density of $5.89\,\mathrm{g\,cm^{-3}}$. In the context of nuclear cladding, pure zirconia could exist in three phases. As shown in the phase diagram in figure 2.8, from 0 °C and up to 1200 °C the oxide has a monoclinic crystal structure. Between 1200 °C and 2372 °C the material is tetragonal and between there and its melting point at 2680 °C it is cubic. Again, due to the typical temperatures and pressures in operating reactors, the zirconia is expected to be monoclinic. According to the phase diagram the pressure needs to be at least an order of magnitude larger than standard PWR pressure (100 bar) for zirconia to transform to its orthorhombic structure.

Investigation of the oxide [40, 43, 44] reveals that the oxide on zirconium alloys is a mixture of monoclinic and tetragonal zirconia phase, dominated in phase fraction by the monoclinic phase. The tetragonal phase is believed to be stabilised by localised stresses, grain sizes, and the dissolved alloying elements [45, 46]. The tetragonal grains appear in higher densities near the metal-oxide interface than in the bulk oxide, which is consistent with other studies [47].

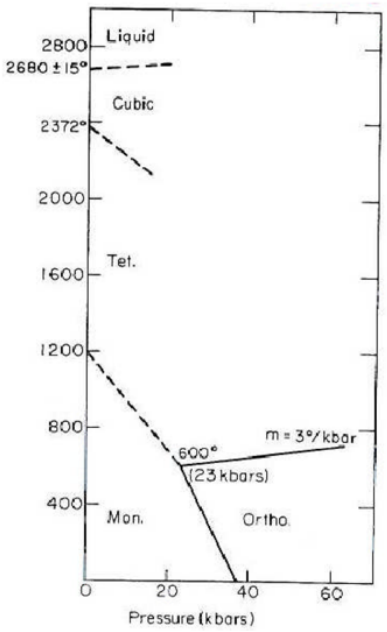


Figure 2.8: Temperature-pressure phase diagram for zirconium oxide [42]

If zirconium is kept at elevated temperatures over time, an oxide much thicker than 40 nm will grow. Figure 2.9 shows the oxide of a sample of Zircaloy-4 after 800 days in a BWR [48]. Here the thickness has reached 9 µm.

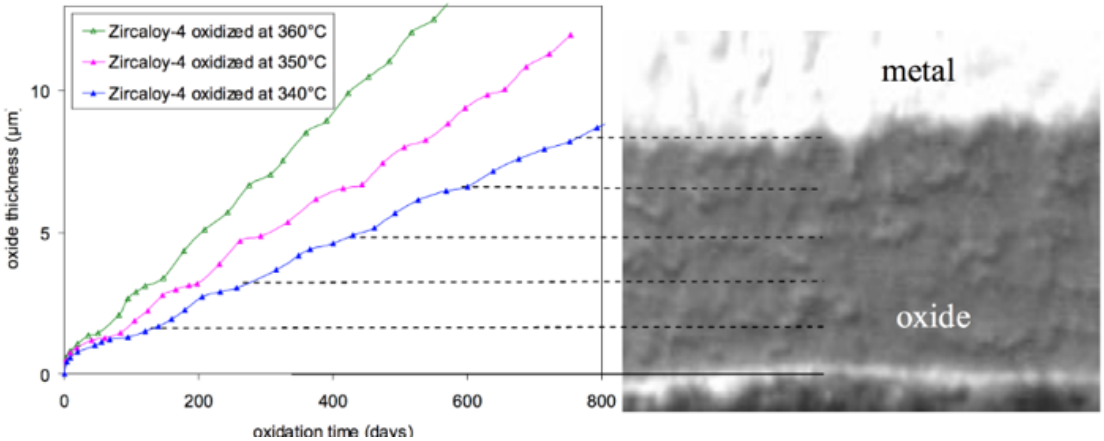


Figure 2.9: The oxide thickness of Zircaloy-4 oxidised over 800 days. [48]

2.4.3 Oxidation kinetics

Before the transition, the kinetics may be described by the rate equation [49]:

$$(\Delta W)^n = kt \tag{2.3}$$

where ΔW is the rate, often measured as weight gain, k and n are constants for the material at a given temperature and t is time.

In the literature [50], the expression is also sometimes formulated slightly differently. This second expression is what is most often returned when fitting a power law with software. One should be aware that the value of k will be slightly different between the two expressions. When fitting the weight gain data in Chapters 4 and 5, it this expression that is used.

$$\Delta W = kt^n \tag{2.4}$$

Many investigators agree that n can either be fitted as 1/2 (parabolic) or 1/3 (cubic) [51, 52]. The parabolic rate is characteristic of a freely diffusion-limited process, where it is the rate of transport of oxidation species to the metal surface that limits the oxidation. The cubic rate is related to reduced oxygen diffusion as a result of crack formation at or near the metal-oxide interface, or due to changes in grain shape or increased grain growth reducing the available grain boundaries that can allow oxygen transport.

As one would expect, the corrosion rate increases with temperature. Hillner et al. [53] provided a database of long-term (up to 29 years!) weight-gain measurements of Zircaloy-2 and Zircaloy-4 oxidised at different temperatures. These are well into the *far* post-transition linear regime of oxidation, where $n = 1$ (in equation 2.3). In equation 2.3, k is the result of the Arrhenius equation:

$$k = B \exp(\frac{-Q}{RT}) \tag{2.5}$$

where B is an empirical constant with units $\mathrm{mg\,dm^{-2}\,d^{-1}}$, Q is the activation energy for the linear corrosion region in units $\mathrm{J\,mol^{-1}}$, R the universal gas constant, $8.31\,\mathrm{J\,mol^{-1}\,K}$ and T the absolute temperature, in units of K.

Calculation using weight-gain and temperature data for Zircaloy-4 oxidised for 2500 days, seen in figure 2.10, resulted in a fit of equation 2.5 for $B = 2.47 \times 10^8\,\mathrm{mg\,dm^{-2}\,d^{-1}}$ and $Q = 107\,030\,\mathrm{J\,mol^{-1}}$ in the earlier stage (stage 1, still far post-transition in the context of this thesis) of oxidation, and $3.47 \times 10^7\,\mathrm{mg\,dm^{-2}\,d^{-1}}$

and $Q = 95\,170\,\mathrm{J\,mol^{-1}}$ in the later stage (stage 2) of oxidation. At the oxidation temperature typically used for the alloys studied in this thesis, 360 °C, the value of k for these two regimes are $0.36\,\mathrm{mg\,dm^{-2}\,d^{-1}}$ and $0.49\,\mathrm{mg\,dm^{-2}\,d^{-1}}$.

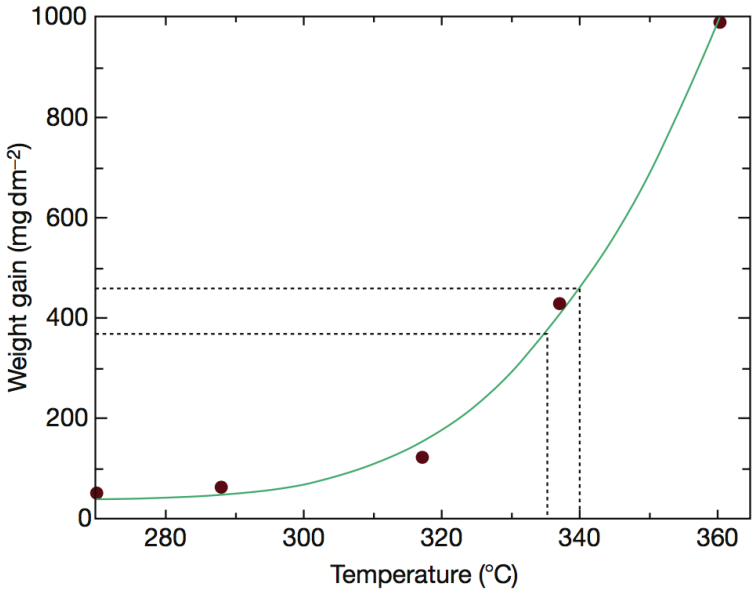


Figure 2.10: The temperature dependence of weight-gain of Zircaloy-4 oxidised for 2500 days [53, 54].

As previously mentioned, the rate-limiting step to oxidation could either be the transport of oxygen in through the oxide or the transport of electrons out. Howlader et al. [55] measured the electrical conductivity of 3 µm thick oxide scales on Zircaloy-2 and Zircaloy-4, as seen in figure 2.11. They concluded that it must be oxygen diffusion that is the rate-limiting factor in oxidation. However, this is shown only for these alloys after oxidation in autoclave for 8 h at 407 °C followed by 16 h at 507 °C. This makes them difficult to place relative to transition - it is not clear whether the oxides are in a stage of fast or slow oxidation at the time of measurement, so electron-limited corrosion could still be a possibility at other stages of the oxidation process.

The oxidation kinetics of zirconium alloys has been studied for over 60 years, and is still not properly understood [2, 56]. Where other materials tend to initially grow a protective oxide that then prevents further oxidation, oxidation of zirconium can be divided into two regimes: An initial period of slow oxidation followed by

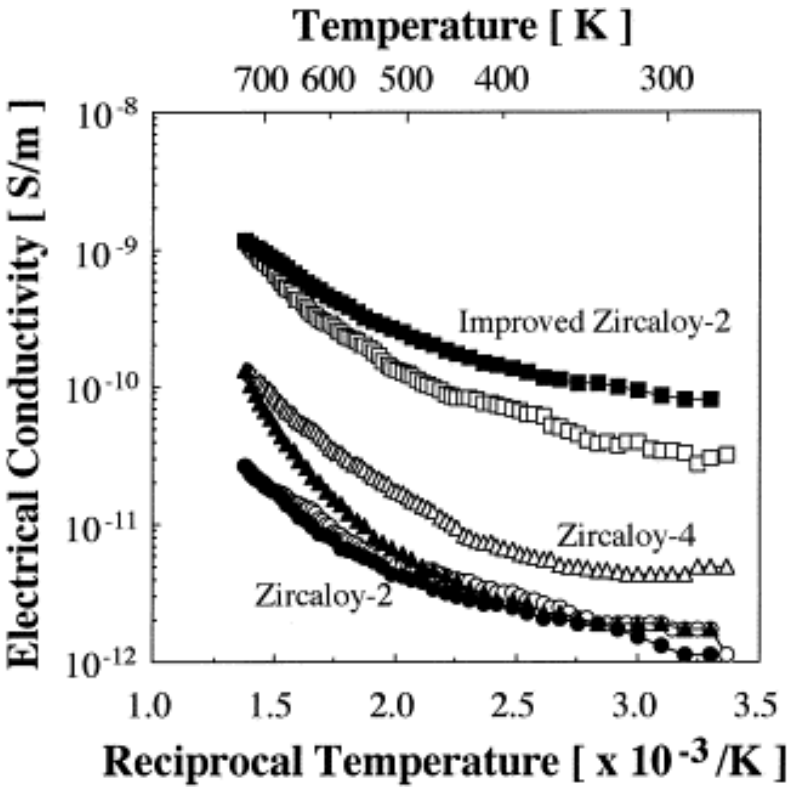


Figure 2.11: The conductivity of various oxide alloys, with oxide thicknesses of 3 µm [55]

oxidation at an accelerated rate [26, 35, 45, 57–61]. This general characteristic of zirconium alloys can be seen in figure 2.12 [53]. The change from slow to accelerated rate has been called "failure", "breakdown" and "transition" [34, 35, 57, 59, 61–64]. It is the latter that will be used in this review.

As the oxide is assumed to consist entirely of zirconium and oxygen, it is convenient to measure its growth as weight gain. An oxide thickness increase of 1 µm is equivalent of a weight increase of 15 mg dm^{-2} [53, 65].

2.4.4 Pre-transition

In the pre-transition regime, corrosion can be fitted accurately using equation 2.3. General observations show that the pre-transition oxide is compact with some porosity and micro-cracks but no large cracks. The grain structure is mainly columnar but interspersed with equiaxed grains, although the transformation of columnar grains to equiaxed in the outer parts of the oxide has been reported.

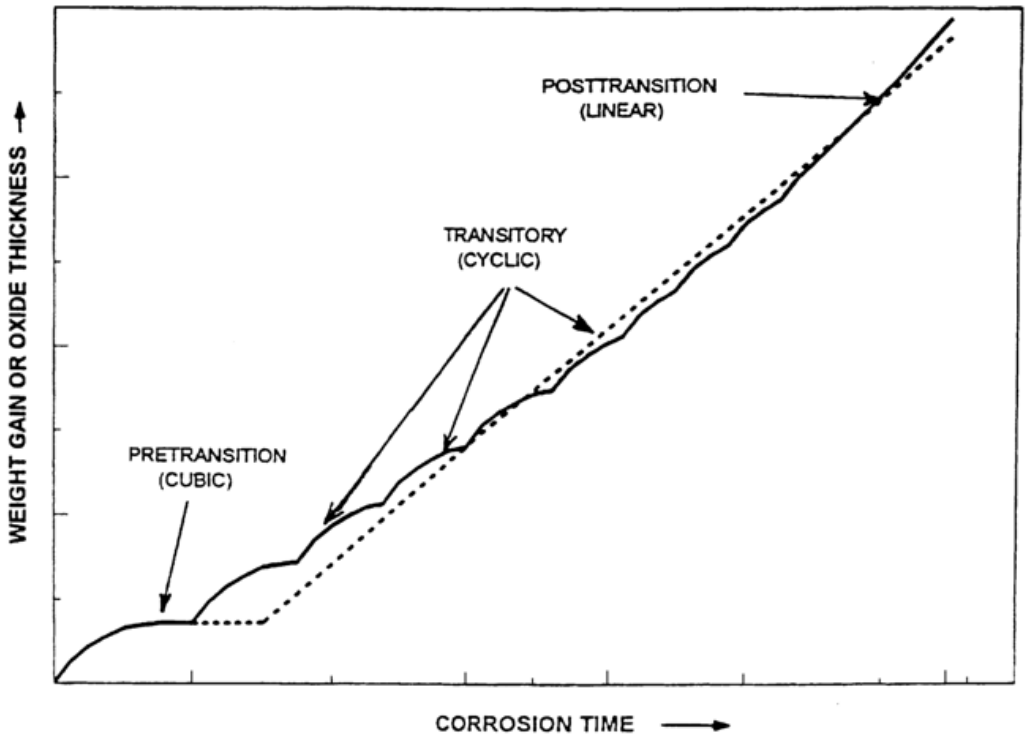


Figure 2.12: Typical example of the rate transition of the aqueous corrosion of a zirconium alloy [53].

However, presence of mainly equiaxed grains has also been reported [61, 66, 67]- in more corrosion resistant alloys in some cases [68], but the opposite has also been found in other research [66]. Finally, no correlation has been found in other cases [61].

Cox and Pemsler [34] showed that during pre-transition the diffusion of oxygen through the oxide is about five orders of magnitude faster than the lattice diffusion coefficient. Thus they conclude that the diffusion must be via crystallite boundaries or other easy path, for instance defects or SPPs.

2.4.5 Post-transition

The rate transition has been the focus of many studies [9, 18, 35, 60, 69–74] and is still poorly understood. The transition normally occurs when the oxide thickens to about 2 µm, where the rate speeds up significantly.

The oxide has been shown to grow by the following sequence. First small grains of oxide nucleate with a relatively high percentage of tetragonal grains. The existence

of the tetragonal phase is explained as stabilisation of this structure due to the small grain size. These oxide grains grow in a columnar fashion, and as they increase in size they transform into the monoclinic phase. This transformation has a volume increase associated with it, which increases stresses in the oxide [75]. It has been found that the oxygen ions predominately diffuse from the coolant along crystallite boundaries into the oxide [44, 66], and it has been proposed that electrons move in the opposite direction to complete the corrosion circuit along paths associated with second-phase particles (SPPs), or due to the semiconducting properties of the oxide [19].

The post-transition quasi-linear time dependency, shown in figures 2.9 and 2.13 has been shown [76] to actually be a periodic behaviour, repeating the pre-transition behaviour in small steps at short to intermediate exposure times. This periodic growth is directly observable by secondary electron microscopes (SEM) [77], and is shown on the right of figure 2.9.

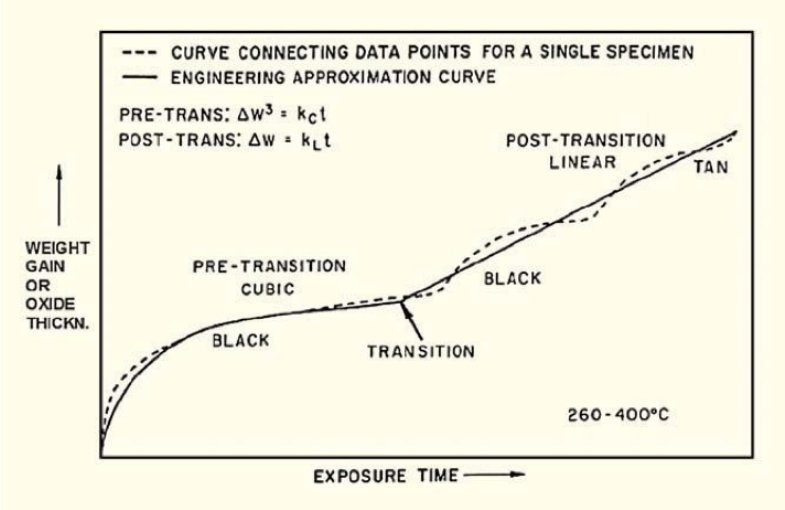


Figure 2.13: Representation of the corrosion behaviour of Zircaloy-4 in the temperature range 260 °C to 400 °C [78].

Each cycle of the corrosion process has its own value of k in equation 2.3. The origin of the activation energy, Q (in equation 2.5) and the rate-limiting process is currently under debate. The rate-limiting factor may be the transport rate of electrons or the transport rate of oxygen to the corrosion site. However, from experiments that measure the potential drop across the oxide during oxidation, it

has been concluded that at least during early oxidation stages it is the electron transport that is the rate determining process [9].

The post-transition linear part (after several cycles have occurred) has been argued to be due the cyclic corrosion rate at different areas on a sample being out-of-phase with each other. These local corrosion rates smooth out the average weight gain over time, giving the impression of a linear corrosion rate where the cyclic corrosion behaviour still is in effect [76].

Beie et al. [79] suggested that post-transition oxidation was governed by oxygen anion diffusion through a "barrier layer" at the metal oxide interface, and illustrated with an equilibrium argument that several rate limiting steps may exist at different areas in the oxide. Several of the rate-limiting steps can be visualised in figure 2.14. Here the zirconium metal is on the left, the oxide is in the middle and the coolant is on the right.

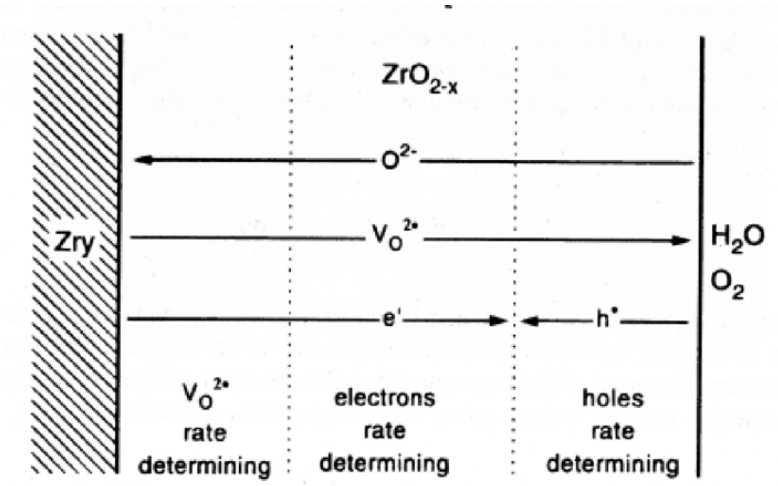


Figure 2.14: A diagram suggesting some of the possible rate determining steps for the oxidation zirconium [79].

2.4.6 Transition mechanism

The mechanism yielding the transition described above has been heavily debated, and there exist several potential explanations for why it happens as it does. However, it has become clear that the transition is related to the breakdown of a protective oxide that exists close to the metal-oxide boundary. For the transition to occur, something

must happen to this inner oxide, for instance the development of pores or cracks. In early suggestions the cracks were proposed to form in the vertical directions, perpendicular to the surface [80]. Instead, the majority of cracks have been found in the lateral direction [21, 38, 81]. There has been debate that these cracks are due to sample preparation for transmission electron microscopes (TEM), but the cracks have also been shown to exist using SEM with gentler sample preparation techniques. Yilmazbayhan et al. [40] studied a sample of Zircaloy-4 oxidised at 360 °C for 784 days. The sample would have gone through many transitions. Very ordered cracks are visible when imaged through a transmitted light microscope, as seen in figure 2.6, suggesting that large cracks and transition are strongly linked.

2.4.7 Mechanical breakdown of the oxide

The simplest explanation is the direct mechanical breakdown of the inner oxide due to a build-up of too high stress levels. The Pilling-Bedworth ratio for corrosion of the alpha-phase, the ratio of the unit cell volume of the oxide to the metal is 1.56. This means that when the oxide thickness grows, a compressive stress at the metal-oxide interface develops, and plastic deformation occurs. This may lead to the occurrence of microcracks and pores [2, 59].

Yardley et al. [82] oxidised low tin ZIRLO in ^{18}O and ^{2}H spiked water after a normal-water pre-oxidation, and found that major lateral cracks in the oxide (seen in figure 2.16) could impede transport of ^{18}O whilst smaller (particularly vertical) cracks (figure 2.15) clearly acted as pathways for oxidation. TEM analysis of the ^{18}O-rich region halfway through the oxide in figure 2.15(A) showed that the equiaxed grain region matches well with the ^{18}O signal. Porosity in the equiaxed grain region [83] is thought to be the explanation for the distribution of ^{18}O. NanoSIMS analysis, the technique used for studying the isotopes, is described in Chapter 3.8 to study the ingress of deuterium through the oxide of several alloys in deuterium-spiked water.

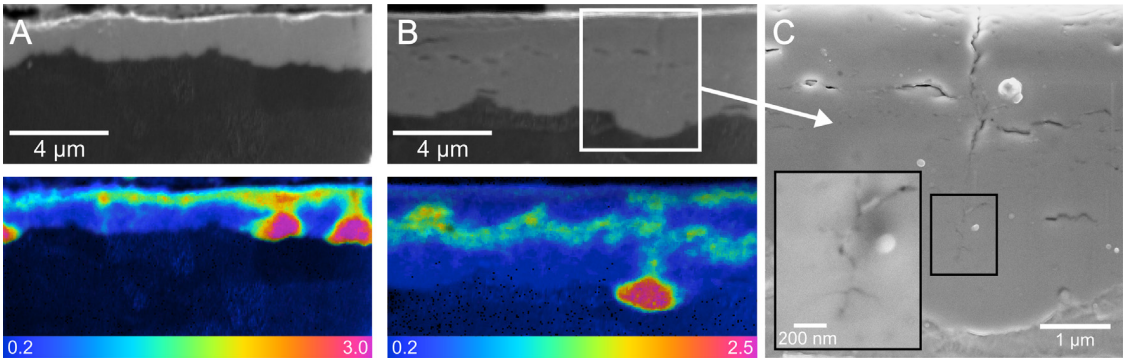


Figure 2.15: Vertical cracks allowing transport of ^{18}O through (A) pre-transition and (B) post-transition ZIRLO oxide [82].

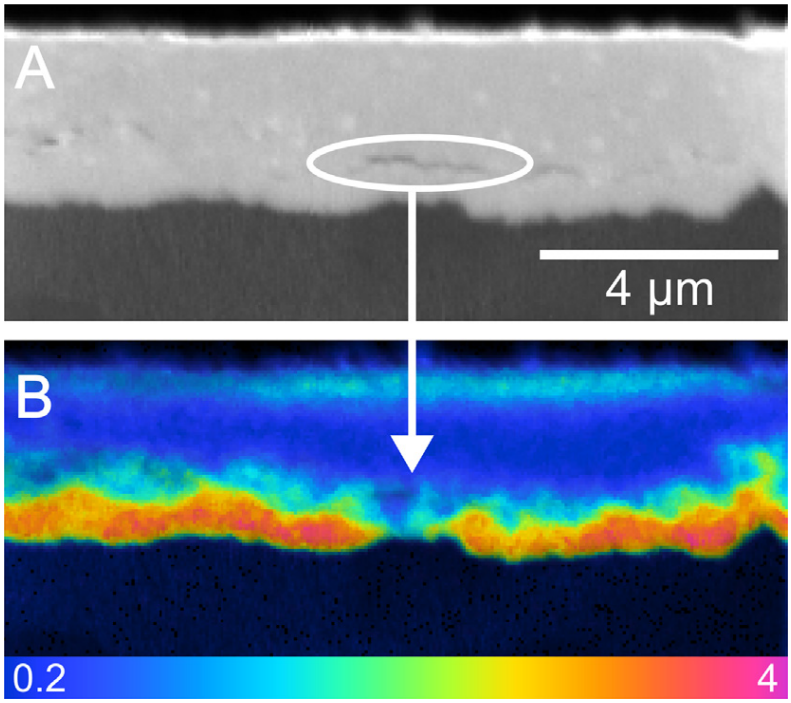


Figure 2.16: Horizontal cracks reducing transport of ^{18}O through a post-transition ZIRLO oxide [82].

2.4.8 Oxide phase transformation

Whilst monoclinic zirconia is the predominant phase of the zirconia formed during corrosion, tetragonal oxide has a tendency to occur close the metal-oxide interface [65, 84]. This phase transformation is considered martensitic in nature, and has a volume expansion of 3 % to 5 %. The tetragonal oxide, normally unstable in nature, is at least temporarily stabilised by the compressive stress due to the Pilling-Bedworth ratio as described above, and possibly by other factors such as grain size

and effects due to the alloying elements. Over time, further slow corrosion may decrease the stresses around the metastable tetragonal oxide. The stresses decrease because the oxide is closer to the waterside of the oxide. There is strong evidence that this leads to at least some of the tetragonal oxide transforming back into the monoclinic oxide, increasing the number of cracks and interlinking of pores [85, 86].

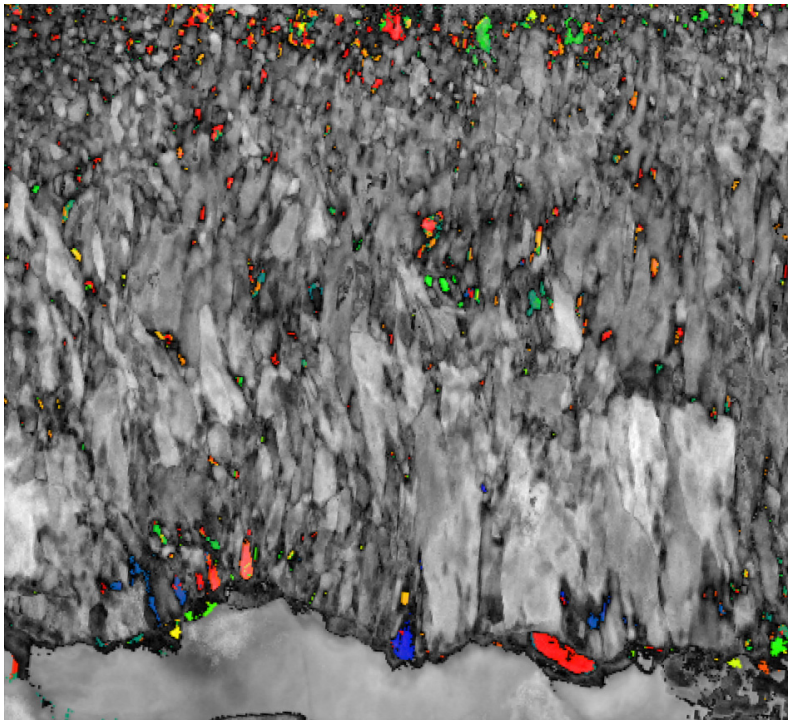


Figure 2.17: Tetragonal grain mapping in Zircaloy-4 in TEM [87]

Garner et al. [87] observed tetragonal grains in the size range 5 nm to 30 nm throughout the oxide in Zircaloy-4, shown in figure 2.17. They are believed stabilised by the small grain size rather than by stress, as the majority of the macroscopic stress in the oxide is relieved upon sample preparation of the thin foil.

2.4.9 Dissolution of the alloying elements in the oxide

The alloying elements dissolved in the Zr-matrix may leave the material once the zirconium has become zirconia, due to lower solubility in the oxide than in the coolant. Therefore the dissolution of the elements in SPPs may result in the formation of pores and cracks in the surface. Dissolution of iron from SPPs has been shown for heavily oxidised SPPs, although it is more frequently shown on irradiated alloys [88–90].

2.4.10 Suboxide phase at the metal-oxide interface

Many authors have described a thin "intermediate" or "sub-oxide" layer at the metal-oxide interface, for instance phases with stoichiometry Zr_3O or ZrO [91]. It often has a characteristic sawtooth shape, as seen in figure 2.18.

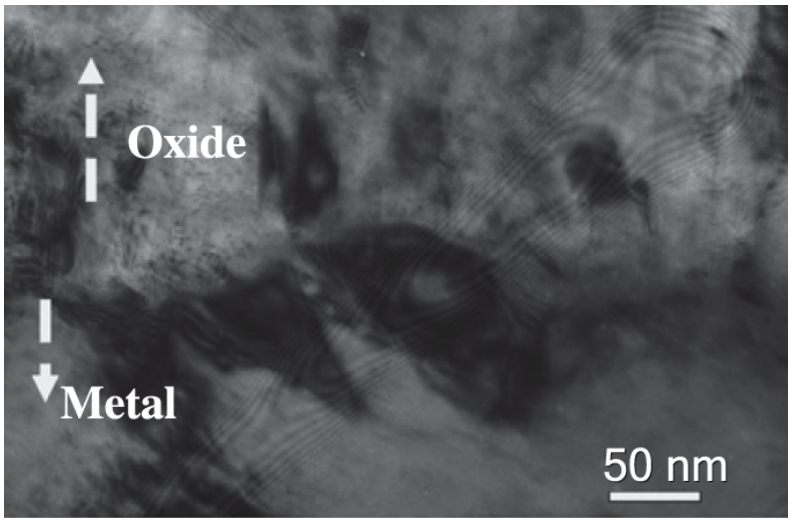


Figure 2.18: Sawtooth-shaped suboxide (black) at the metal-oxide interface of recrystallised ZIRLO oxidised in water for 100 days at 360 °C [47].

A cubic rock salt structure has also been suggested to exist, but without any recent evidence [92, 93]. The same layer has been analysed more recently by electron energy loss spectroscopy (EELS) [71] and atom probe tomography (APT) [47], finding compositions very close to ZrO during the slow oxidation regime in pre-transition. Using stoichiometric ZrO_2 standard powders, to get the energy loss for the Zr M edges and the O K edge, Ni [71] measured the Zr:O ratio in line profiles across the interface. It was found that the suboxide thickness could vary from zero to up to 140 nm, with the thickest regions found on samples at early post-transition. An oxygen saturated metal layer immediately beneath the oxide in the metal was also studied, and found to have a decreasing oxygen concentration as one moved away from the interface and into the metal. This region was found to be thickest in the late pre-transition samples (≈200 nm) and thinner in the early pre- and post-transition (≈50 nm). An example of the oxygen concentration of a sample of recrystallised ZIRLO oxidised for 100 days in water at 360 °C can be

seen in figure 2.19 [47]. There are distinct plateaus designating the ZrO_2, ZrO and oxygen-saturated metal regions on the line profile in (b).

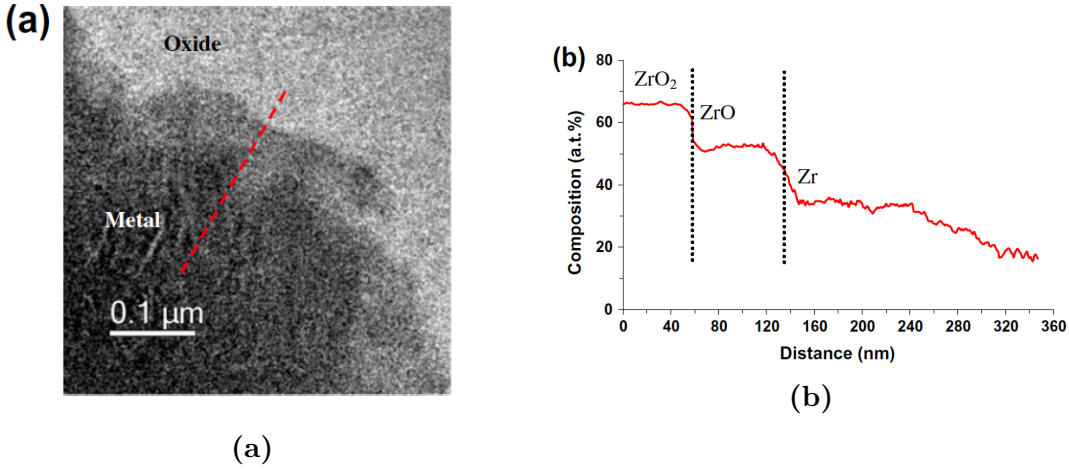


Figure 2.19: (a) Oxygen EFTEM map and (b) EELS oxygen concentration across the metal oxide interface on a sample of recrystallised ZIRLO oxidised for 100 days in water at 360 °C [47].

Nicholls et al. [94] combined density functional theory (DFT) modelling with experimental results, and found two stable forms of ZrO, an orthorhombic structure and a hexagonal structure. These, along with the experimentally shown cubic rock-salt structure, are shown in figure 2.20.

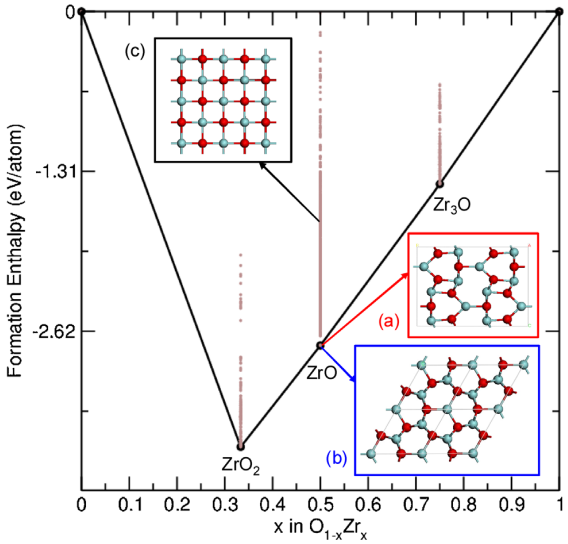


Figure 2.20: DFT modelling of the zirconium-oxygen binary system. The stable orthorhombic (a) and hexagonal (b) are shown, as is the (c) cubic experimentally found phase [94].

The predicted hexagonal structure was found experimentally by Garner and Hu [95] at the metal-oxide region from a development alloy with composition Zr–0.9Nb–0.01Sn–0.08Fe. The structure was found by transmission electron backscatter diffraction (also called transmission Kikuchi diffraction) on an SEM. The grains with the hexagonal structure can be seen in yellow in figure 2.21.

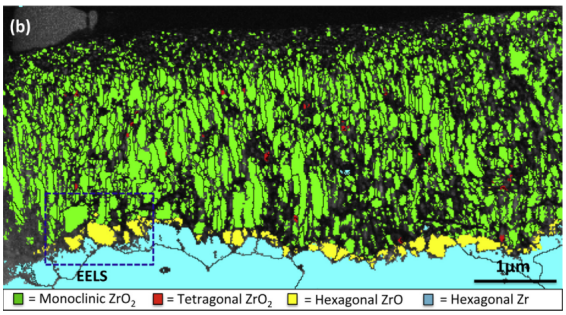


Figure 2.21: Hexagonal suboxide grains found at the metal-oxide interface [95].

2.5 Hydrogen pickup

As shown in equation 2.2, hydrogen is also produced when the cladding reacts with water. Of the total amount of produced hydrogen, a fraction is absorbed into the alloy. This is referred to as the hydrogen pick-up fraction (HPUF). The total HPUF can be anywhere from 2 % to 3 % up to 40 % [90] of the hydrogen released from H_2O during oxidation. The derivative of HPUF with time is known as the instantaneous HPUF.

Hydrogen pickup has been shown to be linked to the oxidation rate, so controlling the hydrogen pickup would be conducive to reducing oxidation. Hydrogen that is immediately expelled into the coolant during oxidation can be controlled for by pH balancing the coolant. However, should all the hydrogen contained in the cladding be expelled simultaneously, the hydrogen gas could explode in the presence of oxygen, as happens in loss of coolant accidents (LOCA).

Metal areas over-saturated with hydrogen form hydrogen precipitates. These precipitates are hydrogen binaries with zirconium and are thus hydrides. The hydrides can be visualised in the secondary electron micrograph in figure 2.22.

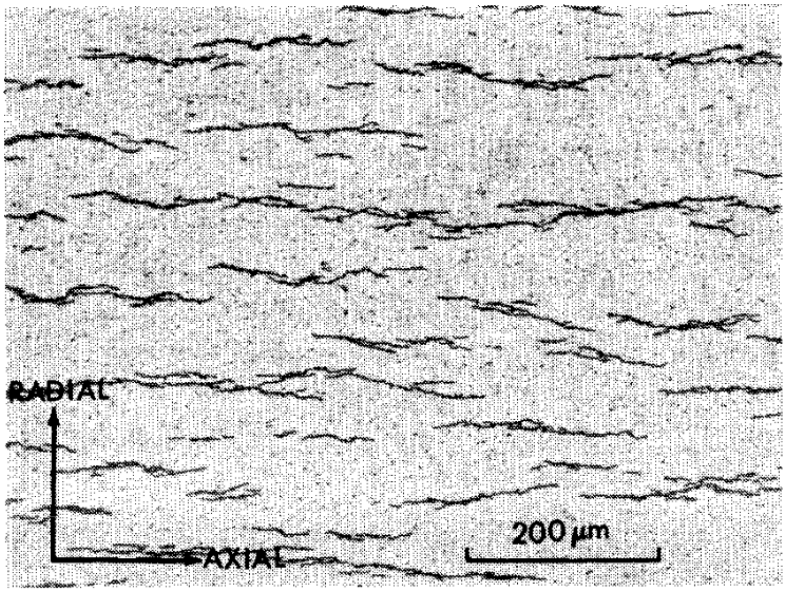


Figure 2.22: Typical SEM micrograph of zirconium hydrides present in the metal. Here a longitudinal section of a Zr-2.5Nb alloy containing ≈300 ppm hydrogen [96].

The hydrides do not much change the mechanical properties of the zirconium at high temperature. At room temperature, however, the precipitating hydrides can embrittle the bulk metal due to the aforementioned volume expansion [97]. This lowers the fragile/ductile transition temperature of the alloy. The phase diagram of the zirconium – hydrogen binary system is presented in figure 2.23.

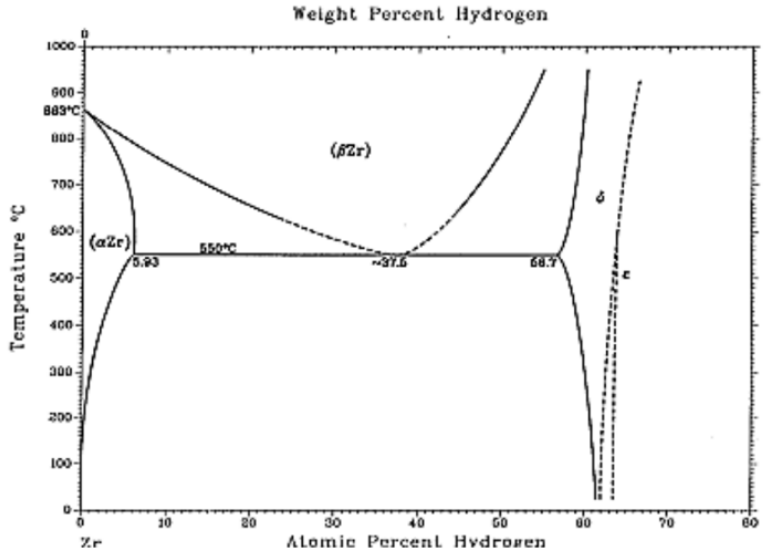


Figure 2.23: Phase diagram of the binary zirconium-hydrogen system [98].

2.5.1 Delayed hydride cracking

Whilst general oxidation of zirconium has been a problem, it is no longer the main focus of research. Delayed hydride cracking (DHC) has become the new challenge for the nuclear industry [99–102]. Hydrogen is soluble at high temperature in zirconium metal, and is able to freely move around within the matrix [74, 103–106]. However, it has been shown that it is particularly concentrated around areas of high stress, like grain boundaries or dislocations [13, 22, 90, 107]. On cooling, the hydrogen precipitates out, forming zirconium hydrides. The volume expansion in the metal due to the hydride forming adds to the stress, and can cause a crack inside the metal. When the reactor is heated up again, hydrogen again becomes soluble, this time building up around the previously formed crack. Over many cycles, the crack will propagate through the metal [38, 64, 108–111] eventually allowing the coolant to reach unprotected nuclear fuel [102, 106].

Two conditions must be reached for DHC to initiate on a crack [112]:

- The stress intensity factor must be higher than the threshold value for the material.
- The hydrogen concentration must exceed a critical value. The critical value for hydrogen concentration is temperature dependant, but on the order of 10 wtppm to 100 wtppm.

McRae et al. [113] showed that despite hydride precipitates being the assumed microstructural feature responsible for DHC, DHC takes place even when there are no hydrides present. Two models were suggested distinguishing how the DHC takes its first step:

- When hydrides are present in the matrix: A crack under load can induce hydride precipitation due to its load. The formation of the hydride reduces the local hydrogen concentration in the crack. The hydride then grows due to a hydrogen concentration gradient, as the hydrogen concentration is then greater in the bulk than in the crack. This is called the “precipitate first model”.

- When all hydrogen is in solution: A crack under load induces a gradient in the chemical potential that promotes hydrogen diffusion to the crack tip. Hydrides then form if the solubility limit is reached. This is called the "diffusion first model".

2.5.2 Hydrogen content in the oxide

SIMS experiments by Elmoselhi et al. [114] show a large variation in the deuterium content on Zircaloy-2 and Zr-2.5Nb oxidised in deuterated water. On the plots in figure 2.24, a short vertical line indicates the beginning of the metal-oxide interface. In (a) deuterium is found to follow a smooth diffusion profile for two of the alloys, whilst the deuterium keeps a nearly constant concentration throughout most of the oxide for the 360 °C sample. There is the implication of the breakdown of a barrier between the two types of profiles. The deuterium profiles in (b) are much more varied, although again sample oxidised at the highest temperature shows a region nearly constant in deuterium. The 310 °C sample shows an unexpected variation in deuterium in the first micron of the oxide. Reproducible deuterium profiles can be found, as shown in (c).

Muta et al. [115] summarised experimental and calculated values for the diffusion coefficient of hydrogen in zirconia. The results can be seen in figure 2.25. At 360 °C, which was the normal autoclave temperature for this project, the expected value lies in the range $10^{-23}\,\mathrm{m^2\,s^{-1}}$ to $10^{-16}\,\mathrm{m^2\,s^{-1}}$.

2.5.3 Hydrogen pickup mechanisms

The rate of hydrogen pickup is normally constant after the oxidation transition, though will vary depending on the alloy and conditions (temperature, pressure and pH). Harada and Wakamatsu [116] showed that the rates of hydrogen pickup vary a lot during pre-transition as well as during the repeated cycles during post-transition, seen in figure 2.26. They found that as the rate of oxidation decreases, the rate of hydrogen pickup increases. This suggests that the hydrogen pickup rates are strongly related to the barriers associated with the oxidation.

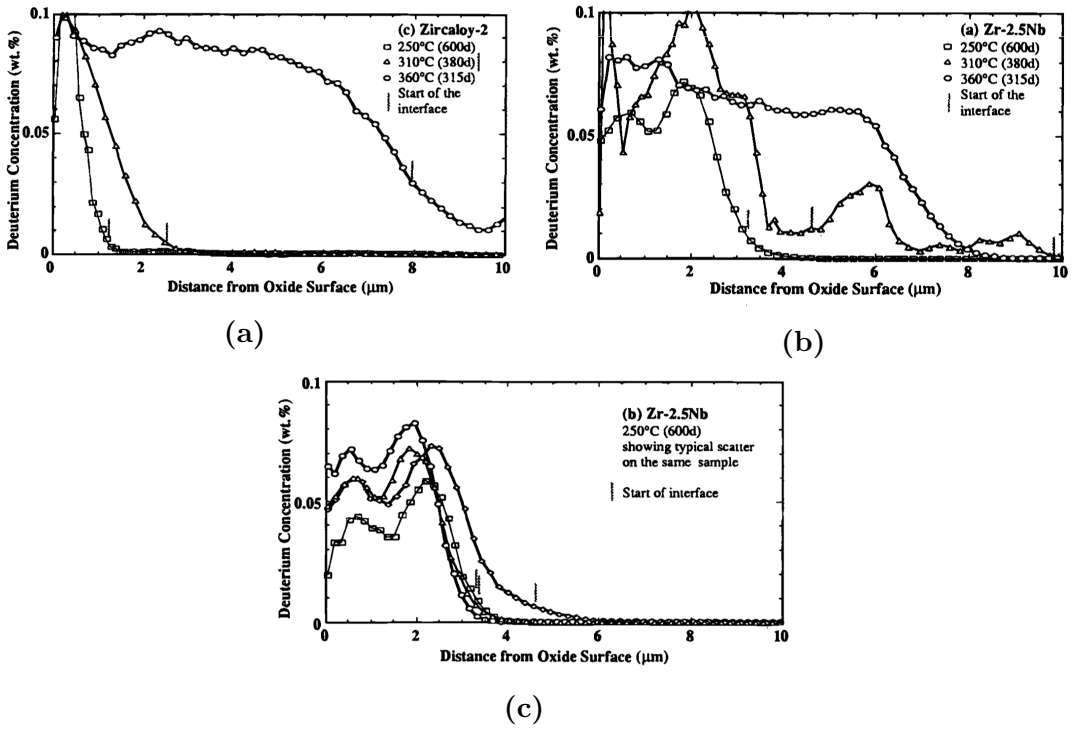


Figure 2.24: Deuterium through-oxide-thickness depth-profiles resulting from out-reactor aqueous exposures to D_2O in autoclaves at 250 °C to 360 °C to for up to 600 days [114].

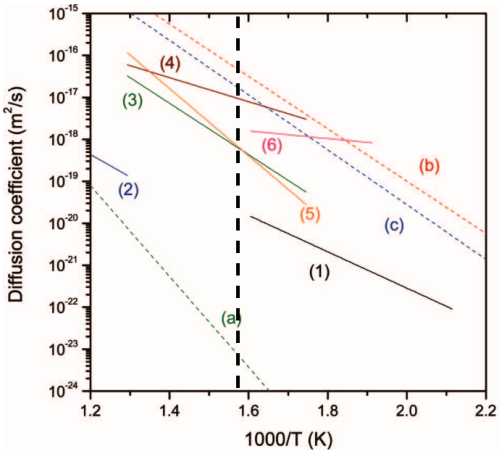


Figure 2.25: Diffusion coefficient of hydrogen in zirconia for a range of temperatures. Dashed lines indicate calculated values, whilst solid lines indicate experimental ones. The vertical black dashed line indicates the temperature most alloys in this project were oxidised at (360 °C) [115].

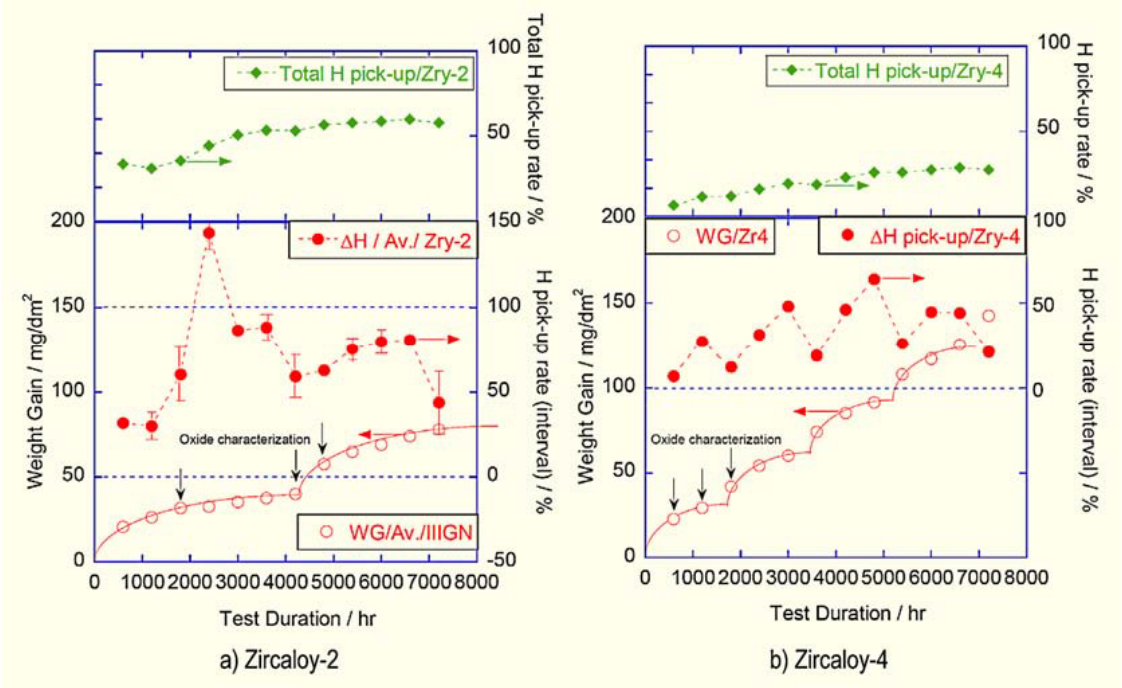


Figure 2.26: From top: Total hydrogen pickup, change in hydrogen pickup and total weight gain for Zircaloy-2 and Zircaloy-4 oxidised at 360 °C in water [116].

The question of what form the hydrogen is in is unanswered. Proposed forms are H^+, H and OH^-, as suggested in the proposed mechanisms below. There are many possible routes for hydrogen migration through the oxide and into the metal. Garzarolli and Cox [90] suggest a range of methods by which hydrogen can pass into the metal. These processes are likely to be competitive, and it is possible that different processes are dominant at different stages of oxidation. The proposed mechanisms are:

- Diffusion of protons or OH^- through the oxide lattice
- Migration of the hydrogen down via pores in the oxide film
- Transport of hydrogen through oxidised SPPs
- Transport of hydrogen through non-oxidised SPPs
- Diffusion of hydrogen in the oxide grain boundaries

Evidence for some of these are presented in the discussion below:

Diffusion of protons through the oxide lattice

Kakiuchi et al. [117] and Une et al. [104] studied zirconium alloys with different iron content and assumed that the diffusivity of hydrogen in the oxide layer was the primary route for hydrogen pickup and that increasing the iron content increases the dissolution of Fe^{3+} into the oxide lattice. They found increasing HPUF with decreasing iron content. Amongst other measurements, Kakiuchi found that the potential gradient across the oxide decreased with iron content. Une then argued that increasing the Fe content (and Fe^{3+} dissolution in the oxide lattice) not only decreases the potential gradient, but also the mobility of interstitial protons. This decrease in mobility is believed to be as the result of the formation of defect clusters of Fe^{3+} containing oxygen vacancies. These arguments form the basis for the argument that it is the rate of diffusion of hydrogen through the oxide is the basic mechanism for hydrogen pickup.

Deuterium analysis by Yardley et al. [82] showed that the metal was rich in hydrides formed on cooling, near the metal-oxide interface as shown in figure 2.27. In the oxide the deuterium counts were very low, and there was a suggestion of a diffusion profile of deuterium going through the oxide. This is in agreement with the literature, as Miyake et al. found an extremely low solubility for hydrogen in zirconium oxide [118], and Bossis et al. [91] and Elmoselhi et al. [114], who saw similar diffusion profiles through the oxide.

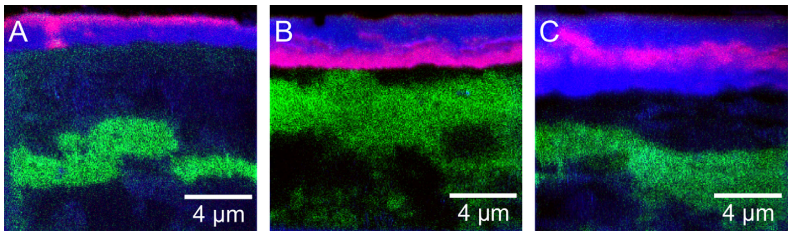


Figure 2.27: Hydrides containing ^{2}H (green) visible in the metal on several samples of oxidised low-tin ZIRLO. The oxide is present at the top of the images, with ^{18}O indicated in purple [82].

Migration down pores in the oxide film

Research by Elmoselhi et al. [114] and Cox and Wong [7] conclude that the most likely locations for the hydrogen to be taken up are the areas where the cracks and pores approach closest to the metal oxide interface. This is demonstrated in the cartoon below in figure 2.28. This research was supported by Ploc [119], who concluded from TEM examination of the oxide layers of Zr-2.5Nb that the deuterium uptake in CANDU reactors is primarily through the boundary between alpha- and beta-zirconia phases.

Copper deposited upon pre-transition alloys revealed [7] that the cathodic sites that the copper was attracted to were almost entirely locations with cracks, rather than SPPs. This argument doesn't fully explain what happens throughout the oxide however.

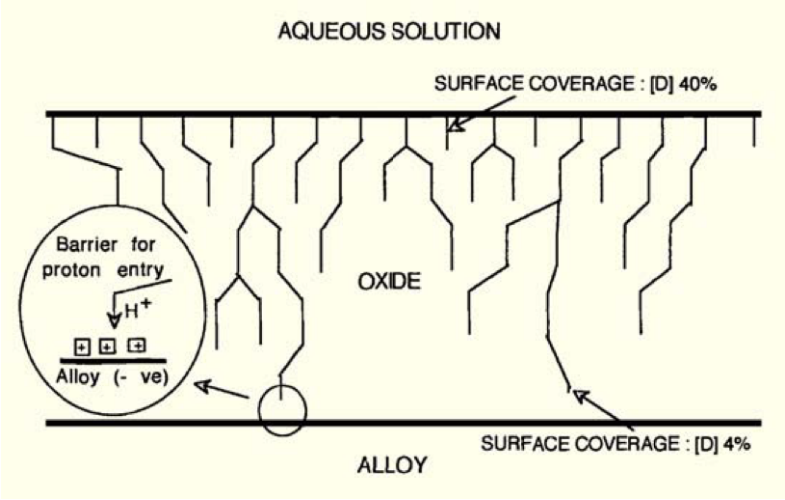


Figure 2.28: Cartoon of the proposed migration mechanism for hydrogen through the zirconium oxide [90]

Transport of hydrogen through SPPs

Hatano et al. [120] studied the effect of varying SPP size on the hydrogen pickup of pre-transition Zircaloy-2 and Zircaloy-4 in 100 bar steam at 350 °C and 450 °C. Slowly β-cooled samples that had SPP sizes around 0.5 µm to 2.0 µm showed $\approx$35 % higher HPUF than fast β-quenched samples with SPP sizes $<$ 50 nm. Hatano concluded that these larger SPPs remain unoxidised in the zirconia and act as a

bridge for the hydrogen through the oxide. The likelihood of the SPPs acting as a bridge does however remain in question. Tejland et al. [21] showed that the size distribution of SPPs in Zircaloy-2 ranged from a minimum of 0.01 µm to a maximum of 0.44 µm with a mean of 0.04 µm. As seen in figure 2.29, the particles are so spread out that even if hydrogen does travel faster in SPPs, the lattice between them will still largely affect the rate of ingress.

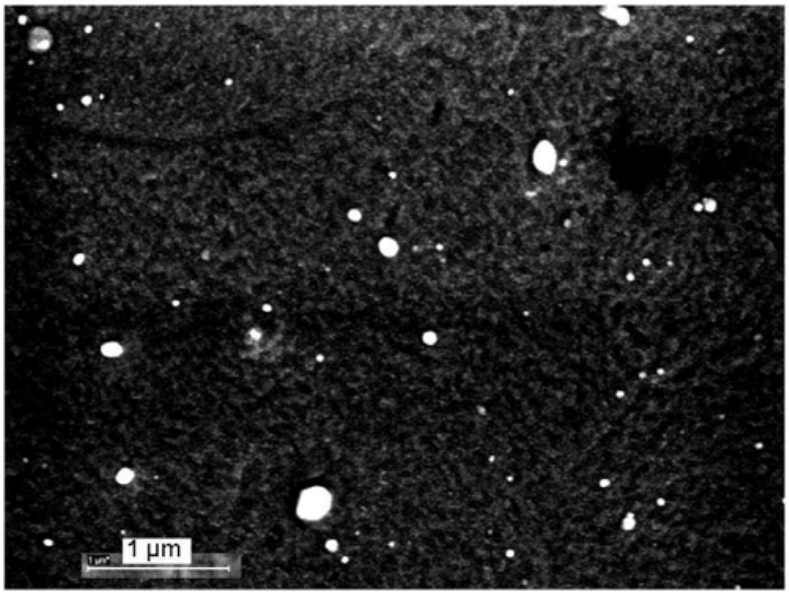


Figure 2.29: Typical distribution of SPPs (bright) in a sample of Zircaloy-2 [21]

SIMS experiments performed by Bossis et al. [91] found that weak channels of deuterium through the metal-oxide interface coincide well with the presence of Fe-containing precipitates in the same location. They also found that there was a tendency for hydrides to form in the metal at locations near these precipitates. The results with a cartoon can be seen in figure 2.30. Here a series of cross-sectional images have been stacked to present a projected view in cross-section through the metal-oxide interface. Note that the X and Z axes are very different. This gives good evidence to support the SPPs acting as pathways through the barrier formed by protective oxide just before the metal-oxide interface.

As a side note, a technique that has proven to give excellent detail on the composition of SPPs and grain boundaries has been APT. APT is an atomic-scale technique where electric fields extract single atoms off a micron-sized needle sample,

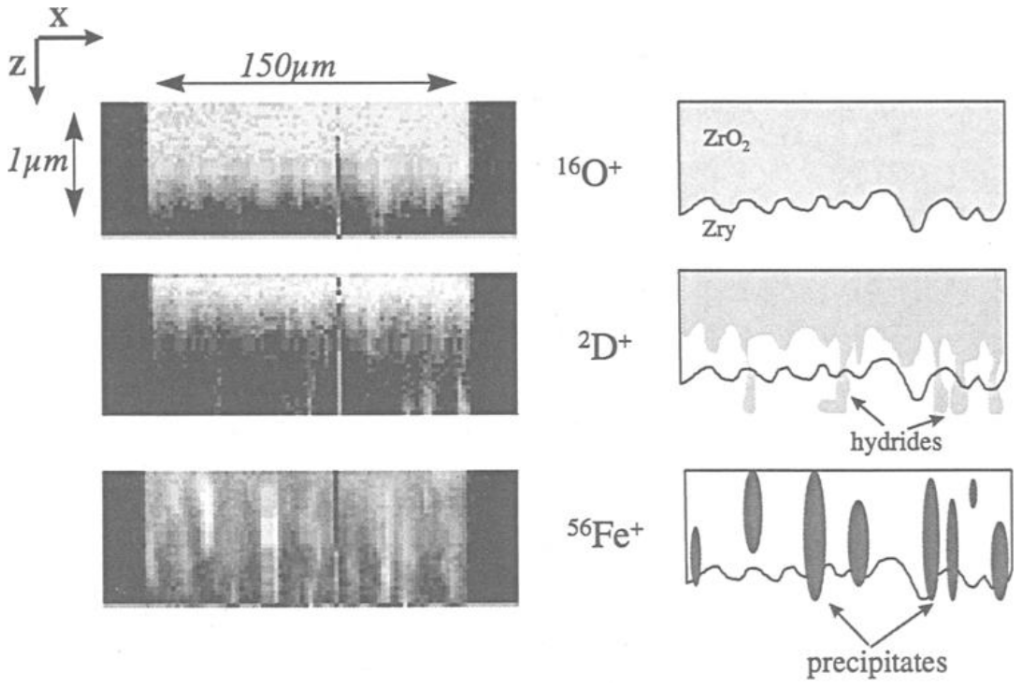


Figure 2.30: SIMS cross section of a 3D reconstitution, distribution, and associated schematic representation of oxygen, deuterium and iron in the oxide of a Zr-4-S2 sample, oxidised 48 h at 673 K in heavy water. Note the different scale between the X and Z axis. [91]

allowing 3D reconstruction of the chemical composition. Initial results on APT of Zircaloy-2 shows the segregation of Fe and Ni to boundaries, thereby providing a potentially conductive pathway for hydrogen ingress, seen in figure 2.31 [22, 121].

2.5.4 Effect of alloying elements on hydrogen pickup

In 1961 Berry et al. [122] studied the effect of binary alloys of zirconium with nickel, tin, iron, chromium and antimony on hydrogen pickup. They measured hydrogen pickup of these alloys over 575 days in water at 343 °C and found large variations in the pickup of the theoretically available hydrogen produced by the corrosion reaction (2.2). The base material was sponge zirconium. As seen in figure 2.32, the addition of nickel has a large, increasing effect on the hydrogen pickup. The addition of tin has a nearly negligible effect, whilst the addition of antimony significantly decreases hydrogen pickup.

The small effect of adding tin is suggested to be due to tin's state in solid

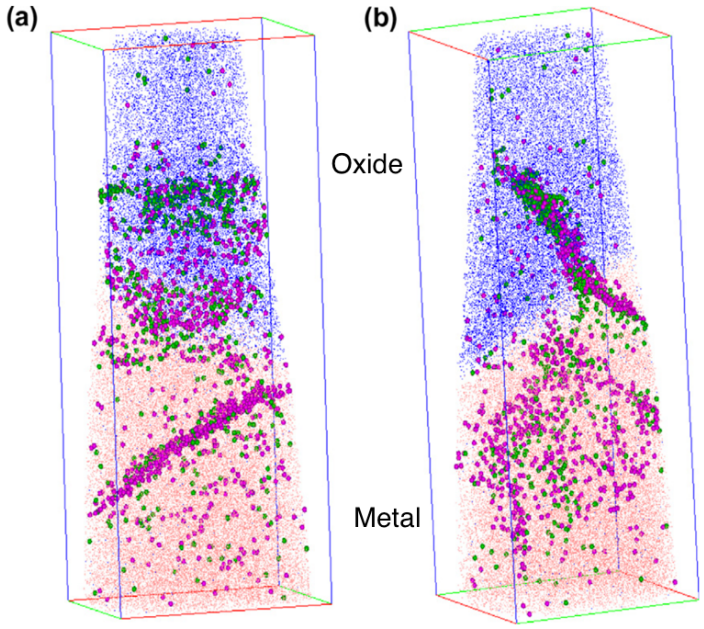


Figure 2.31: 3D reconstruction of APT results of one Zircaloy-2 sample from two different angles a) and b). Nickel has been coloured green and iron coloured purple. The size of the box is 50 x 50 x 140 nm^3 [22].

solution within the metal matrix. Nickel on the other hand forms SPPs, which supports the previous argument of the hydrogen pickup mechanism through SPPs. Antimony is not discussed further, except that it is shown that its effect of reducing hydrogen pickup does not appear when antimony is added to Zircaloy-2 (rather than as a binary with sponge zirconium). It would be interesting to see further research as to why antimony reduces hydrogen pickup.

Oxygen

Oxygen is not deliberately added, but is an extremely important alloying element. This is due to its presence as an impurity during the fabrication of the alloy. As can be seen in the zirconium – oxygen binary system phase diagram in figure 2.33 [123, 124], there exists a number of phases that the material will go through whilst gaining oxygen content at reactor temperatures, especially up to 30 % oxygen. In addition, the solid solubility of oxygen in zirconium is very high.

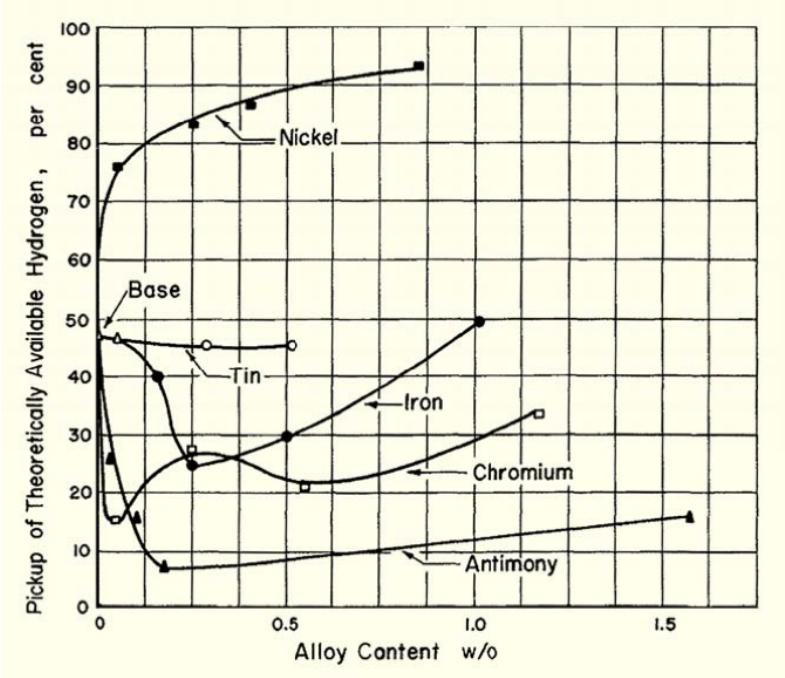


Figure 2.32: Hydrogen pickup effect of elements in binary with sponge zirconium, after 575 days at 343 °C in water [90].

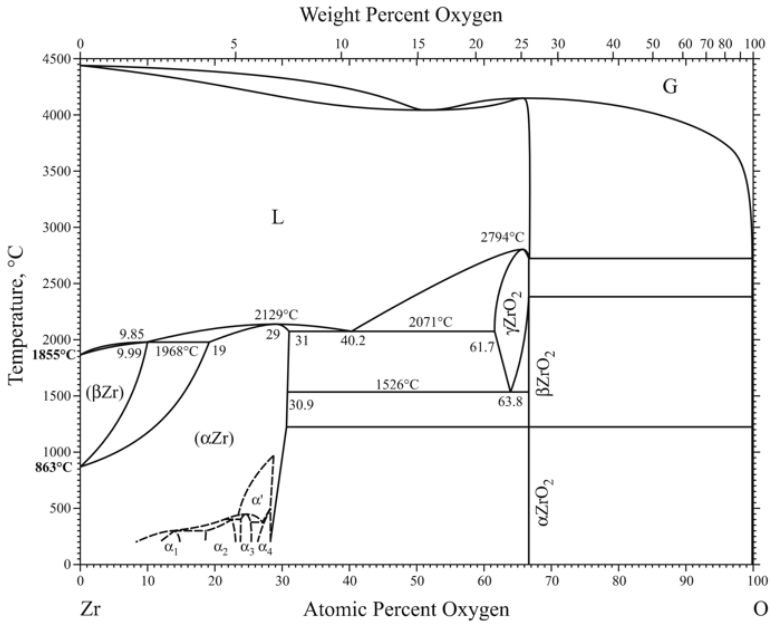


Figure 2.33: Phase diagram of the binary zirconium-oxygen system [123, 124].

Tin

The phase diagram [125, 126] for the tin-zirconium binary system is shown in figure 2.34. It shows that tin may exist in many combinations with zirconium, from pure alpha- and beta-Sn, to Sn_2Zr, Sn_4Zr_5, Sn_4Zr_6, Sn_3Zr_5, Sn_3Zr_6, $SnZr_4$. However, it is the last one that is stable in the concentrations used for nuclear purposes.

Tin (Sn) was first added to zirconium in order to improve the poor corrosion resistance of low-grade zirconium [2]. Tin mainly forms $SnZr_4$ when added in amounts up to 20 %, as can be seen on the phase diagram in figure 2.34.

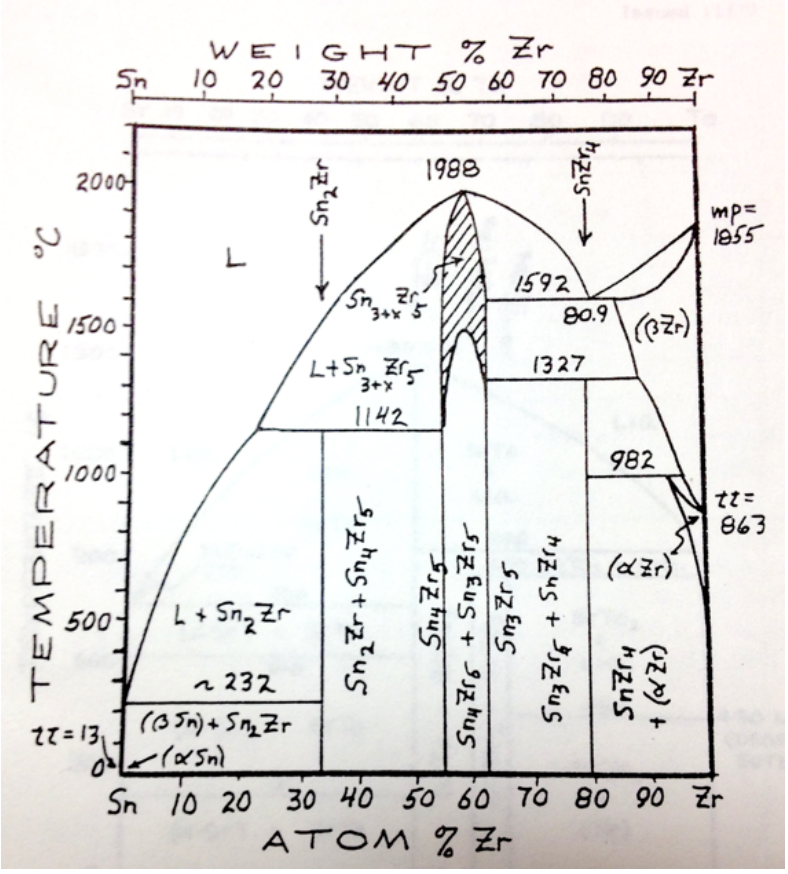


Figure 2.34: The binary phase diagram of zirconium and tin [125, 126].

It was also discovered that in high-grade zirconium the oxide produced by corrosion adhered better to the metal surface than for pure zirconium [10]. The increased adhesion prevented flaking until several hundred mg dm^{-2} ($\approx$13 µm oxide thickness) of oxide had grown. However, it was shown that without iron included as an impurity in the alloy the corrosion life of the alloy was drastically reduced.

Only at 850 ppm iron content was the rate transition delayed until after 68 days in 315 °C water [2]. It was also shown that chromium and nickel behave in this enhancing fashion when added in ppm instead of iron, but with chromium being less effective. The reason that this was discovered later was because nickel and chromium normally were not present in sufficiently high concentrations to promote the positive effect in Zr-Sn alloys. For this reason, variable corrosion results were measured before the beneficial effect of impurities was recognised.

Tin was initially added to zirconium to counteract nitrogen impurities in the metal and to improve yield stress and creep resistance. However, whilst the yield stress and creep resistance increased with increasing tin content, time before transition is reduced and corrosion rate before and after transition increased with tin content after the nitrogen contribution to corrosion had been outweighed [10]. This was highlighted in crystal bar zirconium samples with less than 30 ppm nitrogen, where any tin at all reduced the corrosion resistance, as seen figure 2.35.

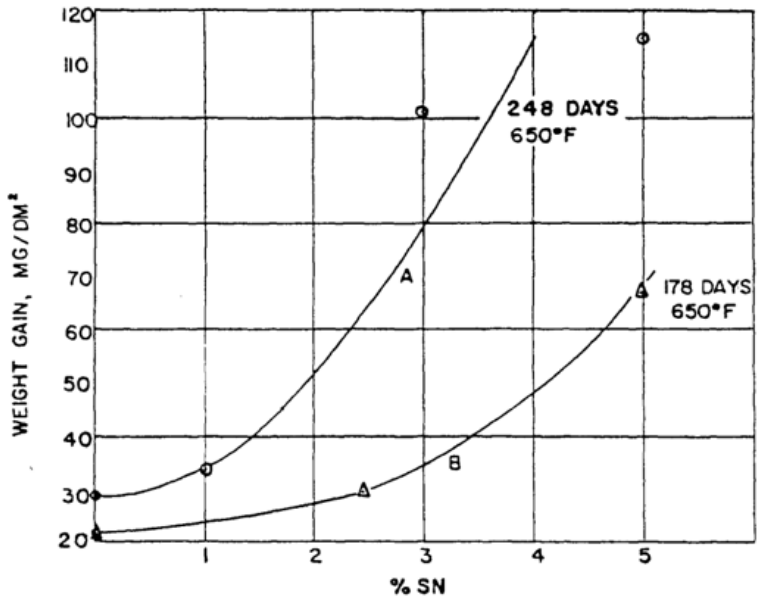


Figure 2.35: Effect of Sn on the corrosion resistance of crystal bar Zr [24]

Garde et al. [127] found that when Sn content was reduced to the lower range of the ASTM recommended content, the corrosion resistance of Zircaloy-4

improved. It has also been shown that the negative effect of tin is more pronounced in high-burn-up in-reactor corrosion [128].

The increased post-transition corrosion rate with tin content was also found by Harada et al. [129]. They found that reducing the tin content from 2.20 wt% to less than 0.10 wt% improved the post-transition resistance markedly.

Niobium

The phase diagram in figure 2.36 [125] shows that the β-Nb precipitate can be present anywhere in the matrix from 5% Nb. A phase diagram focussing around the 0 % to 1 % Nb content would be useful for the purposes of this research.

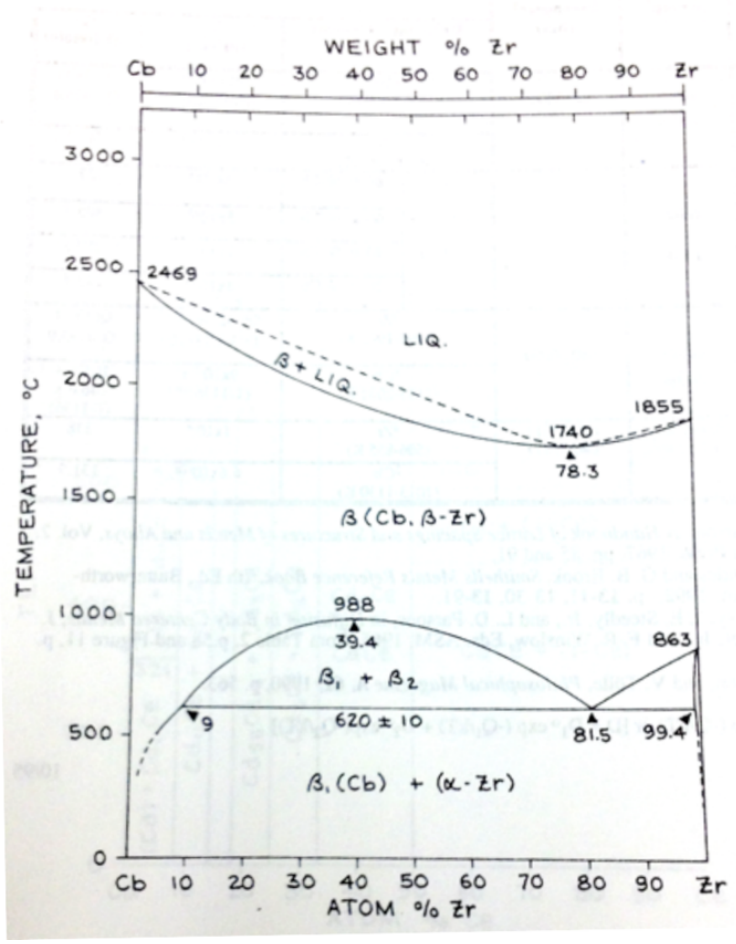


Figure 2.36: The phase diagram of the binary system zirconium and niobium (here symbolised by Cb, columbium, the former name of niobium) [125].

In general the niobium solubility in zirconium is very low, around 0.5 wt% [130]. The solubility of iron, chromium and nickel is even lower, though, and it is the

relatively higher solubility of Nb that is thought to be the reason for the superior corrosion resistance in Nb-containing zirconium alloys (like ZIRLO [68], and the Zr-1Nb variations). Because of the low solubility, β-niobium should form during annealing [131]. These β-Nb precipitates have been observed as second phase particles, figure 2.37, but in alloys also containing Fe (which are most, due to iron being an impurity) both $Zr(NbFe)_2$ and Zr_3Fe can form depending on parameters like annealing temperature and niobium content [73].

The lower hydrogen pickup fraction of Nb-containing alloys has been suggested to be due to the doping effect of Nb in solid solution increasing the electronic conductivity of the oxide, thus reducing the overall hydrogen pick-up [74].

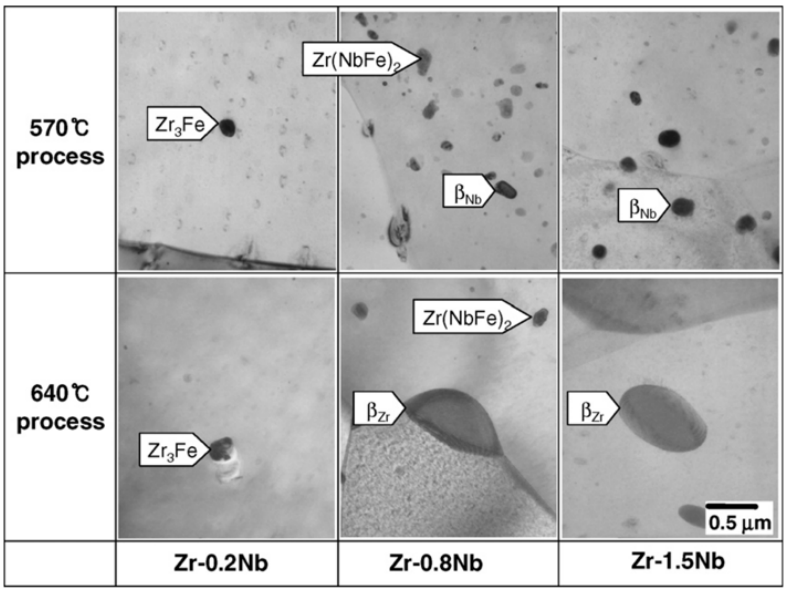


Figure 2.37: TEM micrographs of Zr-Nb alloys annealed at 570 °C and 640 °C with different niobium content [73].

Kiselev et al. [132] showed that for niobium-content in zirconium up to at least 1.4 % the HPUF significantly decreased on samples that had been oxidised in water for 750 days at 350 °C, as shown in the graph below in figure 2.38.

Iron

The phase diagram of the zirconium-iron binary system is shown in figure 2.39. It shows that many phases for iron in zirconium are possible. Iron may be found as pure α-Fe, γ-Fe Fe_3Zr, Fe_2Zr, or $FeZr_2$ [73, 133, 134]. This, in addition to the fact that

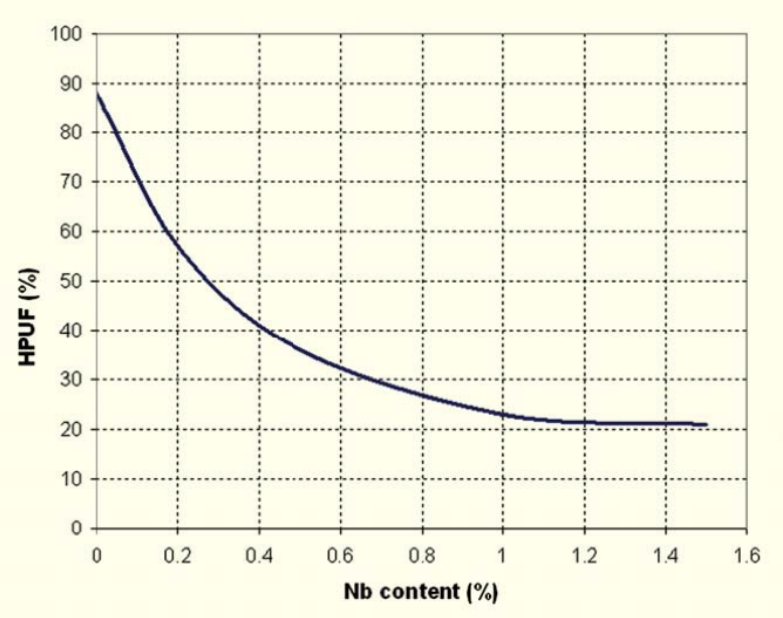


Figure 2.38: Effect of niobium on the HPUF of zirconium on samples oxidised in water for 750 days [132].

iron forms many ternary precipitates lead to a large number of possible routes for the oxidation species during aqueous corrosion to take. It would be worth investigating which of the species are prominent in the zirconium alloys currently in use.

During manufacture of zirconium metal, iron exists as an impurity in the metal. As iron is not removed from the base metal, this means that all nuclear zirconium alloys contain at least a small amount of iron. However, it was realised that iron could improve the mechanical strength of the material, and so slightly larger amounts of iron (enough to make the impurity levels of iron insignificant) were added.

Itagaki et al. [135] showed that a Zircaloy-2 alloy modified to 0.4 wt% iron (approximately twice the ratio of iron in regular Zircaloy-2) displayed approximately half the hydrogen pickup-fraction of standard Zircaloy-2. This reduction in hydrogen pickup was suggested [117] to be caused by an increase in the electric potential of the oxide surface, reducing the electric potential gradient across the oxide film and reducing the proton diffusion across the oxide.

The increase in the oxidation state of iron prior to oxide transition suggests a decrease in electron conductivity of the oxide. Such a decrease is consistent with the observed increase in hydrogen pickup fraction prior to transition [121].

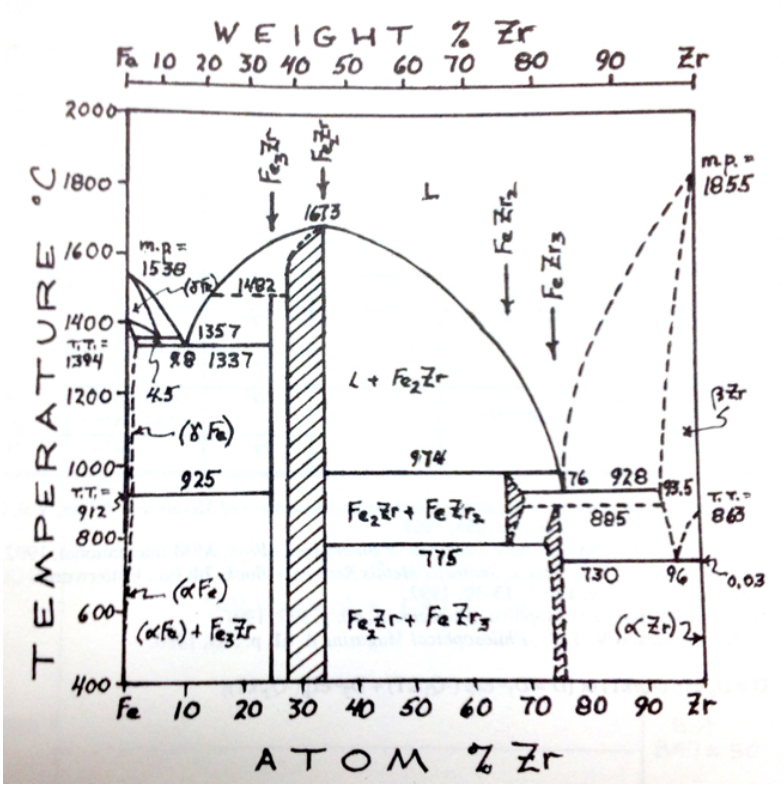


Figure 2.39: The phase diagram of the binary system zirconium and iron [73, 133, 134].

Chromium

The phase diagram [136] in figure 2.40 shows that for any temperature that might exist in a nuclear reactor, chromium will either be found in a single phase of Cr, or in the binary phase α-Cr_2Zr. However, chromium is more often found in ternary phases with Zr and Fe, for instance $Zr(Fe, Cr)_2$ [120].

Chromium has been added to improve zirconium alloys for a long time, but few papers exist that actually describe how chromium improves the corrosion resistance [137]. Peng et al. [138] investigated the corrosion resistance of chromium ion implanted Zircaloy-4. It was found that at low doses (fluence greater than $1 \times 10^{16}\,\text{ions}\,\text{cm}^{-2}$ but smaller than $5 \times 10^{16}\,\text{ions}\,\text{cm}^{-2}$) corrosion resistance was greatly improved.

Nickel

Nickel appears to give a small increase in corrosion resistance after transition when added in small amounts, markedly so at high pressure (1500 psi). Larger amounts

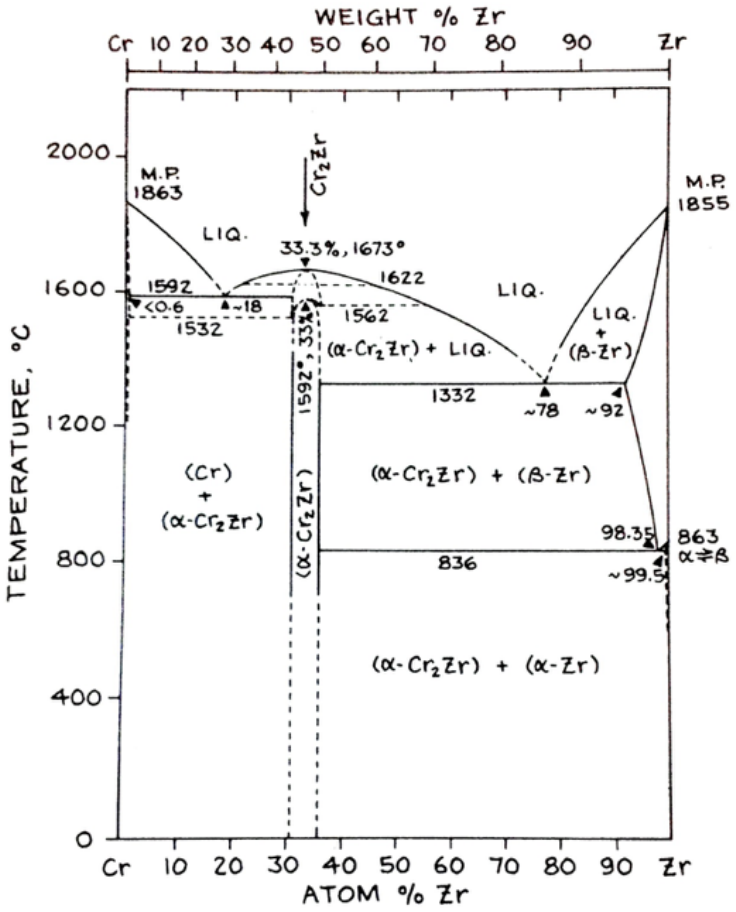


Figure 2.40: The phase diagram of the binary system zirconium and chromium [136].

did not give any significant increase in resistance [129]. Tin contents of 0.088 and 0.165 wt% give a fairly slow corrosion with no apparent transition at the high pressure. However, these samples also showed the highest hydrogen pick-up ratio after 7200 h at both 360 °C and 400 °C compared with other alloys, four times the hydrogen pick-up compared with an identical sample with <0.01 wt% tin.

This effect of nickel on hydrogen pickup was noticed by several scientists early in the history of zirconium alloys. Yeniscavich et al. [13] discovered that a slight increase in the nickel content of Zircaloy-2 increases the HPUF by an order of magnitude. Berry et al. [122] found that SPPs present in the metal contained nickel as a result. It is therefore suggested that the SPPs provide pathways for the hydrogen to move faster through the alloy. Initial results from APT show the segregation of Fe and Ni to boundaries, thereby providing a potential

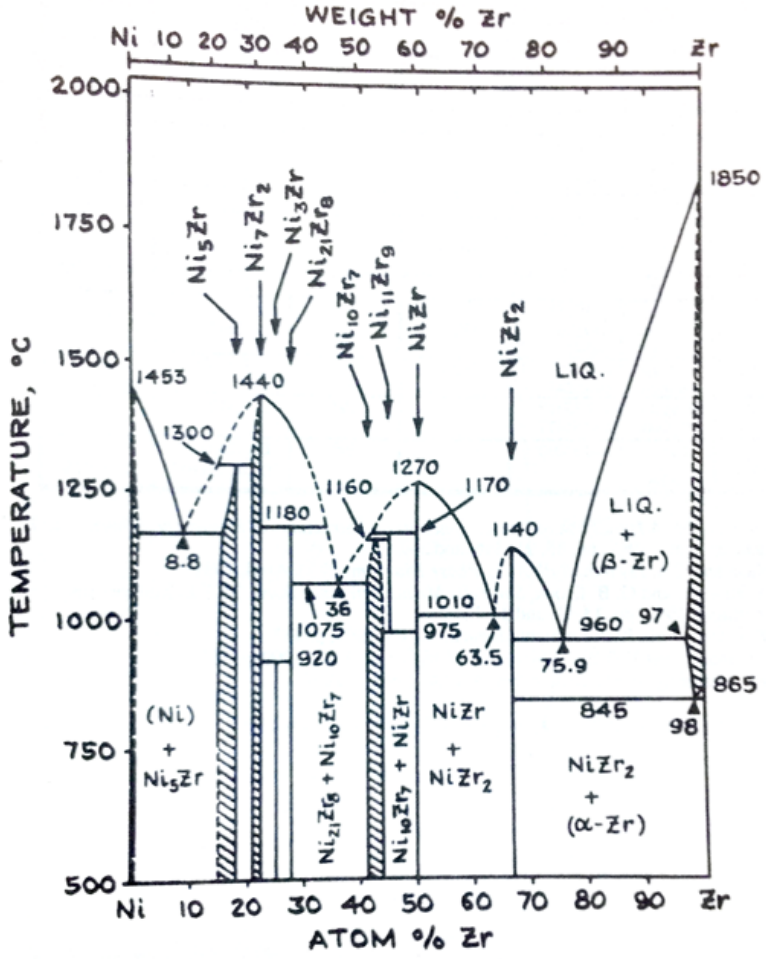


Figure 2.41: The binary phase diagram of zirconium and nickel [139].

pathway for hydrogen ingress [121].

The phase diagram [139] of the zirconium-nickel binary system in figure 2.41 shows that there are many possible phases that the two constituents can exist in. At low concentrations nickel can be found as $NiZr_2$, but NiZr, $Ni_{10}Zr_4$, $Ni_{21}Zr_8$, Ni_3Zr, Ni_7Zr_2 and Ni_5Zr are also possible combinations. However, also here mainly the ternary combinations of Zr(Cr,Ni) and Zr(Fe,Ni) are found in the real alloys, rather than the binary ones [10, 140, 141].

2.6 Effect of sample preparation

Zirconium oxide has a highly stressed grain structure due to its Pilling-Bedworth ratio of 1.56. Thinning FIB lift-outs from the oxide region down to 50 nm is bound

to relieve the stress in the material. Therefore, it should be unsurprising that the thin FIB foil one may be looking at may not reflect exactly on the bulk nature of the material. In discussion with other researchers, there has been some concern that the FIB may be inducing hydrides in the samples. This has already been shown to be the case for titanium [142], and zirconium is a very similar HCP metal. Possible mechanisms include the beam concentrating hydrogen from the surface of the sample, or drawing hydrogen from the (non-perfect) vacuum of the microscope.

2.7 Summary

The purpose of this literature review has been to cover the most important research in corrosion and hydrogen pickup of zirconium alloys, find areas where research is lacking, and then try to show what needs to be done. The study of the corrosion of zirconium alloys has been ongoing for a very long time, and with every improvement to technology used in the various forms of microscopy, new facts are brought to light, yet more questions arise. The cause of "transition" is still not understood, nor is the effect of SPP composition, size and density. Do cracks cause transition, or does the fast oxidation during transition cause cracks? The role of the sawtooth suboxide, oxygen-saturated metal and possibly other intermediary phases at the metal-oxide interface is still being studied heavily. Hydrogen pickup has been shown to have a connection to oxidation rate. The study of hydrogen is a difficult one, as hydrogen is very light and almost everywhere in our day-to-day lives. And it is important to remember that the corrosion procedure happens at several hundred Celsius, making it even more difficult to interpret results. The focus of this thesis is to further the understanding of the above questions with the latest microscopy tools.

3

Experimental techniques and methodology

Contents

3.1 Electron interactions with matter 52
3.2 Scanning electron microscopy 52
3.2.1 SEM instruments used in this project 54
3.3 Focused ion beam - sample preparation 56
3.3.1 Ion interactions with matter 56
3.3.2 TEM sample preparation 57
3.4 Transmission electron microscopy 61
3.5 Energy-dispersive X-ray spectroscopy 63
3.5.1 EDS use in my project 64
3.6 Electron energy loss spectroscopy 65
3.6.1 Multiple linear least squares fitting 72
3.6.2 Suboxide EELS analysis 73
3.7 HyperSpy EELS analysis software package 75
3.8 Secondary ion mass spectrometry 75
3.8.1 Diffusion profiles 77
3.9 Materials 78

The experimental techniques and methodology I have used are described in this Chapter. First I give an introduction to the interaction of electrons with matter, then a basic explanation of electron and ion beam microscopy techniques. After each section I go into further detail regarding the more specialised techniques

available to me during the project.

3.1 Electron interactions with matter

The interaction of high-energy (5 kV to 200 kV) electrons with matter is governed by both elastic and inelastic collisions. In both cases electrons are scattered away from their initial trajectory into the material. The elastic interactions involve a change in direction of the primary incident electron, with very little energy being lost. They are typically detected in the scanning electron microscope (SEM) as backscattered electrons, or in the transmission electron microscope (TEM) on a high-angle annular dark field (HAADF) detector. Inelastic interactions are far more varied, as there are many ways for an electron to lose energy as it passes through the material. The relevant interactions for these electron microscopy techniques include the emission of secondary electrons and X-rays as well as plasmon scattering and inelastic scattering. It is the inelastic interactions that yield chemical information about the material, and are detectable by techniques such as energy-dispersive X-ray spectroscopy (EDS) and EELS, which will be discussed later in this Chapter.

3.2 Scanning electron microscopy

The SEM is used to collect information from the surface of a sample, from a depth of up to a few microns. In the SEM an electron beam is created by extraction of electrons from a source and usually accelerated to between 1 and 30 kV. An objective lens focusses the beam to a spot, and a deflection coil allows the focussed primary beam to be precisely rastered across the sample surface.

There are two main types of electrons that can be detected in the SEM: secondary and backscattered electrons. Secondary electrons are the result of inelastic collisions between a primary electron and the electrons around a nucleus in the sample. If the collision transfers the secondary electron an energy greater than the sample work function, they can escape from the sample. Secondary electrons are highly surface angle oriented, emitting more strongly at sample edges. Therefore, surface

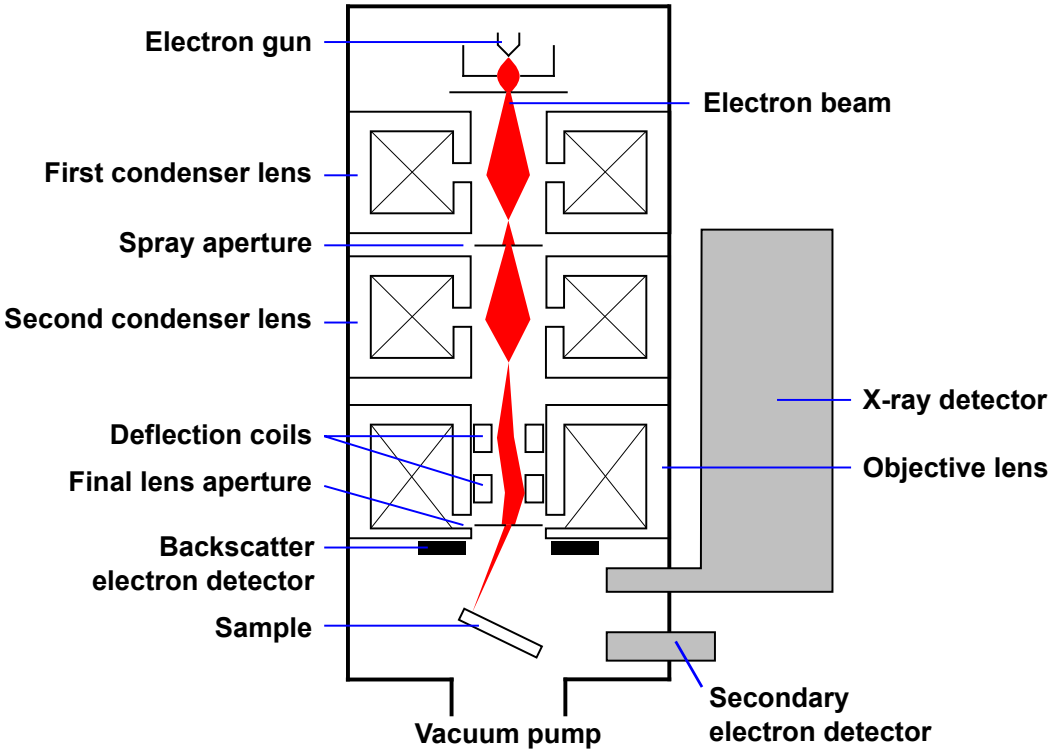


Figure 3.1: Schematic of a secondary electron microscope [143]

morphology can highly affect secondary electron images. The interaction volume for secondary electrons is small, as the energy of the secondary electron is low, less than 50 eV. Whilst the primary electron can continue further into the sample, exciting more and more electrons, the secondary electrons generated are decreasingly likely to reach the sample surface. The low interaction volume allows for the highest spatial resolution in the scanning electron microscope: On a field emission gun (FEG) SEM, it can be down to 0.5 nm.

The depth of the interaction volume is generally of the order of 100 nm. The backscattered electrons are electrons from the primary beam that are re-ejected having been elastically scattered off a nucleus in the sample material. The probability of backscattering increases with the mean atomic number (Z) of the material, so a resultant bright area in the material corresponds to a high average Z relative to the surrounding area. The interaction volume is large as the backscattered electrons have significantly higher energy and so have a higher probability of making it back out of the material.

3.2.1 SEM instruments used in this project

A Zeiss Merlin analytical FEGSEM fitted with an Oxford Instruments X-Max^N 150 mm^2 EDS system was used to image polished cross-sections for studying the oxide, metal-oxide interface and second-phase particle distributions as well as attempting to image the craters on the surface of the oxide following NanoSIMS oxide depth-profile analysis.

Samples were polished by sandpaper to 4000 grit, and then polished and mildly etched using a 40 nm-particle colloidal silica solution for five minutes.

In order to calculate the distribution of second-phase particles in a sample, the interaction volume of the beam had to be calculated. To do this, the Casino software was used. Casino is a Monte-Carlo simulation software used to determine electron interactions in matter [144]. Interaction volume increases with accelerating voltage, as seen in the classic bulbous shape in figure 3.2, so I wished to use the lowest necessary accelerating voltage.

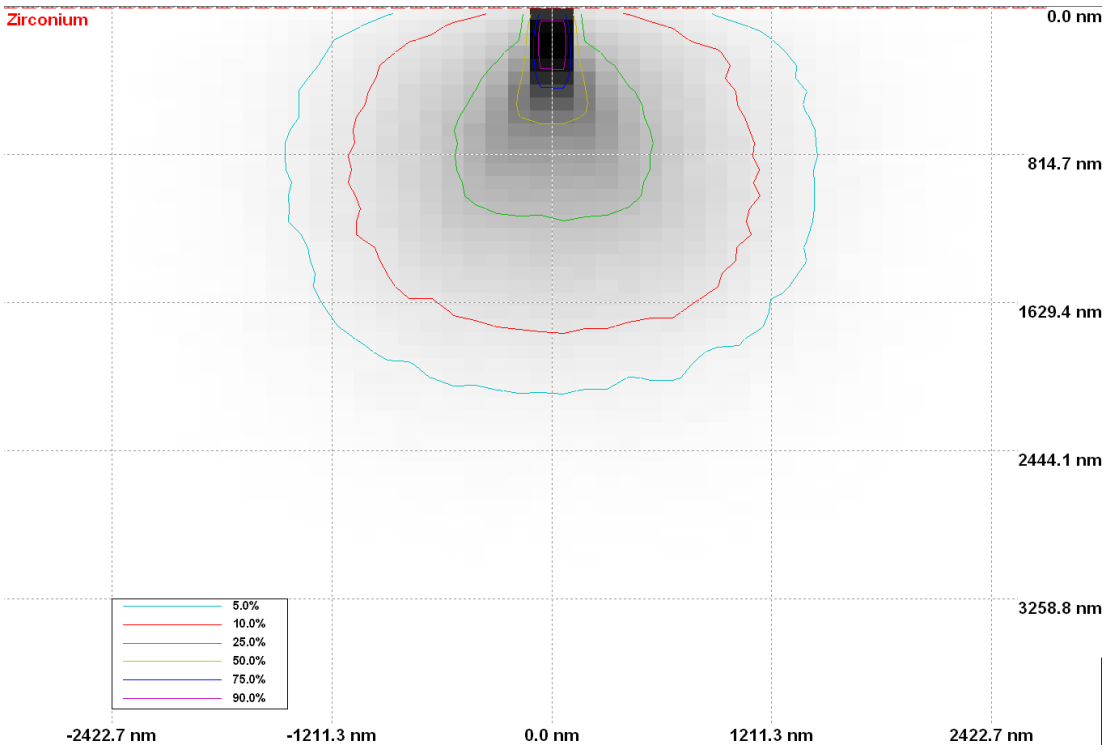


Figure 3.2: Interaction volume of a 30 kV electron beam with Zr modelled by the Casino software.

However, in order to detect the elements of interest (Zr, Nb, O, Fe, Cr, Sn), a certain minimum energy was required to produce an X-ray. Ignoring the Zr and Nb Kα lines, for general EDS the most energetic relevant line was the Sn Lα peak, which has an energy of 4.5 keV. It was found that an accelerating voltage of 8 kV was enough to detect this peak in the ZIRLO metal.

Casino calculations showed that for a beam with a spot size of 1 nm (accurate for the Merlin SEM used for SPP analysis), there was a substantial difference in the emission of X-rays as a function of depth and radial distance from the incident beam, shown in figure 3.3.

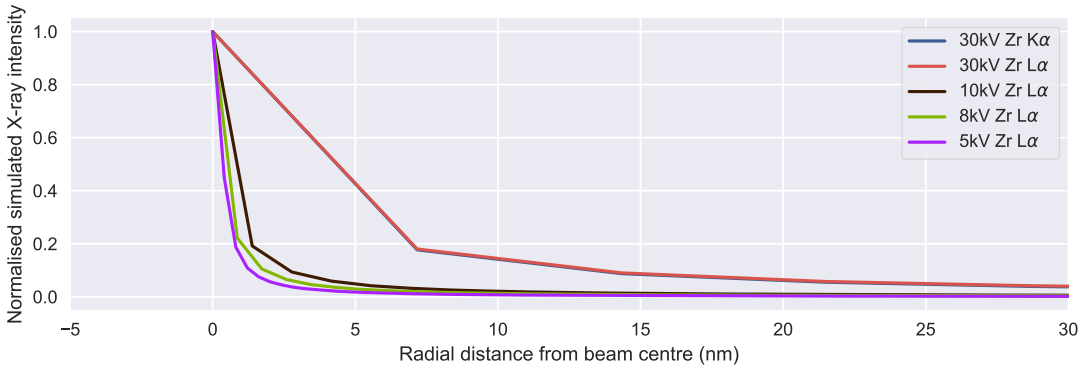


Figure 3.3: Radial emission of X-rays from a 1 nm beam of the specified accelerating voltage modelled by the Casino software. The Zr Lα and Kα lines overlap.

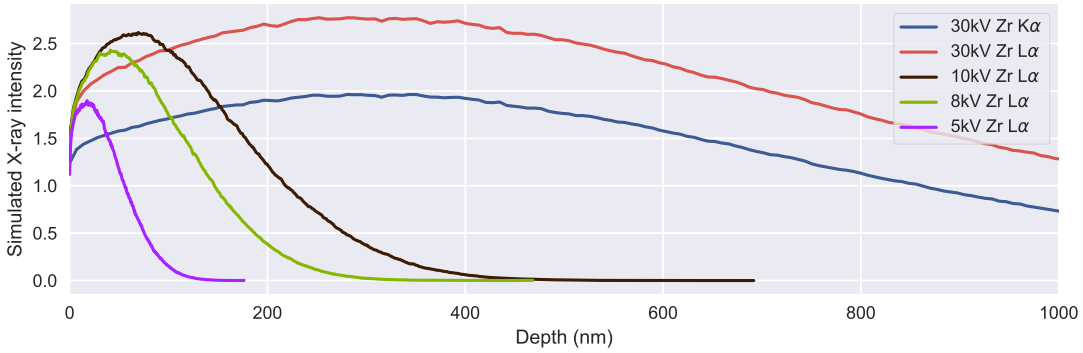


Figure 3.4: The depth of emitted X-rays as a function of accelerating voltage modelled by the Casino software. Counts include self-absorption of X-rays.

For second-phase particle analysis alone, only Zr, Nb, O, Fe and Cr were relevant. For this analysis, an accelerating voltage of 5 kV was chosen. For the elements mentioned above, the X-ray line with the highest energy was the Lα_1 line for

zirconium at 2.0 kV. Using Casino to model the interaction volume, shown in figure 3.4, I find that the peak depth of excitation of X-rays for a 5 kV beam is 17 nm, and for 8 kV it is 48 nm. Hence, for an SEM SPP distribution study on a bulk sample, the SPP density of the reported alloys may vary significantly if the studies used only slightly different accelerating voltages.

3.3 Focused ion beam - sample preparation

The focused ion beam (FIB) is a scanning ion based technique that can be used to deposit or ablate material on a nano- to micro-scale. The single beam FIB consists of a vacuum system and chamber, a liquid metal ion source, an ion column, a sample stage, detectors and a gas delivery system [145]. For this study, the FIB has been used for TEM sample preparation and for tomography by three-dimensional FIB serial slicing and imaging, although these results have been difficult to process. Like the scanning electron microscope, the focused ion beam is based around accelerating a charged particle by an electric field, and focussing it to a point, generally to be rastered across a sample surface. All FIB instruments used for this work use a liquid metal Ga^+ ion source, with energies of 30 kV for general bulk milling, or reduced energy at 2 kV or 5 kV for removing higher-energy FIB damage from the outer edges of the sample [145].

3.3.1 Ion interactions with matter

The ability to mill, image and deposit material using a FIB arises from the interactions between the energetic ions in the beam and the sample. Material removal is a result of physical sputtering of sample surface. Sputtering occurs as the result of a series of inelastic collisions between the incident ion and the target atoms within a collision cascade region [145]. If one of the knock-on atoms receives enough kinetic energy, it can be ejected from the region, either away from the sample or to be re-sputtered onto the sample elsewhere.

The resulting collisions can produce a range of signals in the forms of phonons, X-rays, electrons and ions that can be usefully detected. Most useful in my

application is the electron component. Ion-induced secondary electrons (SEs), can be detected by a simple Everhart-Thornley detector, and used to form an image (map of SE intensity relative to beam position) analogous to the SEM. Changing the detector setting allows secondary ions (SIs) instead of SEs to be detected to form a complementary image. However, the number of secondary electrons generated per incident ion is approximately 10 x to 1000 x greater than the number of secondary ions. Hence SEs tend to produce a clearer image at the same scan rate, however, the positive gallium primary ion beam may lead to charging in non-conductive samples, which may trap the negative SEs. Thus, the combination of SI and SE detection may give the best combination of image quality and contrast [146].

3.3.2 TEM sample preparation

For this project, TEM sample preparation has been done using a single-beam FEI FIB200 and a dual-beam Zeiss NVision. An in-situ lift-out technique developed by Professor Lozano-Perez has been performed on the FIB200 using a custom-built in-situ micromanipulator, utilising a gas-injection system (GIS) to house an electropolished tungsten needle.

For TEM sample preparation of zirconium alloys, the starting material has generally been a flat, 5 mm x 5 mm square oxidised zirconium coupon mounted on a microscope stub using silver dag or conductive carbon paste. In the case of tube samples, the tube was cut across into a 3 mm wide ring, which was then sliced across the diagonal and stuck with silver dag to a microscope stub, with the convex face of the oxide facing up. To improve conductivity of the surface of the sample, the surface of the coupon and stub were coated in 10 nm of gold by gold evaporation. Unless otherwise stated, the accelerating voltage of the FIB column is set to 30 kV.

Initially, a 20 µm x 2 µm x 1 µm rectangle of platinum or carbon is deposited onto the flat oxide surface in order to protect the surface beneath from ion beam damage and preserve surface features. The beam current used is a function of the area of the rectangle: Beam current densities of 2 pA µm^{-2} to 6 pA µm^{-2} provide an optimum deposition of Pt with the Pt_High material file used on the FEI

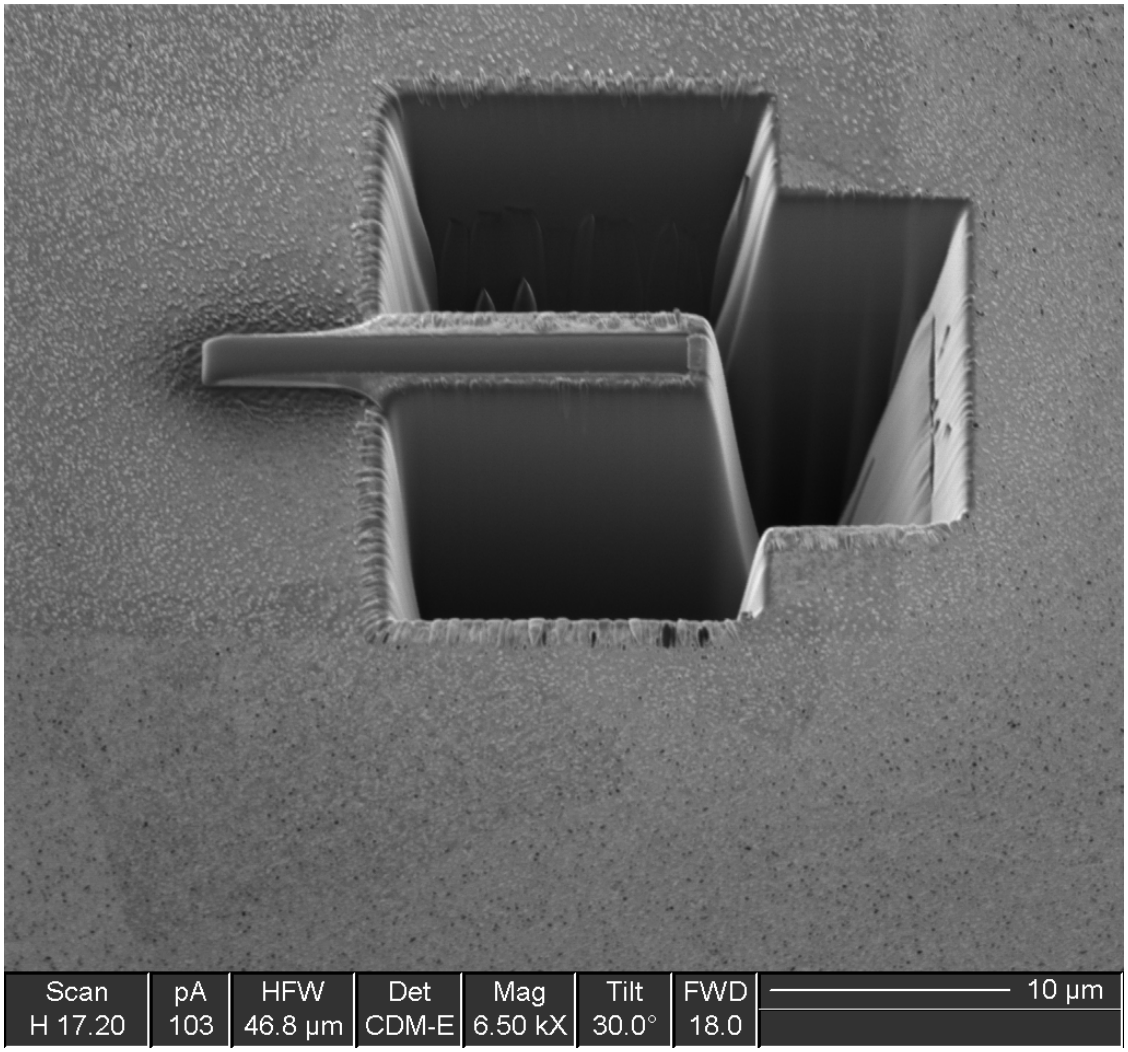


Figure 3.5: Three staircase trenches milled around the protective platinum rectangle.

FIB200. At a high beam current (7000 pA), three trenches are milled around the protected area, as seen in figure 3.5. The depth of these trenches depends on the region of interest. If the metal-oxide interface is of interest, the trench should be deep enough to allow for 3 µm of metal to be visible beneath the oxide of the zirconium alloy. A staircase mill was performed for each trench, allowing access to the sub-surface to reveal the material that is chosen to become a TEM sample. Several geometries were experimented with, settling on a staircase allowing the bottom of the sample to be visible at 45 degrees tilt. Most microscopes are only able to tilt to 45 degrees one way, so the sample was rotated 180 degrees in order to repeat the undercut from the opposite angle.

The tails of the ion beam profile mean that in order to mill without damaging the material of interest, the sample needs to be tilted. For high beam currents (1000 pA to 3000 pA) a tilt of 1.5 degrees away from the normal was used to mill a flat sample. At lower currents this angle was reduced to 0.5 degrees.

By a progressing linear sweep of the beam, the TEM lamella was milled thinner from both sides by cross section polishing at a beam current of 3000 pA. This continued until the sample thickness was 1 µm or thinner, as seen in figure 3.7.

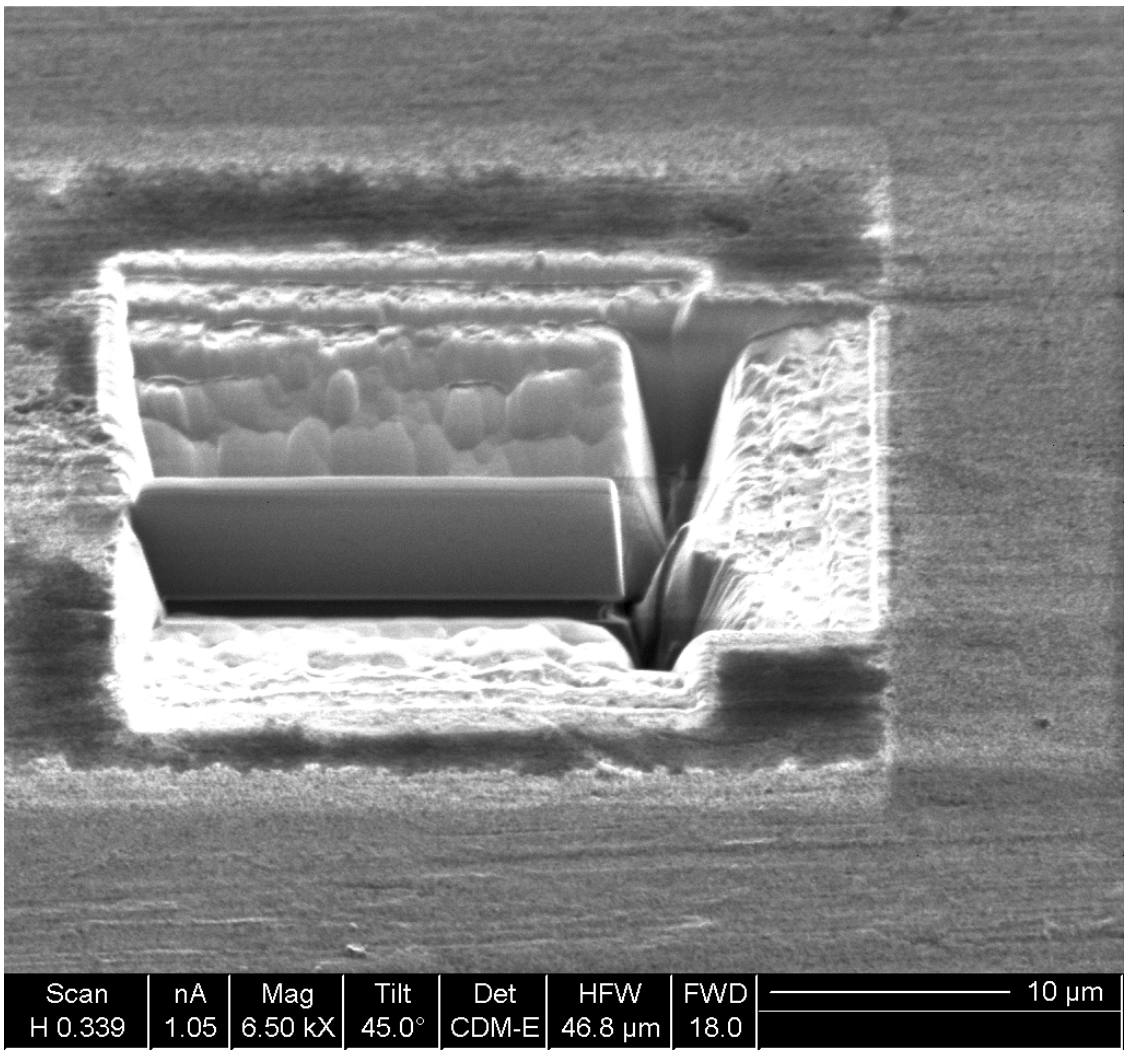


Figure 3.6: The TEM lamella after cross section polishing, seen at an angle of 45 degrees. The sample has been undercut.

At this point, the sample was tilted to 45 degrees in order to undercut and sidecut the sample to prepare it for in-situ lift-out, as seen in figure 3.6. Two rectangular boxes were drawn for normal milling at the bottom of the sample and

along the left-hand side, with a depth of about 4 µm. Using a beam current of 1000 pA, I milled until there was no contrast in the area being milled to ensure separation of the lift-out from the sample. By rotating the sample and carefully milling the same areas on the opposite side, the sample would eventually be hanging free from one end of the original material.

By introducing the in-situ lift-out micromanipulator needle and the carbon/-platinum GIS to the chamber, I then began the lift-out procedure. On the single beam FIB, by adjusting focus and observing the "shadow" due to the needle on the side of the sample, I brought the needle into contact with the edge of the sample. One will often see a contrast change on the needle (seen in figure 3.8) if there is sufficient conductivity between the sample and the needle, which can be helpful to show when there has been made contact.

Depositing carbon/platinum onto the contact point between the sample and needle ensured that the sample did not fall off later. A small box drawn around this area, as in figure 3.7, with a depth of less than 1 µm is sufficient to ensure a good bond.

Finally, the TEM lamella was released from the original material by cutting the remaining edge. This was done at 100 pA, by drawing a single line across the cut to be made. By setting the depth to 20 µm, refreshing the screen whilst it was milling would eventually show that the sample had been released, as seen in figure 3.7 . Sometimes the TEM sample had not been cut free properly, and was being held underneath by redeposited material. The solution was to redeposit carbon/platinum onto the final cut area to reseal it and cut the contact point between sample and needle. After removing the needle, I repeated the undercut and sidecut described above, before reattaching the needle again.

A small trick to help avoid redeposition of milled material onto the undercut when cutting the sample free was to, after depositing and before cutting, move the stage 2 µm to 3 µm downwards. This applied a stress across the sample and onto the needle. One requirement was that enough weld material had been deposited to secure the sample to the needle. When the TEM lamella was cut away from

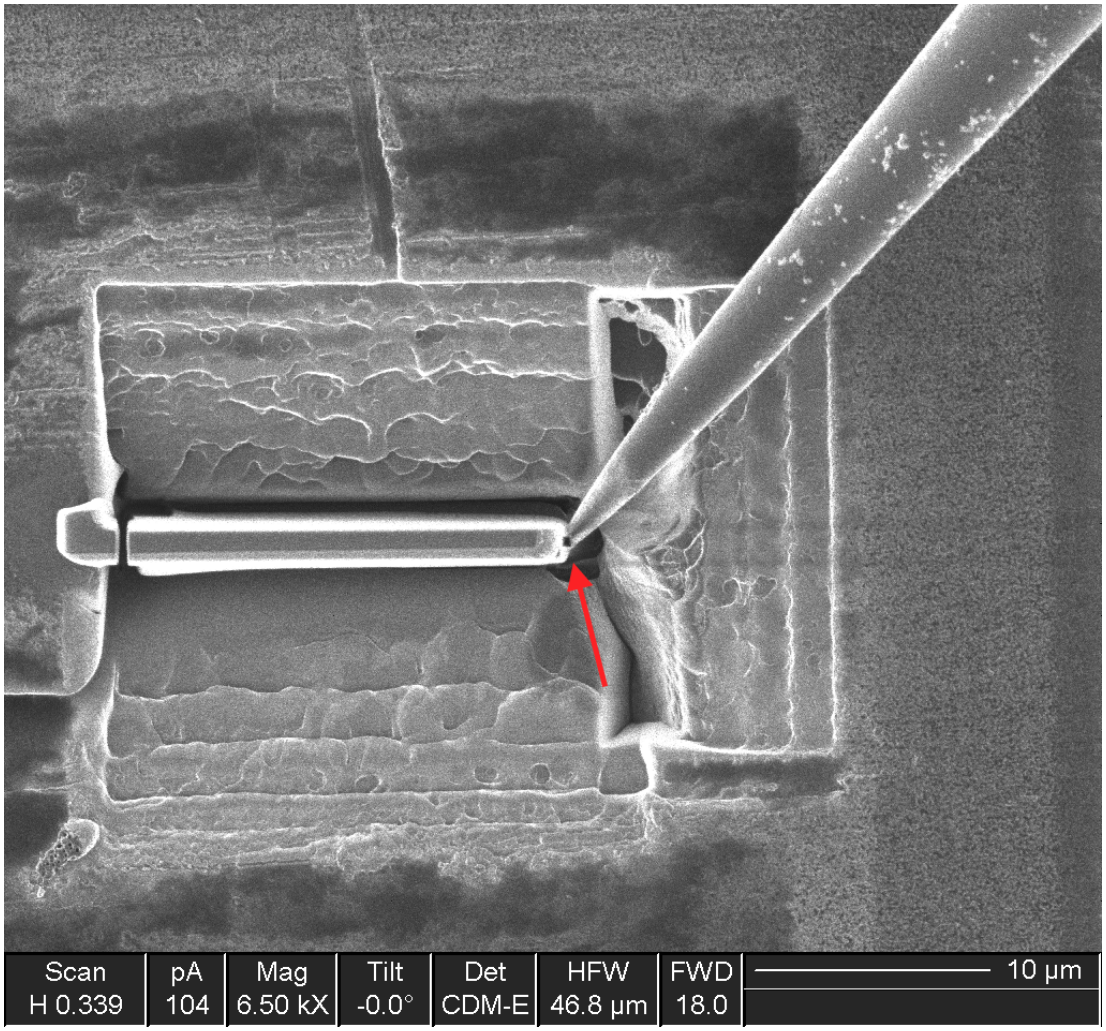
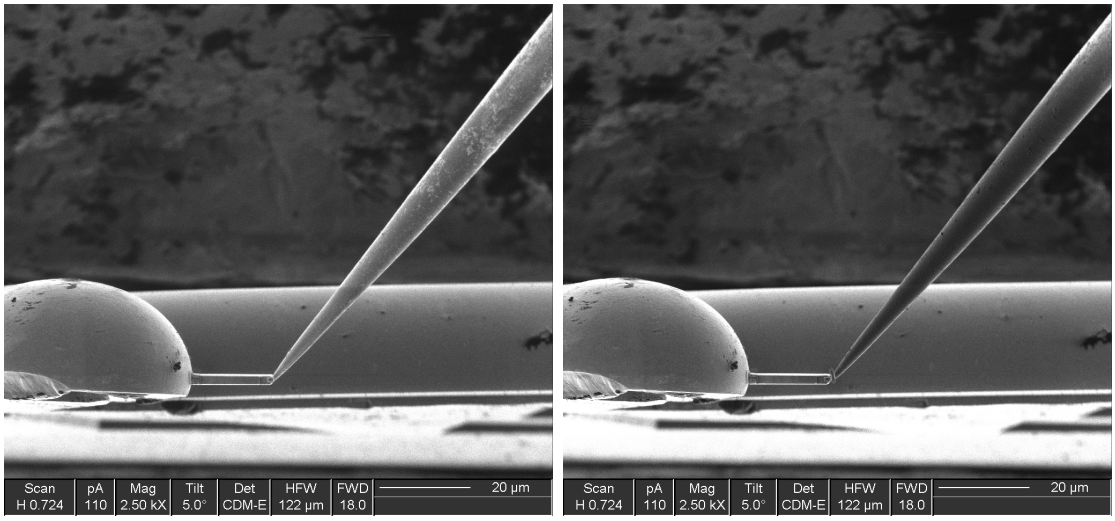


Figure 3.7: TEM lamella after cutting the remaining edge. The small weld attaching the needle to the lamella is indicated by the red arrow.

the bulk sample, the lamella was lifted up by the needle, preventing it from being reattached. An alternative was to look out for small movements or contrast changes of the lamella relative to the bulk sample. If such movement was detected, it was likely that the TEM sample had been cut free.

3.4 Transmission electron microscopy

A transmission electron microscope (TEM) is a microscope that accelerates electrons through the sample, to be detected on the other side. In order for the electrons to pass through, the sample needs to be very thin - for high-resolution work the sample needs to be less than 100 nm in thickness. The resolution of an electron microscope



(a) Needle touching stage **(b)** Needle not touching stage

Figure 3.8: Contrast difference on micromanipulator needle between touching the sample stage and not touching the sample stage.

is highly dependant on the wavelength of the electron hitting the sample. The smaller the wavelength, the higher the resolution, aberrations notwithstanding. As the de Broglie wavelength of the electron is inversely proportional to the square root of its energy (for non-relativistic speeds), microscopists have spent a lot of resources on increasing the accelerating voltage of TEMs. For conventional SEMs the upper limit of voltage is generally 30 kV. At their highest, TEMs have reached 3 MV! However, problems with sample damage due to the high energy electron beam has meant that modern high-voltage TEMs generally operate at either 200 or 300 kV.

TEM has been very well described in the book "Transmission Electron Microscopy" by Williams and Carter [147]. Most of the TEM work in this project has been done in STEM mode, on either a LaB_6-filament JEOL2100 (for bulk analysis and large-region EDS) or a cold field emission gun JEOL ARM200F (for high-resolution work, EDS and EELS). Some STEM was also performed on a Zeiss Merlin SEM with a STEM detector. At the time, this was a new acquisition of the department. It proved very useful for low-magnification bulk work, providing interesting contrast, but admittedly did not provide any substantial analytic benefit over TEMs on the oxidised zirconium alloys in this project.

STEM operates by focussing a high-energy electron beam onto a sample, as seen in figure 3.9. The beam is rastered across the sample, and the scattered and transmitted electrons are detected further down the column. The directly transmitted beam contains electrons that did not experience any interaction with the matter in the sample as well as inelastically scattered electrons. The latter are used for the chemical analysis using EELS, whilst the total count of electrons forms the pixel intensity value in the bright field (BF) image. When the camera length is set appropriately, the two annular detectors - the annular dark-field (DF) and the high-angle annular dark-field (HAADF) detectors can be used to detect diffraction contrast and Z-contrast, respectively on the images produced.

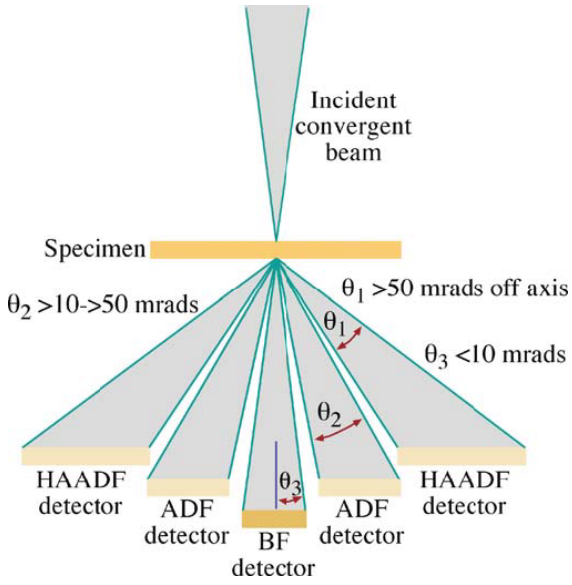


Figure 3.9: Schematic of the detected signals from an electron beam interacting with a thin sample in a STEM [147].

3.5 Energy-dispersive X-ray spectroscopy

Energy-dispersive X-ray spectroscopy (EDS) is an analytical technique used to provide chemical information of the sample [147]. When a secondary electron is emitted from an atom, there is often an X-ray generated by the associated relaxation of higher orbital energy electrons into lower energy levels. By detecting the resulting X-rays, seen in figure 3.10, a spectrum from the interaction volume in the sample

can be generated over time. As the peak energies of the various relaxations are quantised, it is possible to tell what element produced which energy.

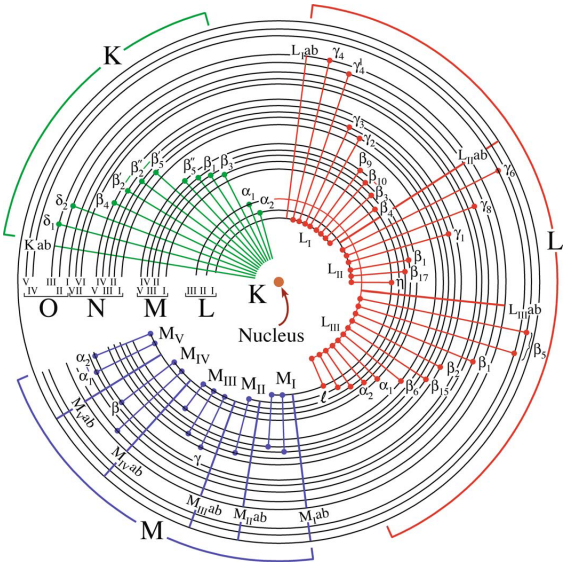


Figure 3.10: Schematic of all X-Ray signals possible from the relaxations of electrons in an atom [147].

The detection of the X-rays, together with the positional information generated by a SEM or STEM (or focused TEM beam), can then be used to reconstruct where the originating atom or atoms sat in the sample. This reconstruction can be overlaid on a SEM or STEM image, and can be used to generate element line-scans or maps on top of structural information of the sample.

3.5.1 EDS use in my project

For this project, on the Merlin FEG-SEM referred to above, I used a cutting-edge Oxford Instruments X-Max^N 150 mm^2 window EDS detector. The detector allowed fast acquisition of X-rays at a working distance of 8.5 mm. In conjunction with that detector, the Oxford Instruments Aztec software was used for analysis. On the JEOL2100 TEM, I used an Oxford Instruments X-MaxN 80T, with an 80 mm^2 detector. On the ARM200F field-emission gun (FEG) TEM, I used a JEOL DRY SD100GV EDS detector, Silicon Drift 100 mm^2, 133 eV energy resolution full width at half maximum (FWHM). The Thermo NSS software was used to analyse and export EDS results for plotting using the HyperSpy Python software.

3.6 Electron energy loss spectroscopy

When the high-energy electrons in a 200 kV STEM interact with the sample, they may lose energy by knocking electrons out of their orbitals or by introducing heat or damage to the sample. As a result, electrons accelerated to 200 kV will now have slightly lower energy. By bending the electron beam using a magnetic field, the electrons can be separated by energy. A detector can then be introduced to capture these electrons and create a three dimensional spectrum image, where at each pixel in the image a signal of energy loss is recorded.

If a charge moves into a magnetic field, with direction perpendicular to the field, it will follow a circular path. The radius of the circular path is given in equation 3.1.

$$r = \frac{mv}{qB} \tag{3.1}$$

where r is the radius of the orbit of the curved electron, m, v and q are the mass, velocity and charge of the electron, respectively, and B is the applied magnetic field. Therefore, electrons travelling with higher velocity, or lower energy loss, will be bent less by the magnetic field and hit the CCD detector lower down (CCD detector shown on the schematic in figure 3.11.

EELS was performed on a JEOL ARM200F with a Gatan Quantum 965 ER GIF for this project. The accelerating voltage was 200 kV. The convergence and collection semi-angles were 31.48 and 41.0 mrad respectively.

The energy loss is in the range of 0 eV to about 3000 eV. The signal drops off with energy loss approximately as a power law. Therefore at higher energy losses the signal is extremely weak. An example of an EELS spectrum plotted in a logarithmic scale is shown in figure 3.12. The higher energy losses must be acquired at a longer exposure time (up to 0.1 s per pixel), however this exposure time would saturate the detector if it were to acquire the zero-loss peak (ZLP). As such, it is common to acquire multiple EELS signals over different energy ranges. For the experiments studied during this project, the following energy ranges and exposure times were generally collected.

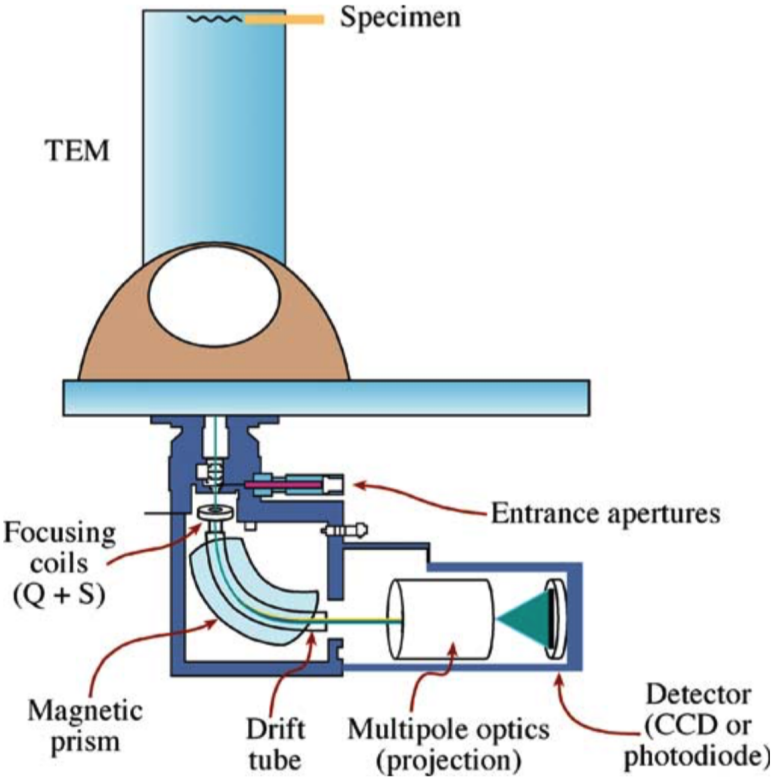


Figure 3.11: Schematic of an EELS detector [147]

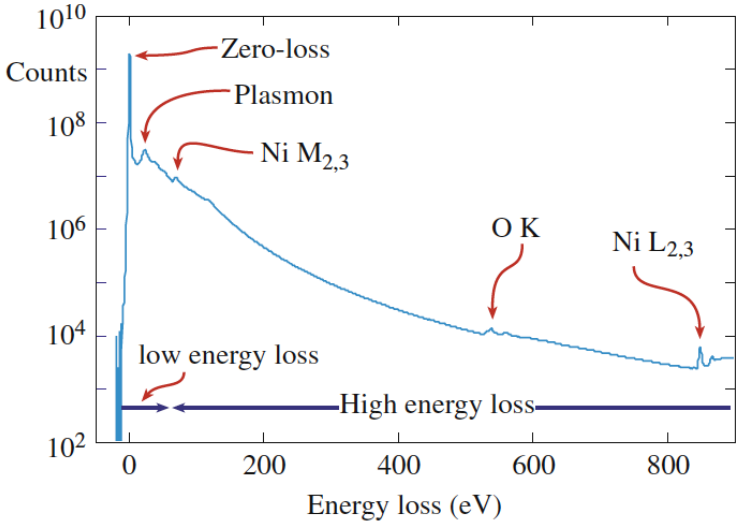


Figure 3.12: An EELS spectrum displayed in logarithmic intensity mode. The ZLP is an order of magnitude more intense than the low energy-loss portion [147].

[0eV, 500eV] - The position of the ZLP, 5×10^{-5} s at 0.25 eV channel^{-1}

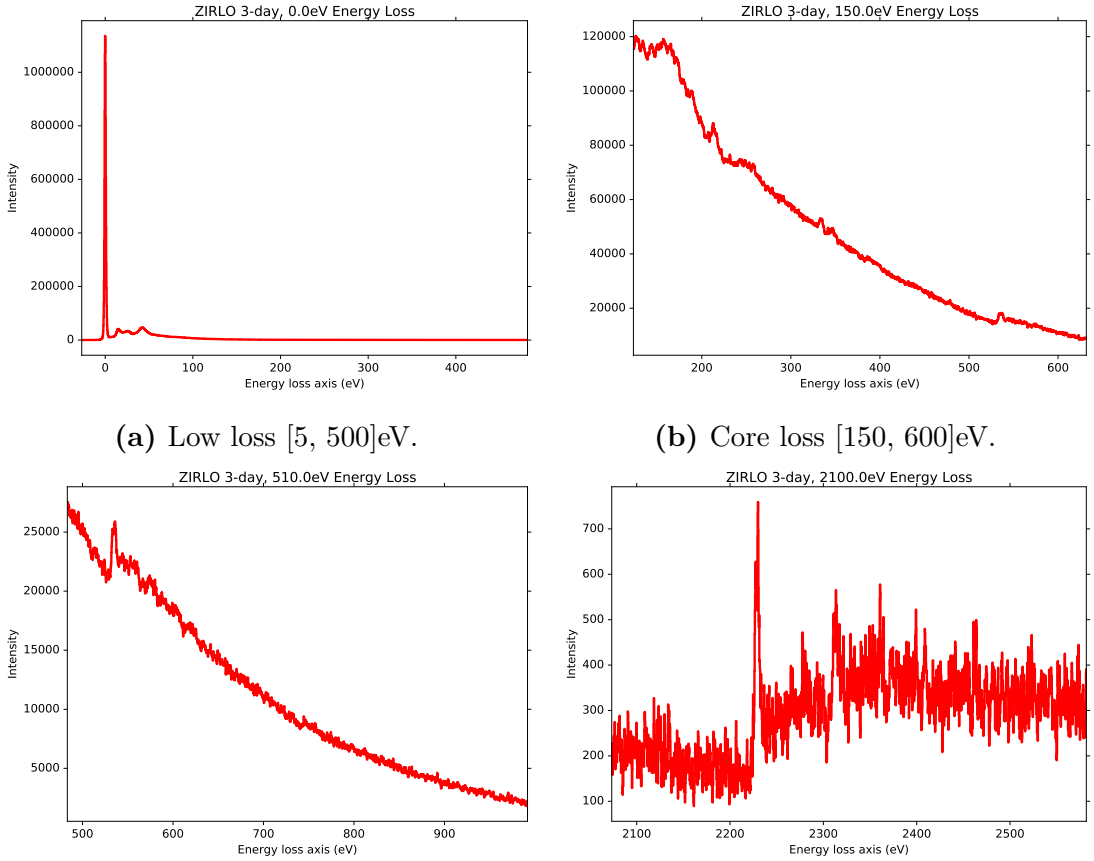
[150eV, 650eV] - Zr M edges and O K edge, 0.01 s at 0.25 eV channel^{-1}

[510eV, 1010eV] - O K edge, Fe, Ni and Cr L edges, 0.01 s at 0.25 eV channel^{-1}

[2100eV, 2600eV] - Zr and Nb L edges, 0.1 s at 0.25 eV channel^{-1}

[0eV, 100eV] - The position of ZLP and plasmon peaks, 5×10^{-5} s at 0.1 eV channel^{-1}

A typical un-processed pixel in a spectrum image is shown in figure 3.13b.



(a) Low loss [5, 500]eV.

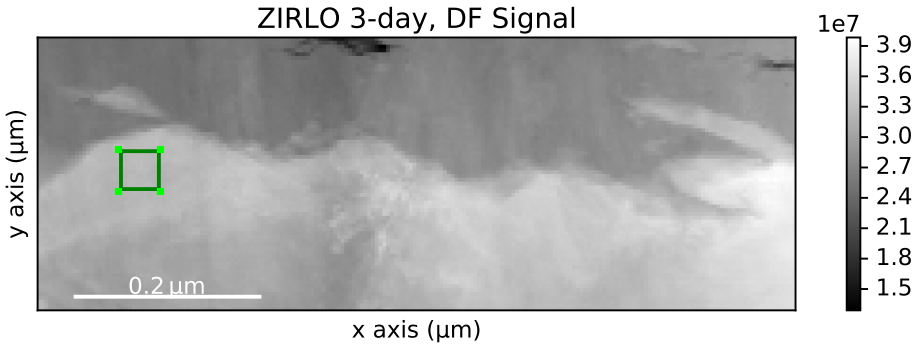
(b) Core loss [150, 600]eV.

(c) Core loss [510, 1000]eV.

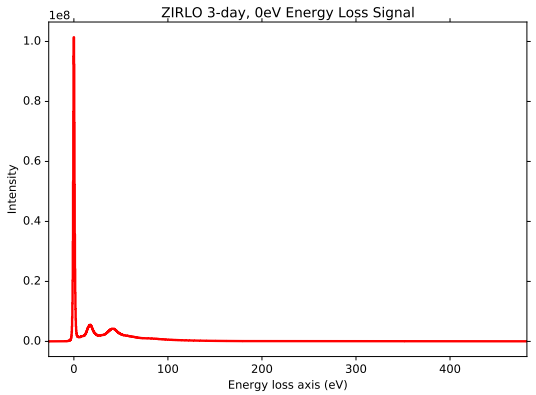
(d) Core loss [2100, 2600]eV.

Figure 3.13: Typical single pixel EELS spectra

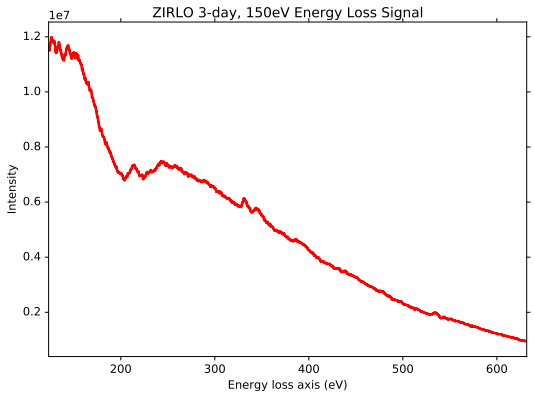
In order to improve signal quality a larger area can be averaged. Figure 3.14 shows the accompanying DF image, acquired with the spectrum image EELS map. The signal of the higher energy losses (the 2100eV range in figure 3.14e especially) are much improved.



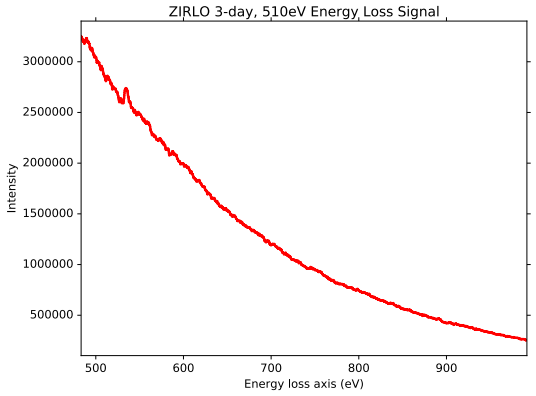
(a) HAADF image.



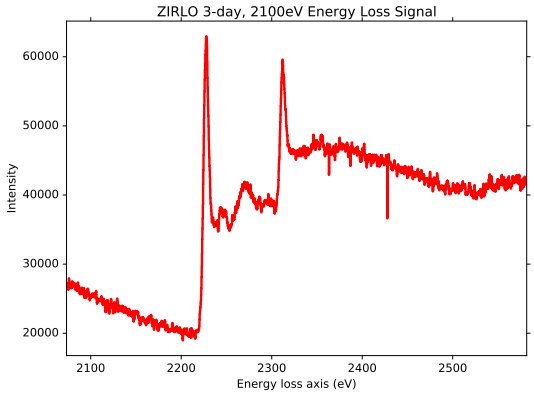
(b) Low loss [5, 500]eV.



(c) Core loss [150, 600]eV.



(d) Core loss [510, 1000]eV.



(e) Core loss [2100, 2600]eV.

Figure 3.14: Typical summed spectra from a region of a spectrum image.

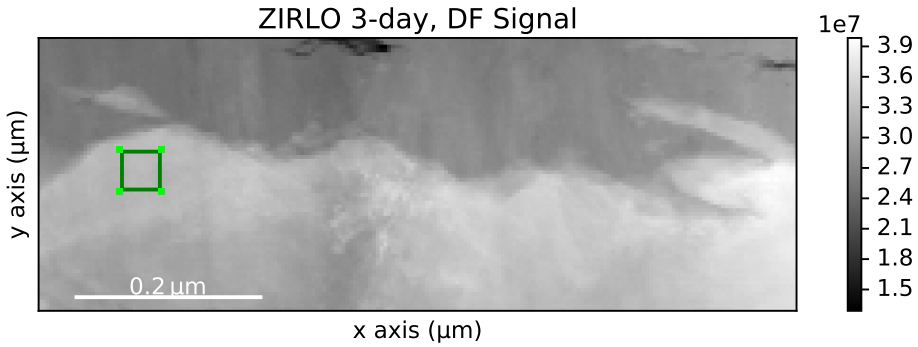
Principal component analysis

However, is it possible to go one step further. Utilising the software package HyperSpy [148, 149], multivariate statistical analysis can be applied on the SIs in order reduce the dimensionality of the data. By first applying principal component analysis (PCA) [150, 151] followed by independent component analysis (ICA) [149, 152] the spectrum image can be reduced into separate components ordered by their statistical significance. By filtering out components that are considered not statistically significant and rebuilding the spectrum image, the noise of the spectrum, especially at higher energy losses where the signal is weaker, can be considerably reduced. A comparison of a raw single pixel, an averaged area and an ICA pixel can be seen in figure 3.15.

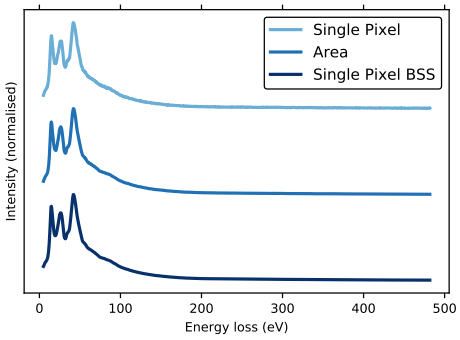
PCA and ICA are well explained in the literature [150–152], but to give a short summary, PCA is used to decompose a multivariate dataset into a set of successive orthogonal components that contain a maximum amount of the variance. Components that do not contribute to the real signal (noise) can then be removed, and the original dataset can be reconstructed without them. ICA relaxes the requirement of the components being orthogonal, and so allows unmixing of a signal into its real-life components. It has successfully been used in EELS and EDS spectroscopy [149]. It must however be used carefully, as components of low-concentration can be removed entirely [153]. When only doing noise-reduction and not blind source separation - the commonly used result of ICA - it is common to reconstruct the noise-reduced dataset using more components than might appear immediately necessary. This improves the situation, but PCA should still be used with care.

Independent component analysis

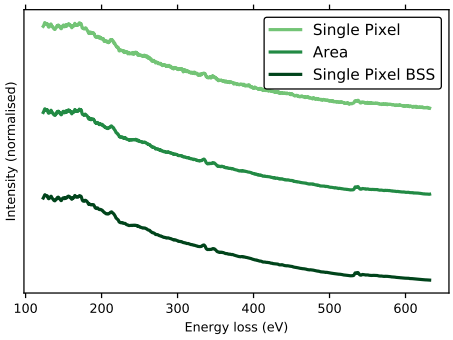
For this project, ICA of low-loss EELS was utilised with great effect to separate the various phases in and around the metal-oxide interface. The ICA implementation used was FastICA [152]. Spectra were acquired on a 2048 channel EELS detector, with a dispersion of $0.05\,\mathrm{eV\,channel^{-1}}$. This produced a spectrum containing



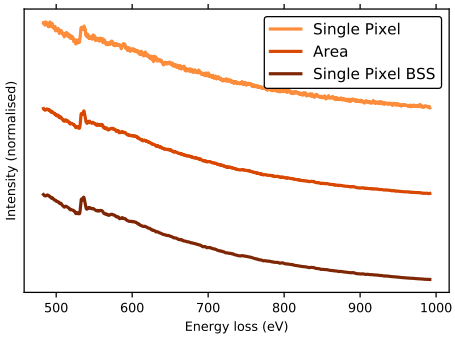
(a) HAADF image.



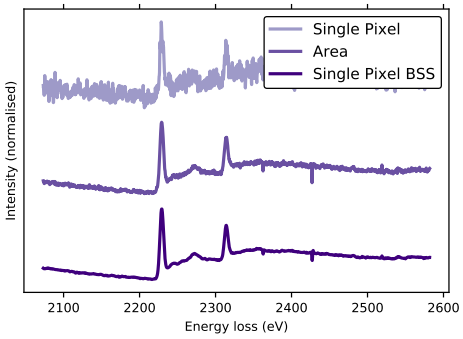
(b) Low loss [5, 500]eV.



(c) Core loss [150, 600]eV.



(d) Core loss [510, 1000]eV.



(e) Core loss [2100, 2600]eV.

Figure 3.15: Comparison of a single pixel spectrum, area-averaged spectrum and ICA reconstructed single pixel spectrum, across the various energy ranges. In particular, the 2100 eV to 2600 eV data in (e) demonstrates significant noise reduction. Here BSS stands for "blind source separation", another label for ICA.

the ZLP and the plasmon peaks, from just before 0 eV to approximately 80 eV electron energy loss. The signal was then cropped to remove the ZLP, as ICA output quality was found to be improved without it. A possible explanation for the improvement is that the height of the ZLP would reduce with increasing thickness, whilst the plasmon peak would increase. This would result in a non-linear component not separable by ICA.

For each component, ICA produces a signal factor; a spectrum associated with certain parts of the spectrum image. A so-called "loading" map gives the intensity of the factor at each pixel. These factors and loadings can be multiplied and linearly combined to reconstruct the noise-reduced spectrum image, or presented separately to show the various regions as in figure 3.16, here showing various phases from around the metal-oxide interface of oxidised ZIRLO.

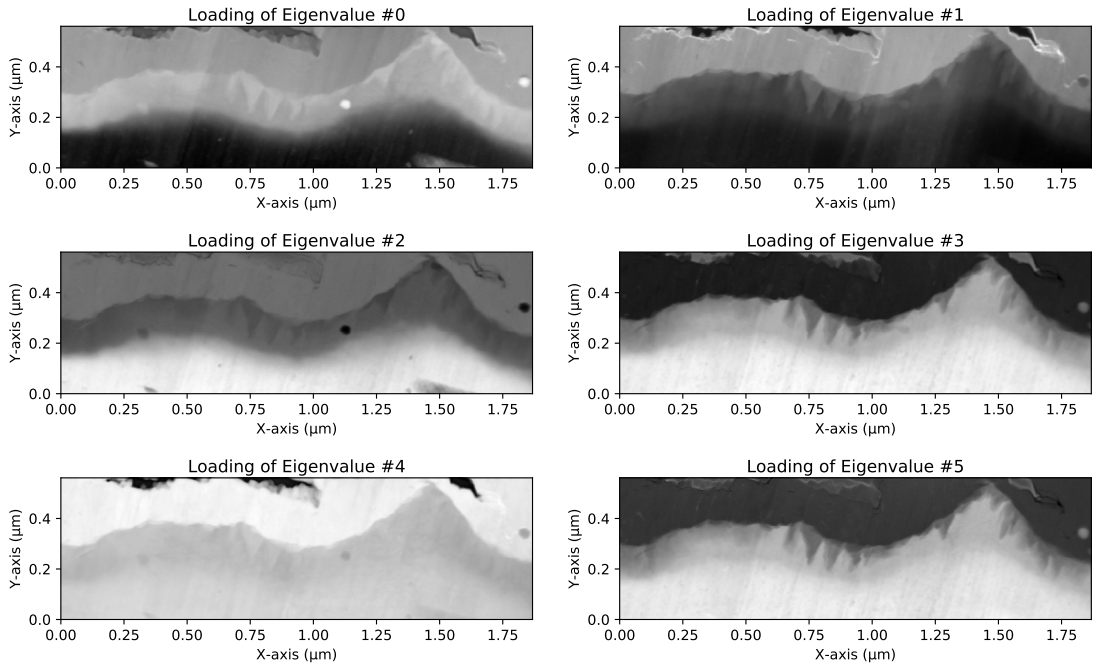


Figure 3.16: Example of the ICA loadings on low-loss EELS. They are presented in order of decreasing statistical significance to the data, but may not always be easy to separate from one another.

A necessary condition for ICA to work properly is that the information that is being extracted is sufficiently significant in the data. Therefore, especially

at low magnification, ICA is not always enough to distinguish phases like the zirconium suboxide.

3.6.1 Multiple linear least squares fitting

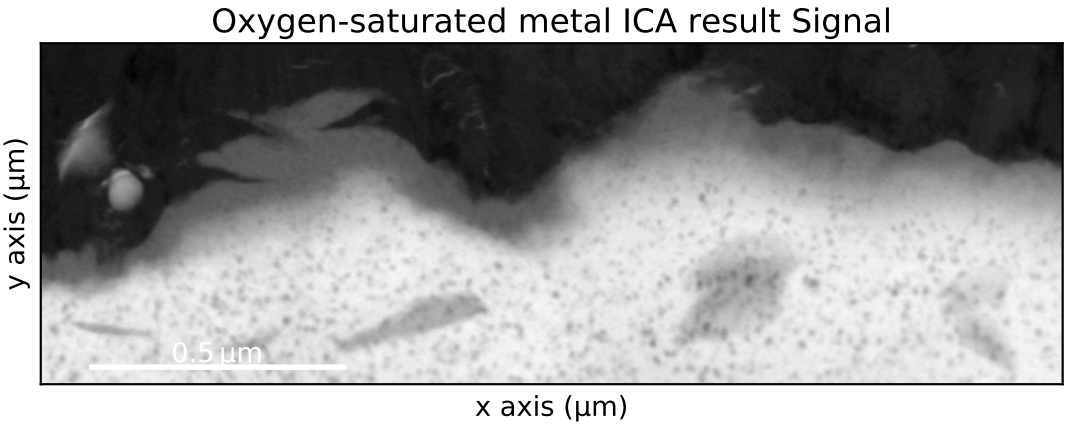
Whilst ICA gives a very good indication of the different chemical signals present in the EELS spectrum image, it does not identify or label the various regions, and will sometimes pair regions together in more than one component. It can therefore be useful to extract the signals from the various interesting regions (suboxide, oxide, etc.) in a correct ICA-cleaned dataset, and do a least squares linear fitting of the various signals. This approach is called multiple linear least squares (MLLS) fitting, and is both fast and robust. For this project MLLS was attempted for separation of EELS features as well as EDS mapping, but only EDS mapping was found to be necessary. For that purpose, the non-linear fitting algorithm present in the HyperSpy software proved easiest to use. The HyperSpy software is detailed in section 3.7.

Measuring the suboxide and oxygen-saturated metal regions

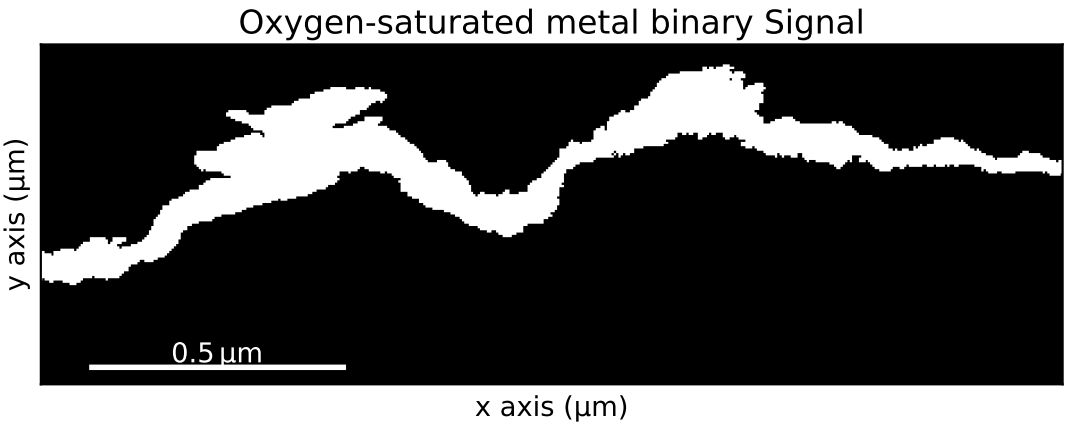
In order to simplify measurement on the EELS spectra, and because the area of oxygen-saturated metal is much greater than the area of suboxide, the area referred to as the "oxygen-saturated metal" is taken as the whole band between the metal and the oxide, *including* the suboxide. This was done by analysing large low-loss EELS spectrum images taken around the suboxide by ICA, like the one shown in figure 3.16. Of the output images, the one showing the oxygen-saturated metal was saved as a Tiff, and then using a combination of the Magic Wand, Ellipse and Fill tools in the software Adobe Photoshop, the region was coloured in white, whilst the rest was coloured black, as seen in figure 3.17.

This binary image was then projected down onto the x-axis, producing a plot of the oxygen-saturated metal as a function of the metal-oxide interface. The plot is skewed in regions of high curvature of the metal-oxide interface, but it was decided that attempting to stretch it out could be introducing artefacts of its own, and therefore left as is. The plot was then binned into a histogram, allowing

the region's thickness to be compared across samples. EELS acquisitions on each sample were taken at the same magnification, making the pixel size identical for analyses on different regions on the same samples.



(a) ICA low-loss output showing the oxygen-saturated metal region in dark grey.



(b) The binary image produced by colouring in the oxygen-saturated metal region.

Figure 3.17: Comparing the (a) DF and the (b) oxygen-saturated area on a 225-day ZIRLO sample. The region of interest is the dark grey band across the sample in (a). Very faint outlines of the sawtooth suboxide can be seen within it. The binary image in (b) is projected onto the x-axis and converted into a plot of the oxygen-saturated metal thickness.

3.6.2 Suboxide EELS analysis

During my investigations of the suboxide and oxygen-saturated metal regions in the oxidised ZIRLO and Zircaloy-4 samples, it became necessary to do quantitative analysis on the EELS spectra. It was of particular interest to determine the ratio

of oxygen to zirconium atoms across the metal-oxide interface. After background reduction, the Zr M, Zr L and O K core-loss edges were fit using EELS edges provided through the software Gatan DigitalMicrograph. As a standard, it was known that the ratio of oxygen to zirconium atoms in the oxide was stoichiometrically 2:1. Therefore,

$$\frac{C_O}{C_{Zr}} = \frac{2}{1} \tag{3.2}$$

Since the ratio of the elements can be expressed as the ratio of the background-subtracted intensities of those lines multiplied by a k-factor dependant on the system [154], the expression becomes:

$$\frac{C_O}{C_{Zr}} = \frac{I_{O_K}}{I_{Zr_M}} \times k_{\frac{Zr_M}{O_K}} \tag{3.3}$$

In the oxide then, k can be solved as follows:

$$k_{\frac{Zr_M}{O_K}} = \frac{2 \times I_{Zr_M}}{I_{O_K}} \tag{3.4}$$

Finally, the expression can be rewritten from a fraction to percentage oxygen (where in the oxide there exists 66.6% oxygen and 33.3% zirconium) as follows:

$$PercentageO = 100 \times \frac{\frac{I_{O_K}}{I_{Zr_M}} \times k_{\frac{Zr_M}{O_K}}}{\frac{I_{O_K}}{I_{Zr_M}} \times k_{\frac{Zr_M}{O_K}} + 1} \tag{3.5}$$

and for Zr:

$$PercentageZr = 100 - PercentageO \tag{3.6}$$

This approach has previously been done by several researchers [155, 156].

In addition to calculating the concentration of zirconium and oxygen, I will be using the white lines on top of the transition element L edges to see if the Zr and Nb oxidation state can be tracked as the metal oxidises as previously shown [156]. The white lines are Gaussian-like peaks on top of some EEL edges, named so because of their relative intensity when they were acquired on film. The white lines have previously been used to determine the oxidation state and 3d state occupancy in oxides [157–159]. Using the HyperSpy software [148, 149], the fit has been performed by convoluting the low loss signal with a model consisting of core loss

edges (using the Hartree-Slater generalised oscillator strength (GOS) calculations from the Gatan DigitalMicrograph software) and Gaussians. The Hartree-Slater edge shape is fit with its onset at the maximum of the white line. The Gaussian then fits the white line on top of the edge. The area of the Gaussian, above the edge, is then considered to be the intensity of the white line used for calculating peak ratios between L_3 and L_2 edges in later Chapters.

3.7 HyperSpy EELS analysis software package

EELS and EDS analysis was primarily done using the Python open-source software package HyperSpy [148], which I helped develop during my DPhil. It aims to be a general statistical analysis package, but has been mainly developed by users in the electron microscopy community. It therefore contains packages for doing EELS ZLP alignment, PCA and ICA, curve fitting and spike removal (shown in example in figure 3.18) and many more tools for analysis. I am very grateful to the development team for valuable help and feedback over the course of my DPhil.

X-ray spikes, resultant from either cosmic rays or stray X-rays from within the column hitting the GIF, were sometimes necessary to remove to correctly quantify the signal. These spikes stand out clearly, and are easily removed by interpolation. However, for spectrum images with many pixels this process can become tedious. I therefore developed Python code to automate this process. It is detailed in appendix 9.

3.8 Secondary ion mass spectrometry

Secondary Ion Mass Spectrometry (SIMS) is the analysis of charged particles emitted by bombardment of a surface with energetic primary ions. Analysis of the mass-to-charge ratio of these particles enables detailed analysis of the surface chemistry. SIMS is excellent for analysing a large range of materials due to its combination of very high chemical sensitivity, excellent mass resolution, surface sensitivity, lateral and depth resolution not being matched by any other technique.

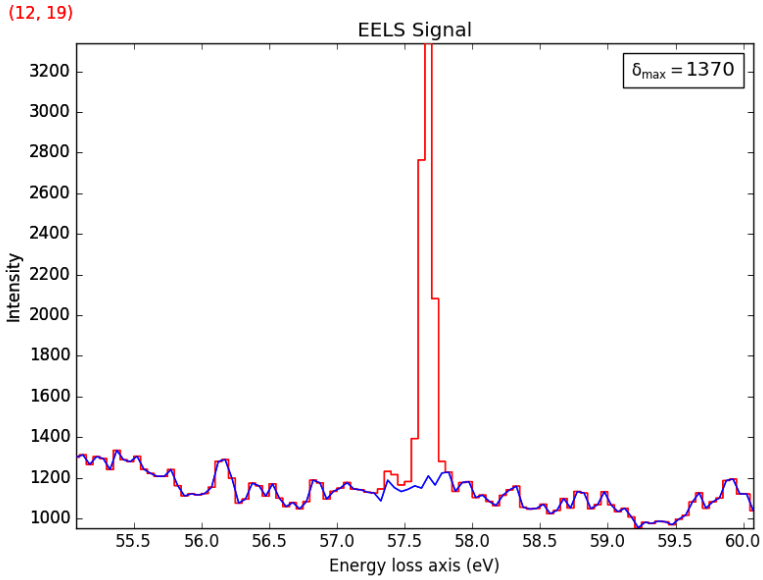


Figure 3.18: X-ray spike removal from EELS spectrum image using HyperSpy. Red line indicates X-ray peak, blue line indicates the proposed background fit.

The energetic primary ion beam causes particles to be emitted from the surface of the material. These emitted (secondary) particles are a combination of electrons, neutral species, atoms, molecules or atomic and cluster ions [160, 161].

The location of hydrogen in the zirconium oxide is unknown in the literature. In order to investigate this, I used a Cameca NanoSIMS to do SIMS mapping on cross-sectioned samples of oxidised zirconium alloy. Of particular interest is the effect of transition (in terms of the oxidation profile) on hydrogen pickup. Pre-oxidising the samples in H_2O to the pre- and post-transition regimes before further oxidation in deuterated water allowed this to be measured. This is similar to the method used by Yardley et al. [82], where ZIRLO and Zircaloy-4 were oxidised in pure water for a set amount of time before being further oxidised in ^{2}H and ^{18}O water.

The samples have been mapped in two ways. Many experiments were done on samples cut in cross section and polished. Here, the metal-oxide interface was imaged at a relatively low magnification to map features from the surface of the oxide and deep into the metal. A second form of mapping was done by milling the sample by SIMS, from the surface of the oxide towards the metal-oxide interface. Here either a one-dimensional depth profile or three-dimensional volume was acquired.

Both methods have advantages and problems. The cross-section method allowed for excellent low-magnification images of hydrides, but suffered from surface-oxidisation of the metal during imaging, as well as hydrocarbon from the nearby resin coating the sample, giving a false hydrogen signal. Milling through the oxide presented its own challenges. In order to mill through in a reasonable time (24 hours), only a very small region could be imaged ($25\,\mu m^2$ to $100\,\mu m^2$), and the acquisition suffered from sample drift. However, the slow acquisition enabled imaging of the position of hydrogen at a length scale not achieved with the cross-sectional imaging.

3.8.1 Diffusion profiles

For the diffusion of hydrogen through the oxide on zirconium alloys in an autoclave, Fick's second law of diffusion applies. I have made the assumption that the concentration of hydrogen is kept constant on the surface of the oxide even though this is likely to be incorrect as the amount of hydrogen produced by the oxidation process (according to equation 2.2) changes with transition. However, as I anticipate diffusion of hydrogen through the oxide lattice to be slow, I will make the assumption. This scenario can be described by equation 3.7,

$$C(x) = C_s \,\mathrm{erfc}(\frac{x}{2\sqrt{Dt}}) \tag{3.7}$$

where C is the concentration at a given distance from the surface of the oxide (or where the barrier to hydrogen diffusion begins), C_s is the concentration of hydrogen at the surface, $erfc$ is the complimentary error function, D is the hydrogen diffusion coefficient and t is the time the sample has been oxidised.

Since I anticipate the metal to already contain a low concentration of hydrogen, equation 3.7 is modified to 3.8.

$$C(x) = (C_s - C_m) \,\mathrm{erfc}(\frac{x}{2\sqrt{Dt}}) + C_m \tag{3.8}$$

where C_m is the concentration of hydrogen pre-existing in the metal. An example of this diffusion curve is plotted in figure 3.19.

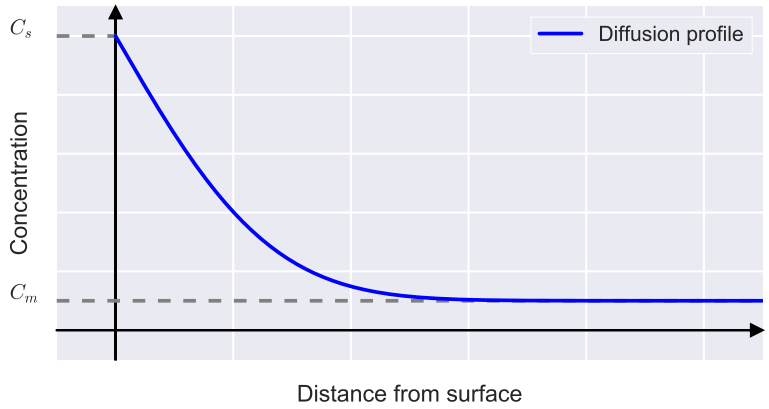


Figure 3.19: Fick's second law of diffusion applied to hydrogen diffusion through zirconium oxide in an autoclave. C_s is the surface concentration of hydrogen and C_m is the pre-existing hydrogen concentration in the metal.

3.9 Materials

Table 3.1 is an overview of all the alloys received through the MUZIC-2 program:

Normal H_2O	**Deuterated**	**High-pH H_2O + D_2O**
Zircaloy-2 LK2	**ZIRLO**	**Zircaloy-4**
Zircaloy-2 LK2 Annealed*	**Zr-1Nb**	
Zircaloy-2 LK3	**Zr-1Nb Annealed***	
Zircaloy-4	Zircaloy-2	
Zircaloy-4 Annealed	**Zircaloy-4**	
Zr-0.5Nb		
Zr-1.0Nb		
Zr-1.0Nb Annealed*		
Zr-1.0Nb Ring		
Zr-2.5Nb		
ZIRLO		
ZIRLO Annealed*		
ZrNbSb		

*The final anneal stage of manufacture was done at 720 °C for 24 hours rather than below the 680 °C phase transformation for α-Zr to β-Zr.

Table 3.1: List of received zirconium alloys. Only the highlighted alloys were analysed in this project.

Of these alloys, the following were chosen to be analysed in this project. ZIRLO and Zircaloy-4 in particular were chosen due their similarities in application (both are used in PWRs), whilst ZIRLO has improved corrosion-resistance. For TEM analysis,

samples of ZIRLO and Zircaloy-4 oxidised to certain states relative to transition were chosen to allow for direct comparison. The ZIRLO material in question is normal ZIRLO, not "Optimized ZIRLO". Other samples were chosen simply due to their availability for SIMS imaging, like the high-pH oxidised Zircaloy-4, which is discussed further in Chapter 7. For the SIMS samples, sample preparation in the form of deuterium oxidation was performed at the University of Manchester and AMEC as part of the MUZIC-2 program. These samples are listed in table 3.2. The samples were prepared for a number of types of analysis, and I was not part of the decision-making for how long the samples should be oxidised for. A set of Zircaloy-4 samples were oxidised at high pH (pH 8.8 at 350 °C) by the National Nuclear Laboratory for James Sayers, a fellow DPhil student for his project. They are included here as they were available at the time.

Other than the set of high-pH Zircaloy-4 samples, all samples were oxidised in pH-neutral water, with a typical initial pH of about 6.8, with some day-to-day variation. For the Westinghouse oxidation, the pH of the water was documented to have increased to between 7.2 and 7.8 after oxidation.

Normal H_2O	**Deuterated**	**High-pH H_2O**
ZIRLO	ZIRLO	Zircaloy-4
Zircaloy-4	Zr-1Nb	
	Zr-1Nb Annealed*	
	Zircaloy-2	
	Zircaloy-4	

Table 3.2: List of analysed zirconium alloys

4

The corrosion of ZIRLO

Contents

4.1 Introduction 82
4.2 Oxidation characterisation 84
4.2.1 The inaccuracy of 'pre'- and 'post'-transition descriptions 84
4.2.2 3D-FIB Sectioning 84
4.3 ZIRLO samples 86
4.3.1 Oxide structure 86
4.3.2 3-day pre-transition ZIRLO 87
4.3.3 45-day pre-transition ZIRLO 90
4.3.4 135-day post-transition ZIRLO 91
4.3.5 225-day post-transition ZIRLO 96
4.4 EELS analysis on ZIRLO 103
4.4.1 Low-loss EELS 103
4.4.2 Core-loss EELS of the metal-oxide interface 115
4.4.3 3-day ZIRLO 119
4.4.4 45-day ZIRLO 121
4.4.5 Necessity of EDS for SPP imaging 125
4.4.6 SPP oxidation state 125
4.5 Discussion 130
4.5.1 3D-FIB sectioning 130
4.5.2 EELS fine structure and plasmon analysis 131
4.5.3 Dissolution of Fe in SPPs 132
4.5.4 The effect of cracks 134
4.5.5 Porosity near the metal-oxide interface 136
4.5.6 Corrosion resistance and oxygen-saturated region 138
4.5.7 Suboxide 139
4.6 Summary 141

My intention with this chapter is to introduce the reader to the ZIRLO cladding material, give an overview of the way in which it corrodes and its hydrogen distribution as a result of corrosion. As this is my most heavily studied alloy, I will go into detail regarding its microstructure, chemical structure, second phase particle composition, hydrogen distribution etc.

4.1 Introduction

The samples studied in this chapter are ZIRLO alloys oxidised as part of the MUZIC-2 program. They were oxidised in an autoclave in pure water at 360 °C and weighed by Westinghouse Electric Company, specifically by Jonna Partezana, to whom I am very grateful.

The alloys studied (with weight gains seen in figure 4.1 and in table 4.1) were from a selection of alloys oxidised from 1 to 225 days. From this range of times, samples were chosen based on their position relative to transition and their oxide growth rate. The three-day pre-transition sample was chosen as there has been very little research on alloys oxidised for such a short time. The 45-day pre-transition sample was chosen in order to investigate a sample where the oxidation rate is slowing down and the 135-day post-transition was chosen because the oxidation rate was speeding up. The final, 225-day post-transition sample was chosen to compare the findings of the first three with one in the far post-transition regime.

The weight gain data for the ZIRLO alloy (oxidised at 360 °C) can be fitted using $k = 7.3\,\mathrm{mg\,dm^{-2}\,d}$ and $n = 0.33$ in equation 2.4. The transition point is at approximately 100 days, at which point the average oxide thickness should be 2.3 µm.

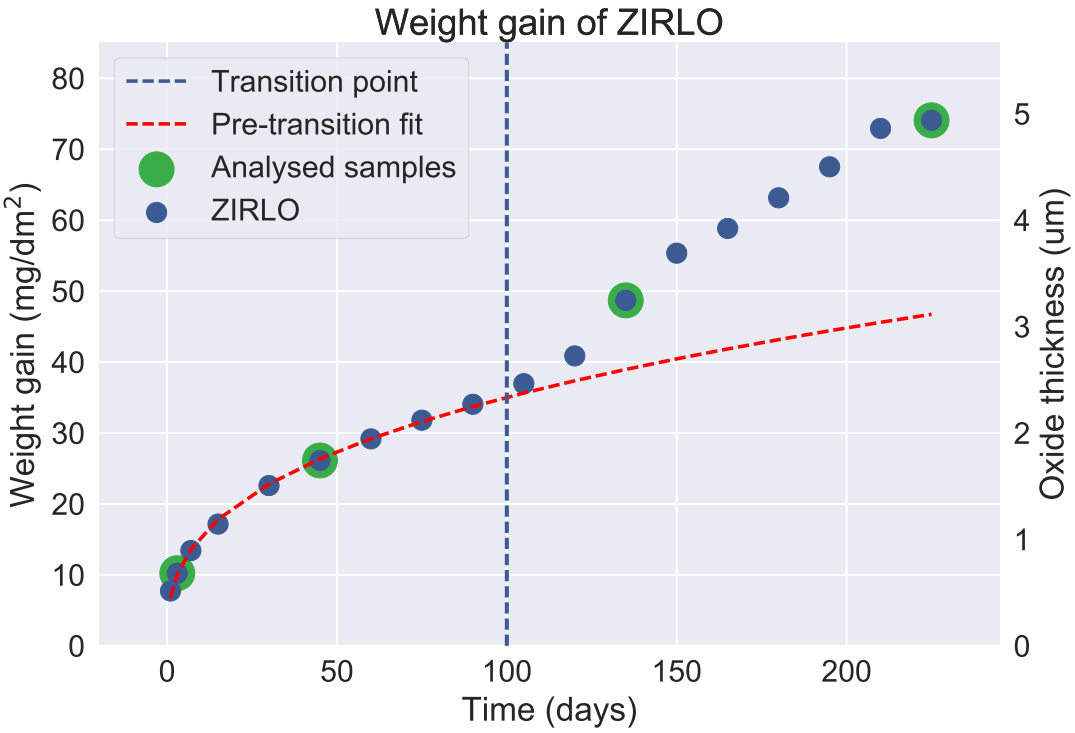


Figure 4.1: Weight gain of ZIRLO at 360 °C. The vertical dashed line indicated the point of first transition, at about 100 days. The right-hand axis indicates the approximate oxide thickness given by equation 4.1. The red dashed curve indicates the fit of the pre-transition weight gain to a power law with $k = 7.3\,\mathrm{mg\,dm^{-2}\,d}$ and $n = 0.33$.

Time (days)	Weight gain (mg dm^{-2})	Oxide thickness (µm)	**Time (days)**	Weight gain (mg dm^{-2})	Oxide thickness (µm)
1	7.74	0.52	**105**	36.96	2.46
3	10.24	0.68	**120**	40.87	2.72
7	13.43	0.9	**135**	48.7	3.25
15	17.16	1.14	**150**	55.35	3.69
30	22.6	1.51	**165**	58.84	3.92
45	26.13	1.74	**180**	63.15	4.21
60	29.17	1.94	**195**	67.52	4.5
75	31.81	2.12	**210**	72.93	4.86
90	34.05	2.27	**225**	74.08	4.94

Table 4.1: Weight gain of ZIRLO in water at 360 °C.

4.2 Oxidation characterisation

4.2.1 The inaccuracy of 'pre'- and 'post'-transition descriptions

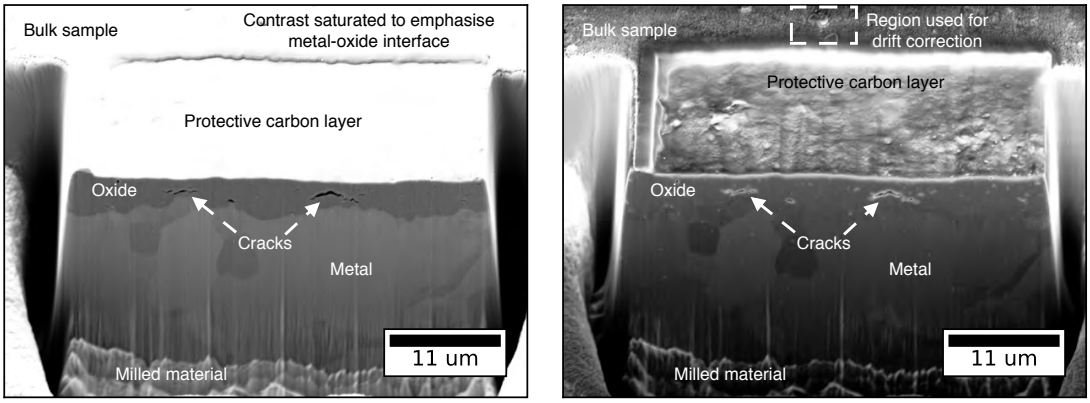
Whilst the weight gain gives us an approximate oxide thickness by the relation

$$\frac{\text{Weight gain (mg/dm}^2)}{15} = \text{Oxide thickness (µm)} \tag{4.1}$$

it is hardly an accurate measurement for the local oxide thickness. Despite this, it is often used when comparing microstructural features between alloys oxidised for different amounts of time.

4.2.2 3D-FIB Sectioning

In a novel experiment, to demonstrate the inaccuracy of using an averaged macrostructural quantity to represent features at the nanoscale, I performed 3D-FIB milling on the samples shown selected in figure 4.1. Volumes of 20 µm × 20 µm × 8 µm were milled and analysed. An example of the two simultaneously-detected signals from halfway through a 3D-FIB-slicing experiment can be seen in figure 4.2. The SE image, on the left, proved to be by far the most useful due to the differing secondary-electron yield between the metal and oxide. The Zeiss Inlens detector was often useful in providing contrast in regions used later for image alignment, but did not provide any useful microstructural information for this particular 3D-FIB work.



(a) SE detector image. **(b)** Inlens detector image.

Figure 4.2: 3D-FIB slicing on a sample of 45-day pre-transition oxidised ZIRLO.

I manually measured the oxide thickness across several slices of each material. By measuring lines every 50 nm on each image, and choosing one image every 4 µm from the 3D block, I got an accurate measurement of the oxide thickness, taking into account the surface and metal-oxide roughness. This is shown by the histogram in figure 4.3. Here, the measured oxide thickness is plotted with the weight-gain average shown as a dashed vertical line.

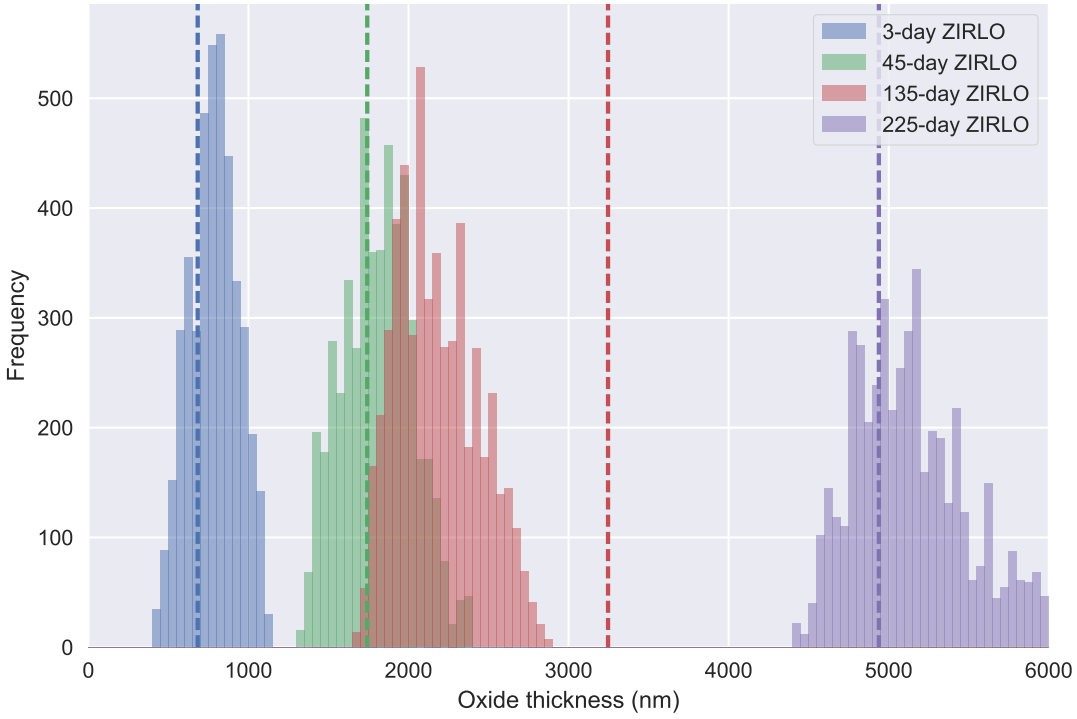


Figure 4.3: Histograms showing the variation in oxide thickness across oxidation time. The dashed lines indicate the expected oxide thickness converted from the weight gain.

The 3-day, 45-day, 135-day and 225-day samples of ZIRLO show similarly shaped distributions, with means at 782 nm, 1812 nm, 2182 nm and 5185 nm respectively. Here the 135-day distribution particularly stands out. The average oxide thickness expected from the weight gain was 3250 nm, which is nearly 50% higher than what is measured here. Presumably, this is just a particularly thin part of oxide that was investigated by FIB.

Attempts were made to automate integration of the oxide thickness across the entire resulting 3D block. However, the contrast provided by the FIBSEM was not enough to separate the phases automatically. The greatest challenges for automatic

reconstruction were the gradual loss of electron signal and loss of focus as the face of the 3D block moved further away from the detector, as well as curtaining effects from the FIB beam. These effects, combined with blending contrast from grain boundaries and cracks made automatic reconstruction difficult.

4.3 ZIRLO samples

4.3.1 Oxide structure

To give an overview of the oxide structure for each of these ZIRLO samples, I have compared two of the STEM imaging modes, HAADF and DF, on FIB lamellas extracted from the samples highlighted in figure 4.1.

The HAADF is built up mainly of Z (atomic number) contrast, emphasising the different phases present, especially contrasting the metal and oxide, but also the second-phase particles (SPPs). HAADF intensity goes approximately as Z^2. Since the average atomic number in the oxide (ZrO_2) is 24 and density is approximately 13 % lower, it scatters fewer electrons and so appears darker than the metal, where the atomic number of Zr is 40. Metallic β-Nb SPPs, with atomic number 41, appear bright in the metal, whilst $Zr(NbFe)_2$ SPPs appear fainter. In the oxide all SPPs should appear bright, but as they oxidise they diminish in intensity.

In contrast, the DF image is formed mainly by diffraction contrast, and emphasises the grain structure in the metal and oxide. When comparing the oxide structure, I will be presenting images from the same region, side by side. The images are typically montaged by acquisition of several regions down the oxide, and in the case of the 225-day post-transition ZIRLO sample these regions are presented separately in order to have a comparable, high magnification between the samples.

In addition to the montaged regions, I have selected several regions of interest from features present in the oxide, and have analysed them with EDS and EELS.

I am now going to go through the samples identified in figure 4.1 using the previously presented characterisation techniques. The aim is to identify differences in the sample structure and chemical composition in order to better understand the corrosion of ZIRLO. In the next chapter, these differences will be compared with

the findings for Zircaloy-4 in an attempt to characterise the distinctions arising from varying the alloy composition. Note that the alloy studied is regular ZIRLO, not Optimized ZIRLO (which is a later, improved, version of the alloy).

4.3.2 3-day pre-transition ZIRLO

The following results are amongst the first on short-term corrosion of ZIRLO. Analysis is normally done on samples that have been oxidised to before and after transition [47, 65, 162] or after years in reactor [53]. The oxidation rate of zirconium alloys is at its most rapid in the first day of oxidation, as metal is freshly exposed to the oxidising species. Whilst a 1-day sample was taken during the autoclave oxidation (its weight gain is shown in table 4.1), only the 3-day sample was made available for TEM preparation. Three successfully thinned TEM foils were prepared from the sample.

The oxide on these samples is very thin, making them particularly prone to damage from the FIB during sample preparation. Figure 4.4 shows a FIB liftout where most of the oxide was preserved, with protective carbon and gold on top.

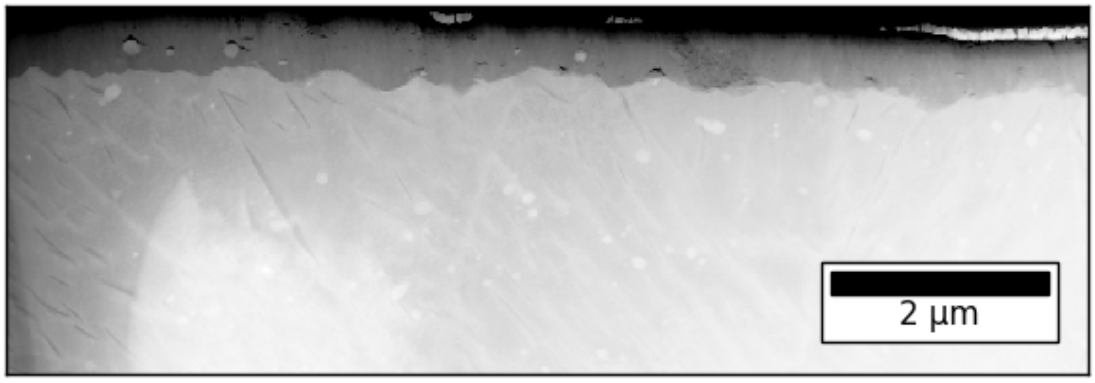
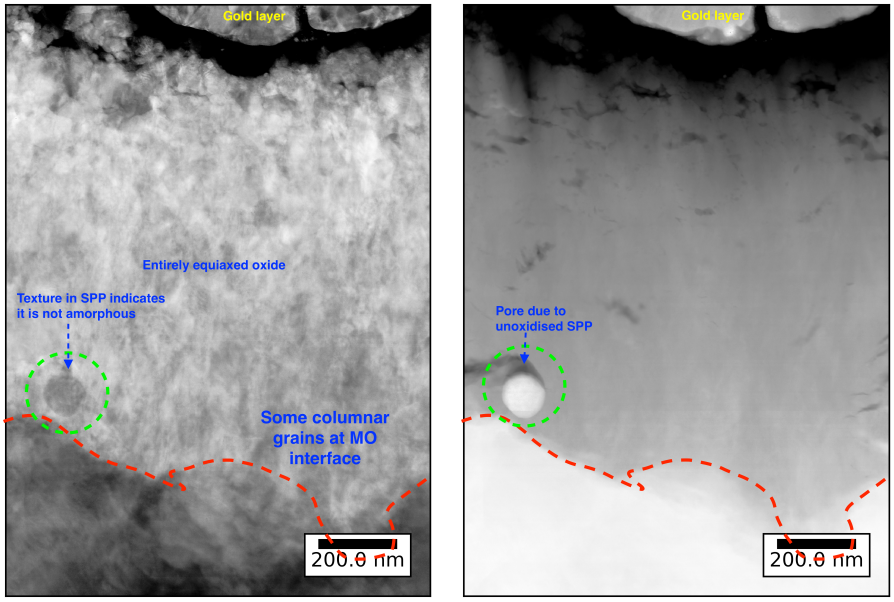


Figure 4.4: HAADF overview image of a 3-day pre-transition ZIRLO sample.

A montage of the oxide on another sample is shown in figure 4.5. The oxide is mostly equiaxed, with no clear formation of columnar grains. The typical equiaxed grain size is approximately 40 nm, but the grains are very difficult to distinguish from each other. The oxide thickness in this region is approximately 1.2 µm, putting it on the upper edge of the oxide thickness range that was measured by 3D-FIB in

figure 4.3. An SPP is present 10 nm from the metal-oxide interface. The texture in the SPP present in the DF image shows that the SPP is not amorphous. The HAADF image reveals that there is a pore on top of the SPP. This is due to the oxide's Pilling Bedworth ratio of 1.56, causing an expansion of the oxide. As the SPP continues to oxidise it will expand to fill the pore. Interestingly, a crack has formed to the left of the SPP, which tails off into the SPP pore. I have seen many cracks occur near SPPs, suggesting there is a connection, although most cracks form in the oxide without the presence of SPPs.



(a) **(b)**

Figure 4.5: DF (a) and HAADF (b) STEM montage of the oxide on a 3-day pre-transition sample of ZIRLO. The metal-oxide interface is highlighted in red.

The 3-day corrosion has formed a generally very dense oxide with few large cracks. Large, open cracks, typically associated with transition, are few but present, as seen in figure 4.6. The outermost region of the oxide (top 100 nm to 400 nm) is very porous, particularly near cracks, but also generally throughout this part of the oxide.

There also exist numerous smaller cracks, typically less than 50 nm long throughout the oxide, although there is no obvious correlation between these and the oxide grain structure.

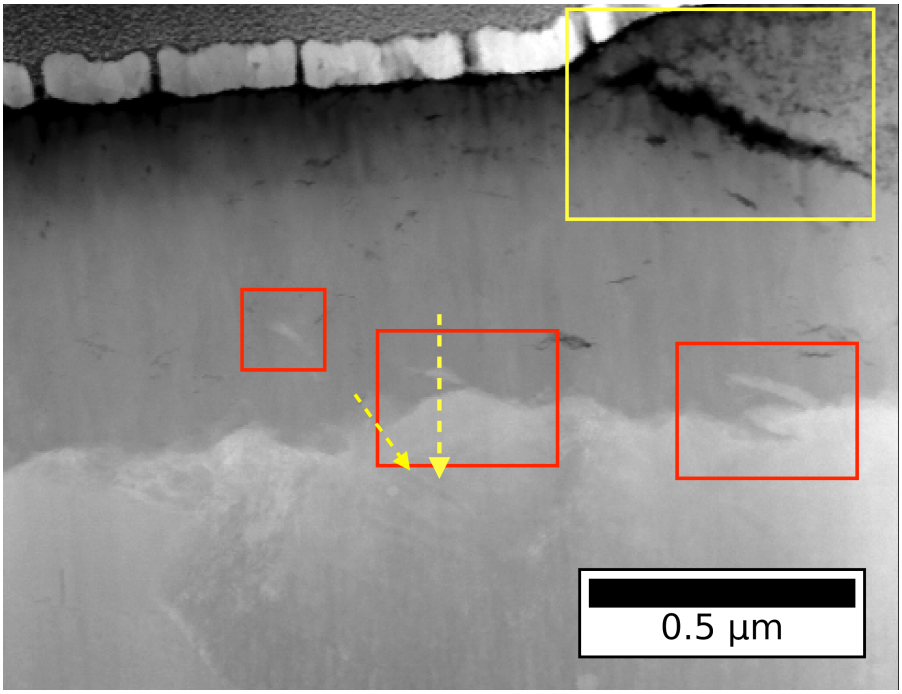
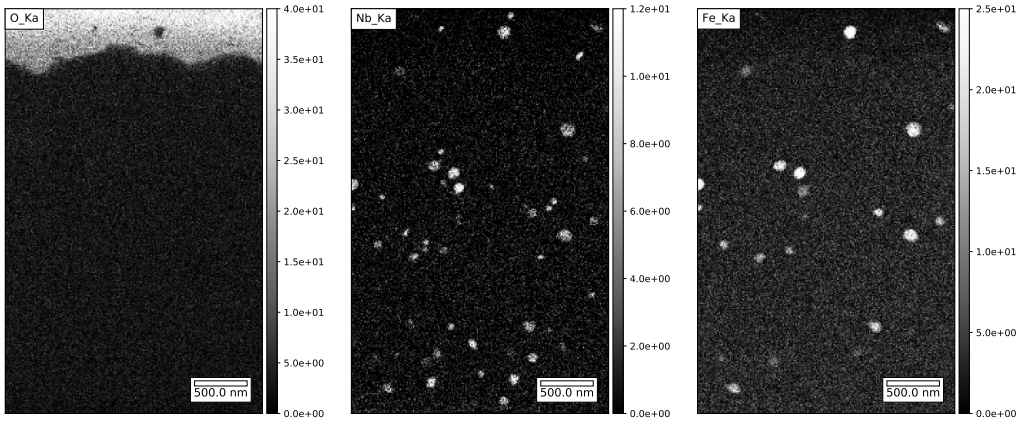


Figure 4.6: HAADF image of 3-day ZIRLO showing Zr-metal or suboxide regions present in the oxide highlighted by red rectangles. The large crack, highlighted by a yellow rectangle, is a feature typically associated with transition, especially when close to the metal-oxide interface. The yellow dotted lines indicate the position and direction of the EELS concentration profiles in figures 4.37 and 4.39.

The suboxide grains around the metal-oxide interface, when present, are typically small and rounded and difficult to quantify. The sawtooth-shaped grains normally associated with large regions of suboxide are rarely present. When they are, they are small, not larger than 50 nm long. It is difficult to say with certainty as to whether what appears as rounded suboxide on these samples is not simply overlap of the metal and oxide projected through the sample thickness. The oxygen-saturated region is much more well-defined, ranging from 0 nm to 200 nm.

SPP content

Figure 4.7 shows an EDS map of the pre-transition 3-day ZIRLO sample, showing a small part of the oxide and much of the metal. There are only four SPPs in the oxide, two α-Nb and two $Zr(NbFe)_2$ SPPs. In the metal there are 23 β-Nb and 20 $Zr(NbFe)_2$ SPPs, making for area number densities of 2.77 and 2.4 μm^{-2} respectively.



(a) O Kα **(b)** Nb Kα **(c)** Fe Kα

Figure 4.7: EDS maps at low magnification on a sample of 3-day pre-transition ZIRLO showing a large region of the metal. (a) shows the oxide, (b) the Nb SPPs and (c) the Fe SPPs.

4.3.3 45-day pre-transition ZIRLO

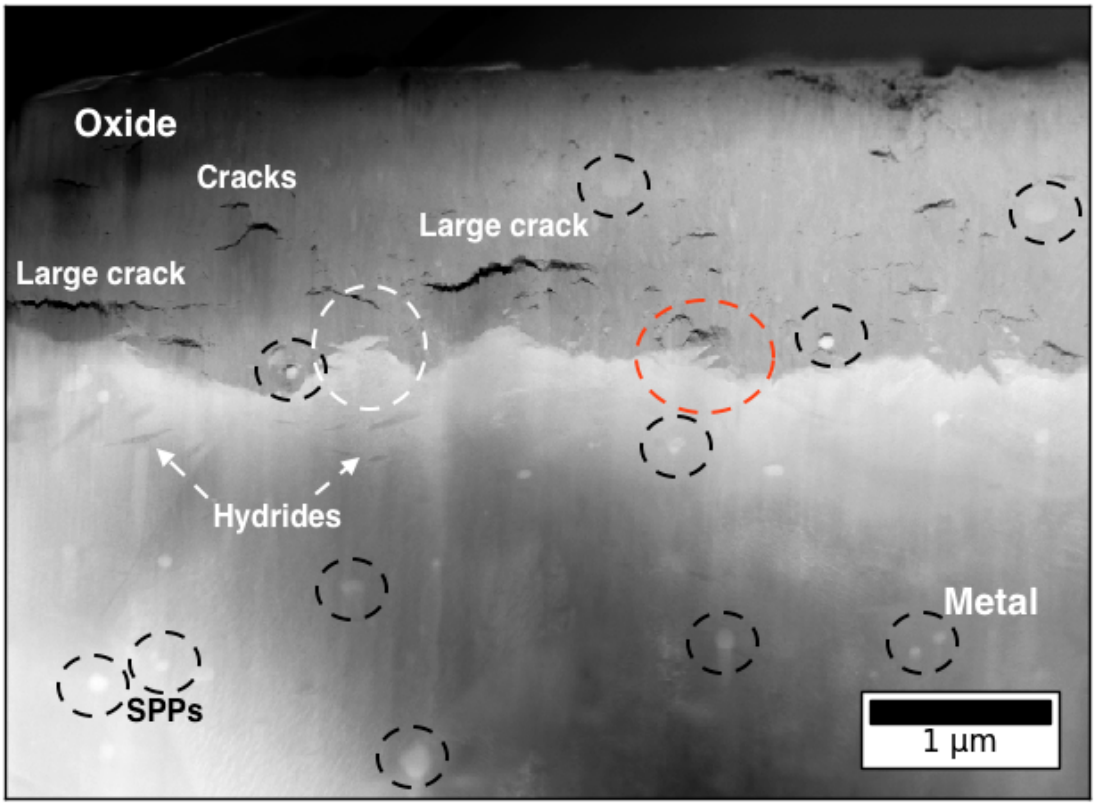


Figure 4.8: HAADF overview image of a 45-day ZIRLO sample. The white dashed circle shows a region of unusally-shaped metal-oxide interface. The red dashed circle shows a region of reversed suboxide, discussed in region 4.4.1.

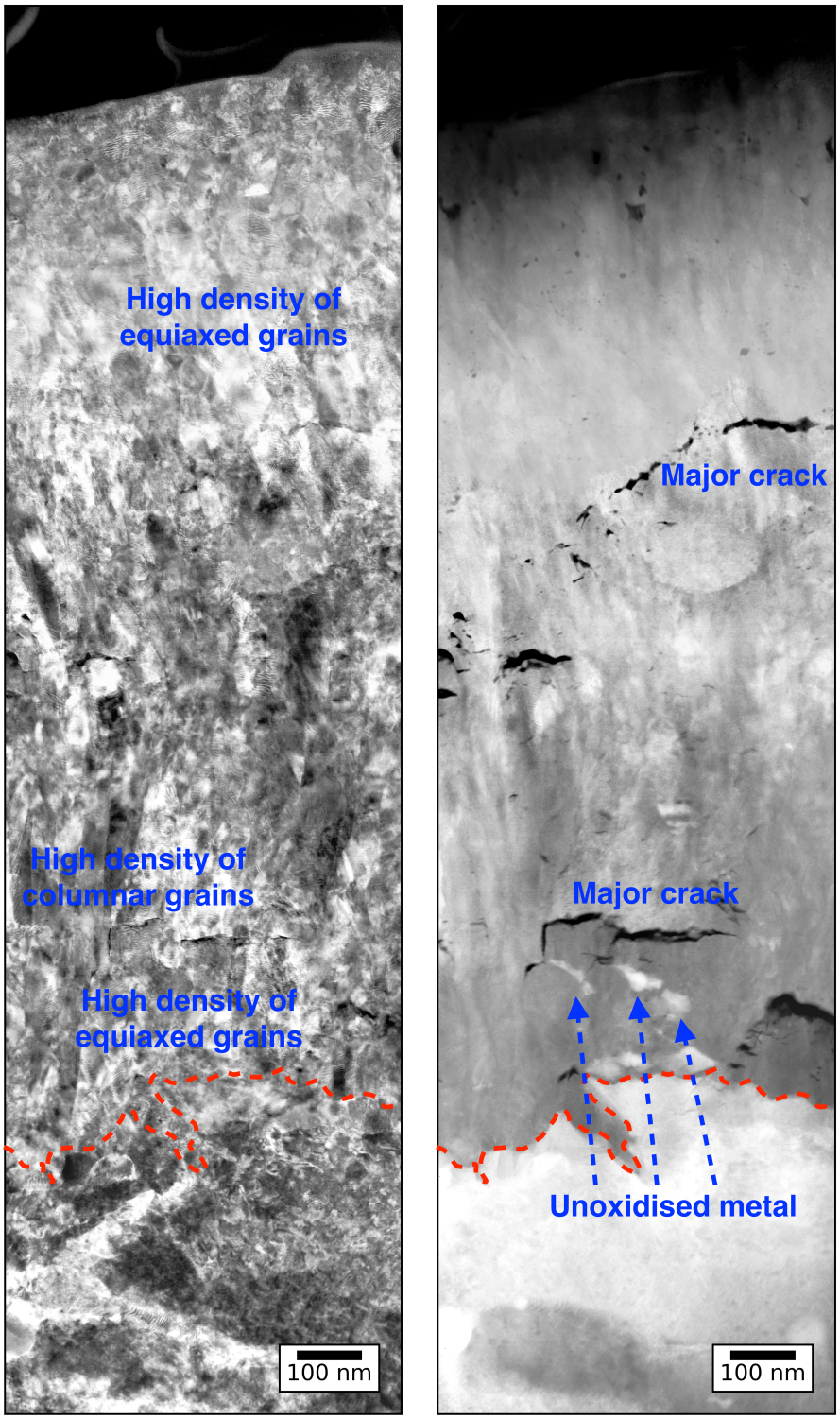
The 45-day pre-transition ZIRLO sample has a thin, densely packed oxide. Three TEM foils from the 45-day sample were successfully thinned. The HAADF overview image in figure 4.8 has an average oxide thickness of approximately 1.7 µm. There are many SPPs present, especially in the metal, and some are highlighted on the figure in black. In the oxide, two small SPPs are bright in contrast near the metal-oxide interface, but further into the oxide only two large SPPs can be seen. These are visible only due to their size. The metal-oxide contains two unusual features: an oddly shaped undulation of metal and a sawtooth shape facing into the oxide. These are highlighted in white and red dashed circles, respectively.

The oxide montage in figure 4.9 is approximately 1.5 µm thick. This is much lower than the anticipated oxide thickness of 1.94 µm from the weight gain measurements in table 4.1. There are several cracks present in the oxide. Figure 4.9b emphasises three regions in the oxide beneath a crack that are still metallic. It is likely that the crack prevented access to the diffusing oxygen species, although a three-dimensional view (for instance from 3D-FIB) would be required to analyse this further.

The 45-day sample mainly contains equiaxed oxide grains of about 20 nm to 50 nm, with some very clear columnar grains that are about 200 nm long and 50 nm thick, giving an aspect ratio of 4:1. This is slightly lower than typically reported ratio of 5:1 [65].

4.3.4 135-day post-transition ZIRLO

An overview HAADF image of the 135-day post-transition sample can be seen in figure 4.10. Four TEM foils were successfully thinned for the 135 day sample. As with other samples, the cracks in the oxide are observed to be correlated with a local reduction in oxide growth. However, there is one large crack, 1.4 µm in length where the oxide has grown quicker in the surrounding areas than where there are no cracks present. It is difficult to surmise why this is, but it is possible that the crack formed early on, and oxygen has had time to diffuse around, whereas the smaller "protective" cracks are relatively new.



(a) **(b)**

Figure 4.9: DF (a) and HAADF (b) STEM montage of the oxide on a 45-day pre-transition sample of ZIRLO. The metal-oxide interface is highlighted in red.

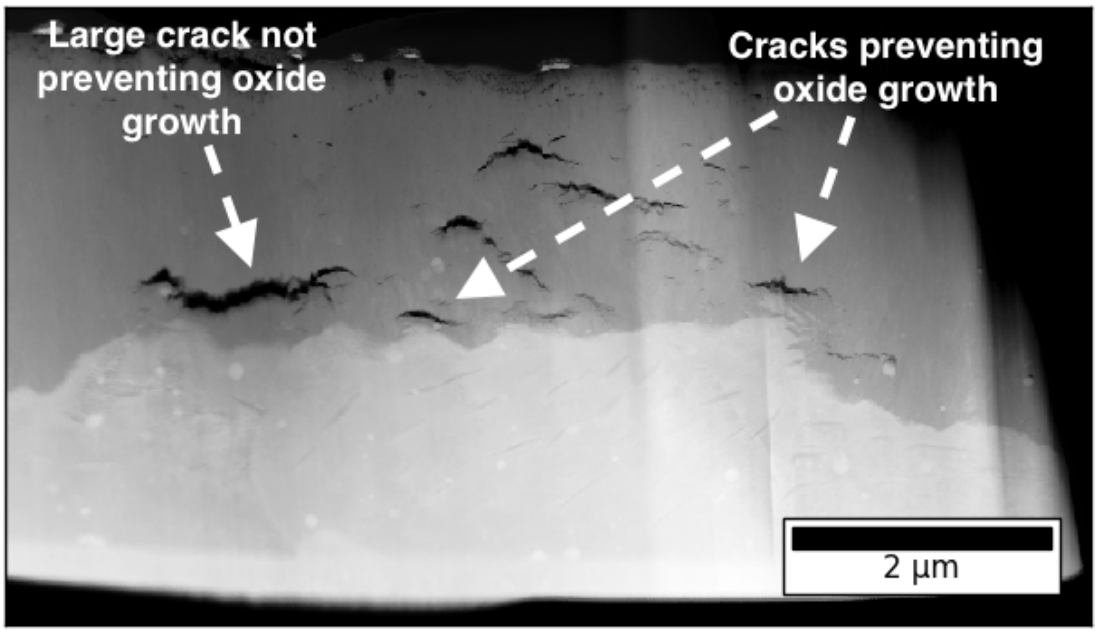
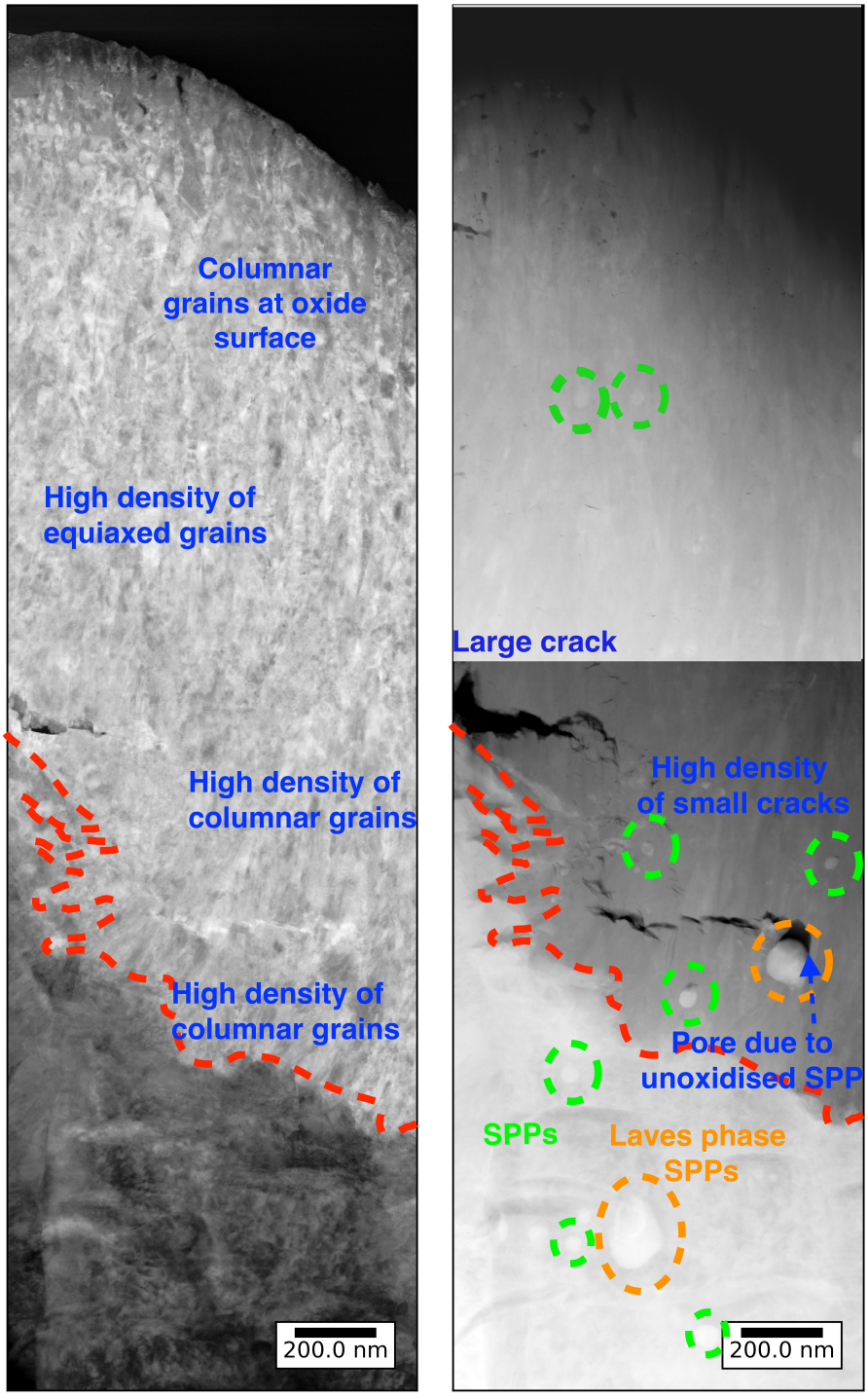


Figure 4.10: HAADF overview image of a 135-day ZIRLO sample.

The oxide in the montaged region of the sample, shown in typical DF and HAADF images in figure 4.11, contains a very large fraction of columnar grains. The smaller, equiaxed grains are present, with typical sizes of about 20 nm, but in small amounts compared to the 3, 45 and 225 days samples. The columnar grains are particularly visible near the metal-oxide interface, despite the increased thickness in this region. The interface, highlighted in a red dashed line, is particularly curved in the region shown on the montage. Just below the sawtooth shaped metal-oxide interface, columnar grains stand perpendicular to the interface, sometimes at sharp angles to the expected oxide growth direction. Cracks often split the columnar grains in two, which I have observed on the other ZIRLO samples as well.

The contrast change halfway down the HAADF image is an artefact from the merging of several images in a montage - the thickness of the sample is increasing towards the metal, which increases the intensity of the image.

The oxide thickness at the thinnest part is 1.9 µm whilst at its thickest it is 2.6 µm. This is substantially smaller than the expected oxide thickness of 3.3 µm calculated from the weight gain measurement. This suggests that the thin part of this particular region still is in pre-transition.



(a) **(b)**

Figure 4.11: DF (a) and HAADF (b) STEM montage of the oxide on a 135-day pre-transition sample of ZIRLO. The contrast-change halfway down the image is an artefact from acquisition of a montage to make these images. The metal-oxide interface is highlighted in red and SPPs visible on the HAADF image in green.

Low-loss EELS performed on the curved metal-oxide interface from the montaged images reveals that there is a large area of suboxide present as seen in figure 4.12. The commonly observed sawtooth shapes face into the oxygen-saturated metal on the left, but where the suboxide meets the curved metal-oxide interface it has a sawtooth shape that faces into the oxide. The oxide around this "reverse" sawtooth shape is all equiaxed, strongly contrasting to the columnar grains further down to the right where the oxide is thicker. In addition to the larger 500 nm long crack at the top of the curved interface, many nanocracks sit along it. The sawtooth shapes seem to emanate from these cracks, suggesting that they may be a source of either oxygen, stress relaxation or other charged species allowing the oxidation to take place. This may be an example of a region frozen halfway through transition, and will be discussed further in section 4.4.1.

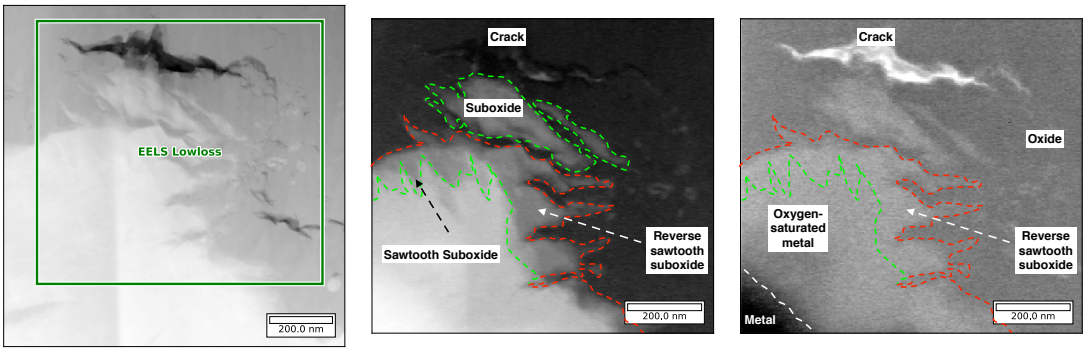


Figure 4.12: (a) HAADF survey image of the sawtooth-shaped metal-oxide interface. ICA loadings (b) and (c) reveal a complicated morphology of the suboxide phase.

Figure 4.13a shows a STEM HAADF image acquired on a Zeiss Merlin SEM at 30 kV in STEM mode. Acquisition on this instrument was attempted as an experiment, to compare its capability to the TEM. Whilst handling the sample was easier on the SEM, and the contrast present from the STEM detectors was good, STEM on the SEM provided no particular benefit over the dedicated TEM. The diagonal line present in the metal is an amorphised region damaged by the FIB thinning process. The EDS results show a distinct lack of SPPs around the major crack in the sample. It would be very interesting to see a 3D-FIB/EDS

segmentation of this type of region, to understand whether the SPPs have been pushed out to the sides of the crack or whether they might have been dissolved by the water likely to have been present in the crack whilst in the autoclave.

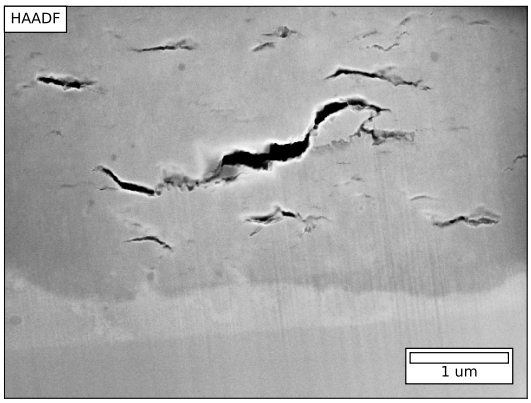
There are 34 niobium-containing SPPs and 13 iron-containing SPPs in this area. Two SPPs in the metal also contain a faint signal of chromium. Assuming that the niobium-containing SPPs that do not contain Fe are β-Nb SPPs and the remainder are Laves phases $Zr(NbFe)_2$ SPPs, which matches the literature [163], the number density of β-Nb is $1.3\,\mu m^{-2}$ whilst the number density of Laves phase SPPs is $0.8\,\mu m^{-2}$.

An SPP with a layered contrast was found in the oxide by TEM, approximately 500 nm from the metal-oxide interface. EDS was performed on the particle, revealing a centre region rich in Si. Note that the y-axis on the EDS profile is on a log-scale in order to simultaneously show all the elements detected. No attempt was made to quantify the exact elemental ratio. Looking at the HAADF image in figure 4.14a, the SPP has a Fe-enriched or $Zr(NbCr)_2$-depleted structure on the top side, although this could be due to overlap of the SPP with the oxide in projection through the sample. With exception of the top layer, the SPP contains Fe, Nb, Cr and Zr throughout and appears crystalline, although its oxygen content is high.

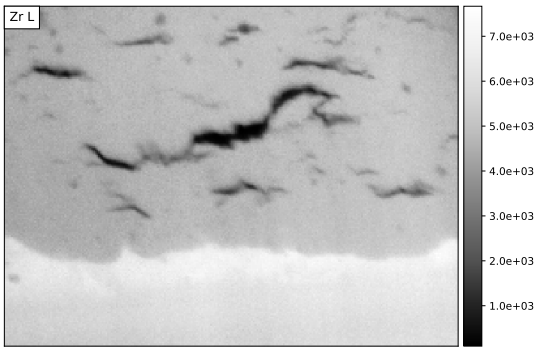
4.3.5 225-day post-transition ZIRLO

A total of eight successful TEM foils were produced from 225-day aged ZIRLO, four from the same batch of ZIRLO samples previously presented in this chapter, and four from a sample oxidised to 180 days and then further oxidised for 45 days in deuterated water. It is mainly the former set that is shown here, as the latter was taken in conjunction with the NanoSIMS work on deuterated alloys in chapter 6. Unless specified, it is the normal 225-day sample which is being shown.

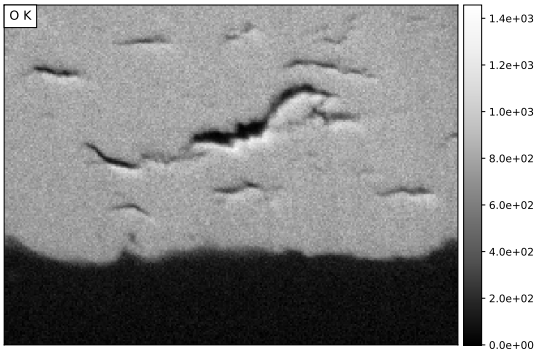
Figure 4.15b shows a HAADF image of a 225-day sample as a stitch of several images. Automatic contrast adjustment is responsible for the apparent brightness of the middle of the oxide region on the sample.



(a) SEM STEM HAADF image



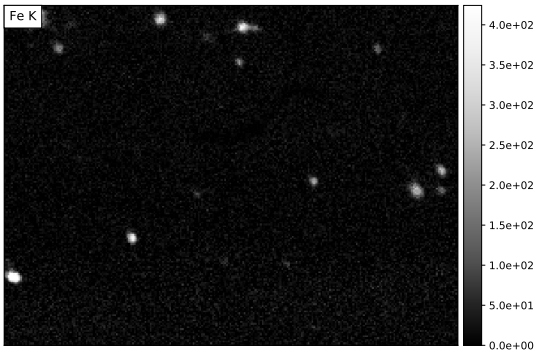
(b) Zr Lα



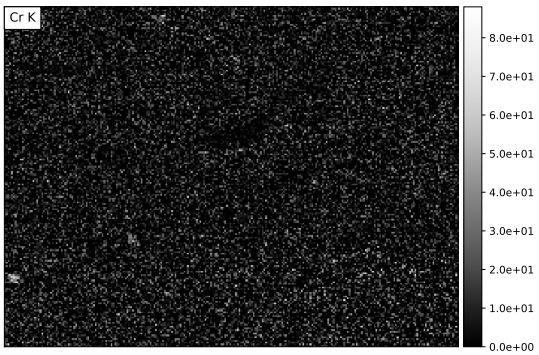
(c) O Kα



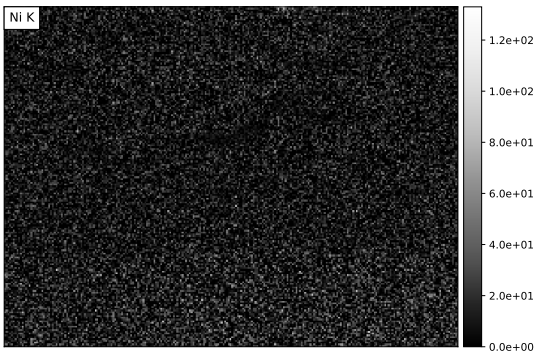
(d) Nb Lα



(e) Fe Kα



(f) Cr Kα



(g) Ni Kα

Figure 4.13: EDS maps of a sample of post-transition 135-day ZIRLO taken by STEM on a SEM. It contained 21 β-Nb and 13 $Zr(NbFe)_2$ SPPs.

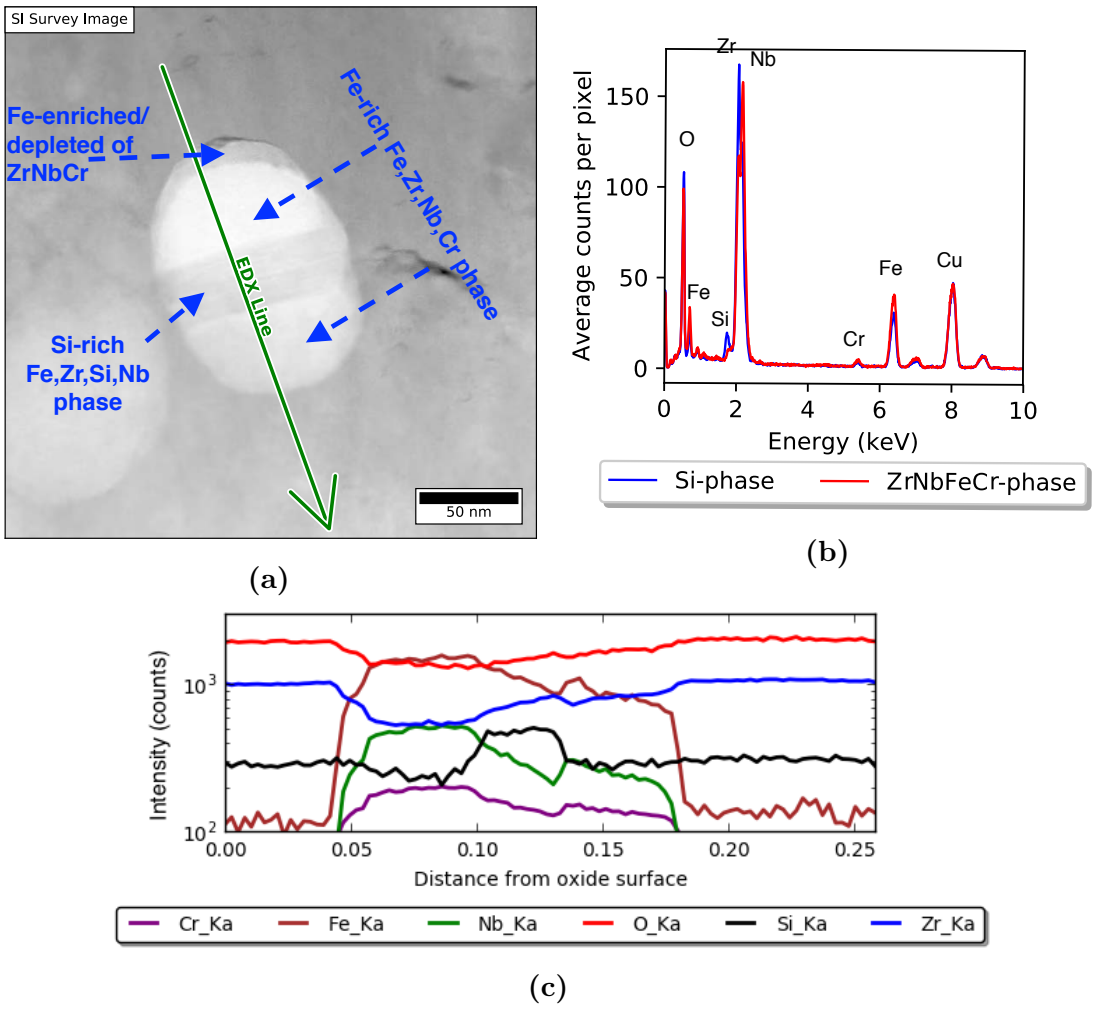
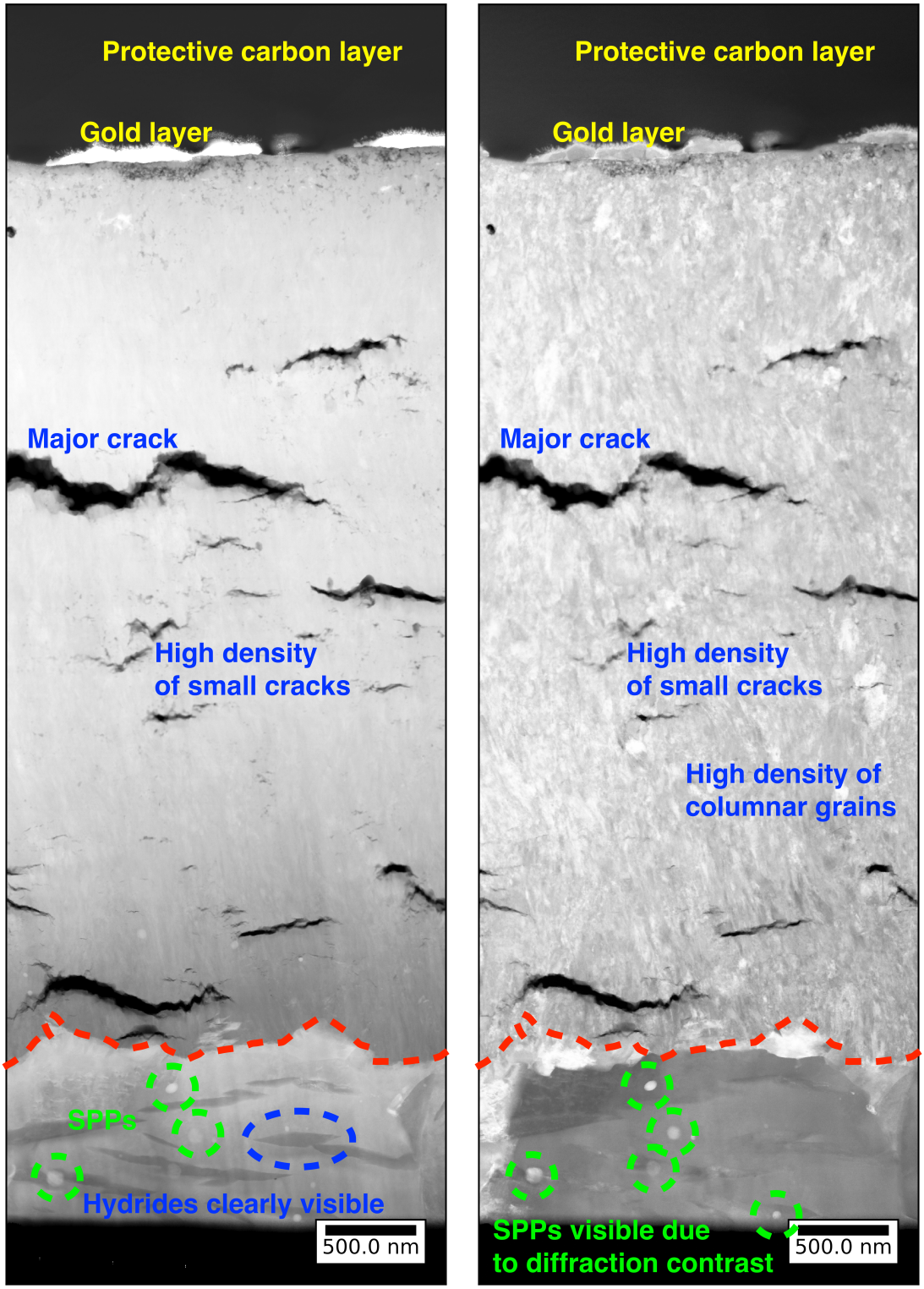


Figure 4.14: Composition of a SPP with unusual contrast on a HAADF image (a) analysed by TEM. The centre layer is Si-rich, as seen in the spectrum in (b) and profile in (c). The EDS profile plot is of the raw counts binned around each X-ray line.

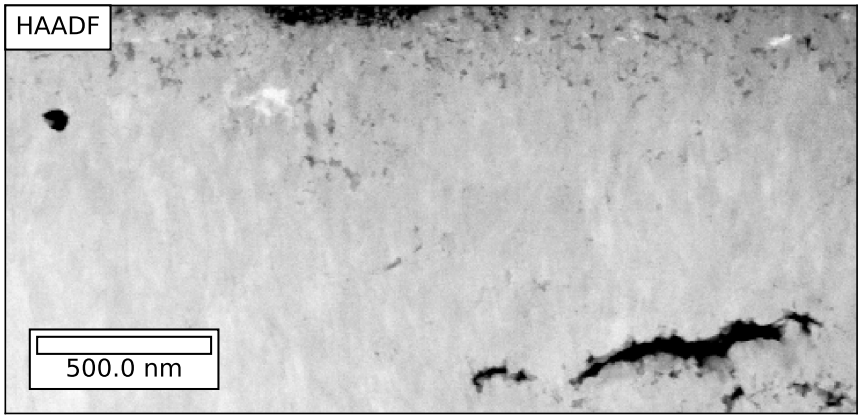
The top two microns of oxide show a few regions with high concentrations of nickel, as seen on the EDS map in figure 4.16. These do not appear in the metal, and as such must be caused by either the oxidation process or be an impurity present from the stainless steel walls of the autoclave where the oxidation was carried out. $Zr_2(Ni, Fe)$ SPPs have been reported in Zircaloy-2 due to the addition of 0.03 wt% to 0.08 wt% Ni [10], as shown in the literature review in section 2. ZIRLO, on the other hand, is not reported to have any addition of Ni. However, Zircaloy-4 does not contain Ni either, yet its presence there has been reported by EDS and APT [69]. To my knowledge it has not been reported in ZIRLO before. The 225-day ZIRLO is the only sample in which I found the segregation of nickel, which implies



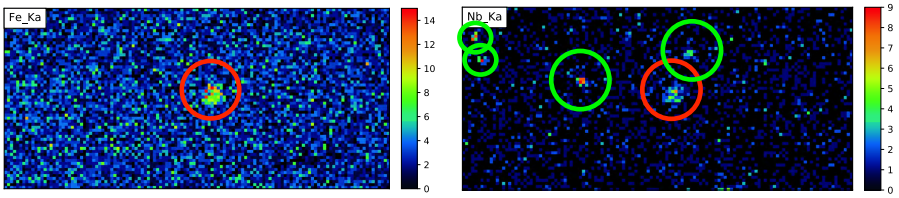
(a) (b)

Figure 4.15: (a) HAADF image of a 225-day post-transition sample of ZIRLO, formed mainly of Z-contrast. (b) Diffraction contrast of a 225-day post-transition sample of ZIRLO. The metal-oxide interface is highlighted in red.

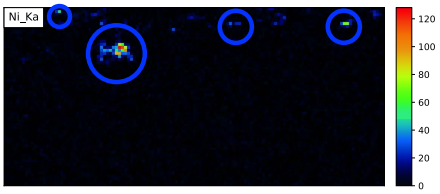
the agglomeration is as an effect of extended oxidation, either from the autoclave walls, or agglomeration through some other process.



(a) HAADF image



(b) Fe Kα signal. **(c)** Nb Kα signal.

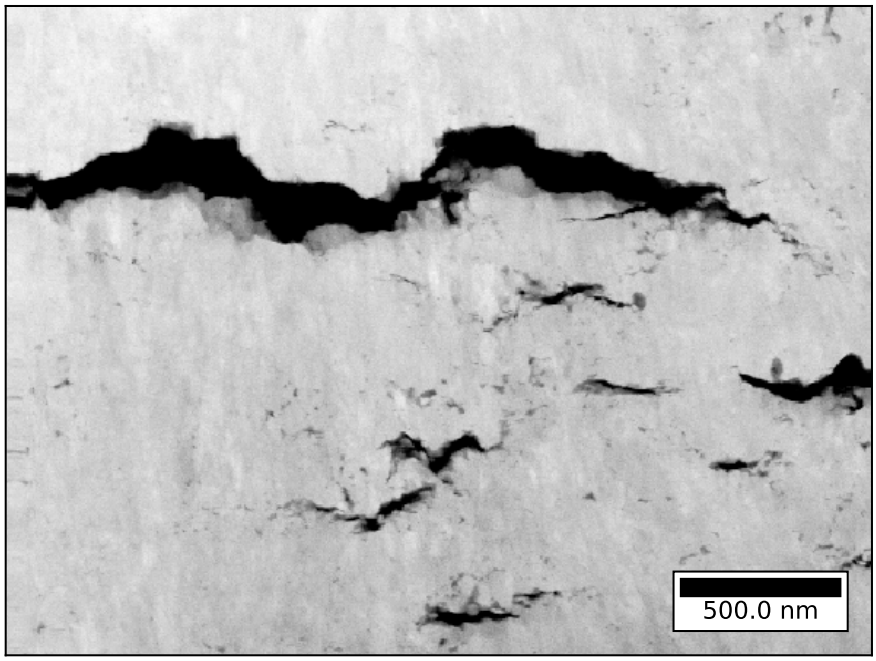


(d) Ni Kα signal.

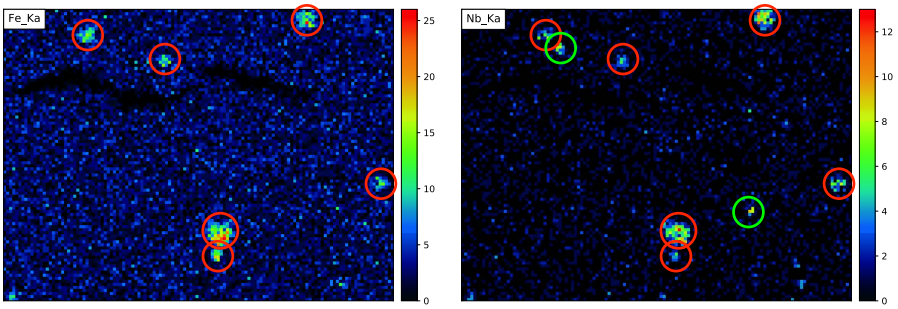
Figure 4.16: The top 1 µm of the 225-day ZIRLO sample and iron and niobium Kα maps from the same area. $Zr(NbFe)_2$ SPPs are circled in red and β-Nb SPPs in green.

In the middle 500 nm of the oxide, seen in figure 4.17, there is a major crack going across the image, approximately 500 nm long. Many smaller cracks exist, in ranges of length from 5 nm to 75 nm. These nanocracks seem likely to be the outer edges of cracks present in the material removed from in front and behind the FIB lift-out. SPPs are frequently found in regions of high crack density (bottom right), suggesting that there may be a correlation between SPP position and crack formation.

The bottom part of the oxide, seen in figure 4.18, is generally less cracked than the previous region, but contains a higher number of large cracks. In particular,



(a) HAADF image.

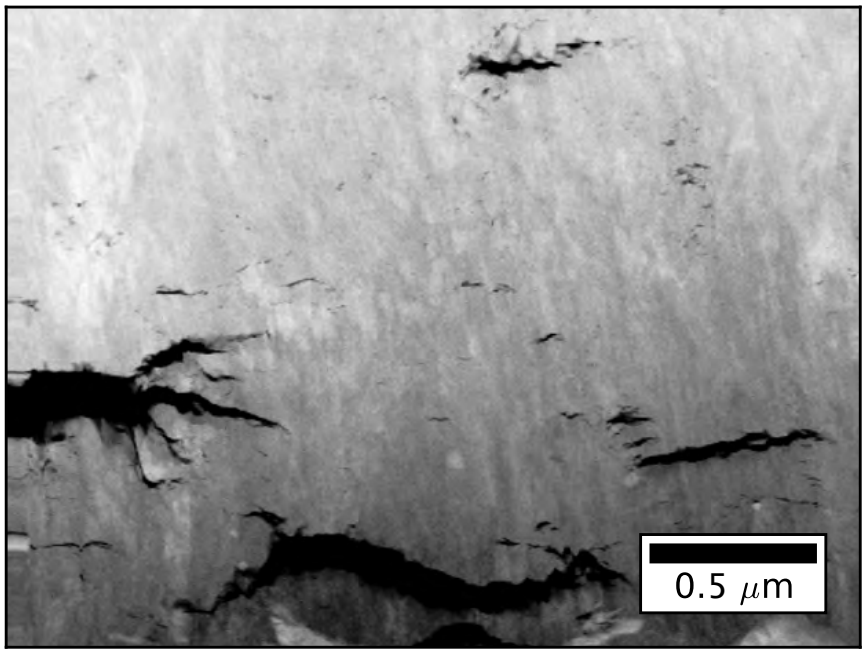


(b) Fe Kα signal. **(c)** Nb Kα signal.

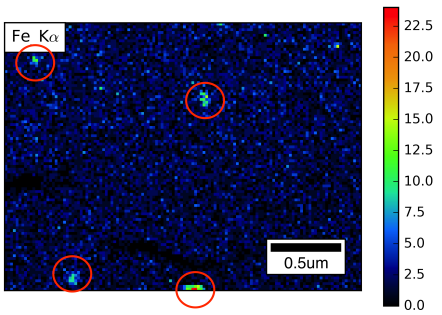
Figure 4.17: The middle 2 µm of the 225-day ZIRLO sample and iron and niobium Kα maps from the same area. $Zr(NbFe)_2$ SPPs are circled in red, β-Nb SPPs in green and Ni rich regions in blue.

the large crack on the left hand side of the image is particularly wide with a gap of nearly 200 nm from bottom to top. Many "fingers" reach out from this large crack. It seems reasonable to assume that the large crack below it is connected via a network of smaller cracks in the planes in front of and behind the TEM sample. SPPs in this region show no particular correlation to the cracks.

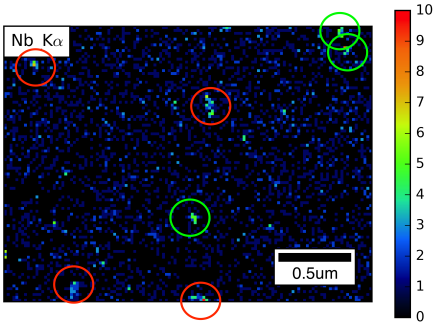
The correlation between SPPs and crack formation has been investigated previously [164], finding that SPPs *can* be responsible for some cracks. In order to investigate this further, it would be useful to perform 3D-FIB slicing with



(a) HAADF image.



(b) Fe Kα signal.



(c) Nb Kα signal.

Figure 4.18: The bottom 2 µm of the 225-day ZIRLO oxide and Fe and Nb Kα maps from the same area. $Zr(NbFe)_2$ SPPs are circled in red and β-Nb SPPs in green.

EDS, allowing for segmentation and comparison of the much larger cracks with the position of SPPs in the oxide.

Finally, in the EDS analysis around the metal-oxide interface seen in figure 4.19, the most obvious feature is that the SPPs are significantly more intense and more sharply defined in the metal than in the oxide. This may be due to the SPPs expanding as they oxidise, becoming less dense and lower in concentration. Fe has previously been shown to dissolve out of SPPs as the particles oxidise [165–167], which may explain the relative lack of Fe-containing SPPs in the oxide versus the

metal. In the metal, in the lower left of the Nb Kα map, there is an needle-shaped elongated Nb-containing structure visible. It is Fe-free. I only saw this type of SPP once in ZIRLO, but it has been shown previously for Zr-2.5Nb [168, 169]. However, EDS analysis [169] suggested they should contain 15.8% Fe, which is not the case here. At the extreme bottom left of the HAADF image shown in figure 4.15a half of the elongated precipitate shown in figure 4.18c is visible. The accompanying ADF image in figure 4.15b shows that the elongated precipitate sits along a grain boundary of two metal zirconium grains. In niobium-rich alloys like Zr-2.5Nb Nb-rich precipitates are frequently found along grain boundaries [169]. The elongated precipitate could be the result of a high density of Nb-rich particles precipitating there, forming one larger precipitate.

β-Nb and $Zr(NbFe)_2$ SPPs were counted by acquiring a longer low-magnification EDS map, and then counting them across the sample, shown in figure 4.20. β-Nb SPPs are circled in green and $Zr(NbFe)_2$ SPPs circled in red. Table 4.2 lists the number density of SPPs. The β-Nb SPPs were found to have a number density of $3.6\,\mu m^{-2}$ whilst there were more Laves phase $Zr(NbFe)_2$ SPPs, with a number density of $5.0\,\mu m^{-2}$.

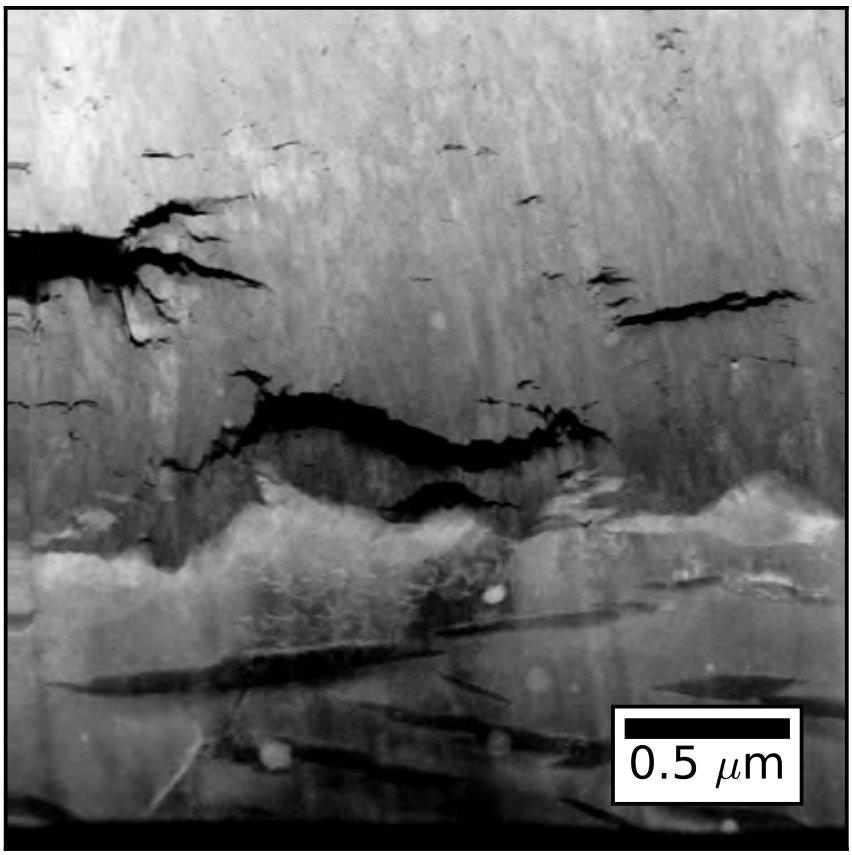
SPP	**Count**	**Number density (μm^{-2})**	**Fraction**
β-Nb	21	3.6	0.42
$Zr(NbFe)_2$	29	5.0	0.58

Table 4.2: Table of SPP number density for a sample of 225-day post-transition ZIRLO.

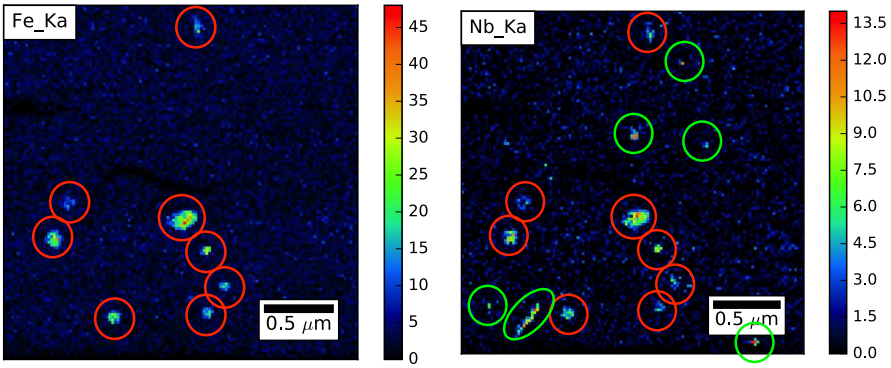
4.4 EELS analysis on ZIRLO

4.4.1 Low-loss EELS

Low-loss EELS has been used in this project in combination with PCA/ICA and MLLS fitting to determine the various phases present in ZIRLO and Zircaloy-4 according to the description in sections 3.6 and 3.6.1. Due to the nature of the multi-channel EELS signal, PCA makes it very easy to quickly determine the components present in the oxide, around the metal-oxide interface and in the metal.



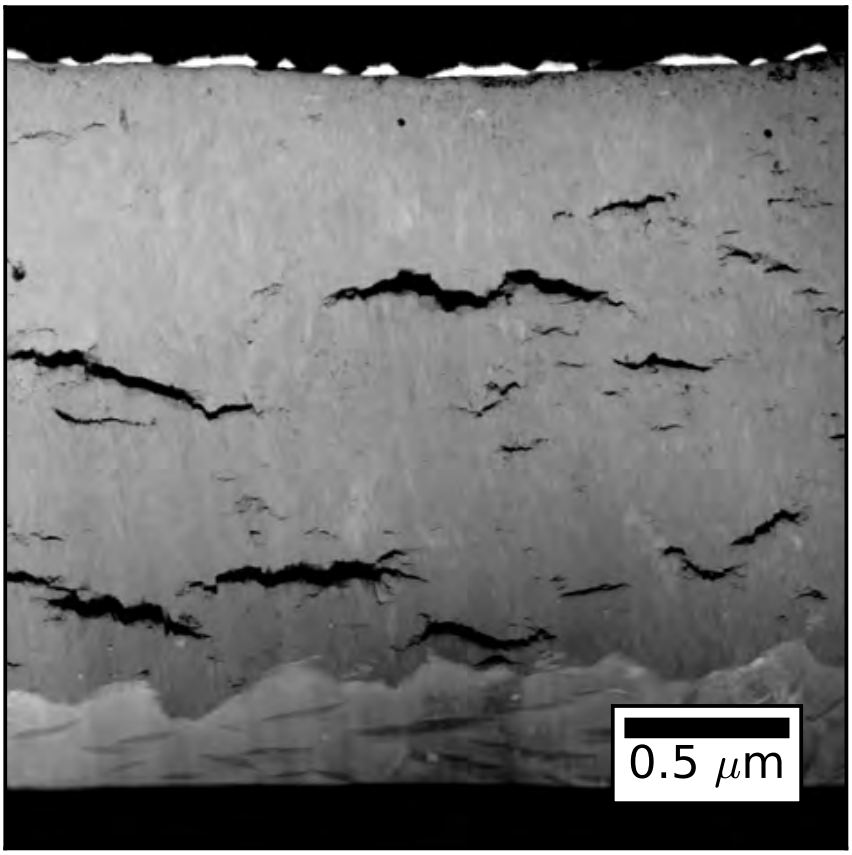
(a) HAADF image.



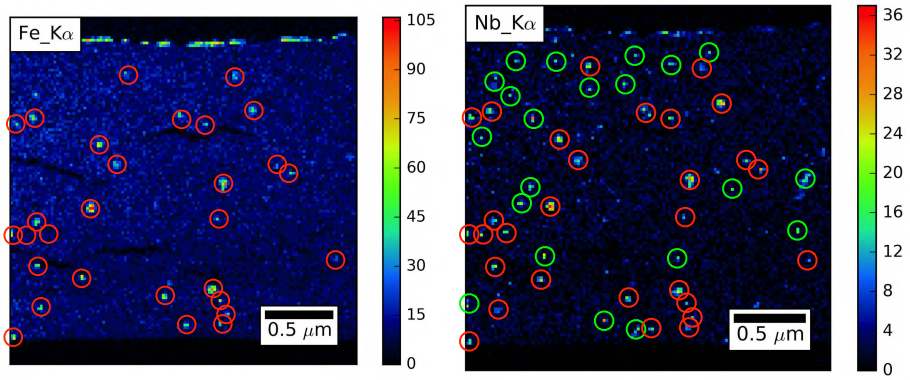
(b) Fe Kα signal.

(c) Nb Kα signal.

Figure 4.19: The bottom 2.5 µm of the 225-day ZIRLO sample and Iron and niobium Kα maps from the same area. $Zr(NbFe)_2$ SPPs are circled in red and β-Nb SPPs in green.



(a) HAADF image

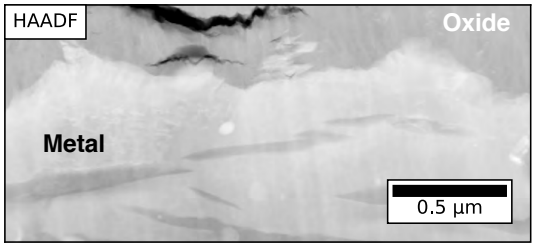


(b) Fe Kα signal.

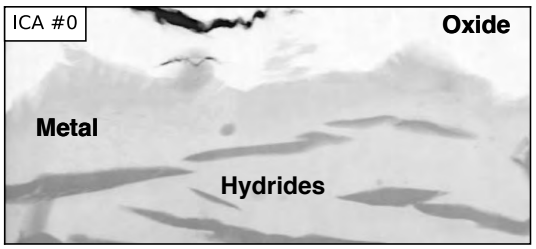
(c) Nb Kα signal.

Figure 4.20: Iron and niobium Kα maps and corresponding low-magnification image of 225-day ZIRLO. $Zr(NbFe)_2$ SPPs are circled in red and β-Nb SPPs in green.

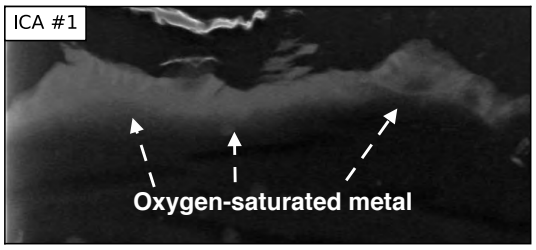
ICA analysis on low-loss EELS spectra from 225-day post-transition ZIRLO can be seen in figure 4.21. Here the oxygen-saturated metal and the suboxide (in particular sawtooth-shaped suboxide) stand out clearly.



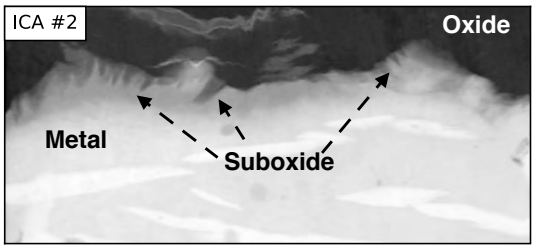
(a) HAADF image.



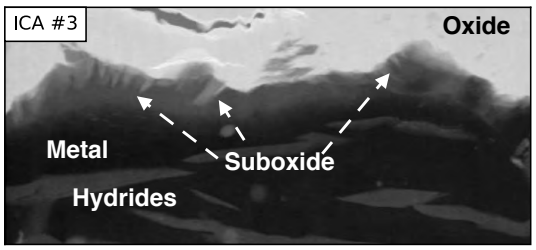
(b) Component 0, contrasting the oxide and hydrides.



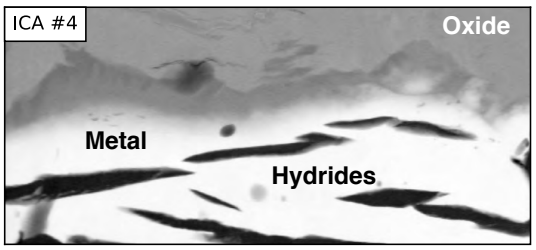
(c) Component 1, emphasising the oxygen-saturated metal.



(d) Component 2, contrasting hydrides and the oxide, including the suboxide sawtooth shapes.



(e) Component 3, emphasising the oxide and suboxide brightly, contrasted with the metal.



(f) Component 4, contrasting the hydrides and SPPs with the metal matrix, also showing the oxygen-saturated metal.

Figure 4.21: ICA results from EELS spectra of the metal-oxide interface of 225-day post-transition ZIRLO.

Measuring the thickness of the suboxide and oxygen-saturated metal layers and projecting it perpendicular to the trace direction of the metal-oxide interface gives the average thickness values in table 4.3. The raw data is plotted in figure 4.22.

However, while the loadings produced by ICA normally directly relate to physical phenomenon, the factors that accompany the loadings normally do not correspond

Region	Mean thickness (nm)
Suboxide	46
Oxygen-saturated metal	830
Total	876

Table 4.3: Measurement of average thickness of the phases around the metal-oxide interface for a sample of 225-day post-transition ZIRLO.

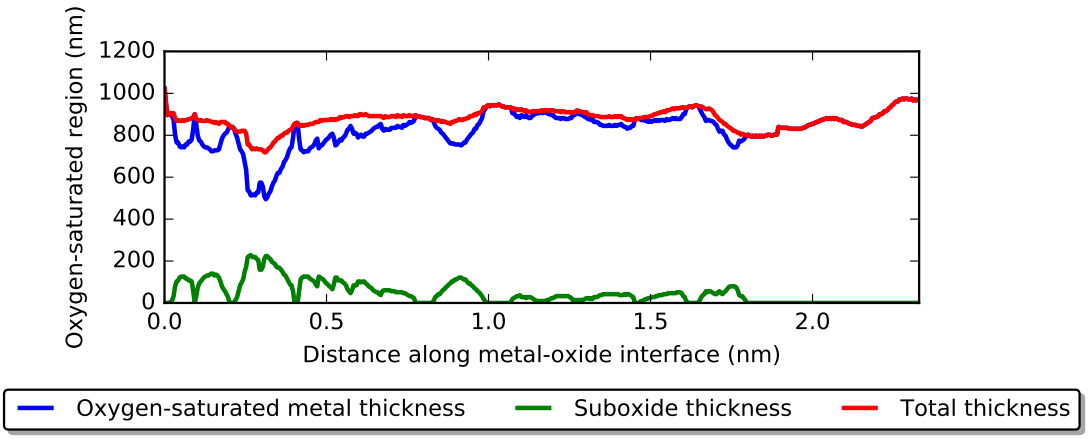


Figure 4.22: Oxygen-saturated metal, suboxide and the sum total of these regions measured along the metal-oxide interface.

to physical spectra (e.g. contain negative values). EELS spectra from the various regions (metal, oxide, etc.) have been acquired to present the differences in the plasmon region, and can be seen in figure 4.23. The energies of the peaks of these spectra have previously been presented by several researchers [94, 156, 170–173], and are compared in table 4.4

The oxide, SPPs, hydrides, suboxide, oxygen-saturated metal and metal stand out clearly in the results. Unfortunately, PCA revealed no component that could be associated with tetragonal oxide. Due to lack of samples with known tetragonal

	Peak 1 (eV)	Peak 2 (eV)	Peak 3 (eV)
Hydride (ZrH)	18.9		42.1
Metal (Zr)	17.1		43.4
Oxygen-saturated metal (Zr(O))	17.6		41.7
Suboxide (ZrO)	15.1		42.8
Oxide (ZrO_2)	14.7	26.5	42.7

Table 4.4: Peak positions of the plasmon peaks for pre-transition 3-day ZIRLO.

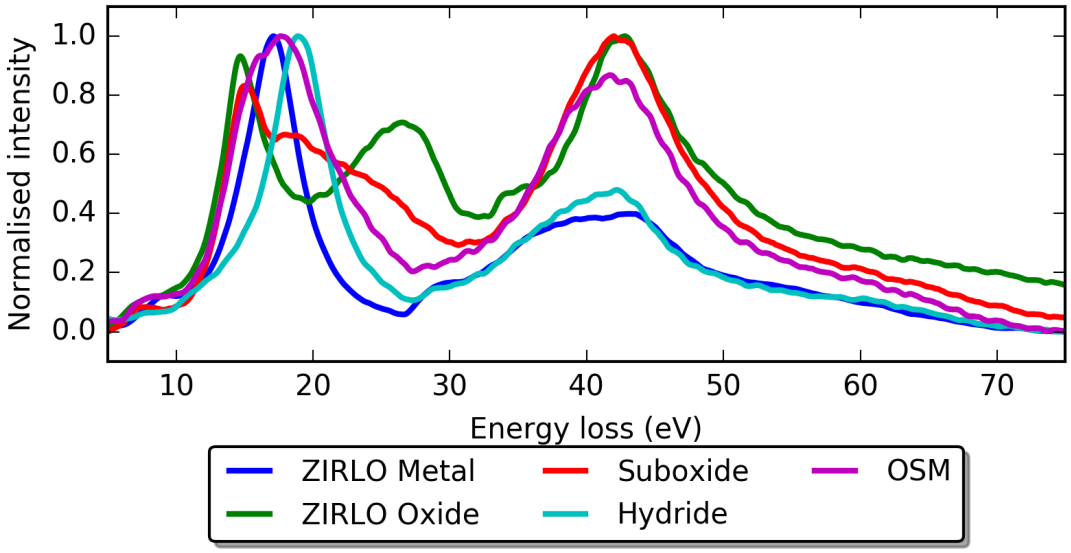
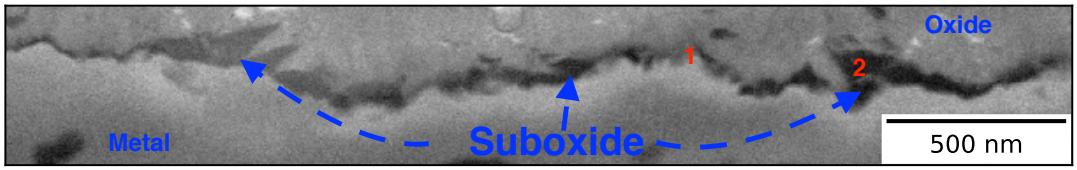


Figure 4.23: EELS spectra from selected regions on pre-transition 3-day ZIRLO. The oxygen-saturated metal is labelled "OSM".

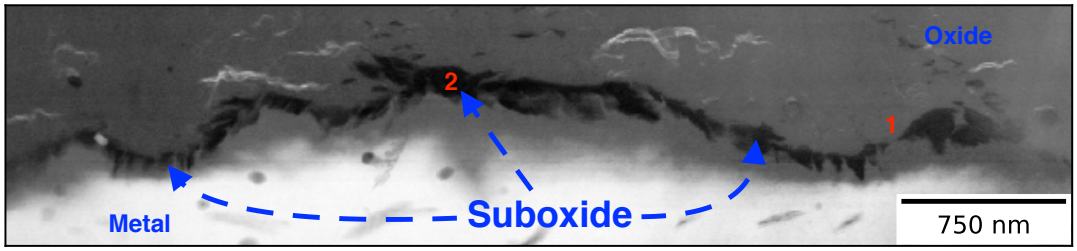
grains, no extensive analysis was attempted, but tetragonal grain structure was not revealed by standard PCA and ICA analysis on high-resolution EELS with energy losses between 0 and 80 eV. Instead, low-loss EELS of the oxide was used to locate oxidised (hidden) SPPs for EDS analysis and for mapping the metal-oxide interface.

Suboxide

Over fifty low-loss spectrum images on ZIRLO have been acquired around the metal-oxide interface in order to determine the shape and distribution of the suboxide and oxygen-saturated metal on the four selected samples of ZIRLO. The sawtooth-shaped suboxide is clearly visible on many samples. Figures 4.24 and 4.25 show the suboxide and oxygen-saturated metal present on 45-day pre-transition and 135-day post-transition ZIRLO samples, after post-processing using PCA and ICA. Here the maximum suboxide thickness was approximately 170 nm and 230 nm, respectively. The typical thickness was 50 nm to 100 nm and 100 nm to 150 nm for the two samples, showing smaller values for the 45-day than the 135-day sample.

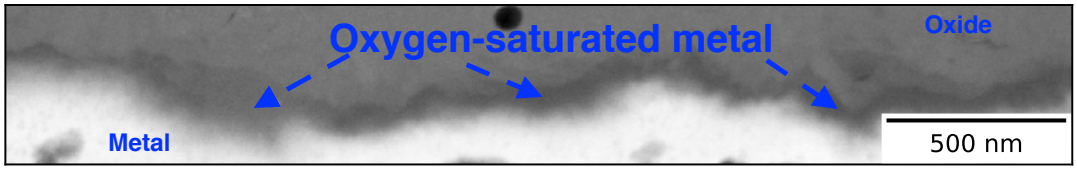


(a)

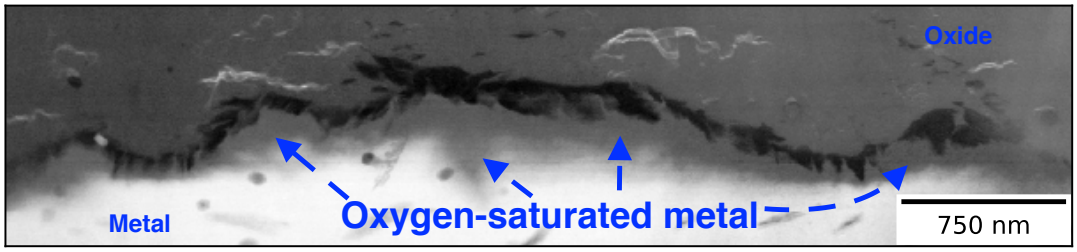


(b)

Figure 4.24: Suboxide example from (a) 45-day pre-transition and (b) 135-day post-transition ZIRLO. "1" and "2" indicate regions of thin and thick suboxide, respectively.



(a)



(b)

Figure 4.25: Oxygen-saturated metal example from (a) 45-day pre-transition and (b) 135-day post-transition ZIRLO. The image in (b) is the same ICA loading as used for the suboxide example in figure 4.24 (b), because that particular loading clearly shows the suboxide and oxygen-saturated metal in the same image.

Reverse direction sawtooth suboxide

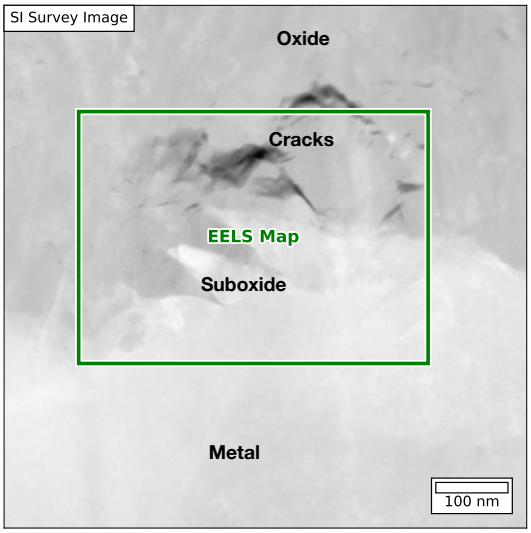
Sawtooth-shaped suboxide normally points in the direction of the metal. On the 45-day pre-transition and 135-day post-transition ZIRLO samples, I found two cases of the sawtooth shape facing the opposite direction as seen in figure 4.26 for the 45-day case. While the regular sawtooth structure is well-known [47, 69, 156], to my knowledge, an oxide-facing sawtooth structure has never been reported before. It seems unlikely that it is only due to metal grain orientation, as it would be seen more frequently. The grain structure in the oxide for the 135-day sample is all equiaxed, and nanocracks are present on both the 45-day and 135-day samples. Since both samples have very similar oxide thicknesses, 1.7 µm and 1.9 µm respectively, it is likely that they are in similar stages of transition, close to the end of pre-transition. The weight gain would be expected to accelerate around 2.2 µm thickness (from the transition point on the weight gain in figure 4.1.)

Oxygen-saturated metal

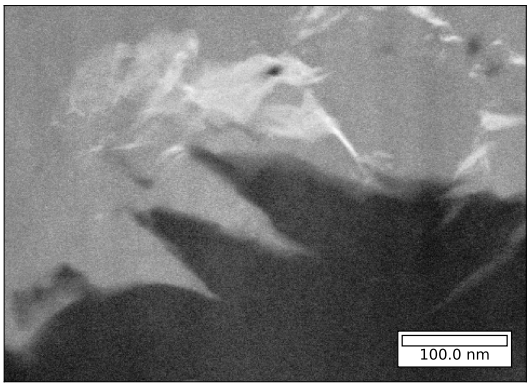
The oxygen-saturated region, revealed through ICA (see section 3.6) has a high-oxygen content (as will be revealed by Core-Loss EELS). It is a reasonably well defined region on the output of ICA of low-loss EELS around the metal-oxide interface, as shown in figure 4.27b.

The thickness of the oxygen-saturated metal was measured across several liftouts for each sample. The average thickness is shown in table 4.5. The data can be plotted as a histogram in order to see how the metal-oxide interface evolves with oxidation time. The measured distance is actually the combined region of suboxide and oxygen-saturated metal - as shown in section 3.6 - as the two are hard to distinguish at the low magnification suitable for measuring a reasonable length of metal-oxide interface at a time.

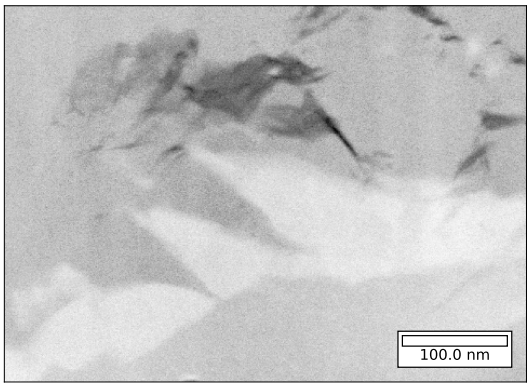
Figure 4.29 shows the result of this analysis for the ZIRLO samples. The 3-day early pre-transition sample shows a consistently very thin oxygen-metal saturated thickness, peaking at 60 nm, whilst the other samples show a much more varied



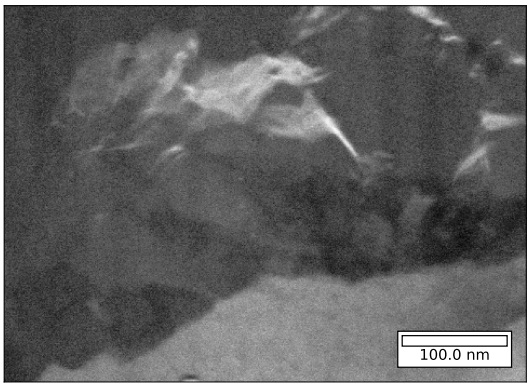
(a) HAADF survey image.



(b) Zirconia MLLS fitting.

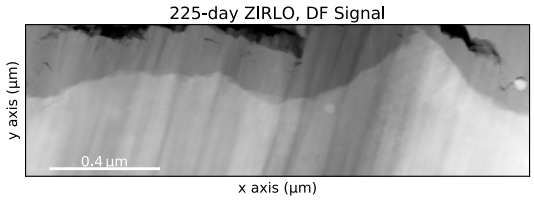


(c) Suboxide MLLS fitting.

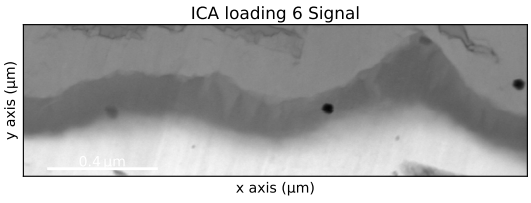


(d) Oxygen-saturated metal MLLS fitting.

Figure 4.26: Reverse direction on sawtooth suboxide on 45-day ZIRLO. b), c) and d) are the MLLS fits of those areas. Note that the cracks were accidentally fitted by the oxygen-saturated metal, as it was difficult to extract a vacuum spectrum representing the crack on this sample. The maximum length of the suboxide was approximately 150 nm.



(a)



(b)

Figure 4.27: Comparing the HAADF (a) and the oxygen-saturated area (b) on a 225-day ZIRLO sample. The region is the dark band across the sample. Faint outlines of the sawtooth suboxide can be seen in it.

Time (days)	Weight gain ($mg\,dm^{-2}$)	Instantaneous weight gain ($mg\,dm^{-2}\,d^{-1}$)	Average combined thickness (nm)
3	10.24	1.02	67
45	26.13	0.22	281
135	48.69	0.48	238
225	74.08	0.08	141

Table 4.5: The average combined thickness of the oxygen-saturated metal and suboxide for the various samples of ZIRLO, listed against their weight gain as well as the instantaneous weight gain calculated from the weight gain data.

range in thickness. This implies a thin oxygen-saturated metal region just after the fast oxidation stage of the metal.

The 45-day late pre-transition samples show a much thicker oxygen-saturated metal region, with two major domains, one centred around approximately 110 nm and one around 320 nm, with a particularly common wide band around 400 nm.

The 135-day early post-transition sample shows a very broad range in the thickness of the oxygen-saturated metal region, with a peak in the population at 235 nm. Looking at the STEM image, seen in figure 4.28, the regions with thick oxygen-saturated metal are where the oxide thickness is the smallest. From the weight gain curve in figure 4.1 one would expect the 135-day and 3-day samples to be in similar conditions due to the fact that they are both in the fast stage of oxidation. However, the TEM samples I looked at for the 135-day sample had very small oxide thicknesses compared to the expected value from the weight gain. The 135-day samples should therefore have properties more similar to the 45-day samples, which they do. However, the very thick band at 400 nm is not present on the 135-day samples, suggesting that the oxygen-saturated metal is shrinking due to being oxidised.

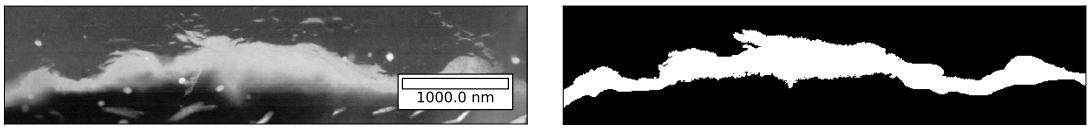


Figure 4.28: Oxygen-saturated metal regions from ICA on a sample of 135-day post-transition ZIRLO.

The 225-day samples show a roughly bimodal distribution, centred around 85 nm and 150 nm. An interesting observation across all samples is that the oxygen-saturated metal region penetrates fairly evenly to a certain distance into the metal, creating a flat interface towards the metal, but has fingers rich in oxygen that stick deeper into the metal in certain locations. Further analysis in these location could be of interest.

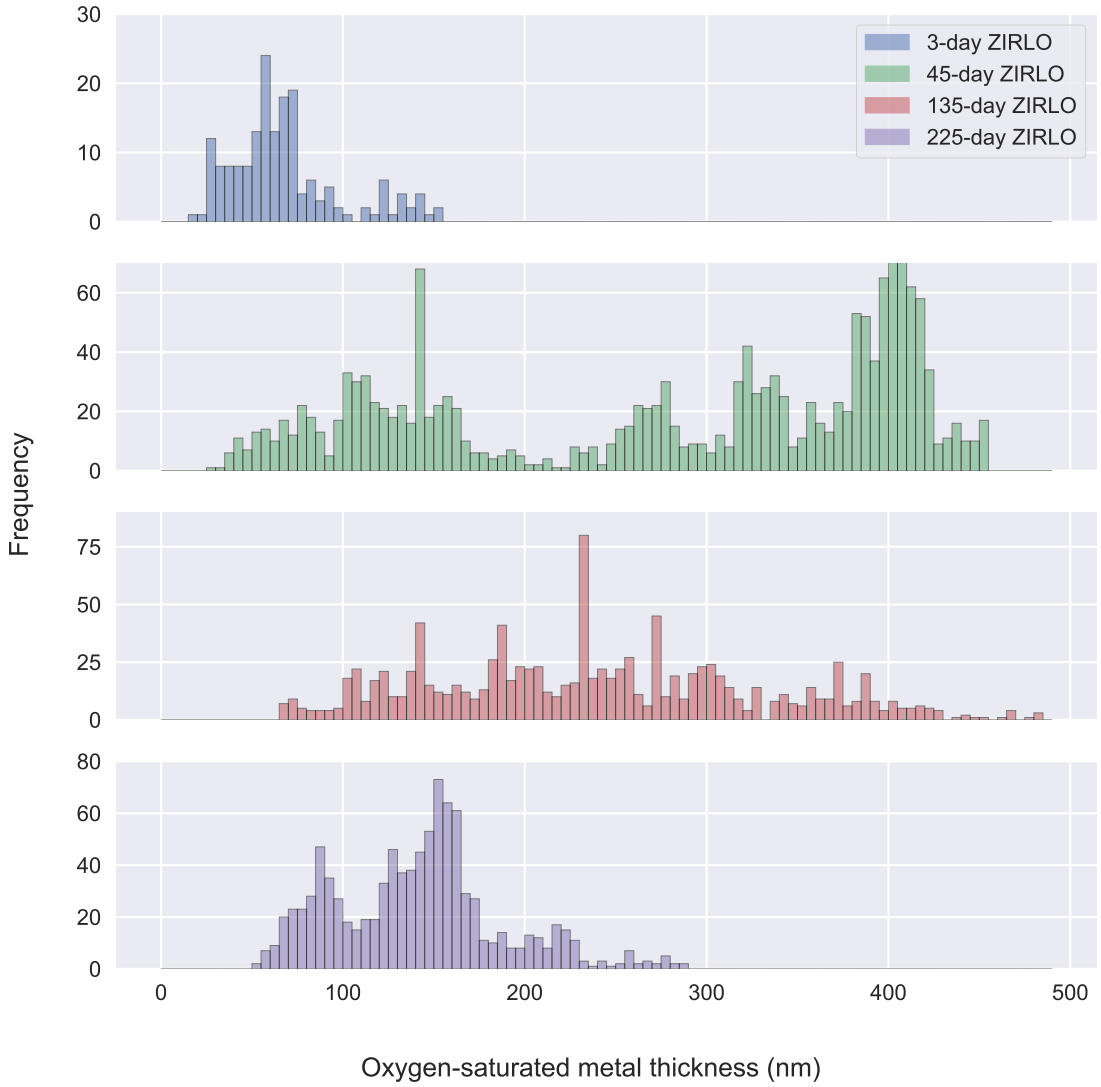


Figure 4.29: Histogram comparison of the oxygen-saturated metal thickness for several samples of oxidised ZIRLO.

As part of the MUZIC-2 project, Zr-1Nb was studied in the same manner as ZIRLO, by Jing Hu and Brian Setiadinata. Both annealed and recrystallised

Zr-1Nb were studied, as the weight gains of the respective alloys showed that recrystallised had improved corrosion resistance compared to ZIRLO whilst the corrosion resistance of annealed Zr-1Nb was worse. By measuring the suboxide thickness individually as well as the combined region of suboxide + oxygen-saturated metal, a scatterplot could be constructed plotting the average thickness of the phase against the instantaneous weight gain of the alloy. The plot is shown in figure 4.30 alongside the weight gain plot, and was published in the ASTM 18th International Symposium on Zirconium in the Nuclear Industry [174]. The points representing ZIRLO in this plot differ slightly from the values given above, and data for 3-day ZIRLO has been added, as more liftouts of ZIRLO were measured after this data was compiled and presented in the paper. The plot shows that there is a tentative decrease in the suboxide thickness, and a more significant decrease in the combined region thicknes, as oxidation rate increases. Looking at the individual alloys, there is a clear correlation between high corrosion resistance and thick suboxide and combined suboxide + oxygen-saturated metal layers at the metal-oxide interface. The alloy with the highest corrosion resistance, Zr-1Nb, has the thickest layers. ZIRLO, which is shown to have the second-best oxidation resistance, has a medium thickness. Annealed Zr-1Nb has the worst oxidation resistance and the thinnest layers.

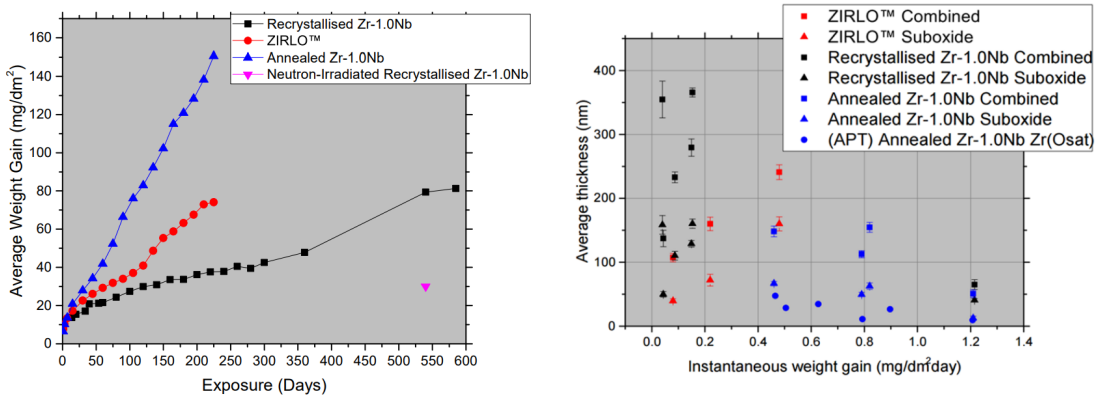


Figure 4.30: (a) Weight gain of ZIRLO and recrystallised and annealed Zr-1Nb. (b) Average thickness of the suboxide and combined regions for the alloys studied, against the instantaneous weight gain calculated from the data in (a).

4.4.2 Core-loss EELS of the metal-oxide interface

In order to investigate the chemical composition of the alloys, I employed core-loss EELS. Two main areas of investigation were the metal-oxide interface and the second-phase particles (SPPs), building on the work of Ni [69].

The exposure time (0.01 s for the oxygen K edge and 0.1 s for the Zr L edges) required to get a good signal-to-noise ratio for the core-loss EELS spectra meant that I had to prioritise line profiles over maps when acquiring results. Initially, these line profiles were placed based on or around features evident in the HAADF survey images taken for each acquisition. Once the benefit of ICA on the (fast) low-loss mapping was realised, the components from ICA were used as an additional guide.

Using the Hyperspy software, the EELS spectra were fitted using a model consisting of a linear combination of components. As a background a single power law was fitted. In order to fit the white lines and their respective edges correctly, Gaussians were fit to the white lines first. The onset-energy of the EELS edges were then set to the value of the centre position of the Gaussian, and the edges were fit. In order to improve the fit, the Gaussian and edge components were convolved with the low-loss spectrum first. An example of the various components fitted to a ZIRLO oxide spectrum can be seen in figure 4.31. An example of a script used for this purpose is given in Appendix 10.2.

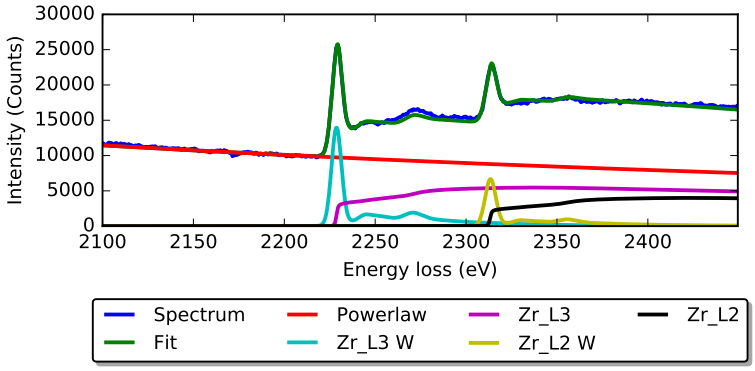


Figure 4.31: Fit of an EELS spectrum taken in the oxide region. The raw data (blue) is fitted by the linear combination of a background, two EELS edges and two white lines.

A region with very clearly defined sawtooth-shaped suboxide was found on a sample of 225-day ZIRLO. Low-loss EELS and ICA was first employed to see the

extent of the suboxide around the interface. A line profile was then drawn from the oxide across the sawtooth shape into the metal, and acquisition of EELS and EDS spectra were acquired to study the chemical composition. A HAADF image showing the region the line profile was taken from can be seen in figure 4.32. The suboxide grains are just visible at area B on the figure, and the line profile was drawn across the widest part of the sawtooth shape. Three different methodologies were applied to study the oxygen content of the alloy, two using EELS and one using EDS, and are compared in figure 4.33. All methodologies demonstrate a plateau region around the metal-oxide interface of 50 % Zr and O. The length of the plateu region was approximately 57 nm from the EELS measurements, and slightly shorter on the EDS measurements. The oxygen-containing metal region extended out nearly 200 nm.

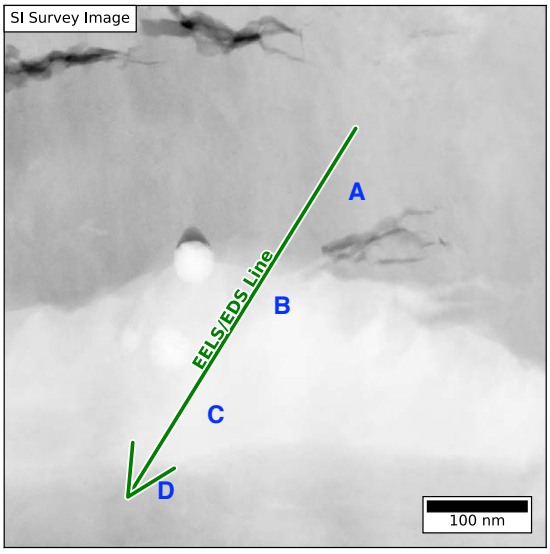
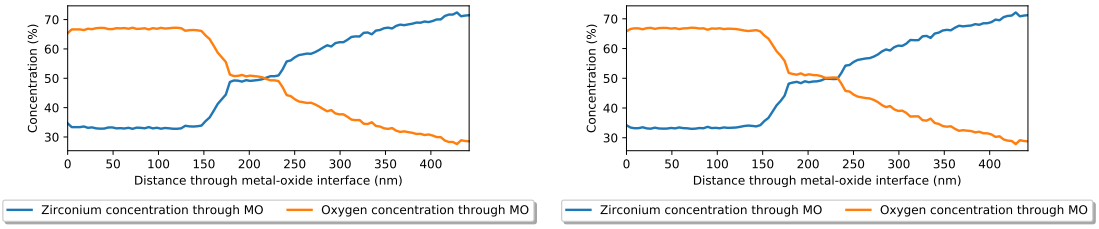


Figure 4.32: Position of line profile acquired across the metal-oxide interface on post-transition 225-day ZIRLO. The labels designate the following positions: (A) oxide, (B) suboxide, (C) metal, (D) second metal grain

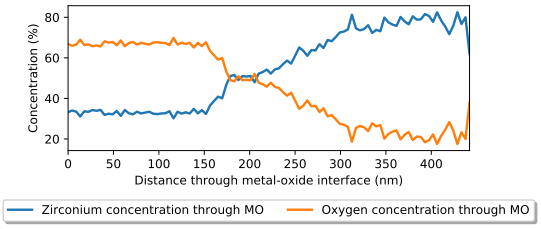
In the first case the Zr M and O K edges were fitted using the Hartree-Slater GOS on top of a power-law background, a standard way of fitting EELS edges

[154]. This is similar to the approach taken by Ni [69]. Each element was acquired on its own EELS spectrum, due to the difference in exposure times needed to get a good signal-to-noise ratio without saturating the detector. This was found to be much more stable than acquiring both the Zr M and O K edges in the same spectrum. The Zr M_5 and the Zr M_3 edges were fitted and added together before comparing with the oxygen signal. The second case used the Zr L and O K edges, fitted using the same technique as in the previous case. Here the Zr L_3 and L_2 edges were compared to the O K edge. The final case considered using the Zr Lα and O Kα lines to fit the spectrum on top of a polynomial background fitted around the peaks. The EDS case was noisier than the EELS cases, although the analysis is faster, and the EDS spectrum acquired over a very short amount of time.



(a) Fit of the EELS line spectrum using the Zr M and O K edges.

(b) Fit of the EELS line spectrum using the Zr L and O K edges.

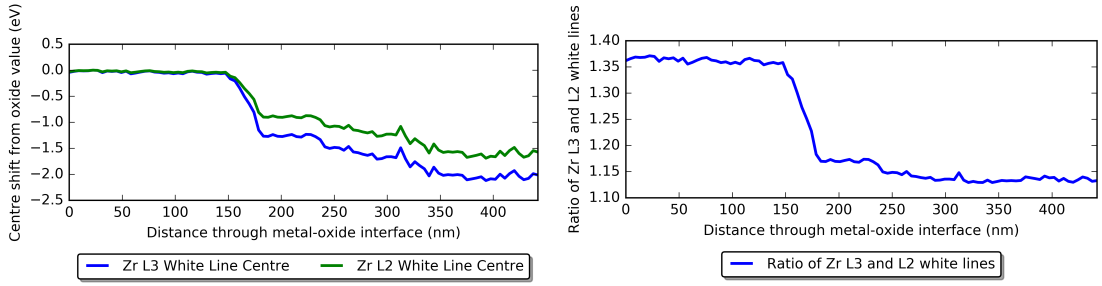


(c) Fit of the EDS line spectrum using the measured Zr Lα and O Kα lines.

Figure 4.33: Oxygen and zirconium concentration using the methods described in the individual figure captions across the metal-oxide interface on post-transition 225-day ZIRLO. The survey image is shown in figure 4.32.

In addition to comparing the oxygen ratio through the metal-oxide interface, the oxidation state of Zr can be measured by considering the Zr L_3 and L_2 white lines. Fitting Gaussians on top of the L_3 and L_2 edges described above, the centre parameter of the Gaussian can be plotted as a function of distance through the

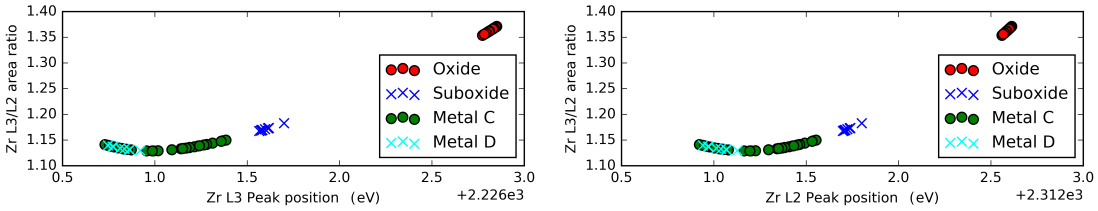
interface. Figure 4.34a shows a very defined centre value for the oxide, and a shift of 0.8 eV and 1.2 eV to a distinct plateau region for the suboxide. The metal is more loosely defined, but there is a definite trend towards less energy loss as the Zr becomes metallic. The ratio between the Zr L_3 and L_2 white line intensity can also be plotted after fitting. It too demonstrates separate plateau regions for the oxide and suboxide, dropping from a ratio of 1.37 in the oxide to 1.18 in the suboxide and 1.13 in the metal, and can be seen in figure 4.34b.



(a) **(b)**

Figure 4.34: (a) Centre parameters of the Zr L_3 and L_2 white lines after Gaussian fitting on post-transition 225-day ZIRLO.(b) Ratio of the intensity of the of the Zr L_3 and L_2 white lines after Gaussian fitting on post-transition 225-day ZIRLO.

It has previously been demonstrated that a varying oxidation state cannot necessarily be shown by looking at either the centre parameter or the ratio of the white lines separately [154, 157, 175–177]. Often the combination of the two is required. The ratio of the white lines can be plotted against the centre in order to determine regions of separate oxidation states. Figure 4.35 shows scatterplots of this style from a line of 100 pixels, for the centre of the L_3 and L_2 white lines. The oxide and suboxide can be clearly defined by the red circles and blue crosses, whilst the metal shows a range that approaches the suboxide region. The largest contrast between the oxide, suboxide and metal is found using the centre parameter of the L_3 white line. The oxide and suboxide are separated by about 1.0 eV whilst the metal and suboxide distance is approximately 0.4 eV. This shows that it should be enough to use the centre parameter of the L_3 white line to determine the oxidation state of Zr, but in uncertain cases it can be helpful to use the ratio between the L_3 and L_2 white lines as well.



(a) **(b)**

Figure 4.35: Scatter plots of the white line L_3/L_2 ratio against (a) L_3 and (b) L_2 peak centres after Gaussian fitting on post-transition 225-day ZIRLO.

4.4.3 3-day ZIRLO

EELS analysis on the metal-oxide interface, shown in figure 4.36, shows that the thickness of the oxygen-saturated region dominates over the 50:50 ZrO suboxide. The orange features on the image are likely suboxide, whilst the green area depicts the oxygen-saturated metal.

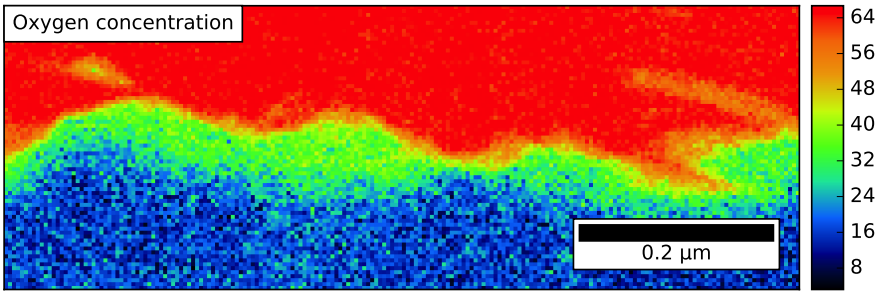
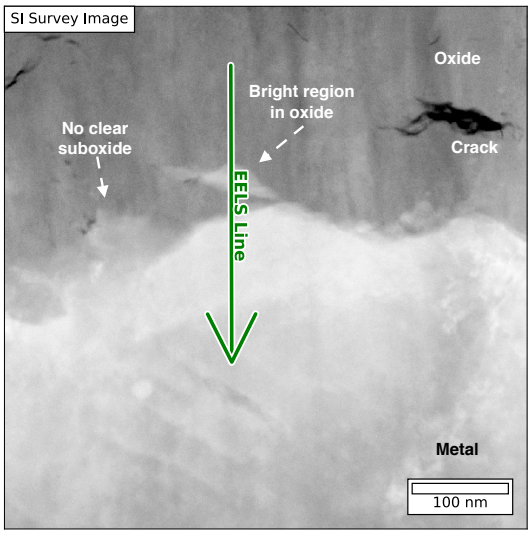
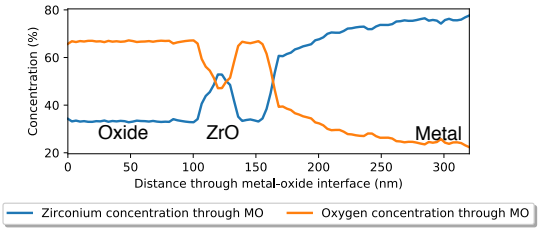


Figure 4.36: The concentration of oxygen around the metal-oxide interface. In this case, the concentration was calculated using the oxygen K and zirconium L edges (avoiding the white lines of the Zr L edges), according to the methodology described in section 3.6.1.

Near the metal-oxide interface in figure 4.6 there can be seen fingers of the same, bright intensity as in the metal, highlighted by red boxes. This implies that the fingers have the same, or similar, average Z values as the metal, and have not been fully oxidised. Indeed, EELS core-loss analysis of the Zr L and O K edges, shown in figure 4.37b tells us that the brighter region contains an approximately 50 % concentration of both Zr and O. Its width is 10 nm. ZrO suboxide is normally reported to have a sawtooth shape. Here it is additionally reported as "fingers" in the oxide. This has previously been shown by Annand et al. [156] where it was found below a crack in a region of slow growing oxide.



(a) Survey image showing the line profile drawn.



(b) The oxygen and zirconium atomic concentration through the metal-oxide interface.

Figure 4.37: Concentration of Zr and O from the EELS line profile drawn on the metal-oxide interface of 3-day pre-transition ZIRLO.

In addition to showing the concentration as a map in figure 4.36, I have plotted a 2D histogram showing the Zr L_3 white line centre position plotted against the oxygen concentration in that pixel. These positions are summed up to create the heat map seen in figure 4.38. There is a distinct band emphasising three regions - the metal (left), oxygen-saturated metal (centre) and oxide (right). The suboxide region was not clearly visible on the heat map. This may suggest that the region emphasised in orange (50% oxygen concentration) as suboxide on the map in figure 4.36 is incorrect, and that the close to 50% concentration is due to overlap between the metal and oxide through the sample thickness. It would be interesting if a programming script could be constructed to redraw the concentration map using only the regions of the heat map, so as to show each individual phase on the original image.

Other EELS line profiles show a lack of clear suboxide. Fitting the Zr L_3 and L_2 white lines across the metal-oxide interface as explained in section 4.4.2 shows no clear 50 % Zr phase across the suboxide, although there is a clear change in both the peak position (figure 4.39c) and the peak ratio (figure 4.39d), highlighting the change in oxidation state from Zr^{4+} in the oxide to Zr^0 in the metal. The method of fitting the white lines and calculating the peak ratio is shown in section

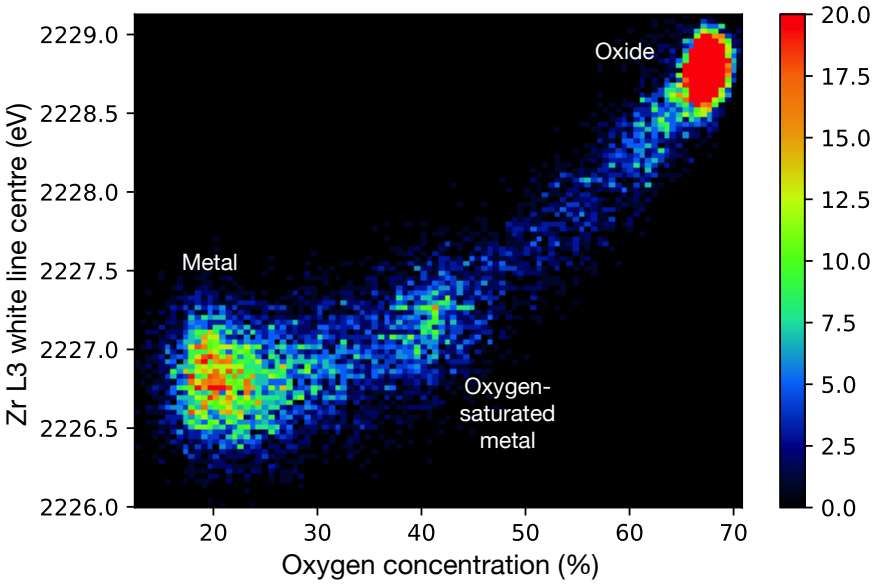


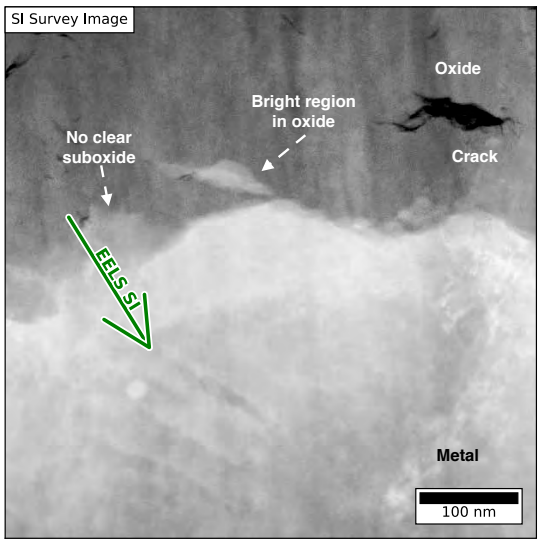
Figure 4.38: 2D histogram heat map showing the Zr L_3 white line centre position against the oxygen concentration in each pixel from figure 4.36. There is a distinct band emphasising three regions - the metal (left), oxygen-saturated metal (centre) and oxide (right).

3.6.2. The lack of apparent suboxide could be due to overlap of the metal and oxide regions in projection, but it is more likely that the suboxide is either non-existent or too small to measure.

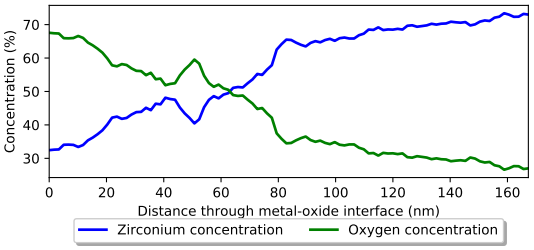
4.4.4 45-day ZIRLO

To investigate the metal-oxide interface, low-loss EELS was performed on the region highlighted in green in figure 4.40a. Three decomposition loadings were chosen to display the phases present in this region. An example of both sawtooth shaped suboxide and rounded suboxide is shown on (b).

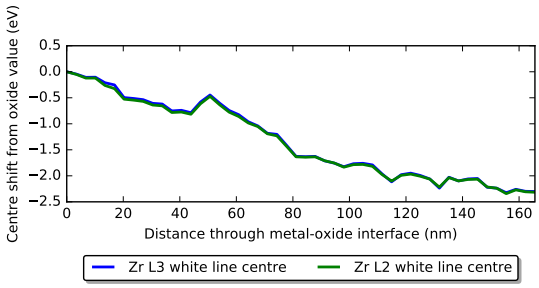
To investigate the chemical composition of the suboxide, core-loss EELS was performed by drawing line profiles across several regions of the suboxide, using the loadings in figure 4.40 as guidance. The Zr M and O K edges were fitted using Hyperspy. Figure 4.41 shows the regions and the concentration profile calculated for Zr and O across the interface. There are four distinct regions: (A) oxide, (B) sawtooth suboxide, (C) oxygen-saturated metal and (D) metal.



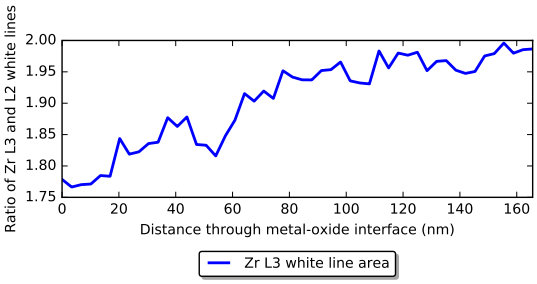
(a)



(b) Zr and O concentration.



(c) The peak position of the white lines relative to the position in the oxide.



(d) L_3/L_2 white line area ratio.

Figure 4.39: Lack of clear 50 % Zr suboxide (plateau) region across the metal-oxide interface on a sample of 3-day pre-transition ZIRLO.

The concentration of oxygen in the suboxide regions varies between 50 and 55 %. For Line 1 (shown in (b)) and Line 3 (shown in (d)), the thickness of the suboxide band was 23 nm and 27 nm respectively. Line 2 (shown in (c)) was drawn diagonally across the suboxide to draw it over a finger of what was expected to be oxide sticking into the metal. As shown on the respective concentration plot, the dark figure contains a much higher concentration of oxygen than the suboxide. The reason the concentration is not as high as in the oxide is likely to be due to projection of suboxide and metal on top of one another through the sample. By cross-referencing the ICA loadings from the same area, the suboxide Line 2 was drawn across is measured to be 45 nm wide.

The 50 % Zr suboxide phase is clearly visible, labelled as B on the concentration

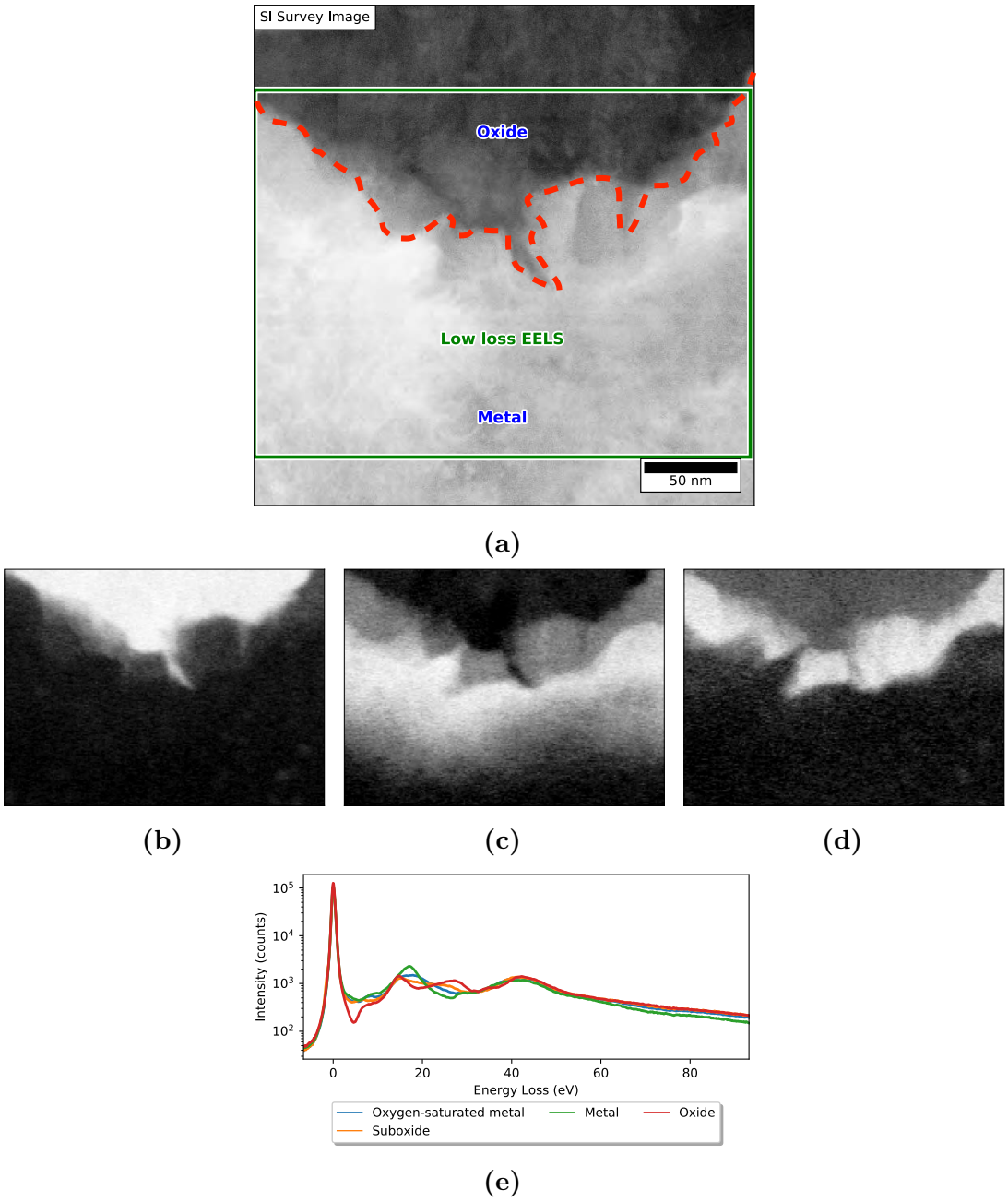
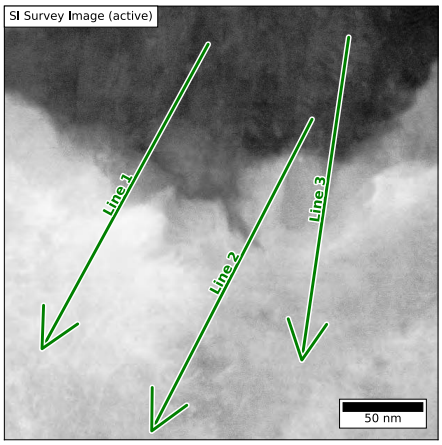
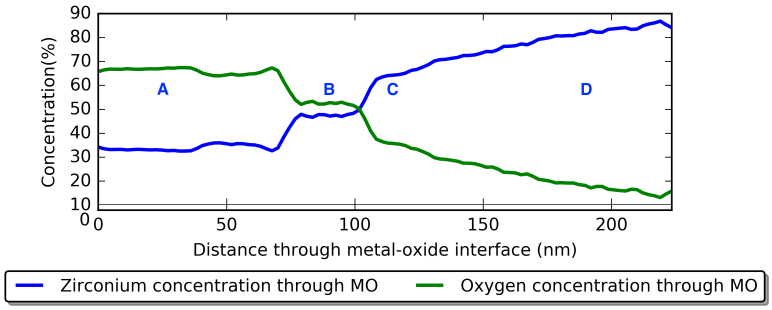


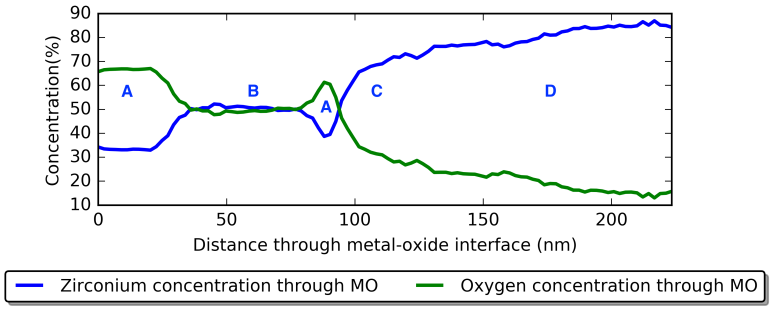
Figure 4.40: Survey image (a) of the metal-oxide interface (red) and location of the EELS SI (green), and three loadings (b-d) from the decomposition of the low-loss EELS SI from a pre-transition 45-day ZIRLO sample. The bright regions on the loadings are: (b) the oxide, (c) the oxygen-saturated metal and (d) the suboxide. The suboxide region is clearly shown between the metal and oxide, with two sawtooth-shaped grains and the rest more rounded in shape. EELS spectra taken from the oxide, metal, suboxide and oxygen-saturated metal are shown in (e)



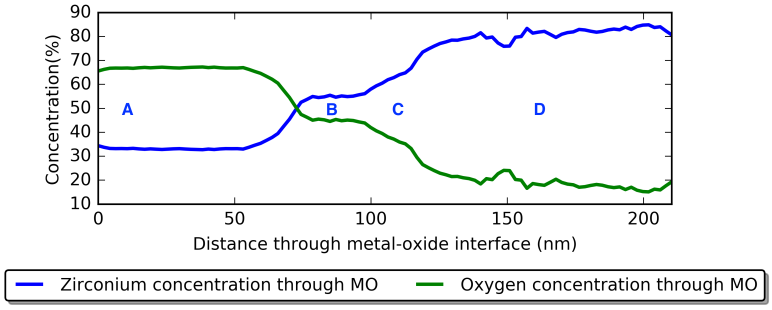
(a) HAADF survey image



(b) Line 1.



(c) Line 2.



(d) Line 3.

Figure 4.41: Survey image (a) of the three core-loss EELS line profiles (b-d) drawn across the metal-oxide interface on a pre-transition 45-day ZIRLO sample.

profiles. Line profiles 1 and 3 suggests that the sawtooth shape and the more rounded suboxide are both of the same composition.

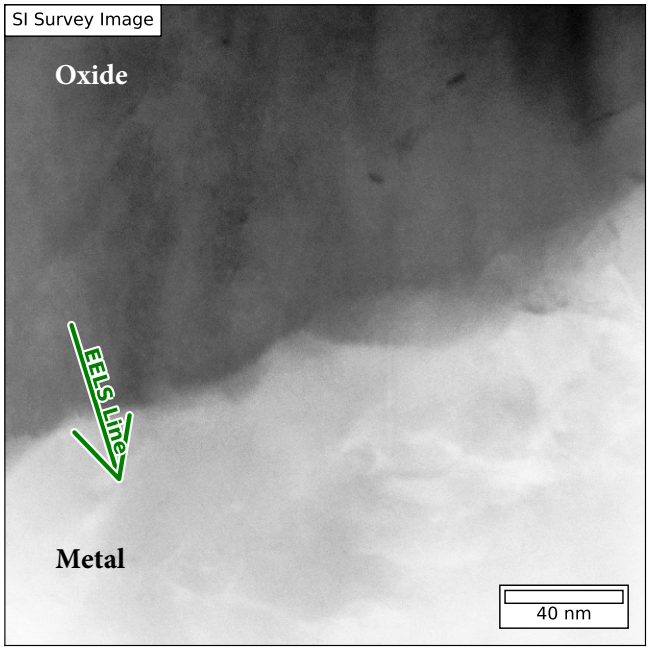
However, suboxide is not present in all the regions of the metal-oxide interface. Figure 4.42 shows EELS analysis using the Zr M and O K edges on the ZIRLO oxidised to 180 days in pure water and further oxidised for 45-days in deuterated water to a total of 225-days. Here the EELS acquisition line was purposefully drawn in a region where the HAADF image appeared to show no intermediate layer between the oxide and metal. No apparent suboxide region is found at all. This is not an unusual finding; most samples have some region present without any apparent suboxide region at the metal-oxide interface.

4.4.5 Necessity of EDS for SPP imaging

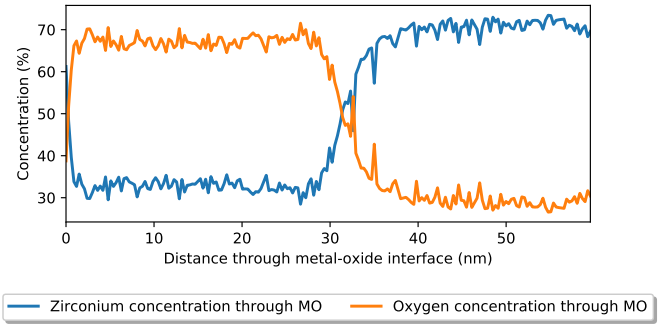
As the SPPs oxidise, they also become amorphous and less dense, and can often become porous and appear damaged. As they lose their crystallinity, they become increasingly difficult to see in TEM mode, and since the average atomic number of the SPP is very similar to that of the oxide, it is effectively invisible in STEM. This necessitates the use of EDS to characterise the SPP number density in the oxide. Low-loss EELS can serve as an alternative, but whilst effective at revealing the SPP as a different phase to its surroundings, it may not be clear what the SPP composition is. Since one is mapping the sample anyway, it is sensible to use EDS as the primary technique. Unfortunately, mapping large areas can be quite slow and with time constraints it can be difficult to provide SPP counts when looking at many samples.

4.4.6 SPP oxidation state

In order to determine the oxidation state of niobium in Nb-containing SPPs, powder standards of NbO, NbO_2 and Nb_2O_5 were acquired. These would have Nb in the 2+, 4+ and 5+ oxidation states, respectively. Nb in the metallic β-Nb SPPs was used as a standard for the 0 oxidation state.



(a) HAADF survey image for the EELS measurements



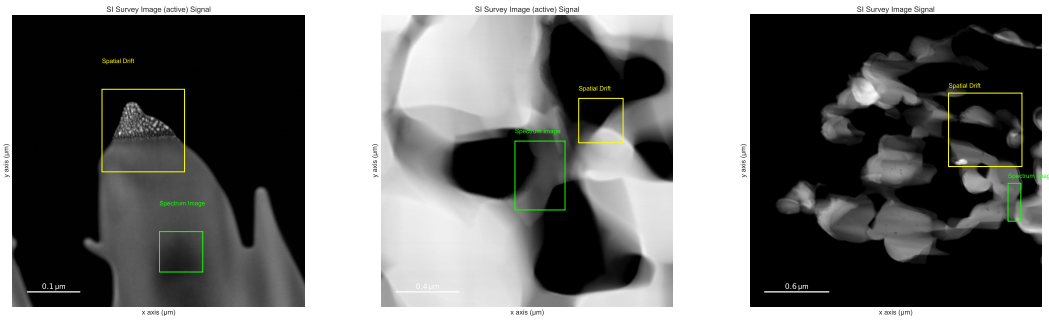
(b) Zirconium and oxygen concentration through the metal-oxide interface

Figure 4.42: Oxygen and zirconium content throughout the metal-oxide interface from EELS analysis of 225-day ZIRLO, seen in the survey image in (a).

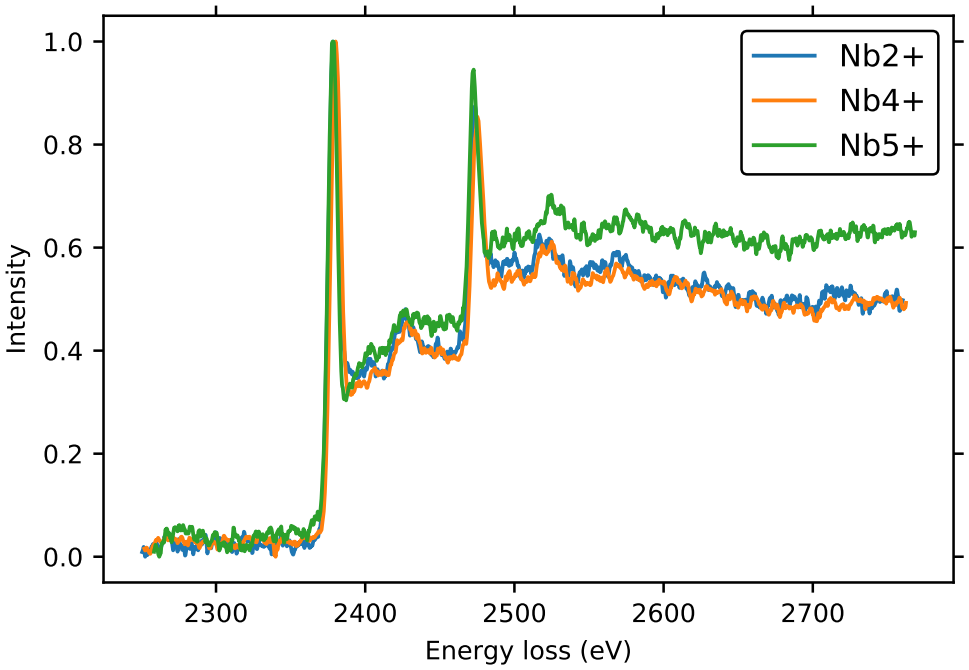
Samples were produced by single-beam FIB-liftout. The microstructure of the three standard samples was quite different, and can be seen in figure 4.43.

Unfortunately, as seen on 4.43d, the energy loss spectra from the three samples appears identical. This is likely due to FIB damage or stress relaxation from the liftout and thinning process.

Instead, comparative EELS spectra, comparing the Nb L_3 and L_2 edges of metallic and oxidised SPPs were acquired. Figure 4.44 shows HAADF images of the four types of SPPs. As can be seen, the oxidised SPPs are completely



(a) Survey Image of NbO **(b)** Survey Image of NbO_2 **(c)** Survey Image of Nb_2O_5



(d) Nb Energy Loss Spectrum

Figure 4.43: Background-subtracted noise reduced (by ICA) energy loss from thin regions of the NbO, NbO_2, Nb_2O_5.

indistinguishable from the rest of the oxide, making them difficult to detect. In order to find them, either EDS mapping or low-loss EELS mapping had to be performed. The former approach was slow but specified the type of SPP ($Zr(NbFe)_2$ vs Nb), whilst the second was much faster but was unable to distinguish between the two.

The EELS spectra, shown in figure 4.45, clearly show a shift to higher energy losses for the Zr L_3 and L_2 white lines when the zirconium is oxidised.

The Nb L_3 and L_2 edges also show a similar increasing energy shift when oxidised, as is shown in figure 4.46. In order to extract accurate centre positions

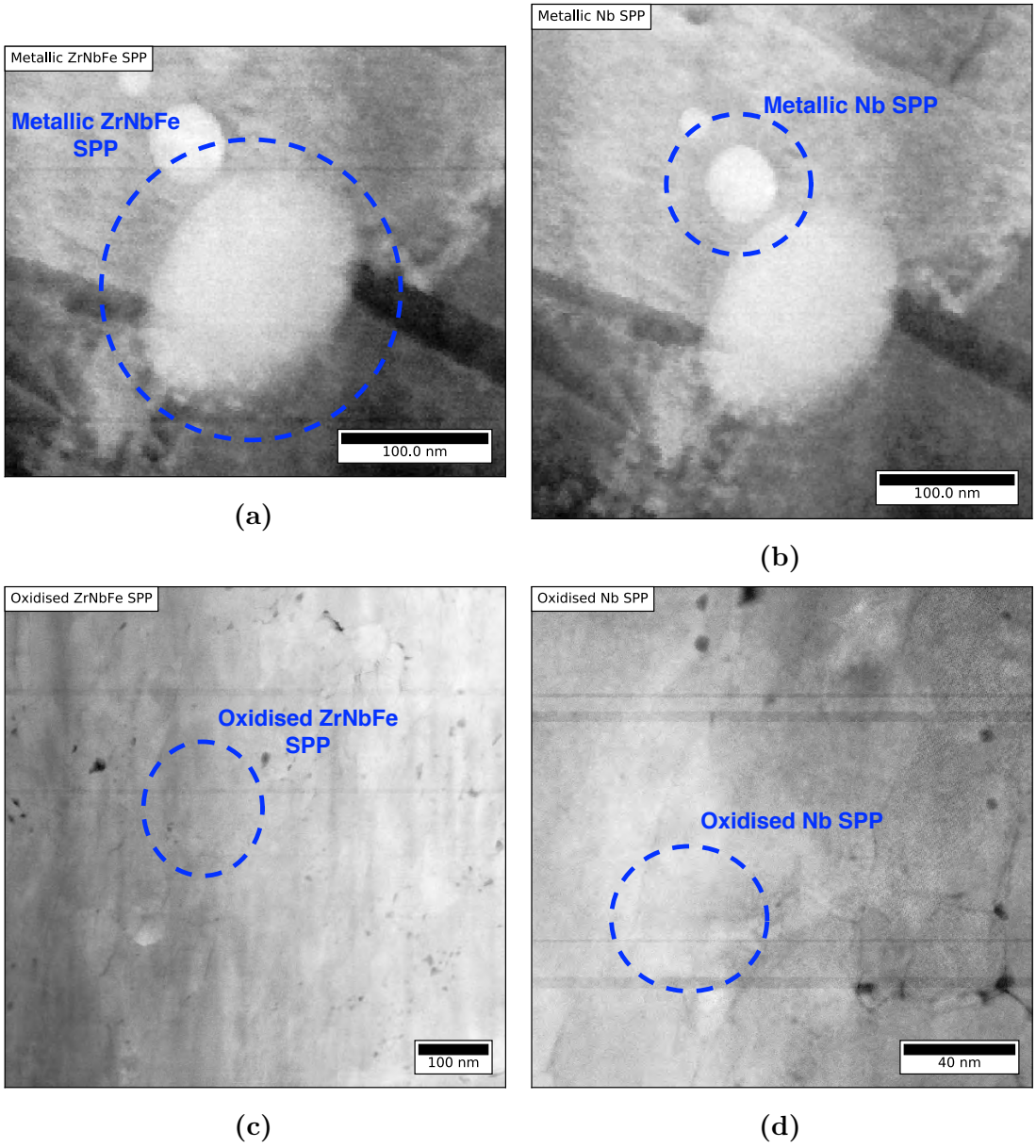
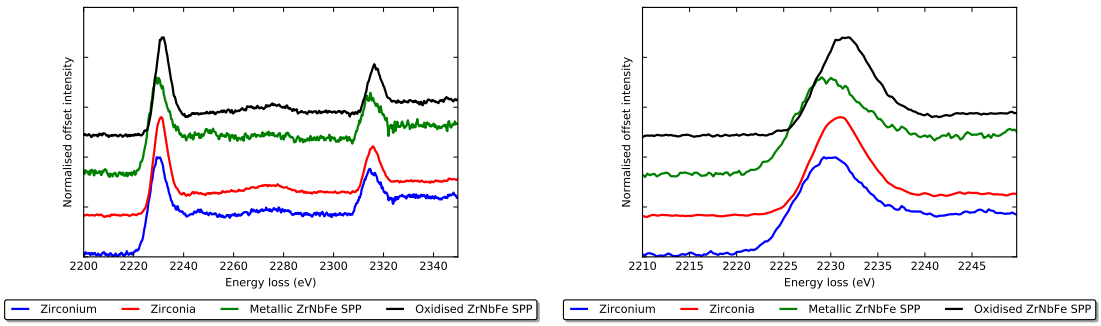


Figure 4.44: Four phases of SPPs present in oxidised ZIRLO.



(a) Zr L_3 and L_2 edges. **(b)** Zr L_3 edge.

Figure 4.45: Zr L_3 and L_2 edges of metallic and oxidised Zr and $Zr(NbFe)_2$ SPPs.

for the white lines, the EELS spectra were fit using the appropriate Zr and/or Nb Hartree-Slater GOS edge shapes, with Gaussians to fit the white lines, all convolved with the low-loss spectrum using the Hyperspy software. An example of this is shown in figure 4.47. The centre positions of the Gaussians are shown in table 4.6. Appendix 10 contains several scripts written to simplify the loading, alignment and fitting of EELS core-loss spectra with the hyperspy software. These should become available as online material with this thesis.

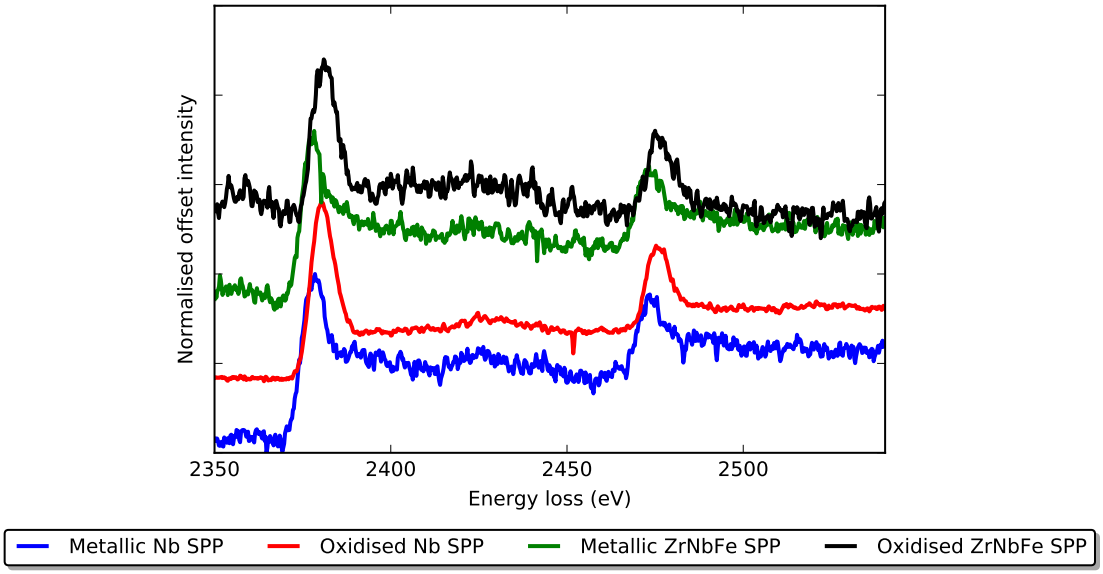


Figure 4.46: Nb L_3 and L_2 edges of metallic and oxidised SPPs.

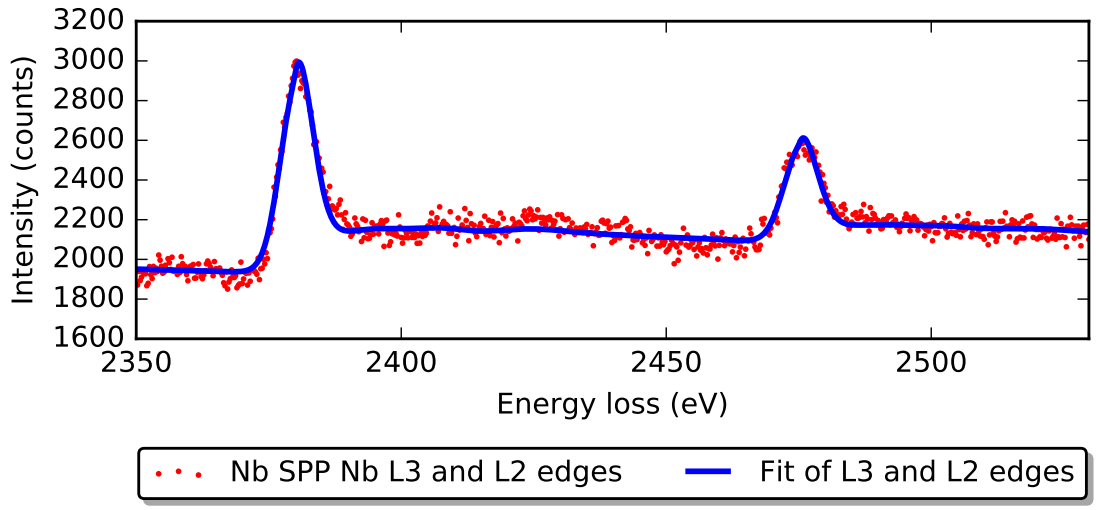


Figure 4.47: The fit of the Nb SPP Nb L_3 and L_2 edges and white lines.

	Zr L_3 Δ	**Zr L_2 Δ**	**Nb L_3 Δ**	**Nb L_2 Δ**	**O K Δ**
Metallic Zr	**0**	**0**	-	-	**0**
Oxidised Zr	1.3	1.3	-	-	-1.4
Metallic Nb SPP	-0.3	-0.6	**0**	**0**	0.1
Oxidised Nb SPP	1.3	1.5	2.3	2	-2.2
Metallic $Zr(NbFe)_2$ SPP	-0.2	-0.7	0	-0.2	-2.2
Oxidised $Zr(NbFe)_2$ SPP	1.8	1.9	2.7	2.4	-2.2

Table 4.6: Shift in energy loss, given in eV relative to the metallic Zr and Nb values and value of the O K edge in the metal (highlighted in bold in the table). The EELS dispersion was 0.05 eV channel^{-1}, giving a minimum error on the shifts.

The intention at this point was to compare the Nb L_3 and L_2 shifts to the shifts of the Nb oxide standard EELS spectra, shown previously in figure 4.43. Unfortunately, there was no clear shift found in the Nb L edges, suggesting that the sample either changes phase during FIB liftout or when exposed to the TEM electron beam.

During the writing of this thesis, a paper by Annand et al. [178] has been published using DualEELS and scanned diffraction to study SPPs in oxidised Zircaloy-4. They demonstrate that upon oxidation $ZrFe_2$ transforms into a nanocrystalline homogenous mixed oxide with a strong crystallographic texture. Meanwhile, the $Zr(Fe, Cr)_2$ SPPs oxidise in a much more complicated manner. Their paper demonstrates that this latter SPP contains separate nanocrystalline phases of varying concentrations of Zr, Fe, Cr and O. This presents a much more complicated mechanism of SPP oxidation than has previously been expected, and shows how methods such as point analysis on SPPs can give very inaccurate results.

4.5 Discussion

4.5.1 3D-FIB sectioning

The amount of overlap of the oxide thicknesses after the very different oxidation times of the 45-day and 135-day samples indicates that two samples may have regions in them that are in the same state (i.e. both at the same point relative to transition). The width of each histogram also suggests that "transition" is a much more local event than it is normally described. Researchers in zirconium oxidation

often make measurements at the nano- or microscale and report results that they report are associated with either "pre" or "post"-transition samples [26, 61, 163, 179], when they need to understand whether the specific region they analysed is in pre or post-transition. As in this thesis, researchers also refer to samples as "3-day", "100-day" etc. [72, 82, 180], which this work shows is not enough to identify the local state of the sample. Nanoscale analysis like high-resolution TEM and APT should be done particularly carefully as they sample such small volumes of material. Despite the above observations, and because it is useful for future comparison, I have chosen to keep the pre- and post-transition labels throughout this thesis, but tried to keep an open mind when looking at the results.

For the ZIRLO 135-day sample, the mean of the measured oxide thickness is 2.18 µm, significantly below the weight-gain measured value of 3.25 µm, which is indicated by the red dashed vertical line in figure 4.3. This implies that the spread is even larger than the histogram suggests, and that the 3D-FIB slicing was done in an area of particularly slow oxide growth compared to other regions on the sample.

No experiments known to this author have been undertaken measuring similar variations in the oxide thickness at the micro-scale. Observations have been made by de Gabory et al. [162] on samples of ZIRLO and Zircaloy-4 that there is large variation in the thickness of suboxide present at the metal-oxide interface. The fact that the sample state (e.g. pre-or post-transition) is only determined by weight gain measurements has consequences when interpreting high-resolution data (e.g. TEM or SEM). Sample state can be quite local and special care needs to be taken when making conclusions.

4.5.2 EELS fine structure and plasmon analysis

By studying the position and intensity of the Zr L white lines, I was able to clearly separate the oxidation states of Zr in the oxide, suboxide, oxygen-saturated metal and metal. This expands on the work of Na Ni [69, 71], who used the Zr M edges with the O K edge in order to characterise the metal-oxide interface. Using the Zr M edges has both advantages and drawbacks. Since the M edge family energies are

close to that of O K, the entire spectrum can be acquired simultaneously, saving time. Since any small shift in energy of the edges has no effect on quantification, if the EELS spectrometer has been well calibrated and sample is sufficiently thin, the ZLP and plasmon peaks are not needed. However, the subtraction of the background coming off the plasmon edges is not trivial and may introduce error. Additionally, the Zr M and Nb M edges overlap badly, which is very hard to remove. The L edges, while requiring a longer exposure, do not suffer these issues, and provide the bonus of information on the oxidation state! For quantifying the metal-oxide interface, I also show that a ZrO_2 standard sample is not necessary, as the oxide provides a good internal standard for the quantification, although it would be interesting to compare the white line characteristics with that of a standard. Additionally, the use of two-dimensional histograms comparing the calculated oxygen concentration with the measured white line peak centre, is a novel new approach. By using the L edges combined with advanced curve fitting software [148], I have improved the methodology for doing EELS quantification of Zr alloys.

In addition to being measureable from the oxygen concentration calculated by conventional EELS measurements, the suboxide and oxygen-saturated metal has been shown to be resolved by Zr L_3 and L_2 white lines that lower in energy loss from the oxide into the metal. These phases have also been shown to be resolved by low-loss plasmon analysis, particularly when combined with independent component analysis. Together, these methods allow a comprehensive analysis of the suboxide phases, and are likely applicable to other materials systems.

Understanding the order of oxidation and dissolution of the elements within SPPs is likely to be important to understanding the general oxidation mechanism of the alloy, and is discussed in the next section. The previously discussed approach could also be applied to the study of SPP oxidation.

4.5.3 Dissolution of Fe in SPPs

Fe-containing SPPs were often seen to reduce in number as a function of oxidation time. The ratio of Fe-containing SPPs to the β-Nb SPPs in the metal of 3-day

ZIRLO and the oxide of the 135-day ZIRLO can be seen in table 4.7, based on the counting of SPPs in figures 4.7, 4.13 and 4.20. There is a noticeable decrease in the fraction of Fe-containing SPPs present. The increase in fraction of Fe-containing SPPs in the 225-day sample over the 135-day sample can be attributed to very high counting statistics - close inspection of the SPP maps in figure 4.20 shows that the intensity of Fe in the SPPs in the oxide is substantially weaker than in the metal. Meanwhile, the intensity of Nb in the SPPs remains fairly constant.

Sample	**SPP**	**Count**	**Fraction**
3-day ZIRLO	β-Nb	23	0.53
	$Zr(NbFe)_2$	20	0.47
135-day ZIRLO	β-Nb	21	0.62
	$Zr(NbFe)_2$	13	0.38
225-day ZIRLO	β-Nb	21	0.42
	$Zr(NbFe)_2$	29	0.58

Table 4.7: Comparison of number of SPPs on 3-day, 135-day and 225-day ZIRLO. For the 3-day sample, the vast majority of SPPs were counted from the metal. For the 135- and 225-day samples the vast majority were from the oxide.

The lack (or reduction in intensity) of Fe content in SPPs indicates that SPPs either dissolve into the oxide, or that the SPPs fall out of the oxide during the sample preparation process. The latter has been observed by circular holes in the oxide, an example of this can be seen in the next chapter in figure 5.4a. Dissolution of the iron in SPPs has been shown for irradiated samples [89, 181], but not for non-irradiated samples. I may also simply have taken TEM samples from regions in-between SPPs (although this seems unlikely seeing the number of SPPs in the metal), or some process relating to manufacture of the alloy could mean that fewer SPPs form near the surface of the sample. That said, the 3-day sample does show a high number of SPPs very close to the oxide surface, which should still exist for the 225-day sample.

The total SPP number density is approximately 45 times higher than the SPP number density on candidate alloys compositions in and around the Zircaloy-2 and -4 composition from TEM analysis done by Eucker et al. [182]. Compared to SEM analysis done on Zircaloy-2 by Ogata et al. [182], my results are approximately

30 times higher, although their results are on bulk sample using EDS on an SEM making them not directly comparable. Interestingly, Dahlbäck et al. found a number density of 1.21 μm^{-2} for Zircaloy-2, which contradicts the other older results [128]. No literature values for the SPP number density of ZIRLO were found.

4.5.4 The effect of cracks

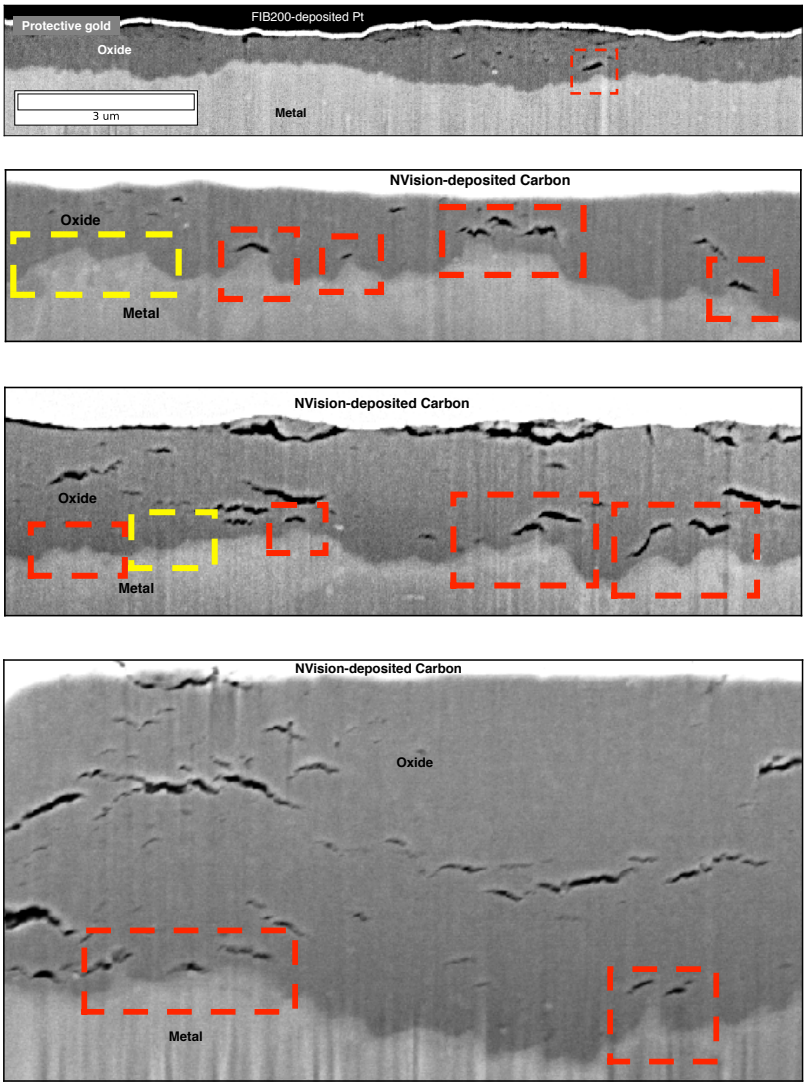


Figure 4.48: Cracks above protrusions (more slowly oxidising areas) highlighted in red on a single slice extract from 3D-FIB analysis from pre-transition (a) 3-day, (b) 45-day and post-transition (c) 135-day and (d) 225-day ZIRLO. The magnification is the same on all images. The areas highlighted in yellow are regions without a crack in this slice of the 3D-FIB stack, but where cracks are visible in the neighbouring slices.

Like previous authors [72, 81], I find that cracks frequently appear above metal

protrusions (more slowly oxidising areas). Typical observations from all four ZIRLO alloys are shown in figure 4.48, where all four images are at the same scale and show samples of increasing time of oxidation. The 3-day pre-transition sample shows very few cracks overall, with a generally very flat metal-oxide interface. The 45-day sample has a particularly angular metal-oxide interface, with very variable oxide thickness. Post-transition, the 135-day sample shows slightly less variable oxide thickness, with a metal-oxide interface that varies less than the 45-day one. Finally, the 225-day oxide contains very many cracks. These are often near the metal-oxide interface, but protrusions are fewer compared to the 45-day and 135-day samples.

The matter of whether the slow oxidation rate is caused by the cracks above them, or whether cracks appear *due* to the slow oxidation growth is still a matter of debate. The large stresses arising due volume expansion on the formation of zirconia are well known [183, 184] due to the high Pilling-Bedworth ratio of zirconium oxide. In Zircaloy-4 the stresses in the metal do not exceed 25 MPa, whilst they reach 1.7 GPa in the oxide [185], and the crack formation due to stress relaxation could possibly explain the phenomenon discussed above.

The fraction of tetragonal grains present in the oxide, which are stabilised either by bulk oxide stress or, for very small grains, internal grain stress, are found to be reduced after transition [40, 44, 65, 84, 85, 87, 186–189]. This reduction implies a stress-relaxation in the oxide after transition. It is therefore possible that lack of crack formation above protrusions in 225-day samples looked at in this thesis are due to the region of the sample being in post-transition. It is not clear whether the tetragonal grain fraction increases again before the next transition: Yilmazbayhan et al. [40] found that for ZIRLO the tetragonal grain fraction followed a periodic pattern. However, whilst the first major reduction in tetragonal grain fraction followed the oxide weight gain transition point, the next cycles of tetragonal grain faction were independent of bulk oxide weight gain rate, as shown in figure 4.49. Of those alloys, only ZIRLO showed a particular change in phase fraction.

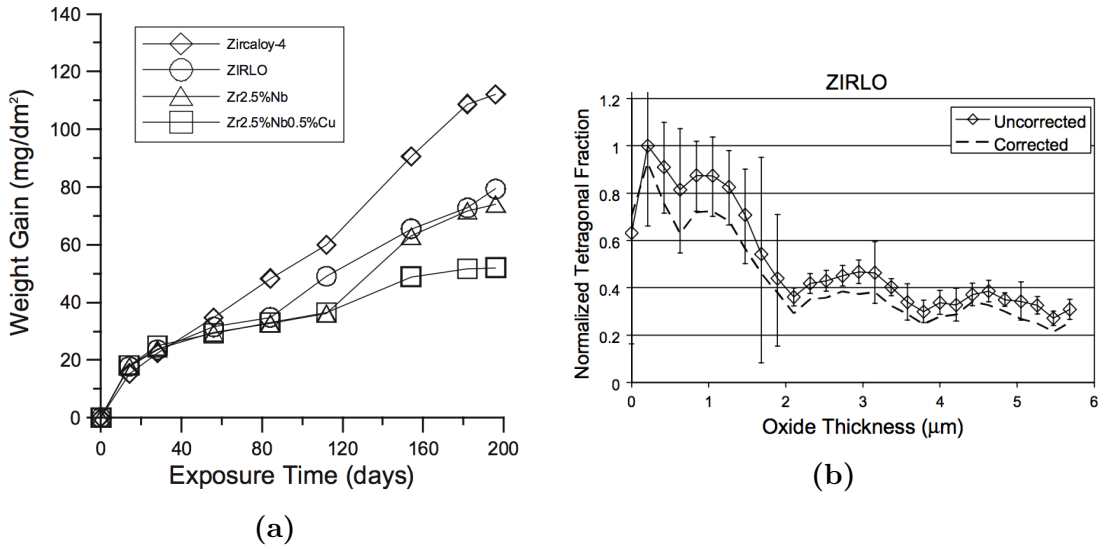


Figure 4.49: (a) Weight gain of ZIRLO and several other alloys oxidised in water at 360 °C. (b) Tetragonal grain phase fraction for the ZIRLO in (a) [40].

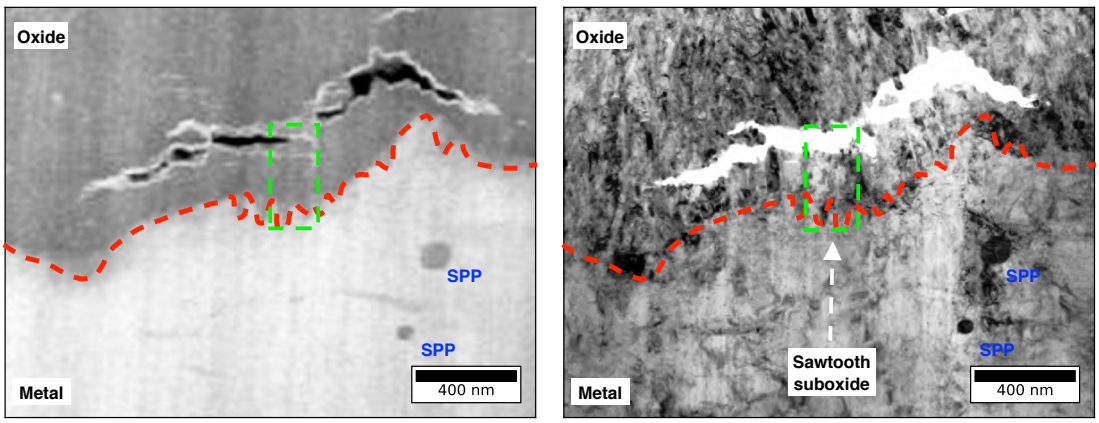
4.5.5 Porosity near the metal-oxide interface

Porosity has been suggested play a major role towards transition. As the oxide grows, these pores are interconnected by microcracks, eventually forming a large connected network. On FIB-foils interconnected porosity is only visible in the plane of the sample. In three-dimensions, these interconnected pores likely allow transport of the oxidising species to access fresh metal.

Figure 4.50 shows a region around the metal-oxide interface using both the HAADF imaging mode of STEM and a bright field mode of TEM. I used the STEM image to locate a region of sawtooth-suboxide present at the metal-oxide interface on a sample of post-transition 225-day ZIRLO. Under Fresnel imaging conditions of over- and under-focus, I was able to image porosity present near a 1300 nm wide crack present just a few hundred nm from the metal-oxide interface.

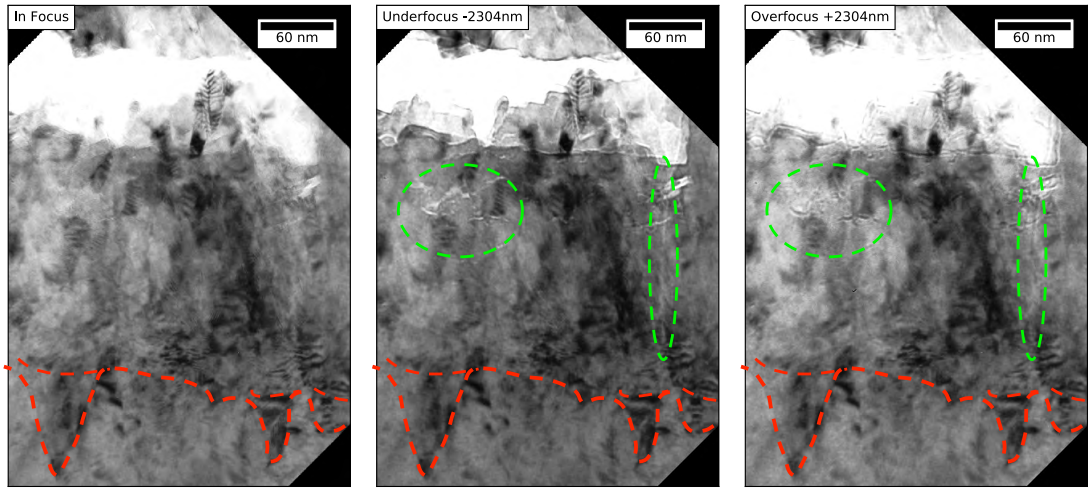
There is much porosity present, as highlighted in green in figure 4.51. In particular, a vertical continuous pore, about 160 nm in length, reaches from the crack and almost entirely down to the sawtooth suboxide shape. Ni et al. [69, 83] found very similar porosity on pre- and post-transition Zircaloy-4.

Na et al. [83] discuss the origin of the porosity. They argue that the porosity can possibly be attributed to the Kirkendall effect when rejected solute diffuses



(a) STEM HAADF image **(b)** TEM BF image

Figure 4.50: STEM HAADF and TEM BF images showing a region containing sawtooth suboxide on a sample of post-transition 225-day ZIRLO. The green rectangle indicates the region shown in figure 4.51.



(a) In focus **(b)** Underfocus by 2304 nm **(c)** Overfocus by 2304 nm

Figure 4.51: Fresnel contrast around porosity near the metal-oxide interface on post-transition 225-day ZIRLO. Porosity is highlighted in green dashed ovals.

away from the metal-oxide interface faster than the matrix atoms diffuse towards it. Specifically, Sn and Ti are suggested as possible candidates due to their much higher rate of diffusion compared to Zr. However, they also note that porosity has been observed in oxides grown on pure Zr where the Kirkendall effect cannot operate, and some other mechanism, for instance stress, must be responsible.

Preuss et al. [190] argue that the tetragonal to monoclinic phase transformation plays a major role in the formation of porosity. They showed that there is a sudden

increase in compressive stresses in the monoclinic phase just before transition. This is argued to be caused by the 3 % to 5 % volume increase [86] of the tetragonal to monoclinic phase transformation as well as shearing caused by the transformation. Cracks and porosity induced by the transformation then provide a fast-track for oxygen to diffuse in towards the metal causing accelerated corrosion (i.e. transition). This is in line with my own observations of porosity being particularly prominent in regions of equiaxed oxide.

Further to this, Garner et al. [87] argue that a significant amount of oxide phase transformation can take place whilst the oxide still remains protective. This is sensible when considering the tetragonal grain size, which is expected to be smaller than the equiaxed grain size [65, 191]. While porosity forms close to the metal-oxide interface, the very local nature of the transformation and the distance from the oxide surface allow it to remain isolated from forming a porosity network. Garner et al. argue that there is a critical value of stress in the protective oxide. Once the stress drops below this value, it leads to the onset of further phase transformation and rapid onset of connected porosity.

Since the tetragonal oxide is shown to be stress-stabilised, and there is a significant volume increase in the phase transformation from tetragonal to monoclinic oxide, the phase transformation to monoclinic oxide should stabilise neighbouring tetragonal grains. It therefore seems likely that further stress-relaxation is necessary in order to provide the type of rapid phase transformation and formation of porosity argued by Garner. Lateral cracks [192] and voids on the surface-side of unoxidised SPPs could provide such means. Lateral cracks near undulations of metal-oxide interface are particularly suited due to their large size and proximity to stresses caused by the difference [193] in oxide thickness around such undulations.

4.5.6 Corrosion resistance and oxygen-saturated region

The low-loss EELS measurements shown in figure 4.30 show a correlation between improved corrosion resistance (recrystallised Zr-1Nb) and the build-up of a thick combined layer of oxygen-saturated metal and suboxide at the metal-oxide interface.

The data suggests that during rapid oxide growth there is less formation of suboxide and oxygen-saturated metal. For suboxide, this has been also seen by Na [71] on post-second transition ZIRLO samples. This implies that the suboxide is formed when the oxide growth is slow and allows some oxygen diffusion in the metal. The accumulated suboxide during the slow oxidation process is quickly consumed during the faster oxidation process at transition. Then there is enough oxygen to develop zirconium oxide directly without going through the suboxide stage. Considering that recrystallised Zr-1Nb has a better corrosion resistance than ZIRLO and annealed Zr-1.0Nb, this implies that alloys with better corrosion resistance have more formation of suboxide and oxygen-saturated metal.

It should be emphasised that the problem of looking at a very small part of the whole is particularly relevant here. For this particular research, one sample of 3-day, two samples of 45-day, one sample of 135-day and three samples of 225-day ZIRLO were looked at. The areas acquired on each sample covered 1.5 µm to 5.0 µm of metal-oxide interface at a time. If a reliable way to acquire the oxygen-saturated metal thickness could be found, say, using energy-filtered transmission electron microscopy (EFTEM) at low magnification, the process could be accelerated considerably, although the problem of looking at very small regions of the whole still applies. The method of separating the plasmons on low-loss EELS can be used, although the scanning nature of the STEM technique does take longer than acquiring it simultaneously in TEM mode. 3D-EDS acquisition whilst 3D-FIB slicing provides another possibility for measuring it, although this technique is still in its infancy. At the time of writing of this thesis, an instrument capable of that type of analysis has just become available.

4.5.7 Suboxide

The suboxide measured on ZIRLO in this project varied significantly in thickness from area to area on the samples. While the 3-day sample showed only occasional suboxide with a thickness of 25 nm, the 45-day and 135-day samples showed thicknesses typically in the ranges 50 nm to 100 nm and 100 nm to 150 nm,

respectively. Finally, the 225-day sample displayed suboxide particularly in regions where the oxide had grown less compared to regions nearby (for instance in figure 4.21). Here the suboxide thickness varied from 0 nm to 240 nm, averaging 45 nm. The trend suggests that the maximum suboxide thickness increases as the sample approaches post-transition. Suboxide on oxidised ZIRLO has previously been measured by Ni et al. [71], who provided guidelines for doing zirconium and oxygen concentration measurements using a high-purity ZrO_2 powder standard and the Zr M and O K edges. This work has complemented theirs, by showing that it is possible to accurately characterise the thickness of the suboxide region also by EDS and by using the Zr L edges and white lines. At the metal-oxide interface on ZIRLO oxidised for 140 days at 360 °C, Ni found suboxide regions that were typically 150 nm wide. The measurements shown in this thesis are in excellent agreement. In her thesis [69], Ni showed that the thickness of suboxide grains can vary widely, and that for samples oxidised through two transitions, the suboxide is barely visible, if present at all. Hu et al. [95] did an extensive analysis on an alloy with similar composition to Zr-1.0Nb, finding a broad range of suboxide thicknesses ranging from no suboxide at all to 326 nm. All of these measurements were done across only 1 µm of interface, suggesting that the variations are very local. Yilmazbayhan et al. [65] found "blocky" suboxide grains 100 nm to 150 nm wide on samples of Zircaloy-4 and Zr-2.5Nb by TEM imaging. The findings of these researchers closely match what is observed on the ZIRLO samples studied in this thesis. The wide distribution of suboxide grain thickness implies that the conditions necessary for suboxide formation are stringent, and must vary locally along the metal-oxide interface. The fact that the amount of suboxide present in samples oxidised through multiple transitions is reduced [69] suggests that stress relaxation may play a role, as residual stress is shown [85] to reduce with oxidation time. Stress stabilisation of the suboxide may be why the suboxide is particularly present under the undulation where the oxide has grown less in figure 4.21. A lateral crack resides 250 nm above the undulation. Measurements on late pre-transition Zircaloy-4 by Annand et al. [156] show sawtooth suboxide varying in thickness

up to approximately 250 nm. These are also concentrated below undulations like the one previously mentioned, with a lateral crack above the undulation. The lateral crack above the undulation may suggest that the formation of suboxide is due to lack of enough oxygen to oxidise the metal fully, if the crack prevents the transport of oxygen. Lateral cracks blocking oxygen ingress is consistent with a ^{18}O tracer study done by Yardley et al. [82]. Alternatively the crack may have been caused *due* to the slow oxidation in this region, by the high tensile stresses perpendicular to the metal-oxide interface [53, 85, 87].

While the thickness of the oxygen-saturated metal region shows a clear trend with respect to transition, any average trend of the suboxide is less clear, although the maximum thickness appears to increase at least until the sample is fully in post-transition. A study of suboxide formation on samples chosen closely around transition might provide answers. The method for characterising the metal-oxide interface quickly by low-loss EELS and ICA, shown in chapter 3, can help speed up this process.

Finally, Dong et al. [194] showed by APT that the suboxide also forms on pure zirconium (crystal bar). The presence of suboxide on all types of zirconium alloys, including pure zirconium, indicates that the formation of suboxide is not specific to certain alloys but is a general mechanism of zirconium oxidation!

4.6 Summary

ZIRLO was oxidised at 360 °C for up to 225 days. The weight gain followed a power law with k = 7.3 mg dm^{-2} d and n = 0.33 until approximately 100 days into oxidation, where, with an average oxide thickness of 2.3 µm, the sample underwent transition and the oxidation rate accelerated. The ZIRLO nuclear cladding alloy oxidises in the hot, wet environment of the nuclear reactor. In this chapter I have used TEM analysis to describe its corrosion as a function of oxidation time. The following is a summary of the most important aspects of the chapter:

- Through novel 3D FIB-analysis of the oxide thickness, the oxide thickness has been shown to vary largely between even very close regions. A FIB-sample taken from a 45-day late pre-transition alloy may have the same oxide thickness as a sample taken from a 135-day early post-transition alloy. This brings into question to what degree one can separate samples using the labels "pre"- and "post"-transition. In addition, the oxide thickness measured directly by FIB sometimes differs enormously from the expected oxide thickness calculated from weight gain. As seen in figure 4.3, whilst the weight gain thickness matches well to the 3-day, 135-day and 225-day ZIRLO FIB analysis, the weight gain thickness is shown to be over one micron higher than the average thickness of the FIB analysis. This means that in previous research, the small amounts of samples analysed for a given (pre- or post-transition) material, may have failed to describe the whole.

- ZIRLO oxide has been shown to have a relatively unorganised structure, especially when compared with the more corrosion-resistant alloy Zr-1Nb. ZIRLO features less of the columnar oxide compared to Zr-1Nb, but shows the same layered structure of equiaxed and columnar oxide. Equiaxed oxide grain size is typically 20 nm and is generally hard to resolve clearly due to overlap through the thickness of the samples.

- Independent component analysis (ICA) has been applied to phase separation on EELS low loss spectrum images in zirconium alloys for the first time. It is found to be an excellent technique for the phase separation and identification of oxide, suboxide, oxygen-saturated metal and metal phases. An alternative to MLLS fitting, ICA does not require reference spectra, but is relatively computer-processing intensive. Second-phase particles were clearly separated from the rest of the sample, but it did not become clear whether ICA can be used to distinguish between different types of SPPs and their oxidation state. The application of ICA to low loss EELS mapping has been shown to

be a powerful technique that may reveal hidden structures in a material and simplify analysis for future researchers.

- The oxygen content of the ZIRLO suboxide has been investigated and compared using EELS and EDS techniques. Whilst EELS yields less noisy results, both EDS and EELS clearly show a band containing 50 % O, in agreement with other literature. This means that for samples too thick to perform EELS analysis on, EDS could suffice in order to determine the chemical composition around the metal-oxide interface. The ZIRLO suboxide has been compared to the suboxide found in the literature on ZIRLO and other alloys, and found to be of similar nature and size.

- In order to determine the oxidation state of Zr, core-loss EELS was performed by either line profiles or maps across the metal-oxide interface. A curve-fitting approach to measuring the peak positions and intensities of the Zr L_3 and L_2 white lines allowed for painless handling of the data. A scatterplot of the Zr L_3/L_2 white line area ratio to the Zr L_3 white line peak position shows a clear clustering of data points according to phase. Both the ratio of the peaks as well as their position are necessary parameters for the correct identification of phase, as the peak position of the suboxide does not shift far from the metal.

- Taking a further step to visualising oxidation state, in a novel approach, a heat map showing the Zr L_3 white line peak centre position against oxygen concentration shows a clear shift in white line position, clearly separating the metal, oxygen-saturated metal and oxide. An indication of changing oxidation state can be clearly shown by relating the Zr L_3/L_2 white line area ratio to the Zr L_3 white line peak position. In order to clearly distinguish the three phases, both the ratio and the position must be measured. This result shows that the oxidation state of a given region on the alloy can be inferred from its position on a heat map such as described above.

- Porosity has been shown to exist throughout the oxide, all the way to the metal-oxide interface. The porosity is particularly prominent around equiaxed grains. The formation of porosity and equiaxed grains due to the transformation from tetragonal oxide due to stress relaxation is discussed with reference to mechanisms from the literature.

- The oxygen-saturated metal layer, which exists between the suboxide and metal has been shown to vary significantly with oxidation time. Histograms of oxygen-saturated metal thickness were shown to be similar for 3-day and 225-day ZIRLO, showing relatively small amounts of oxygen-saturated metal compared to the other alloys. This suggests the possibility of similar mechanisms for oxide growth at these stages of oxidation. Meanwhile, significantly larger oxygen-saturated metal regions were found for 45-day ZIRLO, with thickness larger than 400 nm. Access to large amounts of oxygen is a necessity for oxidation. If the oxygen could be prevented from gathering in the metal near the metal-oxide interface, an improvement in corrosion resistance would likely be found.

This concludes my findings in this chapter. In the next chapter, I have studied the corrosion behaviour of Zircaloy-4 in a similar way, and I will relate my findings to those of ZIRLO.

5

The corrosion of Zircaloy-4

Contents

5.1 Oxidation of Zircaloy-4 146
5.2 Oxidation characterisation 148
5.2.1 3-day pre-transition Zircaloy-4 148
5.2.2 45-day pre-transition Zircaloy-4 152
5.2.3 105-day post-transition Zircaloy-4 160
5.3 Low-loss EELS analysis of Zircaloy-4 163
5.3.1 Plasmon peaks comparison to ZIRLO 165
5.3.2 Combined suboxide and oxygen-saturated metal region . 165
5.4 Discussion 166
5.4.1 The inaccuracy of "pre"- and "post"-transition descriptions 166
5.4.2 Oxide microstructure comparison with ZIRLO 168
5.4.3 Combined suboxide and oxygen-saturated metal region . 171
5.4.4 Hydride formation in thin foils 175
5.4.5 Why does the sawtooth oxide form its shape? 176
5.4.6 The influence of alloying elements on the corrosion of zirconium alloys 177
5.5 Summary of results and discussion 180
5.5.1 Similarities 182
5.5.2 Differences 182

My intention with this Chapter is to compare the previous observations in ZIRLO with any differences in Zircaloy-4. Whilst some of my experiments have involved one material or the other, in many cases they have been analysed extensively using the same techniques. I will first describe what I see in Zircaloy-4 using the same methods

as for ZIRLO (where available), and then move on to comparing the alloy to ZIRLO.

5.1 Oxidation of Zircaloy-4

The alloys studied (with weight gains seen in figure 5.1 and in table 5.1) were from a selection of alloys oxidised from 1 to 225 days. Three samples were chosen based on their position relative to transition. The three-day pre-transition sample was chosen as there has been very little research on alloys oxidised for such a short time. The 45-day pre-transition sample was chosen in order to investigate a sample where the oxidation rate is slowing down and the 105-day post-transition was chosen because the oxidation rate was speeding up. The ZIRLO samples were chosen using the same arguments, making the two sets of samples comparable. Unfortunately, the 225-day post-transition sample, which would be contrasted with the 225-day ZIRLO sample, was not sent from Westinghouse to our lab in Oxford.

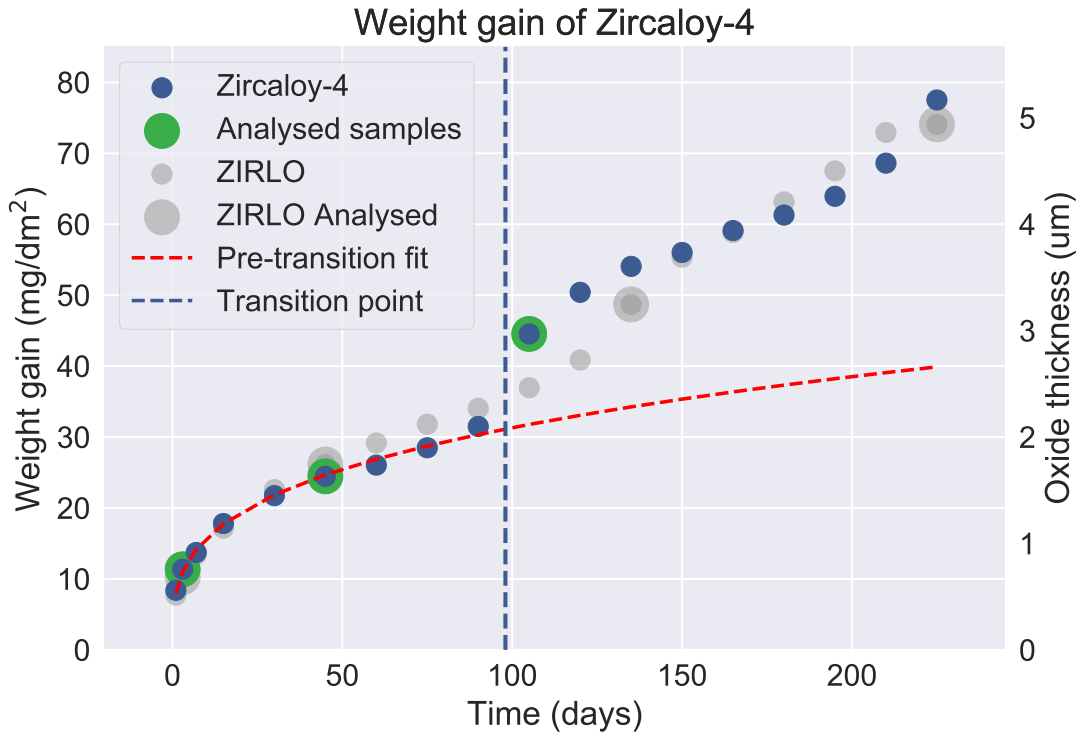


Figure 5.1: Weight gain of Zircaloy-4 at 360 °C, showing ZIRLO from Chapter 4 in grey. The vertical dashed line indicated the point of first transition, at about 98 days. The right-hand axis indicates the approximate oxide thickness given by equation 4.1. The red dashed curve indicates the fit of the pre-transition weight gain to a power law with $k = 8.2\,\mathrm{mg\,dm^{-2}}$ and $n = 0.29$.

The weight gain data for the Zircaloy-4 alloy (oxidised at 360 °C) can be fitted using $k = 8.2\,\mathrm{mg\,dm^{-2}}$ and $n = 0.29$ in equation 2.4. The transition point is at approximately 98 days, at which point the average oxide thickness should be 2.1 µm. This is smaller than the transition oxide thickness for ZIRLO, which is at 2.3 µm.

Time (days)	Weight gain ($\mathrm{mg\,dm^{-2}}$)	Oxide thickness (µm)	**Time (days)**	Weight gain ($\mathrm{mg\,dm^{-2}}$)	Oxide thickness (µm)
1	8.4	0.56	**105**	44.54	2.97
3	11.37	0.76	**120**	50.4	3.36
7	13.73	0.92	**135**	54.06	3.6
15	17.80	1.19	**150**	56.02	3.73
30	21.74	1.45	**165**	59.11	3.94
45	24.46	1.63	**180**	61.3	4.09
60	26.05	1.74	**195**	63.94	4.26
75	28.5	1.9	**210**	68.61	4.57
90	31.49	2.1	**225**	77.51	5.17

Table 5.1: Weight gain of Zircaloy-4 in water at 360 °C.

Using 3D-FIB and TEM observations, I have measured the ranges of oxide thicknesses at various regions on the sample, like for ZIRLO in the previous Chapter. They are presented in figure 5.2. In similar fashion to the ZIRLO results, I observe large variations in the oxide thickness within the 3-, 45- and 105-day samples, with means of 991 nm, 1443 nm and 3039 nm respectively. For the early pre-transition 3-day sample, a very sharp distribution is found. The late pre-transition 45-day sample overlaps significantly with the 3-day sample, but has a nearly binomial distribution of oxide thickness, with the weight-gain thickness nearly centred in the distribution. Whilst in some regions the oxide is only 800 nm thick, in other regions the oxide is nearly three times larger, at 2200 nm. The early post-transition 105-day sample contains an entirely different distribution, centred around the weight-gain thickness, but ranging from 2400 nm to 3800 nm.

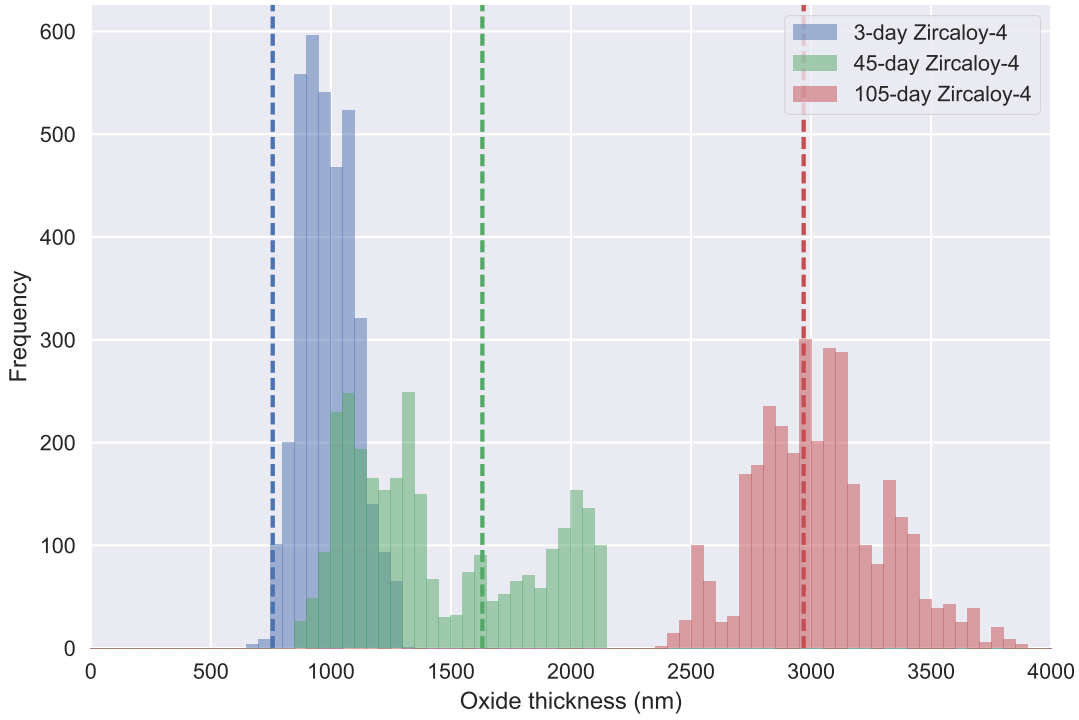


Figure 5.2: Histograms showing the variation in oxide thickness across oxidation time for the Zircaloy-4 samples. The dotted lines indicate the estimated oxide thickness according to the weight gain. The oxide thicknesses were measured by 3D-FIB slicing for the 3-day and 105-day samples, and by TEM samples for the 45-day sample.

5.2 Oxidation characterisation

5.2.1 3-day pre-transition Zircaloy-4

Figure 5.3 shows a typical HAADF STEM image of 3-day pre-transition Zircaloy-4. The largest cracks are on the order of 300 nm. Generally the oxide is without small cracks in the final 200 nm before the metal-oxide interface, but exceptions do occur. The metal-oxide interface is relatively smooth, and the oxide thickness of this sample ranges between 700 nm and 1000 nm in thickness. Three TEM foils were thinned successfully for the 3-day Zircaloy-4.

The montaged sample of pre-transition 3-day Zircaloy-4, seen in the DF and HAADF images in figure 5.4 has an oxide thickness of approximately 670 nm. This is slightly below the 760 nm oxide thickness expected from the weight gain measurement, and at the absolute low-end of the FIB-3D measured oxide thickness. The oxide thickness is much smaller than that of the ZIRLO sample that was

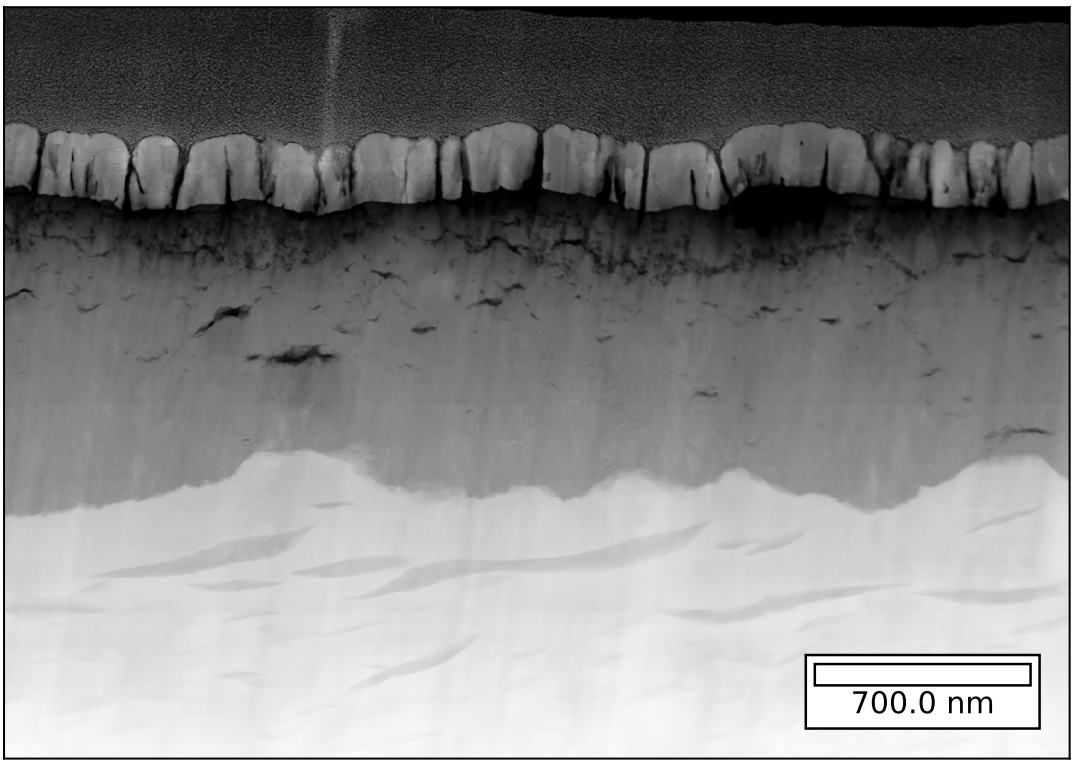
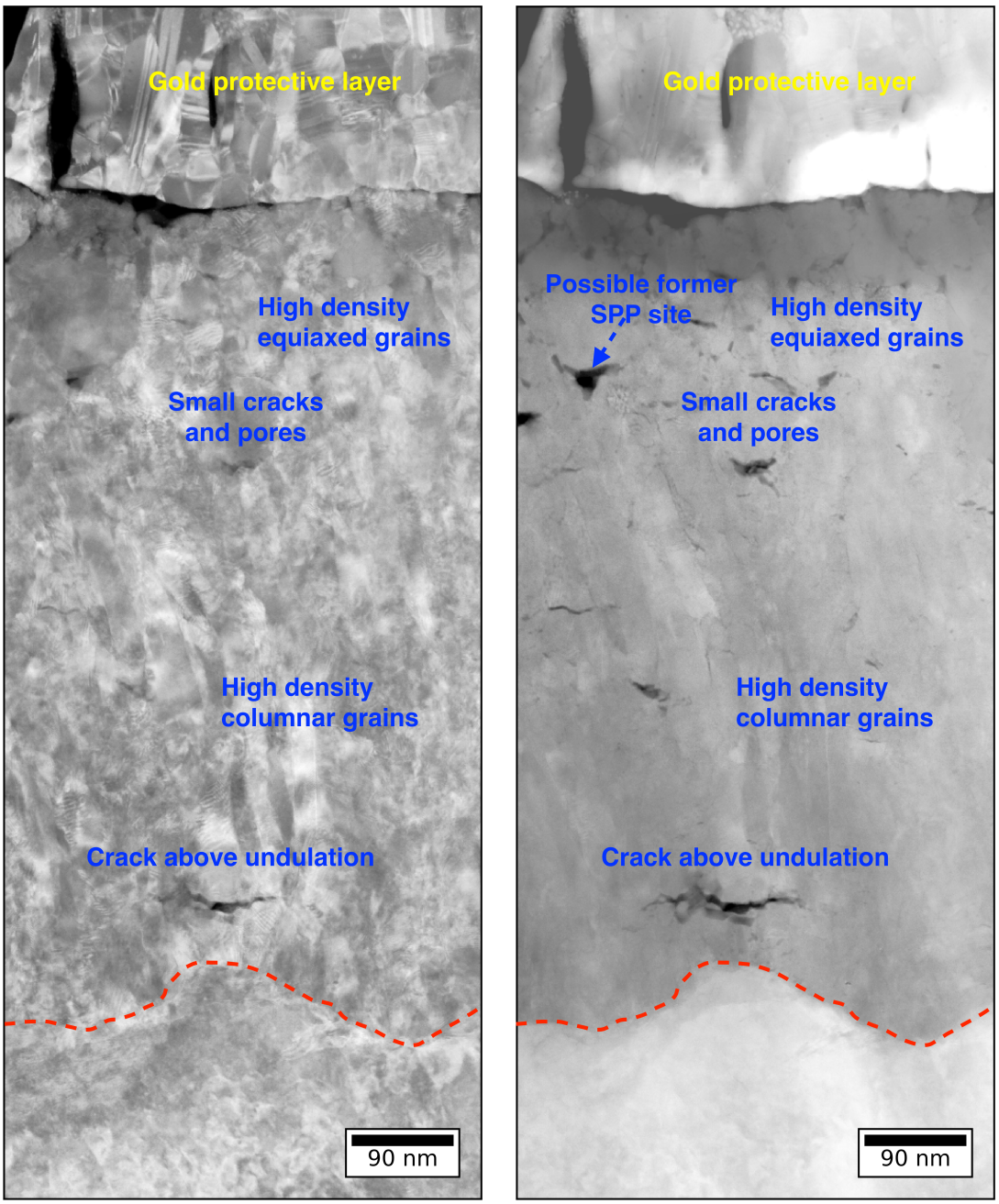


Figure 5.3: HAADF overview image of a 3-day pre-transition Zircaloy-4 sample.

exposed to the same time of oxidation. Comparing the two montages, the oxide thickness of ZIRLO was 1200 nm, almost twice that of the Zircaloy-4 sample. Whilst the weight gain data suggests that the average oxide thickness of ZIRLO should be smaller than that of Zircaloy-4 (0.68 µm compared to 0.76 µm, respectively), in the montage ZIRLO has grown much faster.

The columnar grains are on average approximately 90 nm long and 20 nm wide. The top 200 nm of oxide is mainly populated by equiaxed grains. Their size distribution is very difficult to measure, but they are generally within 40 nm in diameter, typically smaller. The grain structure of the Zircaloy-4 oxide is significantly more well-defined than that of the ZIRLO oxide. On samples that are of the same thickness, ZIRLO oxide grains seem to overlap more than their Zircaloy-4 counterparts.

Near the undulation in the metal-oxide interface in figure 5.4 a 90 nm long crack is visible. Below it, the oxide has grown more slowly than elsewhere. Several



(a) **(b)**

Figure 5.4: DF (a) and HAADF (b) STEM montage of the oxide on a 3-day pre-transition sample of Zircaloy-4. The metal-oxide interface is highlighted in red.

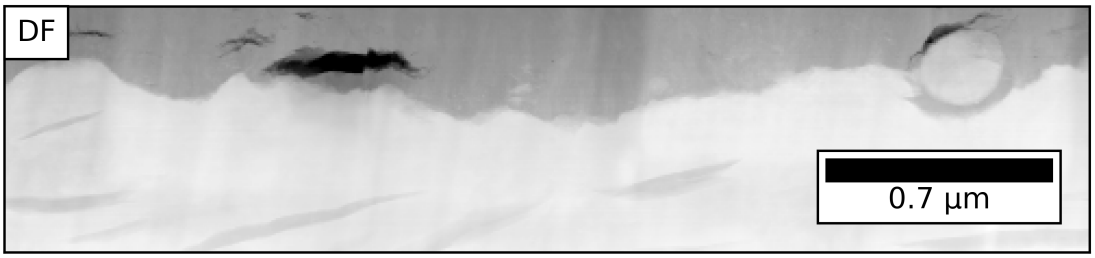
columnar grains are clearly visible above it in both the DF and HAADF images. Looking at the first 200 nm of oxide, a crack approximately 35 nm in length is found with a round hole in its centre (visible on the HAADF image). This could be the former site of an SPP which has fallen out during sample preparation. Many small cracks are present, especially in the first 300 nm of oxide.

However, larger cracks are also present in the oxide on this 3-day sample. Figure 5.5a shows a large crack, approximately 460 nm long, above a slight undulation in the metal-oxide interface. Interestingly, a much larger undulation is present in the top left of the image, but it is covered only by a much smaller crack. Whilst no quantifiable crack analysis was performed during this project, there seems to be a similar number and size-distribution of cracks present in ZIRLO and Zircaloy-4.

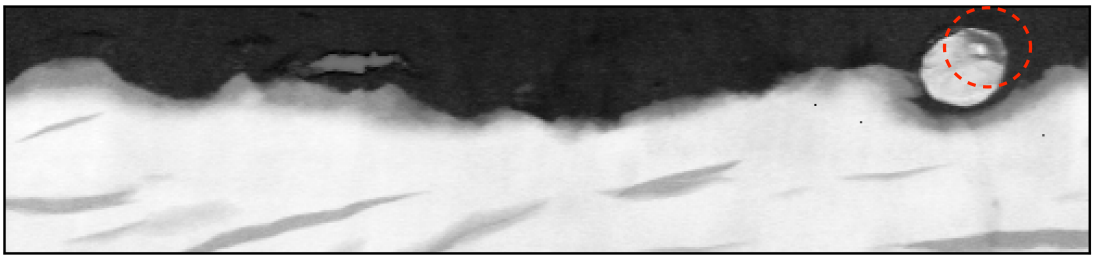
Oxidised SPP

ICA analysis on low-loss EELS data along the metal-oxide interface revealed a partly oxidised SPP at the metal-oxide interface, as seen in figure 5.5. SPPs tend to oxidise more slowly than the surrounding matrix, and it is unusual to see an SPP beginning to oxidise so soon.

An EDS line profile drawn across the SPP, as shown in figure 5.6, reveals that the SPP is Fe-rich (blue), but also contains Si (cyan) and Ni (green). It is also shown to be partly oxidised (red) as on the darker region visible on the HAADF-image. Interestingly, the Si peaks at the oxidation front through the SPP. Si could be related to the early oxidation of the SPP. Si-containing SPPs are mentioned by Rudling et al. [195] and found in silicon-added modified Zircaloy-4 as $Zr(Fe, Cr, Si)_2$ and Zr_2Si [196]. For the silicon-added modified Zircaloy the optimum silicon concentration for improved oxidation resistance is thought to be around 0.01 wt%. Up to this concentration of Si the weight gain of oxidised alloys was lower, but at higher concentrations the weight gain was higher. As the SPP found in figure 5.5 was oxidising faster than normal, it may be argued that it is Si present in the matrix that is the cause of the improved oxidation-resistance, rather than the SPP themselves.



(a) HAADF image of the metal-oxide interface on a sample of 3-day Zircaloy-4.



(b) Low-loss EELS ICA result indicating a change in plasmon peak intensity across the SPP, highlighted in red. Hydrides, oxygen-saturated metal.

Figure 5.5: Partly oxidised SPP present at the metal-oxide interface of 3-day Zircaloy-4.

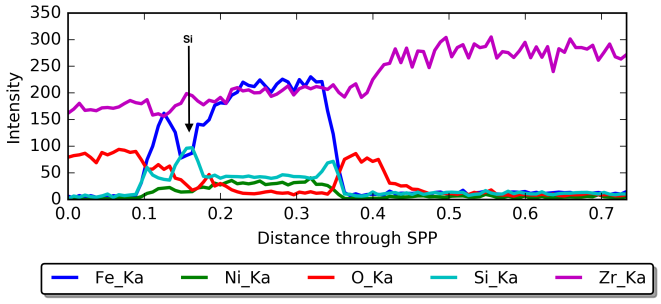
5.2.2 45-day pre-transition Zircaloy-4

Figure 5.7 shows a typical HAADF STEM image of 45-day pre-transition Zircaloy-4. There are some large cracks, but much of the oxide contains cracks only about one hundred nm long. The metal-oxide interface is quite uneven, and the oxide thickness of this sample is between 1.0 µm and 1.5 µm in thickness. Two TEM foils were thinned successfully for the 45-day Zircaloy-4.

The montage of 45-day Zircaloy-4, seen in figure 5.8, has an oxide thickness of approximately 1.5 µm. This is 130 nm below the 1.63 µm oxide thickness expected from the weight gain measurement. The first 450 nm of oxide contain primarily equiaxed grains. The grain sizes are very small, no larger than 50 nm at most. The next 500 nm of oxide consists mainly of columnar oxide, but as one approaches the crack the grain size is very small, and it becomes very difficult to determine the grain shape. Finally, just before the metal-oxide interface, the grain shape is columnar, but very small, typically 30 nm to 50 nm long and 6 nm to 12 nm wide. An aspect ratio of 5:1 seems typical of the columnar grain structure, independent of size and agrees with the literature [65].



(a) HAADF image of a SPP on the metal-oxide interface of a sample of 3-day Zircaloy-4. The line indicates the position and direction of the EDS line profile.



(b) EDS line profile showing the content through the SPP. The interface of the oxidised part and the metallic part of the SPP is Si-rich.

Figure 5.6: Concentration of Fe, Ni, O, Si and Zr on a line profile through a partly oxidised SPP.

The large crack near the metal-oxide interface suggests that this region has recently gone through or is about to go through, transition, depending on whether cracks cause transition or transition causes cracks, which is still not entirely clear. Aside from the crack, the oxide is mostly uniform and dense, with no SPPs apparent. The small cracks are no longer than 60 nm, but are significantly more frequent in the top 300 nm of the oxide. The darker region under the large crack on the HAADF image in figure 5.8b is due to preferential FIB milling under the crack, leading to a thinner region under the crack than above it.

The sample has two large $Zr(Fe, Cr)_2$ SPPs sitting just below the metal-oxide interface, as seen in figure 5.9. The lack of SPPs in the oxide, and their separation in the metal gives the impression that SPPs are an unlikely route of hydrogen ingress. While Bossis et al. [91] found that hydrogen ingress was significantly

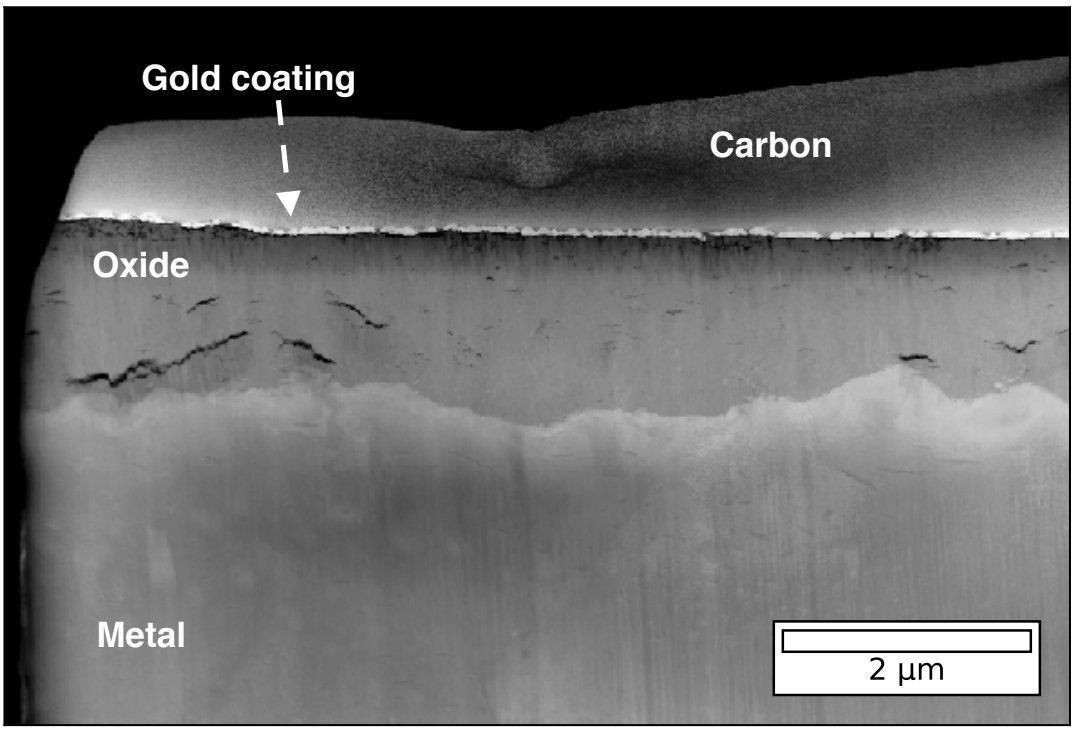


Figure 5.7: HAADF overview image of a 45-day pre-transition Zircaloy-4 sample.

increased by having very large (0.5 µm to 2.0 µm) SPPs in the oxide, these SPPs are much smaller, on the range of 150 nm to 220 nm. It seems unreasonable to assume that these small SPPs, separated by distance on the micron scale, act as a primary pathway for hydrogen ingress. A possible explanation for the ingress of hydrogen in samples with larger SPPs could be the large SPPs acting as tunnels through the dense protective oxide, which is unlikely for smaller SPPs. This is discussed further in Chapters 6 and 7.

This sample's oxide thickness is the same thickness as the 45-day ZIRLO sample studied in Chapter 4. However, oxide thickness of the ZIRLO sample was 400 nm thinner than the expected weight gain value. The crack distribution is similar, with most cracks present near the metal-oxide interface above undulations of metal. Crack sizes are also similar, ranging from less than a hundred nm to above 1 µm. Like for the 3-day samples, the Zircaloy-4 oxide is more well-defined than the ZIRLO oxide. However, for Zircaloy-4 the columnar grains are less well defined on the 45-day samples than the 3-day samples.

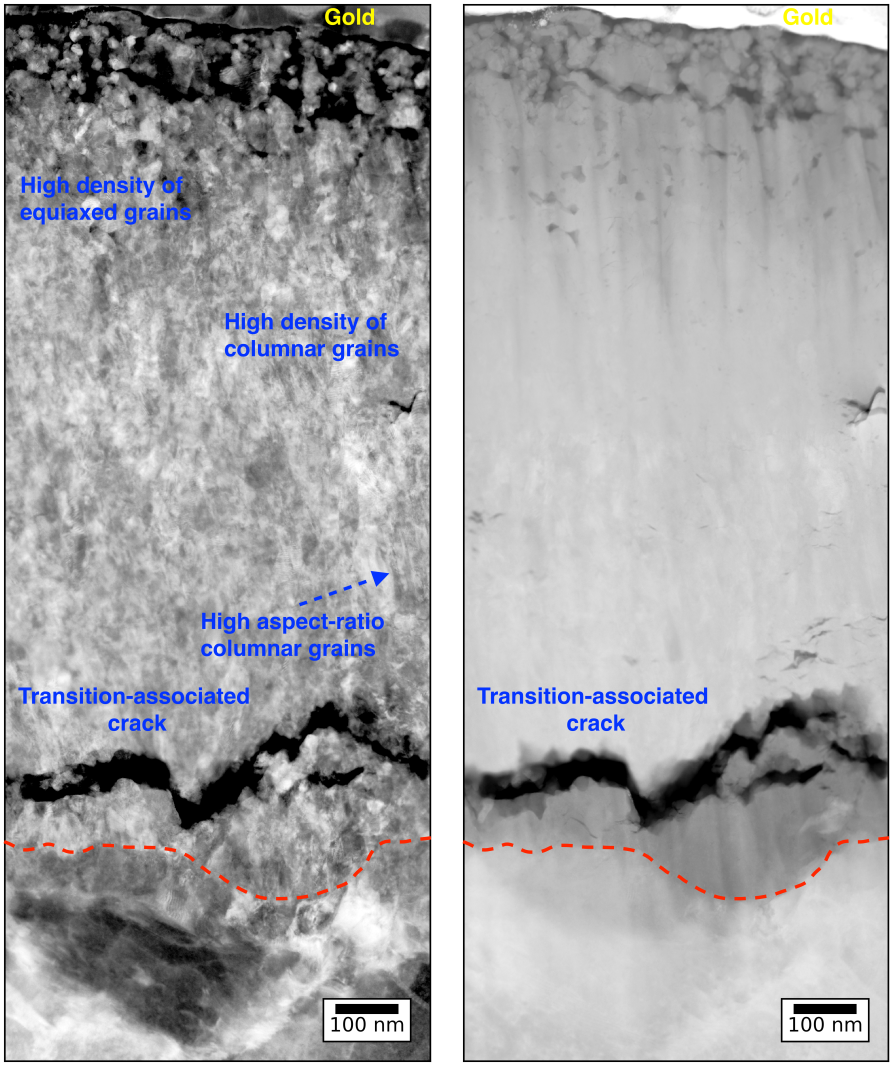
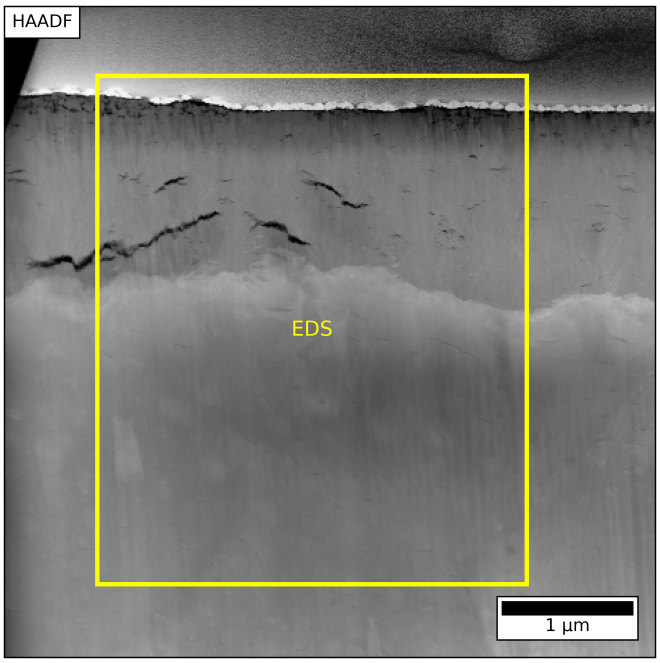


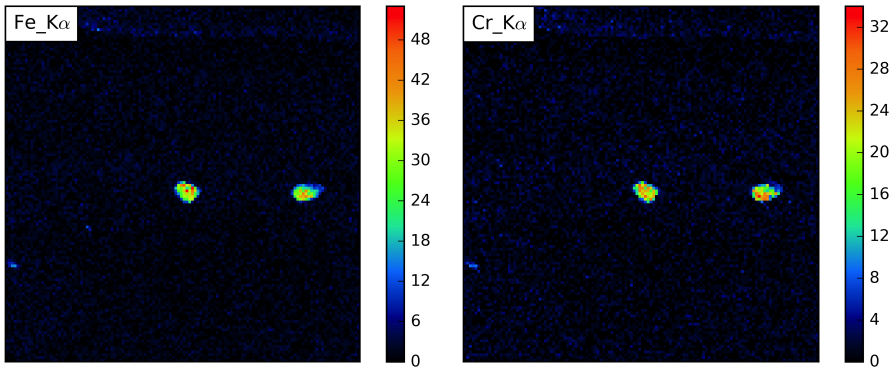
Figure 5.8: DF (a) and HAADF (b) STEM montage of the oxide on a 45-day pre-transition sample of Zircaloy-4. The metal-oxide interface is highlighted in red.

A relatively unusual feature, with long thick (250 nm x 50 nm) fingers sticking into the oxide was found at the metal-oxide interface, and can be seen in figure 5.10.

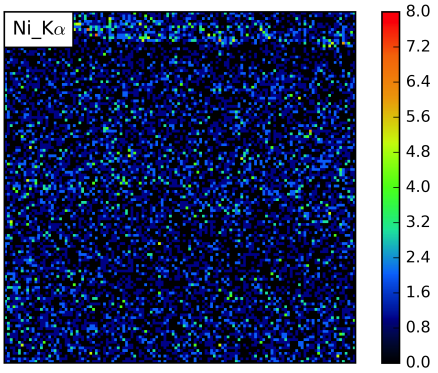
Using the oxide for reference, the zirconium and oxygen concentrations were calculated by EELS core-loss analysis using the Zr L and O K edges. Regions A and C are ZrO_2, B and D are likely to be the suboxide ZrO phase, E is the oxygen-saturated metal, and F is the metal. The relative concentrations of Zr and O at region E is approximately 60 % and 40 %, which would be stoichiometric Zr_3O_2. The oxygen-saturated Zr_3O phase found by Nicholls et al. [94] should have 25 % O.



(a) HAADF image.



(b) Fe_Kα signal. **(c)** Cr_Kα signal.



(d) Ni_Kα signal.

Figure 5.9: EDS maps taken on the region of a 45-day Zircaloy-4 sample shown in the HAADF image (a). Two Zr(Cr, Fe) SPPs are visible in the metal, though none are present in the oxide. There is no sign of Ni clustering in the sample.

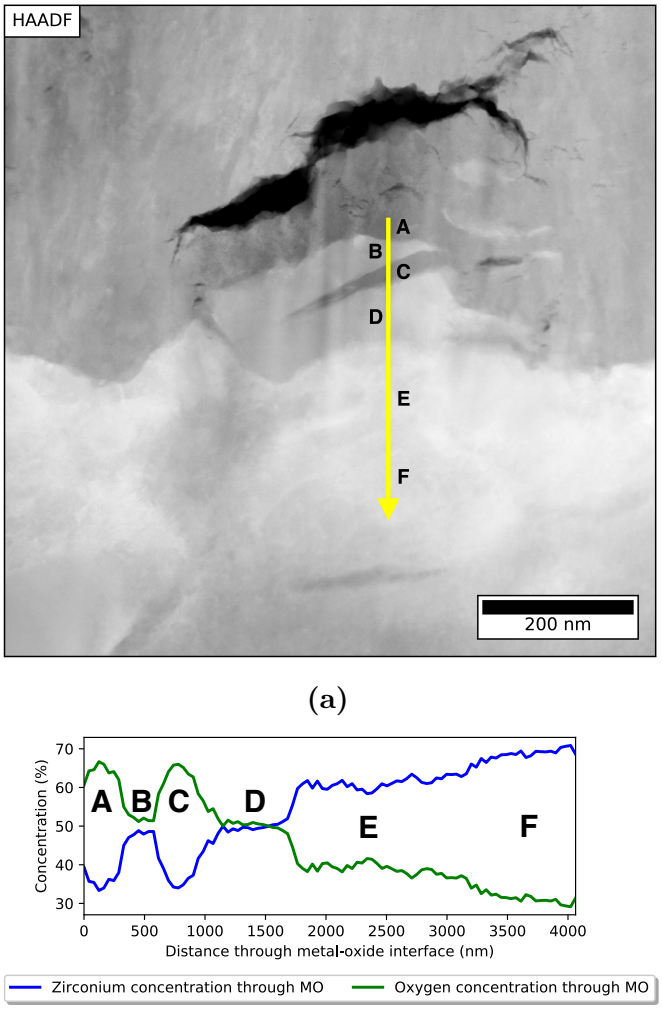
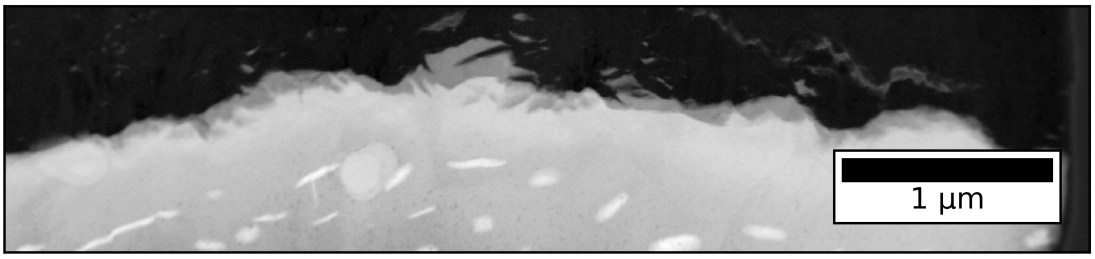


Figure 5.10: Zr and O composition (a) from EELS analysis of an unusually-shaped feature on the metal-oxide interface (b).

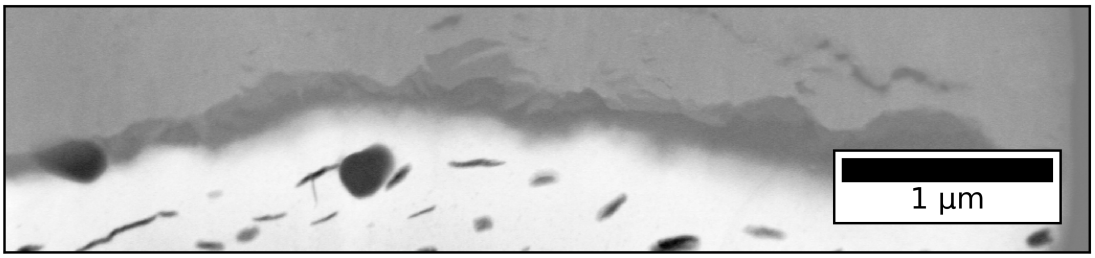
The increased value could be explained as the sample surface having oxidised in contact with air or may be a result of an inclined interface running through the sample thickness. Here there could be a contribution from overlapping Zr and ZrO grains. However, this relative concentration of 60 % and 40 % has been detected in the past [95] and explained by the same arguments as I present here. Whilst a flat region (plateau) in the concentration region is normally found (and generally shown to be at 50 %), I often find that the measured concentration of the plateau can vary between 50 % and 60 % O from sample to sample. Whilst this is likely to be because of air oxidation of the sample between the FIB-liftout process and

imaging in the TEM, future work could look into whether the concentration is always 50 % on freshly extracted samples.

Two ICA loadings emphasising the feature are shown in figure 5.11. 5.11a suggests that the feature is of the same phase as the rest of the suboxide, including the sawtooth-shaped suboxide present on the left hand side of the metal-oxide interface. The oxygen-saturated metal, shown in figure 5.11b, is particularly broad on the right hand side of the image, near the crack.



(a) ICA loading emphasising the feature in figure 5.10 and the suboxide.



(b) ICA loading emphasising the oxygen-saturated metal (dark).

Figure 5.11: ICA loadings from the metal-oxide interface region, showing the suboxide and oxygen-metal interface containing the region shown in figure 5.10.

The oxide thickness can vary enormously on the pre-transition 45-day samples. Figure 5.12 shows a FIB-liftout imaged using a FIB-SEM. Here the oxide thickness ranges from 1.13 µm at its thinnest to 2.43 µm at its thickest. The fact that these differences can happen within 10 µm along the metal-oxide interface emphasises the importance of doing macroscale analysis before doing nanoscale measurements. The variation in oxide thickness on the sample shown is approximately the same as the histogram variation for the ZIRLO sample shown in figure 4.3.

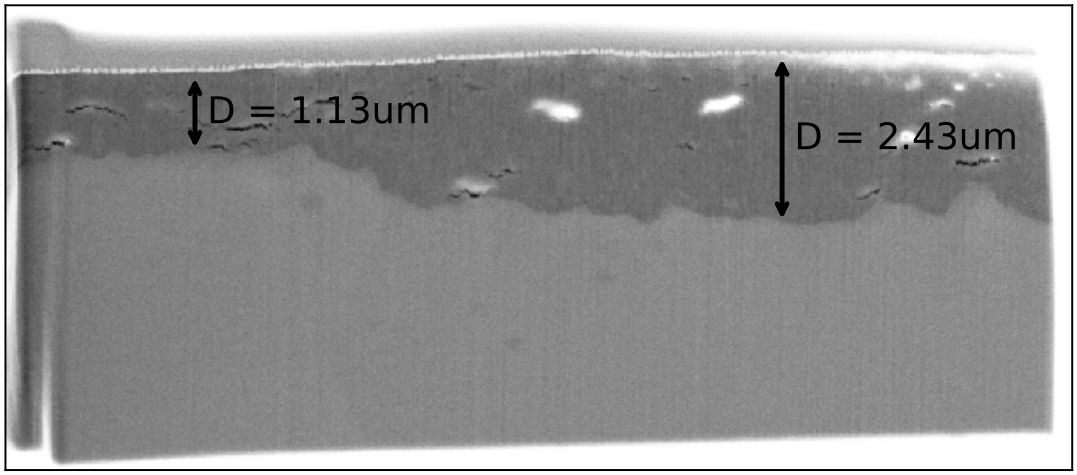


Figure 5.12: Large variation of oxide thickness on one sample of pre-transition Zircaloy-4.

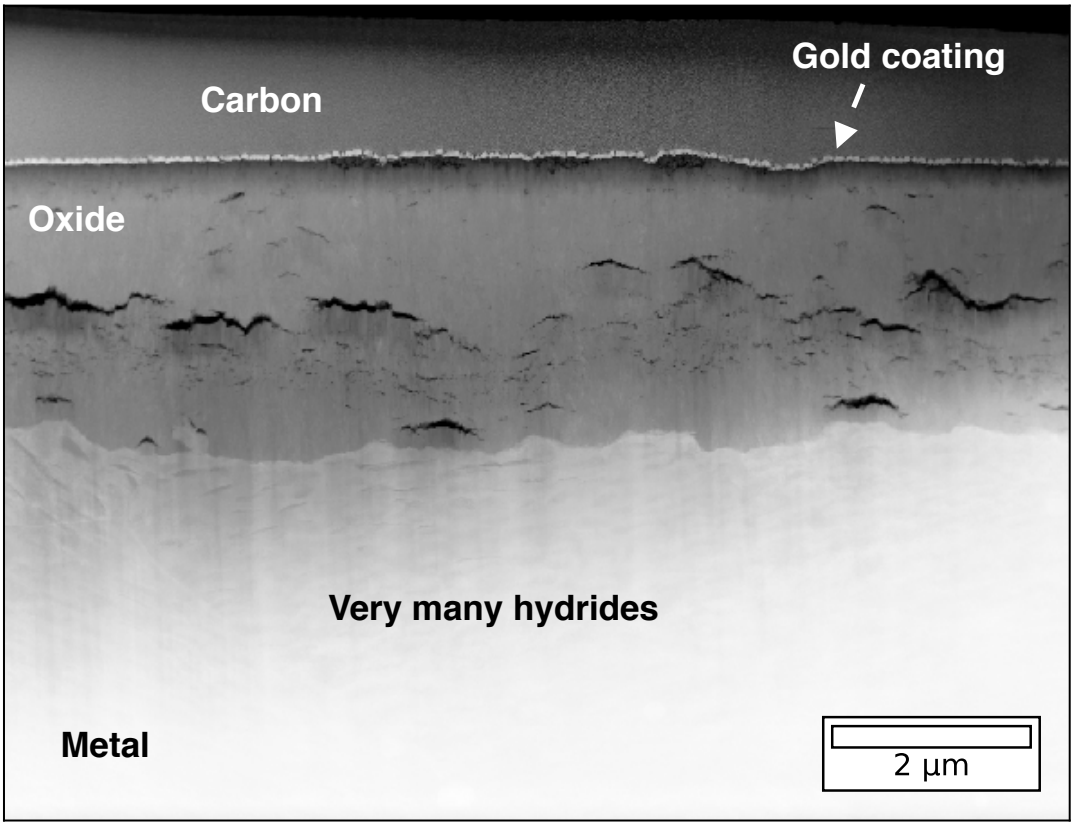


Figure 5.13: HAADF overview image of a 105-day post-transition Zircaloy-4 sample. The metal region on this sample is covered in hydrides.

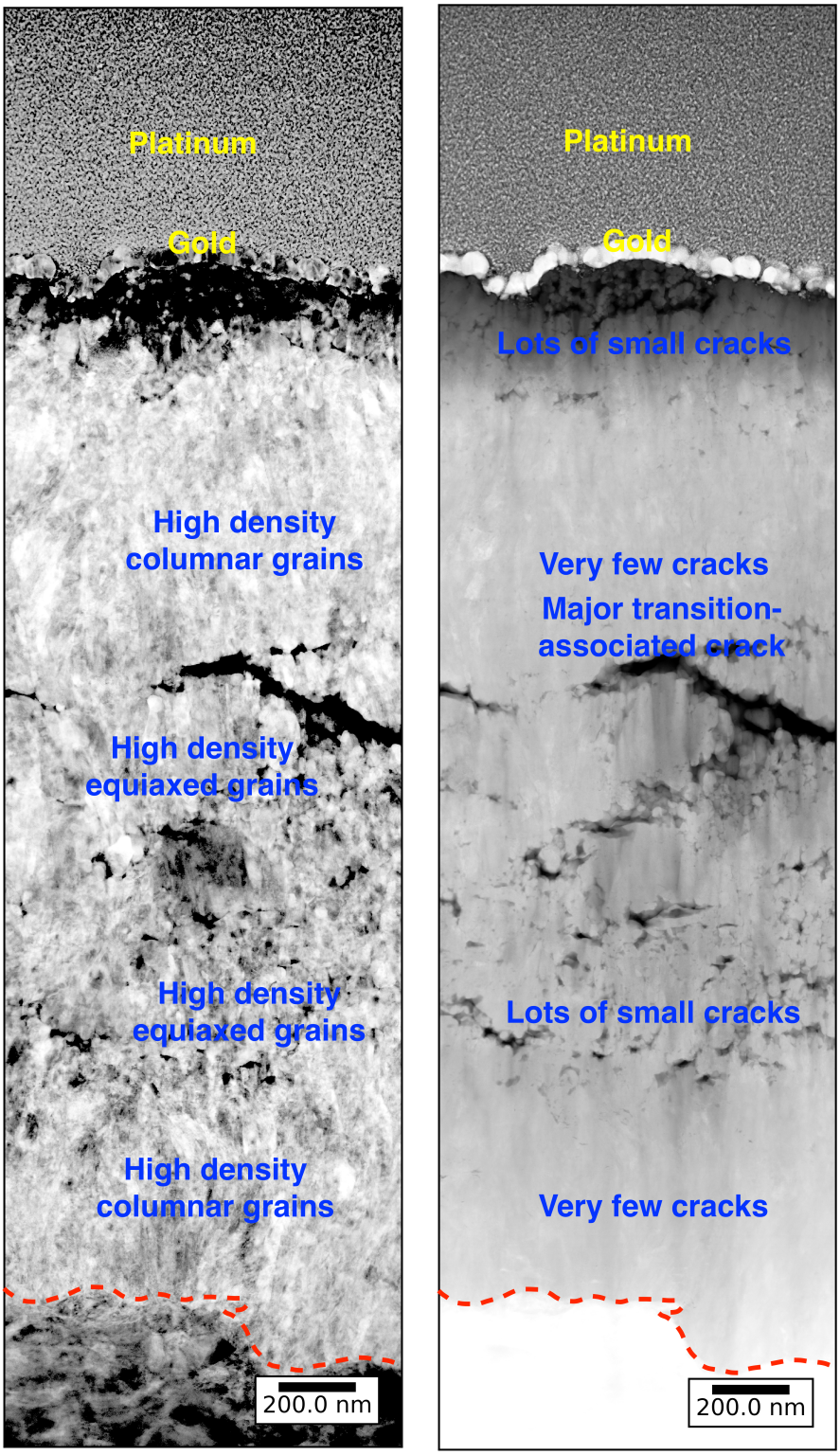
5.2.3 105-day post-transition Zircaloy-4

Figure 5.13 shows a typical HAADF STEM image of 105-day post-transition Zircaloy-4. There are many large cracks, particularly in a layer approximately halfway through the oxide. The average oxide thickness of this sample is approximately 2.8 µm thick. Particularly many hydrides are present in the metal. These may be difficult to see on the HAADF overview image, as they are present nearly everywhere in the metal, more so than I have seen in the ZIRLO samples.

The DF and HAADF images in montage in figure 5.14 show that this sample of 105-day Zircaloy-4 has an oxide thickness of approximately 2.9 µm. This is very close to the 2.97 µm oxide thickness expected from the weight gain measurement. This implies that the region is probably locally in post-transition. Three TEM foils were successfully thinned for this sample.

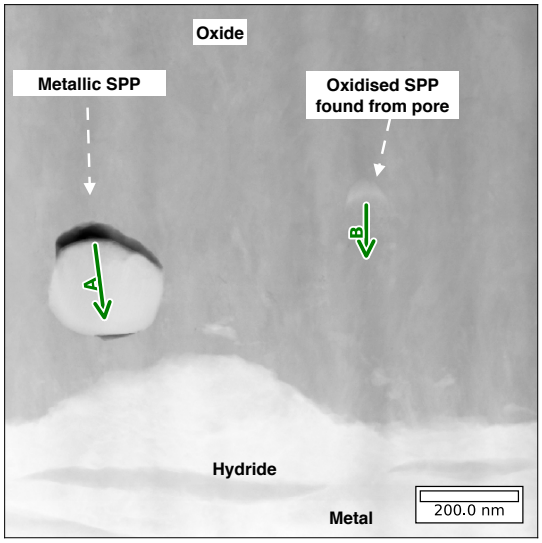
EDS analysis was not performed in the montaged region, but no SPPs appear to be present from the HAADF or DF images. Like with the other Zircaloy-4 samples, the columnar grain structure is clearer than on the ZIRLO samples, seen for the 135-day ZIRLO sample previously in figure 4.11. The oxide structure is similar in that the oxide close to the metal-oxide interface is dominated by columnar grain structure. The equiaxed grains are similar to those found on the other samples, with sizes less than 50 nm The oxide appears to maintain a layered structure of first columnar, then equiaxed and finally columnar grains. This is not unlike what Ni [69] found when studying recrystallised ZIRLO. In similar fashion I find that cracks tend to have small amounts of equiaxed but mainly columnar oxide around them.

Figure 5.15 shows a region near the metal-oxide interface. One SPP is clearly present (indicated by an "A") less than 100 nm from the metal-oxide interface by the Z-contrast present on the image. To its right, another SPP is barely visible, indicated by a "B". It was made apparent by the characteristic pore formed on top. The existence of the pore, which is associated with the slower oxidation of SPP versus the matrix and the fact that the Pilling-Bedworth ratio of Zr is larger than one, suggests that this type of $Zr(Cr, Fe)_2$ SPP does not expand as much as the matrix when oxidised.

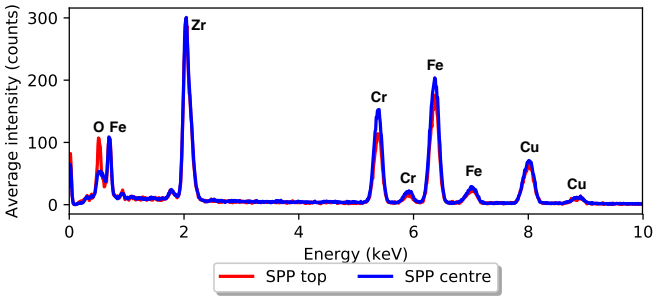


(a) **(b)**

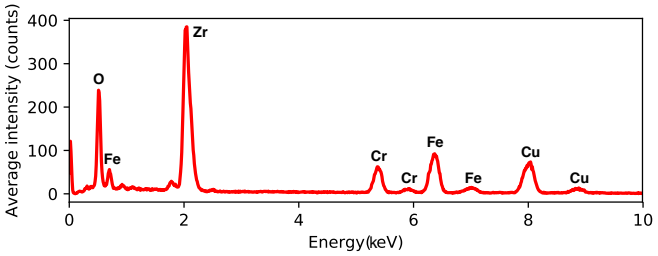
Figure 5.14: DF (a) and HAADF (b) STEM montage of the oxide on a 105-day post-transition sample of Zircaloy-4. The metal-oxide interface is highlighted in red.



(a) HAADF survey image.



(b) EDS spectra from line A taken at the top third of the SPP (red, "SPP top") closer to the oxide surface, and at the bottom two thirds of the SPP (blue, "SPP centre"). The oxygen content is twice as high near the top, despite the large pore present above it.



(c) EDS spectrum from line B averaged across the line profile in the SPP region. The oxygen and zirconium content is much higher than on this SPP than on in line A.

Figure 5.15: EDS results from a metallic (A) and oxidised (B) SPP within 300 nm from the metal-oxide interface on post-transition 105-day sample.

EDS analysis of these SPPs shows that they are both $Zr(Cr, Fe)_2$, whilst the metallic SPP has twice as high oxygen content in the top third of the SPP compared to the bottom two thirds. This is despite the large pore above it. Cracks and pores like these are normally thought to prevent the progress of oxygen (due to their frequent appearance above unoxidised undulations near the metal-oxide interface). The oxygen content could have come from the oxygen-saturated metal that existed around the SPP before it became oxidised, although it is surprising that the rest of the SPP has a lower content.

The second SPP was not visible on a regular HAADF image, due to it being oxidised, but was confirmed by applying ICA to EELS low-loss mapping, as seen in figure 5.16. In fact, across the three TEM samples studied, only one SPP was found within the first 500 nm of oxide. This is most likely just an observation due to low statistics of samples as many SPPs have been measured in Zircaloy-4 oxides previously [69]. There are likely to be SPPs near the surface of the oxide in the material adjacent to the liftouts shown in this thesis. With the advent of simultaneous EDS and 3D-FIB-slicing, this should be straightforward to confirm.

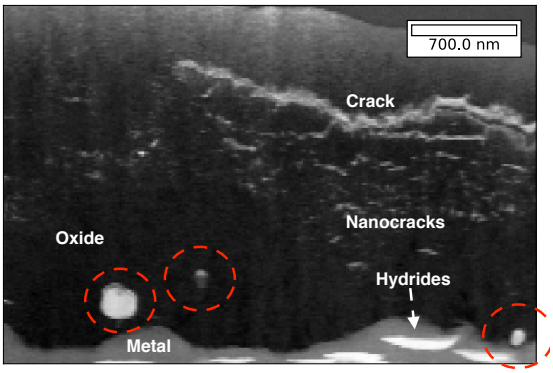


Figure 5.16: ICA result of low-loss EELS showing the only SPPs present on a sample of post-transition 105-day Zircaloy-4. All three SPPs are very close to the metal-oxide interface.

5.3 Low-loss EELS analysis of Zircaloy-4

The low-loss spectra from the various regions on the samples of Zircaloy-4 have been collected in figure 5.17. There appear to be three separate peaks in the

	Peak 1 (eV)	Peak 2 (eV)	Peak 3 (eV)
Hydride (ZrH)	18.1		40.8
Metal (Zr)	16.7		41.3
Oxygen-saturated metal (Zr(O))	17.9		41.0
Suboxide (ZrO)	14.8		41.4
Oxide (ZrO_2)	14.5	26.2	41.8

Table 5.2: Peak positions of the plasmon peaks for pre-transition 3-day Zircaloy-4.

plasmon spectrum, two of which are present in all regions. Table 5.2 lists the energy loss of the highest intensity of each peak for hydrides, metal, oxygen-saturated metal, suboxide and oxide for Zircaloy-4.

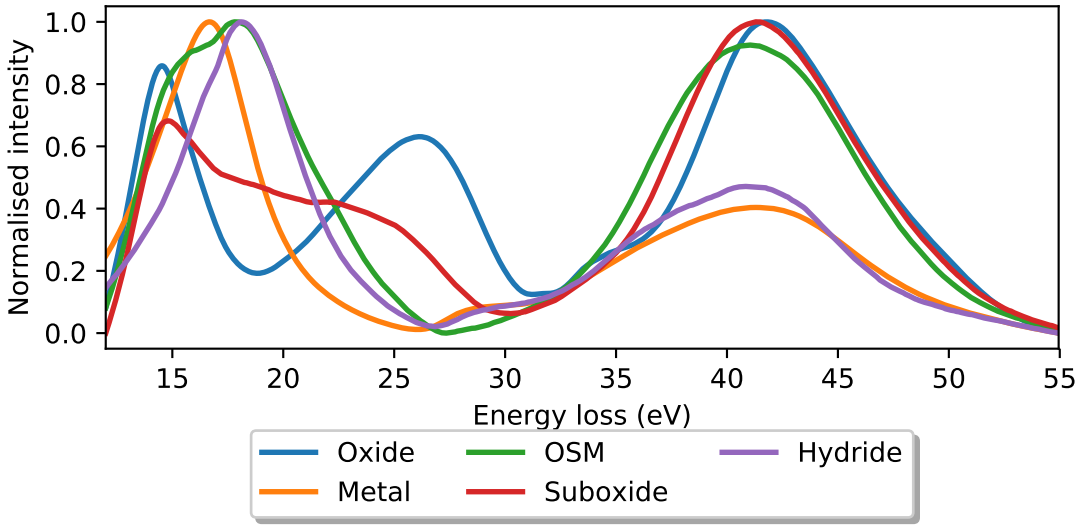


Figure 5.17: Normalised EELS spectra from selected regions on pre-transition 3-day Zircaloy-4. The oxygen-saturated metal is labelled "OSM".

The first peak is at 16.7 eV in the metal, but shifts left to lower energy loss going from metal to oxide at 14.5 eV. The intermediate oxygen phases have very different shapes to the metal and oxide. The second peak, found only in the oxide (although it appears as there could be peak overlap between several features for the suboxide) is found at 26.2 eV. Finally, the third peak, found around 41.0 eV is strong and approximately similar for all the oxygen-containing regions, whereas it is much weaker for the metal and hydride peaks. The hydrides and metal have very similar plasmon peaks, but the first peak is shifted 1.4 eV to higher energy loss.

5.3.1 Plasmon peaks comparison to ZIRLO

The values for the plasmon peaks vary slightly between ZIRLO and Zircaloy-4. This can probably be explained due to slightly poorer calibration of the EELS spectrometer for the ZIRLO samples. As the microscope was likely calibrated better for the sessions spent analysing Zircaloy-4 than for the ZIRLO, I have chosen to compare the values measured for this alloy to the literature. Table 5.3 compares my results to the values measured and compiled by Annand et al. [156]. The values are very similar, particularly close to the theoretical values calculated through DFT calculations by Nicholls et al. [94]. Variations in reported values may be due to the lack of a standardised method for defining the centre of the plasmon peaks, differences in energy resolution of the microscopes, or variations in the alignment of the energy filters used to measure the spectra.

	Metal (Zr)	Oxide (ZrO2)	
	Peak 1 (eV)	Peak 1 (eV)	Peak 2 (eV)
This work	16.7	14.5	26.2
Annand et al. [156]	17.8	15.7	27.3
Prieto et al. [170]	16.3	14.3	26
Palacio et al. [171]	15.9	13.9	27.6
Axelsson et al. [172]	16.2	13.8	27.3
Frandon et al. [173]	16.9	14.8	26
Nicholls et al. [94]	16.8	14.4	25.4

Table 5.3: The first two plasmon peak positions compared across the literature.

5.3.2 Combined suboxide and oxygen-saturated metal region

The thickness of the combined oxygen-saturated metal and suboxide region was measured for Zircaloy-4 in the same way as it was for ZIRLO in Chapter 4. The results, shown in figure 5.18, show thin regions for the 3-day early pre-transition and 105-day early post-transition samples. Both distributions peak around 40 nm, with the 105-day sample having some regions with thickness up to 150 nm. The 45-day pre-transition sample shows a much wider distribution of thickness of the

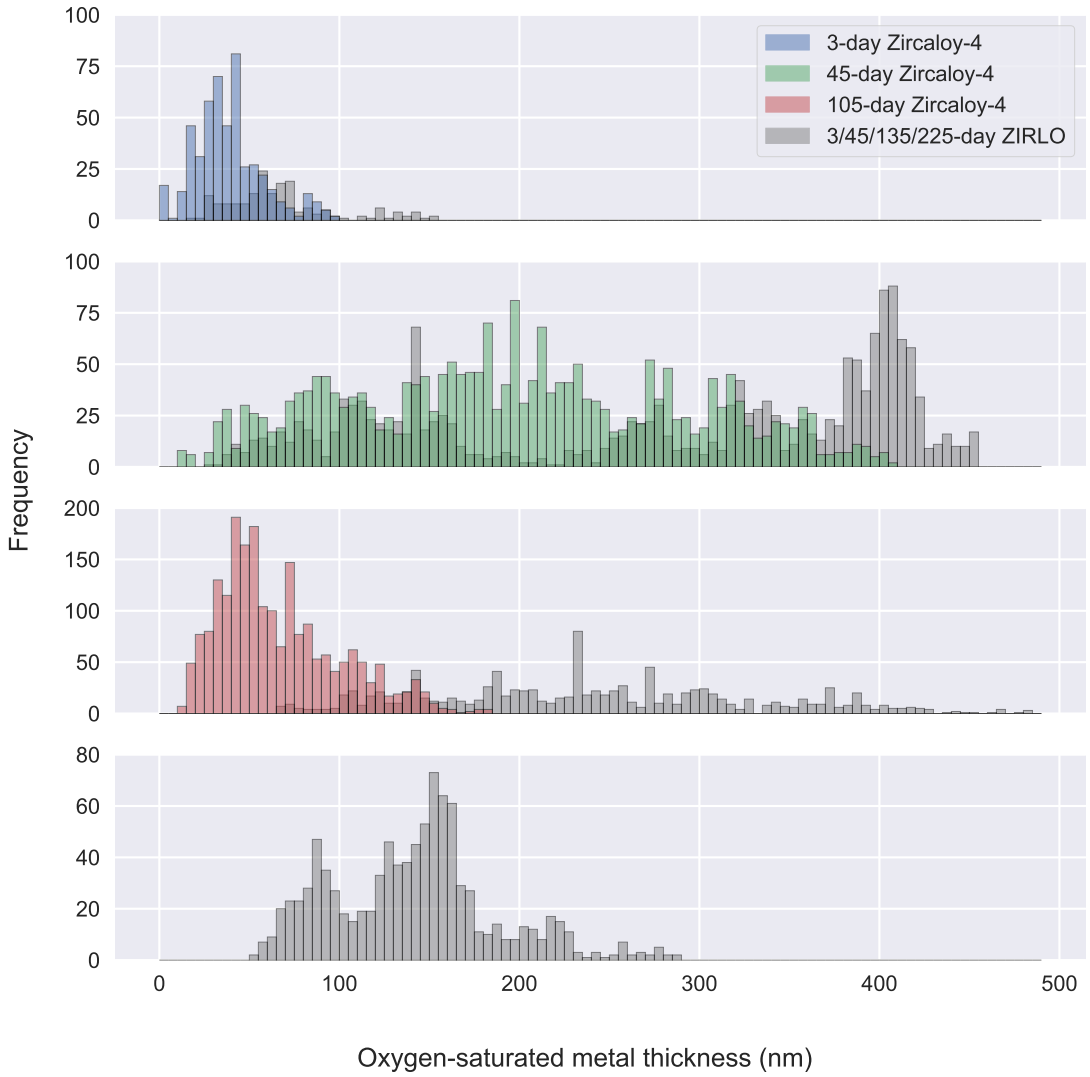


Figure 5.18: Histogram comparison of the oxygen-saturated metal thickness for several samples of oxidised Zircaloy-4.

region, with thicknesses between 20 and 400 nm, peaking at 200 nm. The average thickness of the oxygen-saturated metal is shown in table 5.4.

5.4 Discussion

5.4.1 The inaccuracy of "pre"- and "post"-transition descriptions

For the 3-day sample, the thickness from the average oxide thickness estimated from the weight gain data is rarely found anywhere in the milled material. This suggests

Time (days)	Weight gain ($mg\,dm^{-2}$)	Instantaneous weight gain ($mg\,dm^{-2}\,d^{-1}$)	Average combined thickness (nm)
3	11.37	1.04	38
45	24.46	0.15	198
105	44.54	0.63	66

Table 5.4: The average combined thickness of the oxygen-saturated metal and suboxide for the various samples of Zircaloy-4, listed against their weight gain as well as the instantaneous weight gain calculated from the weight gain data.

that the milled region was relatively ahead of the rest of the oxide in terms of weight gain. The binomial distribution of the 45-day sample suggests that this sample was removed from autoclave at a point where it had partly undergone transition. The central position of the weight-gain mean (green dashed vertical line on figure 5.2) indicates that this weight gain measurement is possibly representative of the sample, although more measurements from different regions of the sample would be needed to confirm this. Like for ZIRLO, these results emphasise the fact that measurements taken from the same sample in different regions can be under very different conditions, for instance pre- versus post-transition. Similarly, measurements from two different samples that have undergone different conditions, can show the same result.

The point of transition is much clearer on the Zircaloy-4 samples than it is on the ZIRLO samples. This could either mean that the physical process of transition happens more slowly on ZIRLO, or that the local transitions in oxidation rate of the ZIRLO sample are more out-of-phase. The possibility of the out-of-phase behaviour accounting for the apparent linear behaviour of post-several-transition oxidation is suggested by Bryner et al. [76], and could be starting earlier on ZIRLO than Zircaloy-4, explaining the less abrupt change at transition present on the ZIRLO graph. This implies that a larger fraction of the 105-day Zircaloy-4 sample may be in post-transition than on the 135-day ZIRLO sample. This argument is supported by looking at long-term oxidation. In the long-term weight gain analysis done by Hillner et al. [53] referred to in section 2.4.3 of the literature review, values for B, an empirical constant, and Q, the activation energy, had been calculated for what they

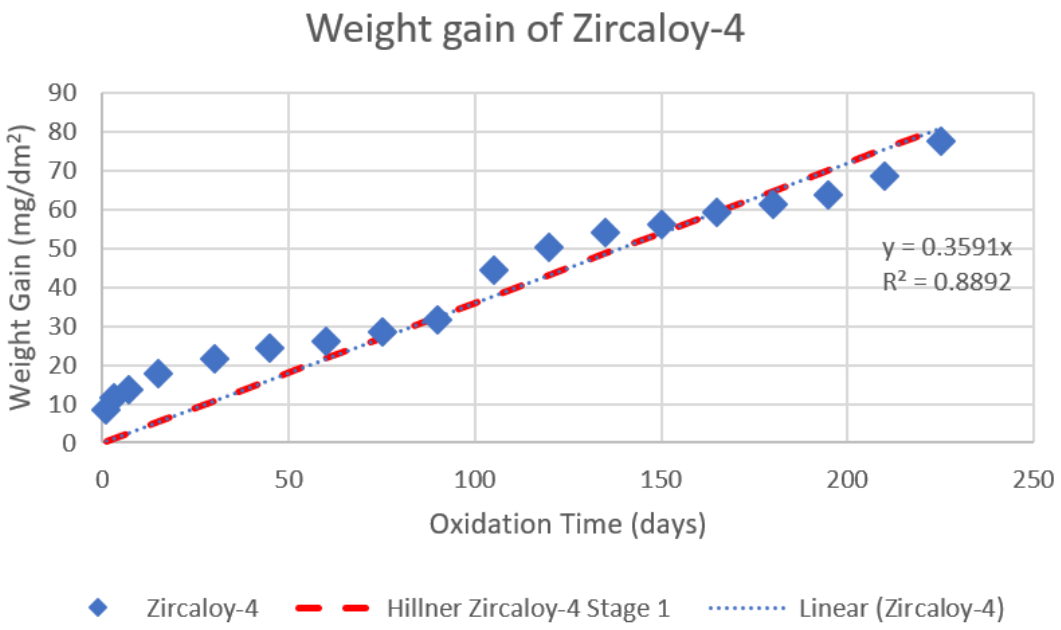


Figure 5.19: The weight gain of Zircaloy-4 fitted with a trend line going through (0,0). Equation 2.3 is also plotted using values for the linear (n=1) oxidation regime at 360 °C by Hillner et al. [53]

term "Stage 1" of the Zircaloy-4 oxidation. For the temperature of 360 °C studied in this thesis, equation 2.5 results in a value for k (the prefactor in equation 2.4) of 0.36 mg d^{-1}. The Zircaloy-4 data previously shown in figure 5.1 is plotted with a linear trend line fixed through (0,0) in figure 5.19. The linear weight gain calculated from the Hillner data is also plotted in dashed red. The Hillner result matches extremely well with the Zircaloy-4 dataset shown in this thesis, and the trend line fitted to the weight gain results in a slope of k=0.36, matching the Hillner data perfectly. This clearly shows that the linear trend of post-transition oxidation rate is just the normal cyclical transition behaviour, but out-of-phase across the oxide, in line with the previous argument. Additionally, it shows that the "Stage 1" oxidation referred to by Hillner does not just apply to "post-transition" oxidation behaviour, but in fact represents the entire "early" (on the scale of years) oxidation behaviour.

5.4.2 Oxide microstructure comparison with ZIRLO

The oxide microstructure of the two alloys is generally similar for all oxidation times. Starting at the top, both alloys show a very porous surface oxide, consisting

either of connected large pores or cracks connecting to the top surface. The next approximately 500 nm oxide is perhaps surprisingly intact and without large pores, except for certain cases. The lack of cracks in this region can be attributed to low strain due to the fact that the oxide is allowed to expand out towards the surface in the early days of oxidation. From about 1 µm in, the first layer of cracks typically associated with transition are encountered. For the pre-transition samples these cracks are consistently found near the metal-oxide interface. For all samples, cracks near the metal-oxide interface are typically found above undulations of the metal-oxide interface. They are likely caused by the stress difference due to the Pilling-Bedworth ratio of the oxide, as argued in the discussion of cracks in section 4.5.

The columnar oxide in both alloys have an aspect ratio of about 5, which agrees with Yilmazbayhan et al. [65]. However, de Gabory et al. [163] report an average aspect ratio close to 7 for both Zircaloy-4 and ZIRLO, with a range between 4 and 12. It is unclear why they report different values. A possible explanation is that the grain growth occurs at various angles, and that the grain growth was more aligned with the plane of the TEM-foils in the samples of de Gabory. Alternatively, one can consider why the columnar grains do not grow indefinitely. Motta et al. [197] suggest that the reason for the termination of columnar grain growth is stress accumulation due to small mismatches between the grain growth direction of the various grains. This is partially supported by TEM t-EBSD analysis done by Garner et al. on Zircaloy-4 [87]. They show that there is a considerable spread in grain orientations in the oxide, and therefore grains will not be able to grow beyond a critical size.

Of the samples studied in this Chapter, the oxide-side of the metal-oxide interface is typically found to consist of columnar oxide, although the 3-day sample has a mix of equiaxed and small columnar grains at the interface. The presence of columnar oxide at the interface is particularly evident for the 45-day and 105-day cases, and has been previously shown by Park [137] to be a typical feature of Zircaloy-4. Columnar oxide at the metal-oxide interface was also found by Wadman [198] to be a characteristic of Zircaloy-4 alloy variations with good corrosion-resistance. This is in agreement with most of the results reported in the previous Chapter on

ZIRLO, with one exception. A region of metal-oxide interface on the 45-day ZIRLO sample (shown on figure 4.9) near an oxide "finger" reaching into the metal mainly consisted of equiaxed oxide. Most of the rest of the interface consisted of columnar oxide. The finger growing into the oxide may be the result of fast oxidation. I therefore speculate that equiaxed oxide may be the result of the fast growth, which can explain the layered behaviour seen on multiple-post-transition samples. More snapshots of the oxidation front over transition is necessary to confirm this.

The most noticeable difference between the two alloys is for the 3-day samples. The Zircaloy-4 3-day sample displays far more cracking in the upper half of the oxide than the ZIRLO does. Looking only up to transition, this is surprising, as the weight gain up to the first transition is lower for Zircaloy-4 than for ZIRLO. However, in the long-term the weight gain of Zircaloy-4 is higher than for ZIRLO, which could be caused by increased cracking. If the Zircaloy-4 oxide cracks more rapidly under stress than the ZIRLO oxide, this could explain the very sharp rise in the weight gain from transition, which is much sharper than for ZIRLO.

In the oxide (especially close to the metal-oxide interface) voids are often seen above SPPs on the side away from the metal-oxide interface. This has been previously shown by many researchers [95, 163, 178] to be a characteristic of a non-oxidised SPP. The void is attributed to the lack of volume expansion from oxidation of the SPP. But since the oxide is extremely compressive (as previously argued, the stress must be present to stabilise the formation of tetragonal oxide grains), it may seem unlikely that the voids will form under these conditions. Tejland et al. [199] offer a suggestion as to what happens: Since the SPP oxidised slower than the surrounding matrix, the particle represents an absence of volume increase. This absence gives rise to tensile stresses in the oxide surrounding the particle. They suggest that this tensile stress can be relieved either by forming a void above the SPP, or by forming a crack further up the oxide. For $Zr(Fe, Cr)_2$ SPPs that appear fully oxidised, but also have a void above them, Annand et al. [178] argue that it is possible that only the zirconium has oxidised whilst the Cr and Fe have not. This would lead to a reduction in the Pilling-Bedworth ratio and explain the formation

of a void. In their paper, Annand et al. measure the elemental composition by DualEELS, and show segregation of iron as the Zr and Cr oxidise. To complement the theory of Fe not oxidising, it could be interesting to perform core-loss EELS on the SPPs, measuring the Fe L_3 and L_2 edges and their white lines at a low dispersion. Measuring the shift and area of the white lines, as is done in this thesis for Zr, could be used to track the oxidation state of the Fe.

5.4.3 Combined suboxide and oxygen-saturated metal region

The oxygen-saturated metal layer at the metal-oxide interface is found for Zircaloy-4 as it was for ZIRLO. Since the 45-day sample was in the slow domain of the oxidation, and the 3-day and 105-day were both in the fast domain of oxidation (see the weight gain curve in figure 5.1 for reference), this suggests that during the slow oxidation the oxygen-saturated layer builds up at the metal-oxide interface. Once transition happens, the oxygen-saturated metal layer is consumed quickly, resulting in fast oxide growth.

This is in agreement with Annand et al. [156], who showed clear correlation between fast oxide growth and small thickness of "oxygen-loaded metal" and much larger thicknesses of Zr(O) where the oxide growth is slower. It remains unclear exactly how the instantaneous oxidation rate is changed by the presence of oxygen-saturated metal. Is the oxygen-saturated metal consumed nearly instantaneously once certain conditions are met? Or does the oxide front "catch-up" with the oxygen-saturated layer while the layer is still growing?

In contrast to the oxygen-saturated metal layer, the suboxide above it does not show an obvious trend in increasing thickness before transition on these samples. Instead it varies in thickness along the metal-oxide interface, sometimes clearly visible and sometimes not. This agrees with Hu et al. [95], who characterised large regions of the metal-oxide interface by the transmission Kikuchi diffraction technique to find that there was a large variation in thickness, but disagrees with de Gabory et al. [163] for ZIRLO and Zircaloy-4. In the study done by Hu, the

suboxide grains are shown to vary in size, from several hundred nm to below the 10 nm spatial resolution of the technique, without a clear change from pre- to post-transition. The suboxide grains are shown to be hexagonal, and most, but not all, inherit their orientation from the metal grain from which they formed. Meanwhile, bright-field TEM images by de Gabory show what they describe to be a "significant" trend of decreasing thickness of the layer between late pre- and early post-transition. Since ZrO grains are not always seen at the interface and can vary significantly in thickness, one can speculate that stress is also an important component. ZrO grain formation is an indication of the tensile stress existing in the metal at that region. More STEM studies with a method of clearly distinguishing ZrO (such as the previously described ICA method on low-loss EELS) are needed to clarify whether ZrO changes substantially across transition, and to determine the role ZrO suboxide plays in the mechanism of oxidation.

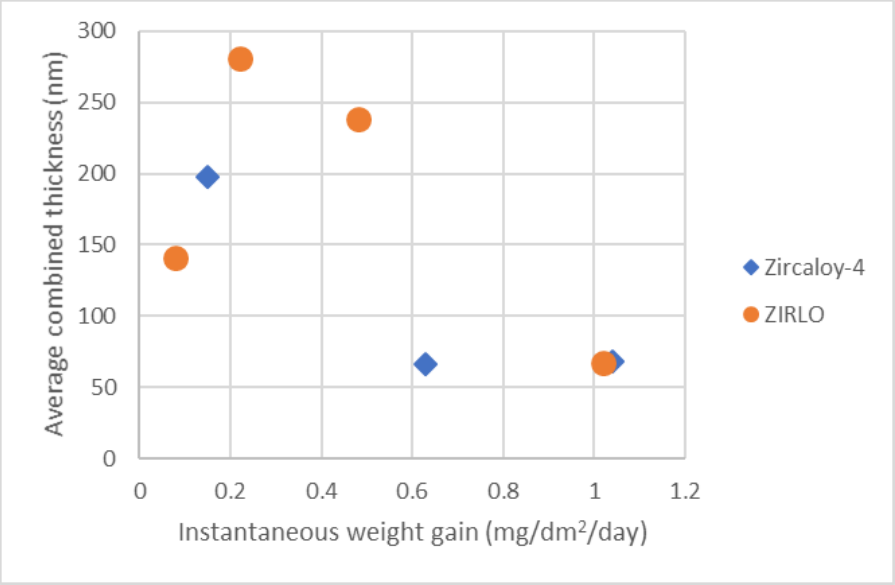


Figure 5.20: Comparison of the instantaneous weight gain against the average combined thickness of suboxide and oxygen saturated metal for ZIRLO and Zircaloy-4

In Chapter 4, the correlation between a thick combined oxygen-saturated metal and suboxide layer and high corrosion resistance was presented, which has been published [200]. Figure 4.30 was presented showing the relation between the average thickness of oxygen-saturated metal and the instantaneous weight gain for samples

of ZIRLO, as-received Zr-1Nb and annealed Zr-1Nb. Here it was shown that when the rate of weight gain is high, there is less formation of the combined suboxide and oxygen-saturated metal layer. As the rate of oxidation slows, the rate of diffusion of oxygen is high enough to build up such a layer, and the weight gain slowly increases. At the point of transition, we speculate that the layer is quickly consumed in the production of fresh oxide. The measurements of the combined region thickness on Zircaloy-4 (shown in table 5.4 and compared to ZIRLO in figure 5.20) are in agreement with the results for ZIRLO and Zr-1Nb, further emphasising the correlation. This suggests that the same mechanism of slow and rapid oxide growth applies to the three alloys, and may be a general mechanism for oxidation of zirconium alloys. Interestingly, the average combined thicknesses are lower in all cases for Zircaloy-4 than for ZIRLO. Zr-1Nb, which has a very high corrosion resistance, displays much higher values. As Zircaloy-4 displays poorer corrosion resistance than ZIRLO (as seen in figure 5.1), the average thickness of the combined suboxide and oxygen-saturated metal may be another measure of corrosion resistance, where higher is better.

The impact of the suboxide and oxygen-saturated metal layer on the oxidation mechanism is discussed by de Gabory et al. [162] They argue that the fact that some oxygen is used to form the saturated layer should slow down the formation of stoichiometric ZrO_2, but not by much due to the relatively low oxygen concentration in the layer. However, they also note that the Zr metal present at the interface can act to reduce the stress in the oxide by plastic deformation. Further, since the oxygen build-up in the metal will make the metal harder and more resistant to plastic deformation [201], this will result in the transfer of higher stress to the oxide and increase the likelihood of cracking, giving way to transition. This seems to me an intuitive hypothesis, which would be of interest to study further. Since the oxide appears well-organised and free of cracks near the interface in pre-transition areas, stress can not be relieved. The lack of equiaxed oxide near the interface (which is associated with porosity and thus stress-relaxation) further strengthens this hypothesis.

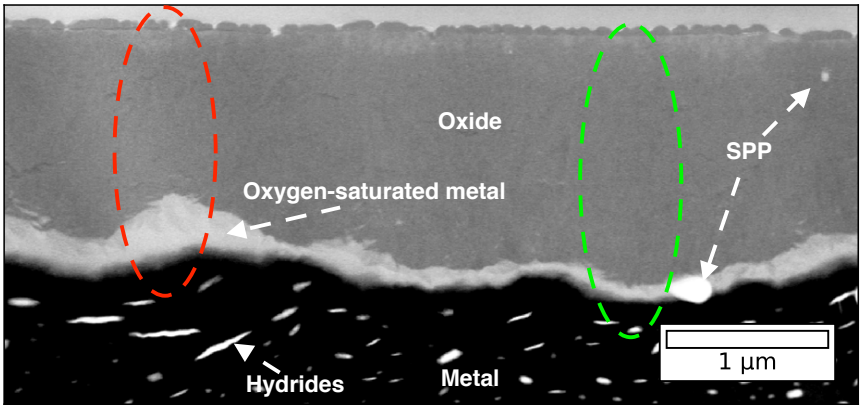


Figure 5.21: ICA loading of low-loss EELS on 45-day pre-transition Zircaloy-4. The red region has low oxide thickness and high oxygen-saturated metal content whilst the opposite is the case for the green region.

To show an example that the oxygen-saturated layer builds up in regions of thin oxide, figure 5.21 shows the case for 45-day Zircaloy-4. Here the region indicated with a red dashed circle has a low oxide thickness of 1.0 µm and an oxygen-saturated layer of 360 nm. The region highlighted in white has a high oxide thickness of 1.6 µm but an oxygen-saturated metal thickness of only 85 nm. This observation was repeatedly found throughout the project.

However, in contrast to the previous observations, there has been published research where the trends described are not observed. Tejland et al. [199] studied the oxidation of Zircaloy-2 tube, and characterised the oxygen content in line profiles by EDS on sample oxidised for 3, 15 and 150 days. They describe that there is essentially no variation between the samples, with all line profiles showing a combined suboxide thickness of about 200 nm. The paper only describes a few line profiles, and is done on far fewer TEM samples than has been studied in this thesis. It is likely that samples happened to be taken from regions that were locally in medium to late pre-transition, where the rate of oxidation is slow and the thickness of oxygen-saturated metal is building up.

The formation of the various phases at the metal-oxide interface are undoubtedly important parts of the general oxidation mechanism. Here I have shown that Zircaloy-4 and ZIRLO both show an inverse relationship between the instantaneous

oxidation rate and average combined region thickness, contributing to the current understanding of the oxidation mechanism.

5.4.4 Hydride formation in thin foils

As previously mentioned, hydrides are present in the metal near the metal-oxide interface on all samples. The general shape of the hydrides is in good agreement with previous TEM observations of hydrides both in ZIRLO [163] and Zircaloy-4 [202]. In comparison with the ZIRLO low-loss data, at first glance there are no outstanding differences. On the ICA-decomposed loadings, most noticeable are the hydrides, which are present in large numbers for Zircaloy-4 as they were for ZIRLO. As commented in the literature review in section 2.6, there is concern that hydrides are nucleating not from conditions arising during autoclave cooling, but from sample preparation, in particular from use of FIB. Ding et al. [142] showed an increase in formation of hydrides in pure Ti and Ti alloys, as a result of both sample preparation in water or acid, as well as from FIB thinning of the specimen. Both local enrichment of hydrogen and rearrangement of the host metal atoms are necessary for hydride precipitation. Since diffusivity of metal atoms in zirconium is very small [203], the hydrides must be formed either by a shear or martensitic mechanism. Ding et al. find that hydrogen can be sourced from the bulk of the sample, or by absorption to the sample surface. Ion sputtering by the FIB is known to cause the formation of defects (vacancies, dislocations and dislocation loops), phase transformation and amorphisation of the sample. These defects could cause metal atoms to rearrange and provide nucleation sites for the hydrides. A similar study for Zr alloys would be very useful. There is much literature being produced on the study of hydrides in zirconium alloys, but no large-scale effort into the investigation of the effect of sample prep is known to me. In particular, it is my suspicion that very fine thinning of the FIB sample can further increase hydride content over a reasonably thin specimen.

5.4.5 Why does the sawtooth oxide form its shape?

In this Chapter, the interface of the metal and oxide has been shown to be of varying roughness. There exist regions of the oxide that have oxidised faster causing the interface to lie much further into the metal, up to 1.3 µm as shown in figure 5.12. In addition to the variation in surface roughness, there exists a variation in the shape of suboxide formed at the interface. There is a combination of rounded grains as well as the more noticeable sawtooth shape. Tejland et al. [21] suggests that the varying shape is the result of a 2D slice (i.e. FIB sample) cut through a 3D "cauliflower" shape. Through private communication [204], Annand indicates that suboxide observed by her is more "hilly" and less "jagged". She suggests the following: "There are micro-scale undulations along the metal-oxide interface, made up of advanced and delayed portions of the oxide front. Where the oxide front is delayed, there is significant growth of suboxide in line with the "cauliflower" model." It still remains unclear why the suboxide forms such "fingers" into the metal. Puchala et al. [205] and Nicholls et al. [94] performed theoretical DFT calculations on the structure of suboxides. They both agree that the ZrO monoxide phase is hexagonal. Puchala found a whole range of additional ZrO_x candidates. If several of them coexist at the metal-oxide interface, mismatch due to different crystal structures and orientations may explain the variation in grain morphology along the interface. Additionally, different oxygen diffusion rates through these grains may affect oxygen ingress to the metal.

The size and geometry of the three-dimensional suboxide shape is difficult to image. Since high-resolution electron microscopy techniques always work in transmission, other techniques may provide better insight. It is possible that atom probe tomography can provide a better indication of its 3D structure, but that would require increases in the sample size that the technique can currently handle. Alternatively, high-resolution NanoSIMS may provide another means of characterisation, although the fine sizes of the suboxide may be beyond the resolution of the instrument.

5.4.6 The influence of alloying elements on the corrosion of zirconium alloys

In the past two Chapters, ZIRLO and Zircaloy-4 have been studied in detail. In the next Chapter, Zr-1Nb is also studied. The main difference between these alloys is the variation in alloying additions to zirconium. As per table 2.1 in Chapter 2, the major differences between ZIRLO, Zircaloy-4 and Zr-1Nb are that Fe is present mainly in Zircaloy-4 and ZIRLO, Cr is only present in Zircaloy-4, Nb is only present in ZIRLO and Zr-1Nb, and Zr-1Nb is Sn-free.

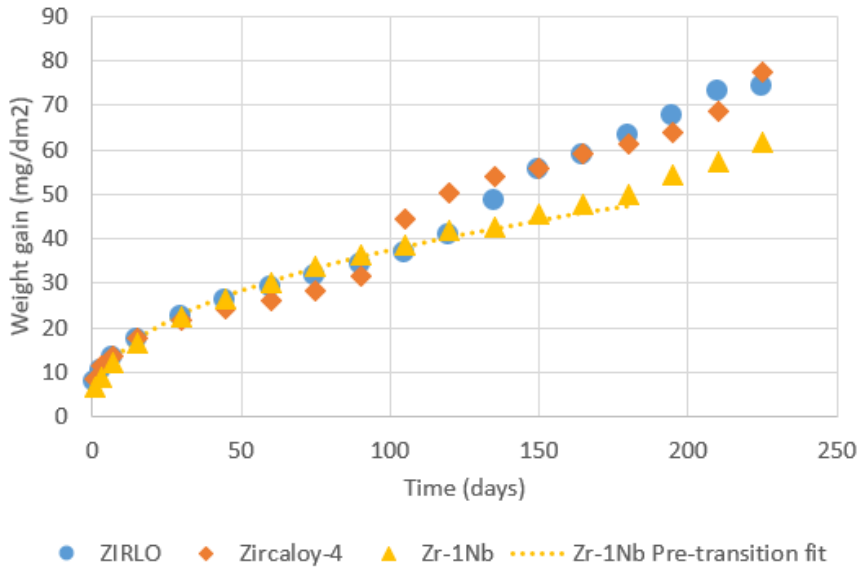


Figure 5.22: Weight gain of the ZIRLO, Zircaloy-4 and Zr-1Nb samples oxidised as part of the MUZIC-2 project. The yellow dashed curve indicates the fit of the Zr-1Nb pre-transition weight gain to a power law with $k = 6$ and $n = 0.4$.

While the weight gain of the ZIRLO and Zircaloy-4 samples studied in this thesis showed very similar values, ZIRLO was designed to be the successor to Zircaloy-4, and has previously been shown to have better corrosion resistance [10, 206], as discussed in Chapter 2. As seen in figure 5.22, from the samples studied in the MUZIC-2 project, Zr-1Nb displays a significantly improved corrosion resistance compared to ZIRLO and Zircaloy-4. This is also seen elsewhere in the literature [40]. On our samples of ZIRLO and Zircaloy-4, the pre-transition weight gain curves displayed approximately cubic oxidation kinetics, with k = 7.3 and 8.2 $\mathrm{mg\,dm^{-2}\,d}$

and n = 0.33 and 0.29, respectively. A set of Zr-1Nb samples also oxidised as part of the MUZIC-2 program show closer to parabolic oxidation kinetics, with k = 6 and n = 0.4. These differences in composition and corrosion resistance can, together with literature, be used to explain the influence of the most important alloying elements on the corrosion of zirconium alloys.

Understanding the impact of alloying additions is complicated by the lack of a clearly known rate-limiting mechanism for oxidation. As discussed in Chapter 2, the rate-limiting step is likely to be either the the diffusion of oxygen anions through the oxide into the metal, or the diffusion of electrons out to the water. In order for an alloying addition to impact the oxidation behaviour, it should impact the rate-limiting step. Which mechanism is rate-limiting is still under debate [207, 208].

By substituting Zr in an oxidation state of 5+, Nb is generally assumed to suppress the formation of oxygen vacancies in the oxide [208–210]. This reduces oxygen ion conductivity and, if the rate limiting process is oxygen transport, slows oxidation. Some part of this effect should be visible in the weight gain of ZIRLO compared to Zircaloy-4, although, by the weight gain comparisons shown in figure 5.1, this is not the case, at least over the relatively short time-frame the alloys were exposed to water. The lack of improvement from the Nb addition is possibly due to the presence of Sn. As discussed in Chapter 2, Sn was originally added to zirconium to suppress the detrimental effect of small amounts of nitrogen on the corrosion [2, 24, 127]. Sn in a Nb-containing Zr alloy is suggested to counter the Nb oxygen vacancy suppression [210], crippling the corrosion resistance provided by Nb. This is what is seen when comparing alloys such as ZIRLO and Zr-1Nb, where the latter is nearly Sn-free and has superior corrosion resistance [40]. This argument is what led Westinghouse to select low-Sn ZIRLO as one of their major alloys [3, 211].

A study [45] of three Zr-Nb-Sn alloys with 0.92, 0.66 and 0.01 wt% Sn showed that corrosion resistance is significantly improved with reduced Sn content. This shows that the removal of Sn is the most important change in alloying with regards to oxidation resistance. There is no mention in the literature as to what the

impact of Sn-free alloys is with regard to the previously mentioned detrimental effect of nitrogen.

Space charge theory has been used to explain the cubic oxidation kinetics of Zircaloy-4 [79]. The relatively low concentrations of Fe and Cr dope the oxide, sitting interstitially [212], contributing to anion vacancies in the metal. Since oxygen is freely available to fill anion vacancies on the oxide-side of the metal-oxide interface, this causes an anion vacancy gradient to be established across the oxide layer. The gradient gives rise to an electric field that is negative in the direction of the metal. This should increase the rate of oxygen anion diffusion to the metal [49] and be detrimental to corrosion, particularly if oxygen anion diffusion is the rate-limiting step. However, if electron transport is the rate-limiting step, then Fe and Cr should be beneficial to corrosion resistance, due to the electric field [50]. The reduction in Fe content and elimination of Cr by industry in the development of ZIRLO from Zircaloy-4 suggests that there may be an improvement in corrosion resistance to be found in removing these elements. One may from this speculate that the rate limiting step is oxygen diffusion, although a study on Fe- or Cr-containing binary alloys might help clarify this. On Nb-containing alloys, Couet et al. [50] used the same space charge approach to show that aliovalent Nb substituing for Zr in the oxide, can eliminate the space-charge forming in the oxide. This reduces the electric field causing the oxidation kinetics to be closer to parabolic than cubic. This is in agreement with the weight gain measurements of the MUZIC-2 project, where the Zr-1Nb value of n was 0.4, higher than that of Zircaloy-4 and ZIRLO. With an increase in n, the improvement in long-term corrosion resistance is then given by the delayed transition point of the alloy, which occurred nearly 80 days after the other two alloys. The delayed transition point must be related to the elimination of Sn, since that is what distinguishes Zr-1Nb from ZIRLO. This implies that Sn must be strongly related to the cause of transition.

Finally, Zr-1Nb also shows a much improved reduction in the hydrogen pickup (further discussed in Chapters 6 and 7). However, this is expected as the production of hydrogen is directly linked to the oxidation, as shown in equation 2.2. A study

showing how the HPUF [207] changes with Nb content would be of interest to show the effect on the hydrogen pickup independent of oxidation rate.

5.5 Summary of results and discussion

This Chapter has given an overview of the oxidation of Zircaloy-4. I will now summarise the results and discussion, and follow with a list of the main similarities and differences between ZIRLO and Zircaloy-4.

- Zircaloy-4 was oxidised at 360 °C for 225 days. The weight gain followed a power law with k = 8.2 mg dm^{-2} d and n = 0.29 until approximately 98 days into oxidation, where, with an average oxide thickness of 2.1 µm, the sample underwent transition and the oxidation rate accelerated. By reference to data of long-term oxidation, the linear domain of far post-transition weight gain is proven to be a result of the cyclical transition behaviour becoming out-of-phase.

- The oxide and metal-oxide interface has been studied by simultaneous HAADF and ADF STEM montaging. The oxide structure is found to alternate in layers between equiaxed and columnar oxide grains. Columnar grain size is found to vary, but with a constant aspect ratio of about 5:1. For the 3-day sample the grain size is 90 nm long and 20 nm wide on average, whereas later on the typical grain size is much smaller, between 30 and 50 nm. Equiaxed oxide grain size is typically 20 nm, and is generally hard to resolve clearly due to overlap through the thickness of the samples.

- Independent component analysis (ICA) is shown to clearly separate the phases present in the sample, as shown for ZIRLO. Since low-loss EELS signals contain a relatively high amount of signal (particularly compared to core-loss), it is possible to acquire such spectrum images with a very high pixel number at the same time as acquiring regular ADF STEM images. The simultaneous acquisition of such data can allow for powerful comparisons between structural

and spectroscopic analysis in the future, at little to no cost. However, increases in data size can make handling the data awkward. Therefore it is important that new techniques be developed and elegantly implemented to handle this increase in information. Dimension-reducing techniques such as PCA and ICA are ideal for this type of processing.

- The thickness of the oxygen-saturated metal is shown to correlate strongly with transition, showing similar low thickness for samples early pre-transition and early post-transition when the oxide has been growing quickly. Higher thicknesses are found in areas where the oxide is growing slowly. This behaviour is shown to be particularly clear for the samples measured on Zircaloy-4, whilst the samples of ZIRLO displayed a much more varied distribution of oxygen-saturated thickness.The formation of oxygen-saturated metal is suggested to be strongly related to the oxidation mechanism.

- Suboxide has been identified as a complex, stress-stabilised layer at the metal-oxide interface. It is found particularly at regions of undulating metal-oxide interface, where there is high tensile stress. Mechanisms of its formation are discussed with reference to the literature. Suboxide is found to form on all zirconium alloys, including pure zirconium, suggesting that it is a general mechanism of zirconium oxidation!

- Low-loss EELS spectra of the plasmon peaks present in the metal, oxide, hydrides, oxygen-saturated metal and suboxide are presented. The peak energies of the metal and oxide are found to be in good agreement with the literature. Whilst the exact values of the ZIRLO plasmons differ slightly from Zircaloy-4 due to tuning of the microscope, the overall shape of the plasmons remains identical between the two alloys.

- The impact on corrosion of the most common alloying additions is discussed with reference to experiment and theory from the literature. The elimination of Sn is identified as the most beneficial to corrosion resistance, and a doping mechanism is identified as likely responsible.

The following are the main similarities and differences between ZIRLO and Zircaloy-4:

5.5.1 Similarities

- ZIRLO and Zircaloy-4 hit transition at approximately the same point in time, at about 100 and 98 days, respectively.
- For a given weight-gain, both alloys demonstrate a broad range in oxide thickness based on FIB analysis.
- The grain morphology of the oxides of ZIRLO and Zircaloy-4 is shown to not be significantly different. For columnar grains, an aspect ratio of about 5:1 is almost always found.
- Cracks in the oxide are typically found above undulations in the metal-oxide interface.
- SPPs of varying internal composition are found. For ZIRLO, an SPP with a layered silicon-rich structure is found. In Zircaloy-4, an SPP with similar Si-content but with a less crystalline structure is found.
- Suboxide with an oxygen concentration of 50% is found repeatedly, with both sawtooth and more rounded morphologies.
- Combined suboxide and oxygen-saturated metal thickness is found to correlate inversely with instantaneous weight gain of the sample.

5.5.2 Differences

- According to the weight gain data, Zircaloy-4 displays a much sharper point of transition than ZIRLO.
- The 3-day samples of Zircaloy-4 display much more cracking in the top half of the oxide than for ZIRLO.

- The combined suboxide and oxygen-saturated metal thickness is shown to be larger for ZIRLO than for Zircaloy-4. With references to similar observations in the literature, it is argued that a larger average combined thickness is correlated with slow oxidation.

This concludes the STEM analysis on ZIRLO and Zircaloy-4. In the next Chapters, the hydrogen pickup of several zirconium alloys will be discussed.

6
Hydrogen pickup

Contents

6.1 Introduction 186
6.2 Materials 186
6.3 Results 188
6.3.1 A note on sample-preparation 188
6.3.2 Typical NanoSIMS results 189
6.3.3 Using the SE image to identify the oxide 192
6.3.4 Proving that the deuterium signal is not from natural H_2O 194
6.3.5 Hydrocarbon contamination from resin 195
6.4 Overview of alloys 197
6.4.1 125-day pre-transition ZIRLO 197
6.4.2 225-day post-transition ZIRLO 200
6.4.3 225-day pre-transition Zr-1Nb 200
6.4.4 585-day post-transition Zr-1Nb 203
6.4.5 Hydrides compared between STEM and NanoSIMS . . . 203
6.5 High-resolution oxide analysis 205
6.5.1 Peak of hydrogen in first part of the oxide 205
6.5.2 Pre-transition 125-day ZIRLO 206
6.5.3 Pre-transition 225-day Zr-1Nb 208
6.5.4 Pre-transition 61-days Zircaloy-4 208
6.5.5 Post-transition 225-day ZIRLO 210
6.5.6 Post-transition 585-day Zr-1Nb 213
6.5.7 Barrier to hydrogen in oxide 214
6.5.8 SEM imaging of post-SIMS areas 215
6.5.9 Deuterium hot-spots in the oxide 217
6.5.10 FEGSEM and EDS of hot-spot 219
6.5.11 Deuterides in the metal 220
6.6 Discussion 223

6.6.1 Comparison of alloys and impact of alloying additions on hydrogen pickup 223
6.6.2 Oxide barrier to hydrogen ingress 225
6.6.3 Hydrogen hot-spots in the oxide 226
6.7 Summary 227

6.1 Introduction

This Chapter will focus on the nanoscale secondary ion mass spectrometry (NanoSIMS) technique applied to a variety of zirconium alloys. The intention is to map the local concentration of hydrogen, or hydrogen isotopes, in the oxide, metal-oxide interface and metal. First I would like to show that in the context of hydrogen pickup, the deuterium isotope can be used to simulate hydrogen. I will then demonstrate the usefulness and necessity of deuterium imaging instead of hydrogen imaging. The results section of this Chapter will be concerned with imaging the samples in cross-section, obtaining single images across the metal-oxide interface. The following Chapter deals with NanoSIMS imaging in 3D, imaging repeatedly from the oxide surface and inwards.

I have attempted to answer the following questions:

- What is the distribution of hydrogen in the oxide layer?
- What is the distribution of hydrogen across the metal-oxide interface?
- Does the distribution of hydrogen change with the stage of oxidation?
- What effect, if any, does transition have on the distribution of hydrogen?

6.2 Materials

ZIRLO and Zr-1Nb were oxidised in H_2O at 360 °C for 80 and 180 days and 180 and 540 days, respectively. The large variance in duration was due to the desire to have samples comparable in terms of position relative to the transition on the weight gain curve shown in figure 6.1. Zr-1Nb had much better corrosion resistance,

Sample ID	Material	Pre-exposure (days)	Weight gain ($mg\,dm^{-2}$)	w/D_2O exposure (days)	Weight gain ($mg\,dm^{-2}$)	Oxide thickness (µm)	D_2O oxide growth (µm)
ZLR19	ZIRLO	80	25.94	125	29.91	1.99	0.26
X2RX46	Zr-1Nb	180	34.01	225	≈ 38*	2.53	0.27
ZLR46	ZIRLO	180	55.09	225	≈ 60*	4.00	0.33
X2RX37	Zr-1Nb	540	77.60	585	81.34	5.42	0.25

The oxide thicknesses were calculated by dividing the weight gain by 15.
*estimated from optical measurements.

Table 6.1: Deuterated zirconium alloys.

so needed to be oxidised for far longer to reach post-transition. All samples were then oxidised again for 45 days in D_2O but at 350 °C (the lower temperature was not deliberate, but should not have had a significant impact on the oxidation rate or mechanism for this experiment). Figure 6.1 compares the weight gains for the samples against the weight gain curves for the MUZIC-2 alloys. It should be noted that these samples were initially oxidised as part of the MUZIC-1 program, and then oxidised in deuterated water at AMEC. The large disparity in oxidation rate is because these samples were oxidised in simulated primary water - by the addition of LiOH. Regardless, the weight gains tell us that the alloys - on the macro scale - are likely to be in different regimes of oxidation (pre- and post-transition).

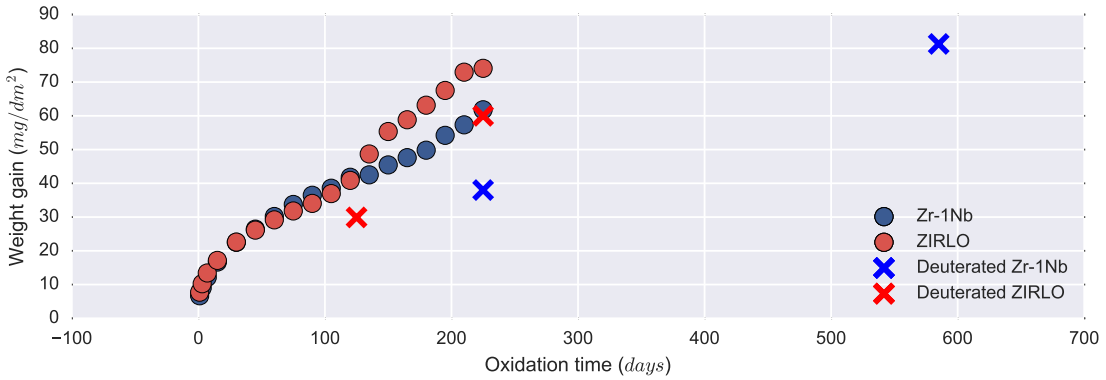


Figure 6.1: The weight gains of the deuterated alloys (crosses) compared to the weight gains of the same alloys oxidised in the MUZIC-2 program. Note that the temperature of the last 45-days of oxidation for the analysed samples was at 350 °C rather than 360 °C (done by AMEC as part of the MUZIC-1 program).

The first set of samples were polished in cross-section, revealing the metal and oxide, as shown in the NanoSIMS secondary electron image in figure 6.2. These

samples of ZIRLO and Zr-1Nb had been pre-oxidised to both pre-transition and post-transition stages. As the samples were subsequently oxidised in deuterium-rich water, deuterium was to act as a contrast-agent against the ever-present hydrogen background of our natural world.

The intention was to investigate how and where hydrogen travelled as it was absorbed by the material. Did the oxide act as a strong barrier? If so, was any part of the oxide easier to permeate? And how did samples where the oxide was growing quickly (immediately post-transition) differ from the samples with slower oxide growth (immediately pre-transition)?

Most acquisitions were done with the following NanoSIMS settings:

- FCp (Primary current): In the range of 3.0 nA to 6.0 nA.
- FCo (Actual current hitting the sample): In the range of 0.8 pA to 2.6 pA.
- D1 (Aperture): Setting 2 - 300 µm.
- AS (Aperture): Out.
- ES (Aperture): Out.
- Raster size: 50 µm × 50 µm.
- Pixel number: 256 px × 256 px.
- Dwell time: $10\,\mathrm{ms\,px^{-1}}$.
- Frame time: $655.36\,\mathrm{s\,plane^{-1}}$.

6.3 Results

6.3.1 A note on sample-preparation

Polishing the metal-oxide interface flat enough for the NanoSIMS analysis proved to be a difficult endeavour. All methods either resulted in smudging of the metal-oxide interface or contamination by colloidal silica in some areas. This is due to the significant difference in hardness between the soft metal and the hard oxide. The

medium the sample was set in also gave different results: Samples set in a carbon resin saw carbon contamination across the surface (as seen later in figure 6.10) whereas samples set in Wood's metal *melted* in the NanoSIMS (thankfully without damaging the instrument) due to its low melting point. I believe it was the lamp used with the optical camera that melted the metal.

Despite the problems of silica contamination or medium melting, many regions were good enough to perform analysis, so they are included here. I would advise the use of a good vacuum impregnated cold-mounting resin like Struers' Specifix-20, and to avoid polishing with colloidal silica. There are several new ion beam sample polishing techniques that are being released or improved, which may be useful as a replacement for this step. Several other sample preparation technqiues were not tried: Instead of grinding and polishing the samples using conventional sand paper, polishing using lapping films can be attempted. Since lapping films of equivalent "grit size" down to 100 nm can be readily purchased, this step can also replace the contaminating colloidal silica step. Ion beam thinning the region of interest can also be attempted, although personal experience has shown that for zirconium such thinning can create a wavy topography across the surface.

6.3.2 Typical NanoSIMS results

Figure 6.2 depicts a typical SE image accompanied by a cartoon explaining the visible features. The SE image is always acquired during NanoSIMS analysis, independent of elements chosen.

The NanoSIMS does not include a scan rotation function for its primary beam, nor can it do stage rotation. As such, the orientation of the sample on an image is dependant on its physical positioning on the stub. Since multiple samples are set on the same sample stub at different angles, the orientation of the metal-oxide interface will sometimes vary in the results shown in this Chapter.

As convention, I have chosen to keep the oxide on the left and the metal on the right - where possible. When convenient, I have rotated the image and cropped

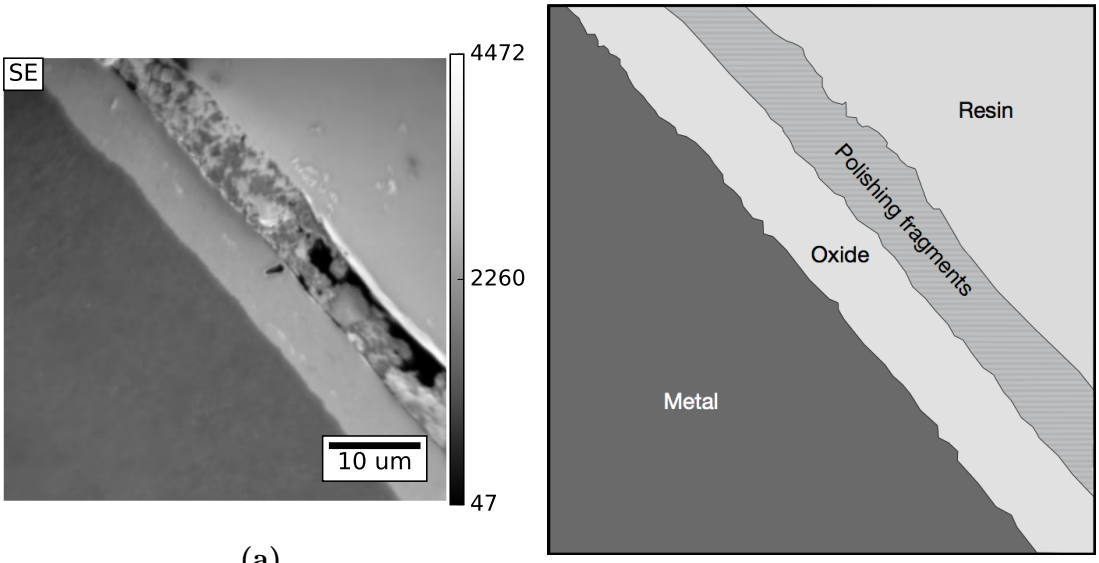


Figure 6.2: An overview of a typical cross-section, showing the SE image of a post-transition 585-day Zr-1Nb sample. The cartoon describes the features on the SE image.

it. The cropping leads to the effect that when comparing samples some images may have a higher apparent magnification than others.

The mass dispersion M_{max}/M_{min} on the NanoSIMS 50 is 13.2 as a result of the minimum physical separation of the detectors. This means that when analysing hydrogen (1 Da) on the first detector, the highest mass I can detect is carbon (12 Da) on the fifth. When detecting deuterium (2 Da) as the lightest element on the first detector, the heaviest relevant element I can detect is oxygen (16 Da).

Since the count rates of hydrogen and deuterium are particularly important, when presenting the images I have chosen to centre the secondary electron image and include numbered colourbars at either end of the image set that describe the adjacent image. The colour scheme used for the non-SE images is the "Cameca" colour scheme, which is common for publications reporting NanoSIMS results [82, 213, 214]. It is a linear scale, and can be seen in figure 6.3.



Figure 6.3: The Cameca colour scheme.

Figures 6.4 and 6.5 show typical NanoSIMS results as they will be presented in this thesis. On the left is the resin or metal that the samples have been embedded in before polishing. In the middle is the oxide. On the SE images, the oxide is typically the brightest feature of the image. On the right is the metal.

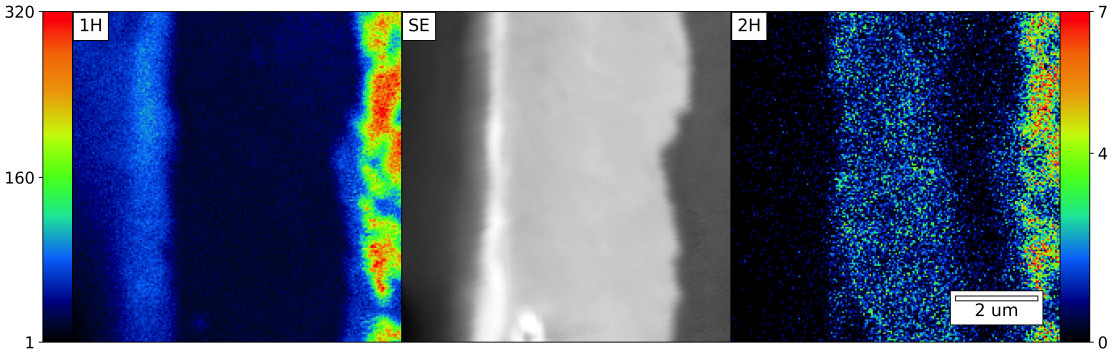


Figure 6.4: Typical high-magnification NanoSIMS result of the metal-oxide interface on *585-day Zr-1Nb*, showing (from left) the resin, oxide and metal.

Figure 6.4 shows a high-magnification image with a window size of less than 10 µm × 10 µm, acquired on the Oxford NanoSIMS 50. Figure 6.5 shows a low-magnification, image with a window size of 30 µm × 30 µm.

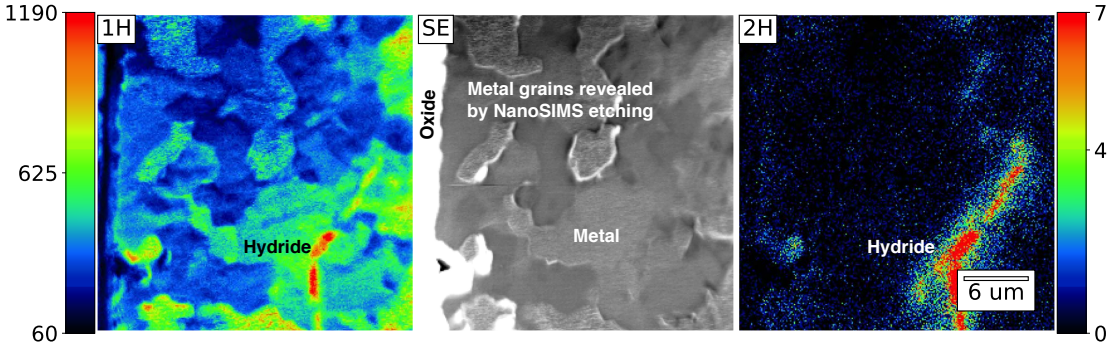


Figure 6.5: Typical low-magnification NanoSIMS result of the oxide and metal on 125-day ZIRLO, showing (from left) the resin, oxide and metal. A large deuteride can be seen in the metal.

In this image the oxide is a thin strip along the left side of the image, and a deuteride can be seen in the metal in the ^{2}H map. In the metal, grain contrast is sometimes very clearly visible, especially on analysis acquired on the newer NanoSIMS 50L at the Cameca HQ in Gennevilliers, France. The grain contrast

was especially useful in overlaying SEM and NanoSIMS results, as discussed in section 6.5.8.

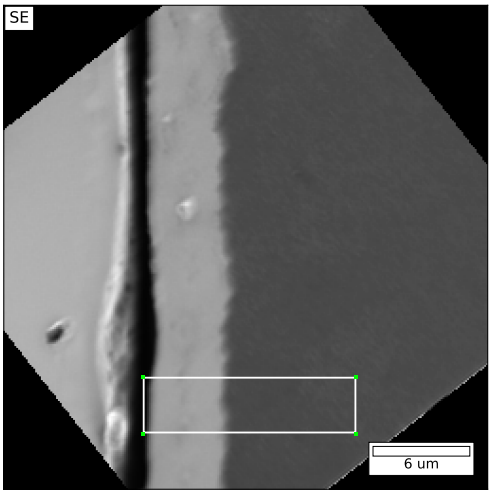
The scanning technique of NanoSIMS means that the time scales linearly with the number if pixels in the image. Due to sample drift and stability of both sample and instrument, this means that one has to choose between high resolution or high field-of-view. It is a combination of low and high-magnification that is necessary to get a proper understanding of the samples. There are features that are too small to be visible on a low magnification image, but focussing too much on a small sector of the material can hide important features that are further away.

Over 150 NanoSIMS analyses were carried out in the course of this project. I have extracted line profiles from regions-of-interest (ROIs) on the image sets, as seen in figure 6.6. Typically the line profiles are averaged across a 3 µm thick line.

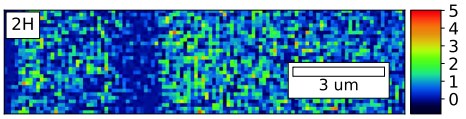
Figure 6.6 shows a rotated view of a 225-day post-transition ZIRLO sample. Most images will be rotated and cropped in order to present the relevant feature on the image. Here a ROI has been drawn on it in white in order to emphasise the oxide and metal, shown in (b) and (c) on the figure.

6.3.3 Using the SE image to identify the oxide

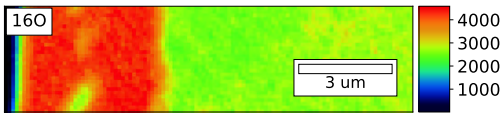
Due to the limitation of mass dispersion on the NanoSIMS 50 (described in section 6.3.2), it was not possible to analyse oxygen and hydrogen simultaneously. Therefore, when detecting for ^{1}H, I would not be able to tell where the metal-oxide interface was. However, because the oxide has a much higher secondary electron yield than the metal, I found that I could use the secondary-electron image as a replacement indicator for the oxygen signal. As seen in figure 6.7, a line profile taken across the metal-oxide interface shows far more counts for the oxide than it does for the metal. The high oxygen content in the metal, shown on the ^{16}O image can be explained as the reactive zirconium metal surface oxidising in air after polishing. The formation of this rapid oxide layer was effectively unavoidable as I did not have access to polishing facilities in non-oxidising atmospheres, and the NanoSIMS



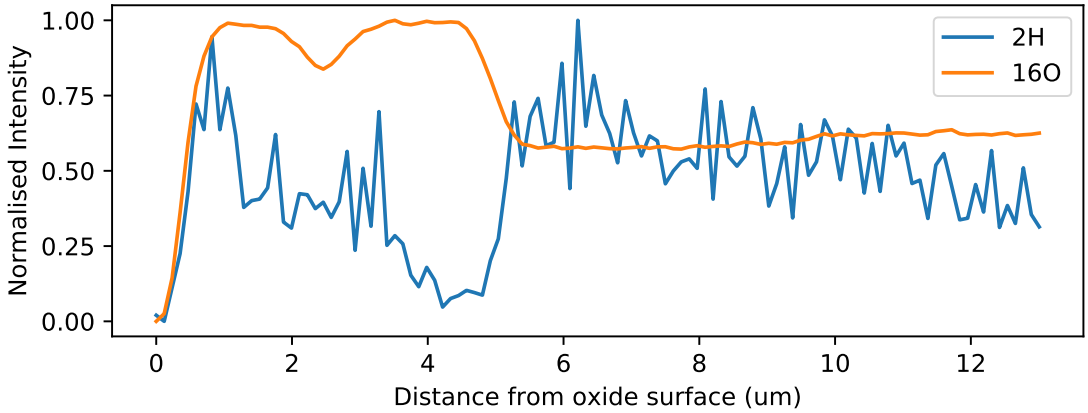
(a) Post-transition ZIRLO SE image. The image has been rotated to align the oxide vertically. The ROI is highlighted in white.



(b) Deuterium signal in the ROI.



(c) Oxygen signal along the line profile.



(d) Normalised line profile comparing the deuterium and oxygen signals.

Figure 6.6: A typical NanoSIMS dataset from post-transition 225-day ZIRLO with regions of interest highlighted.

was not equipped for vacuum sample transfer. This nanometre-thin oxide layer did not impede the NanoSIMS experiments.

By rotating and cropping the SE images so that the oxide was the only feature in the image with strong contrast (figure 6.8a), I was able to filter the image into a binary image (figure 6.8b) and sum it perpendicular to the oxide surface. Any pixel outside of the oxide was set to zero, and any pixel in the oxide was set to 1 and multiplied by the size of individual pixels. This produced a graph of oxide thickness

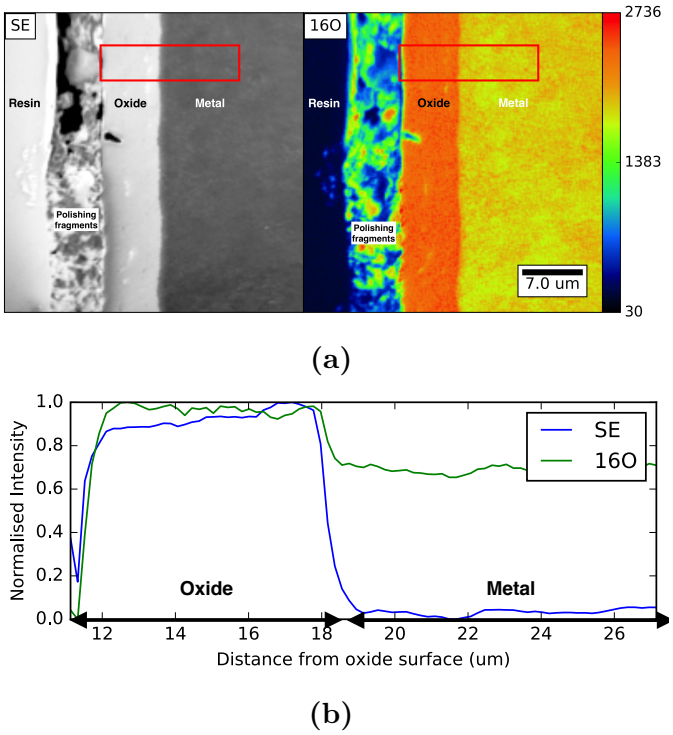


Figure 6.7: Normalised line profile (b) comparing the secondary electron and oxygen signals from the red ROIs drawn on the SE and ^{16}O maps (a).

as a function of the distance along the metal-oxide interface, as seen in figure 6.8c.

6.3.4 Proving that the deuterium signal is not from natural H_2O

The natural ratio of deuterium to hydrogen in water is approximately 1/10,000. Operating under the assumption that the NanoSIMS secondary ion beam was well-aligned, any deuterium counts higher than 1/10,000 of the hydrogen counts should therefore be due to 45 day oxidation in the heavy-water, rather than from hydrogen present in hydrocarbon contamination. Taking the pixel by pixel ratio of the pickup down the D and H image from the typical dataset in figure 6.5, multiplied by a factor of 10,000 allows us to visualise the deuterium ratio above the natural abundance directly, seen in figure 6.9. Note that the colour-bar on the plot is such that green counts indicate concentrations 100 times higher than natural concentration. This image shows that there is very little deuterium detected in the bulk of the Zr metal matrix as expected from its very low solubility at room temperature [103, 215, 216].

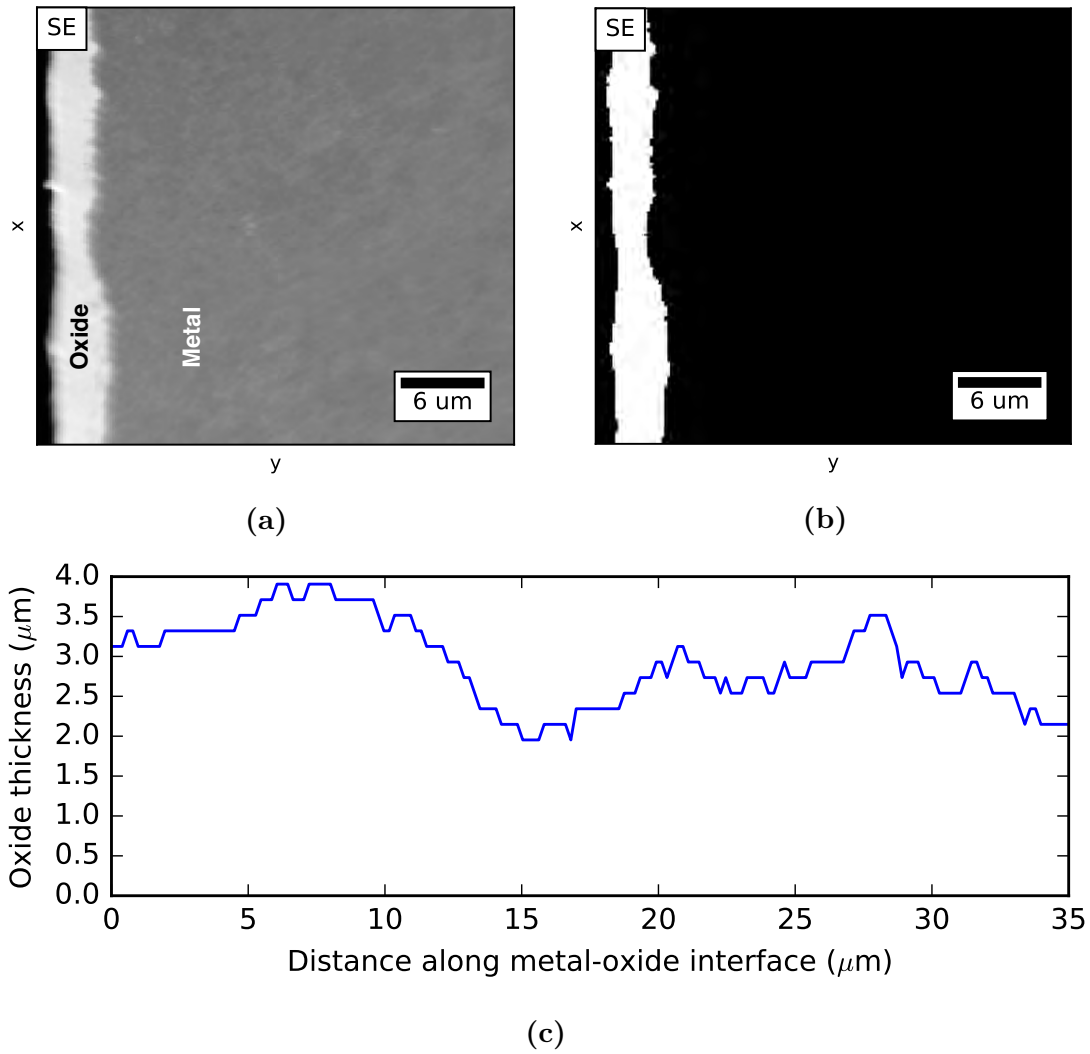


Figure 6.8: Extracting the oxide thickness by filtering counts in the SE result.

6.3.5 Hydrocarbon contamination from resin

Over longer (≈45 min) analysis, hydrocarbon species from the Specifix-20 resin used to embed the samples contaminated the results. This was evident from an increased ^{12}C and ^{1}H presence during the later stage of a single analysis. Figure 6.10 shows an example of this where the beam is rastered from top left to bottom right in a series of line scans (the normal way of acquiring a map). The red arrows on the ^{12}C image indicates how during analysis, the resin has slowly crept across the sample. This type of result led to the attempt of using Wood's metal as a replacement for resin.

The carbon contamination was generally easy to work around, but prevented me from doing analysis with longer dwell time on large areas. Generally, performing

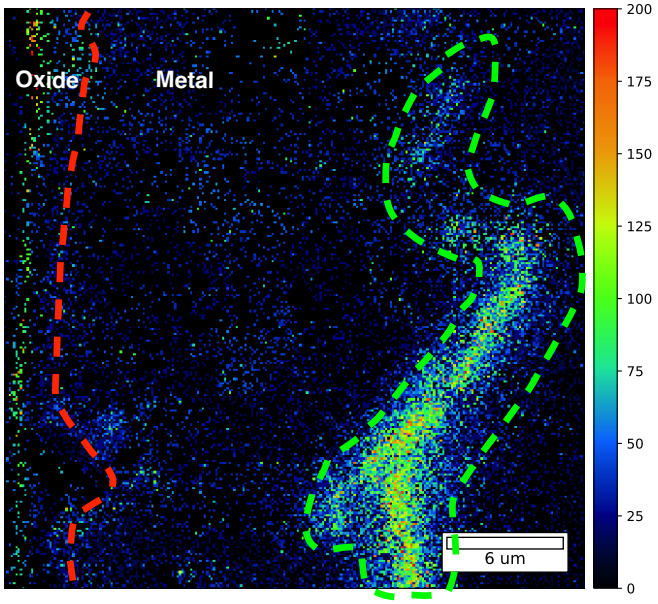


Figure 6.9: $^{2}H/^{1}H$ ratio map showing the concentration above natural abundance of deuterium in H_2O on a sample of pre-transition 125-day ZIRLO. The metal-oxide interface is highlighted in a red dashed line. The large feature outlined in green is a hydride/deuteride.

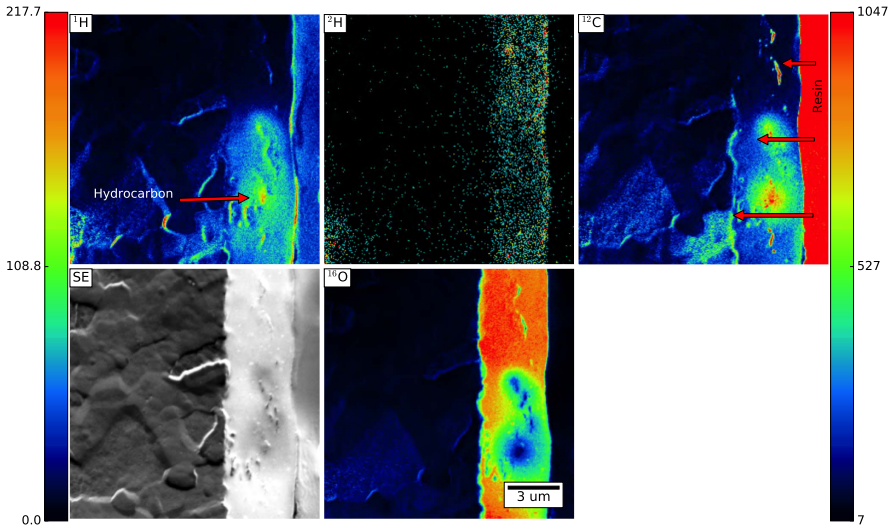


Figure 6.10: Hydrocarbon contamination creeping across the sample from the resin during analysis. The left and right colourbars refer to the ^{1}H and ^{16}O images, respectively.

post-analysis on cropped regions outside the carbon contamination was acceptable, but it would have been better to do analysis with higher counts - especially when looking for deuterium "hot-spots" in the oxide region, like in section 6.5.9.

6.4 Overview of alloys

Below is a NanoSIMS image overview of the alloys most studied by NanoSIMS. Each image has a window size of 50 µm × 50 µm, with pixel resolution of 256 px × 256 px. The pixel dwell time was 10 ms px^{-1}, resulting in a time of about eleven minutes per image. FCo, the incident primary beam current on the sample, held roughly constant around 2 pA.

The samples were stacked next to one another and embedded in the cold-mounting resin Specifix-20 before polishing. Figure 6.11 shows a stitched optical image of the samples after polishing. The transparent, red region indicates the region where the analysis was done.

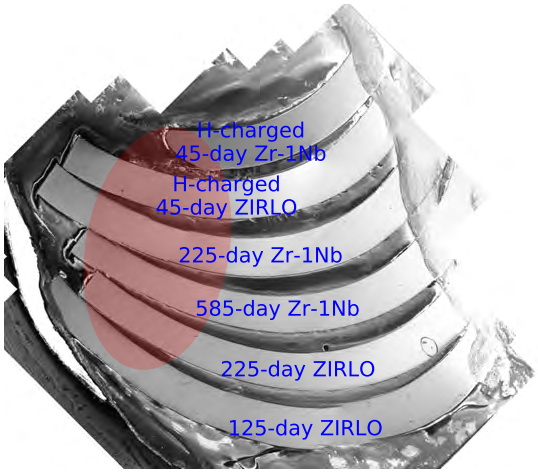


Figure 6.11: Stitched optical overview of the first set of NanoSIMS samples. The oval red region indicates where the analysis was done. This region had the best polish on the sample. The hydrogen-charged samples were not imaged for the project.

6.4.1 125-day pre-transition ZIRLO

Figure 6.12 shows typical low-magnification results for the 125-day ZIRLO alloy. The metal-oxide interface on each image is about 35 µm long. On the ^{16}O image,

the blue, circular marks visible along the oxide are contamination. There is no peak in the carbon signal evident from the contamination region, as shown in the extracted region of interest in figure 6.13. The contamination is also visible on the SE image, and is likely to be silica particles from the colloidal silica polishing step of the sample preparation.

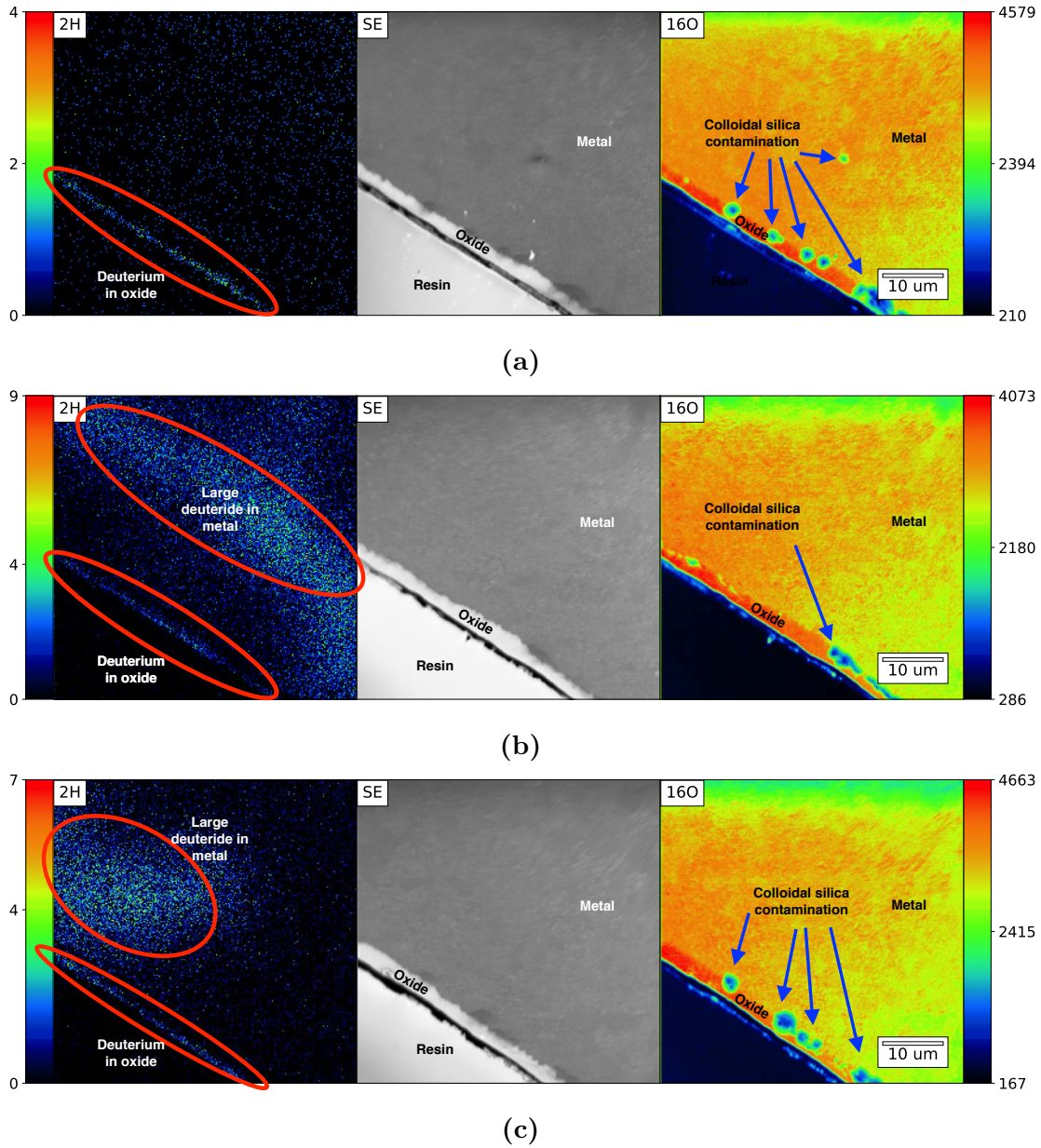


Figure 6.12: NanoSIMS results from several regions on a sample of pre-transition 125-day ZIRLO. The red ovals indicate regions of high deuterium counts.

All 125-day ZIRLO images show a relatively high concentration of deuterium in

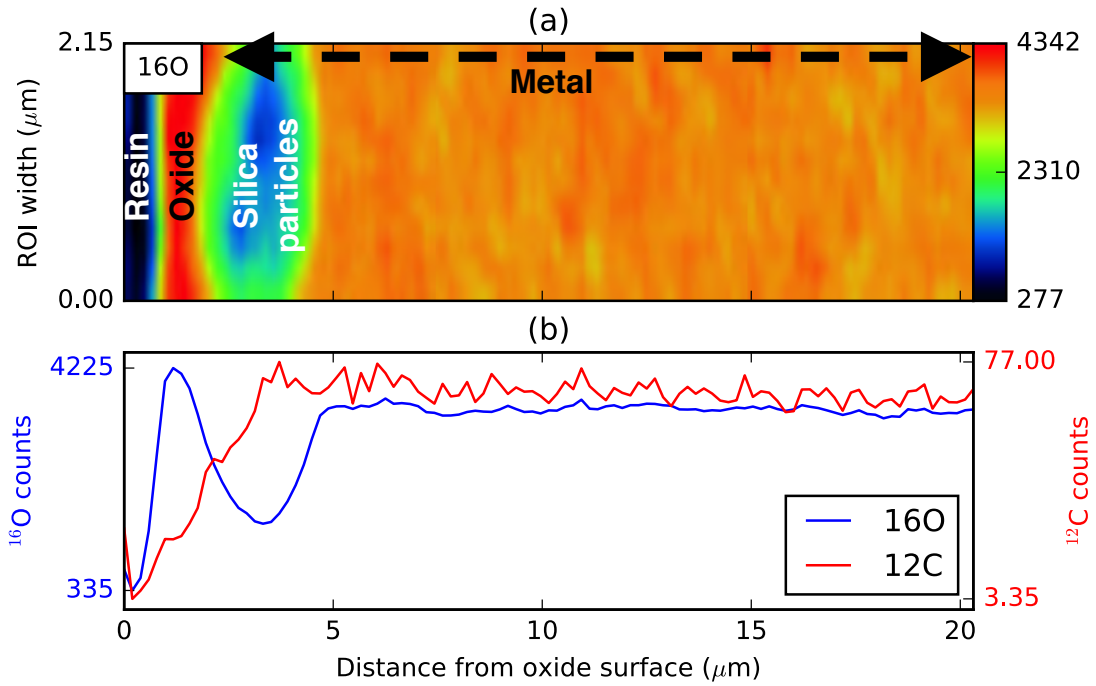


Figure 6.13: Magnified ROI showing the effect of contamination of the oxygen signal in figure 6.12c. The oxide is on the left. The line profile demonstrates that through the contamination, the carbon signal is constant, implying that this is not hydrocarbon contamination, but rather a dried colloidal silica particle.

the first $1-2\,\mu m$ from the surface of the oxide compared to closer to the metal-oxide interface. This is emphasised by the ^{2}H image figure 6.12a. Since I did not have access to standards for ^{1}H and ^{2}H in zirconium and zirconia, I was unable to quantify their absolute concentration. The secondary ion yield of the metal and oxide are very likely to be different, which means that it is not possible to determine the relative concentration of ^{1}H and ^{2}H of the metal to the oxide. Instead, the position of and relative concentration of the isotopes within each phase will be discussed.

Figures 6.12b and 6.12c have large deuterides in them, although the size and shape of them was hard to identify as the NanoSIMS alignment had not been optimised for low-mass elements at that point in time. The deuteride region is very large, and ranges from close to the metal-oxide interface to 30 µm into the metal. The oxide thickness varies significantly, between 1.75 µm and 3.1 µm. The oxide thickness can often change abruptly, giving rise to a very uneven metal-oxide interface.

6.4.2 225-day post-transition ZIRLO

Figure 6.15 shows a selection of NanoSIMS maps from the post-transition 225-day ZIRLO sample. They show evidence of substantially more cracking than the 125-day sample. The cracks are visible in the oxide in both the SE and ^{16}O images and are emphasised on the cartoon in figure 6.14. The oxide thickness ranges from 4.4 µm to 5.2 µm. The variation in oxide thickness on this 225-day post-transition sample is much smaller than on the 125-day pre-transition sample. This could indicate that there are regions on the 125-day sample that have begun to go through transition, locally accelerating the oxide growth rate.

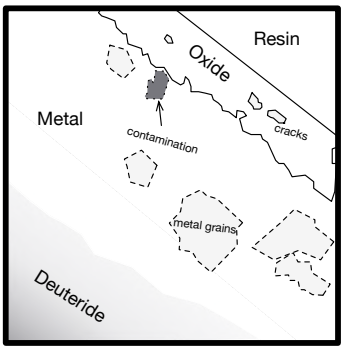


Figure 6.14: Cartoon of the post-transition 225-day ZIRLO sample giving a breakdown of the general features present from the NanoSIMS analysis.

Deuterides are more common on the 225-day sample than on the 125-day sample. Here, every image contains a large region in the metal concentrated in deuterium. However, close to the metal-oxide interface there is a distinct gap with a lack of ^{2}H counts. This is particularly noticeable in figure 6.15b where the deuteride is close to the metal-oxide interface.

6.4.3 225-day pre-transition Zr-1Nb

Figure 6.16 shows typical low-magnification results for the 225-day pre-transition Zr-1Nb sample. The oxide thickness appears to vary substantially, between 1.9 µm and 3.6 µm. In the oxide, the strongest deuterium signals are found in regions with thick oxide. These regions do not appear to coincide with cracks on this sample, in fact, no cracks were found when imaging using the NanoSIMS, although it almost

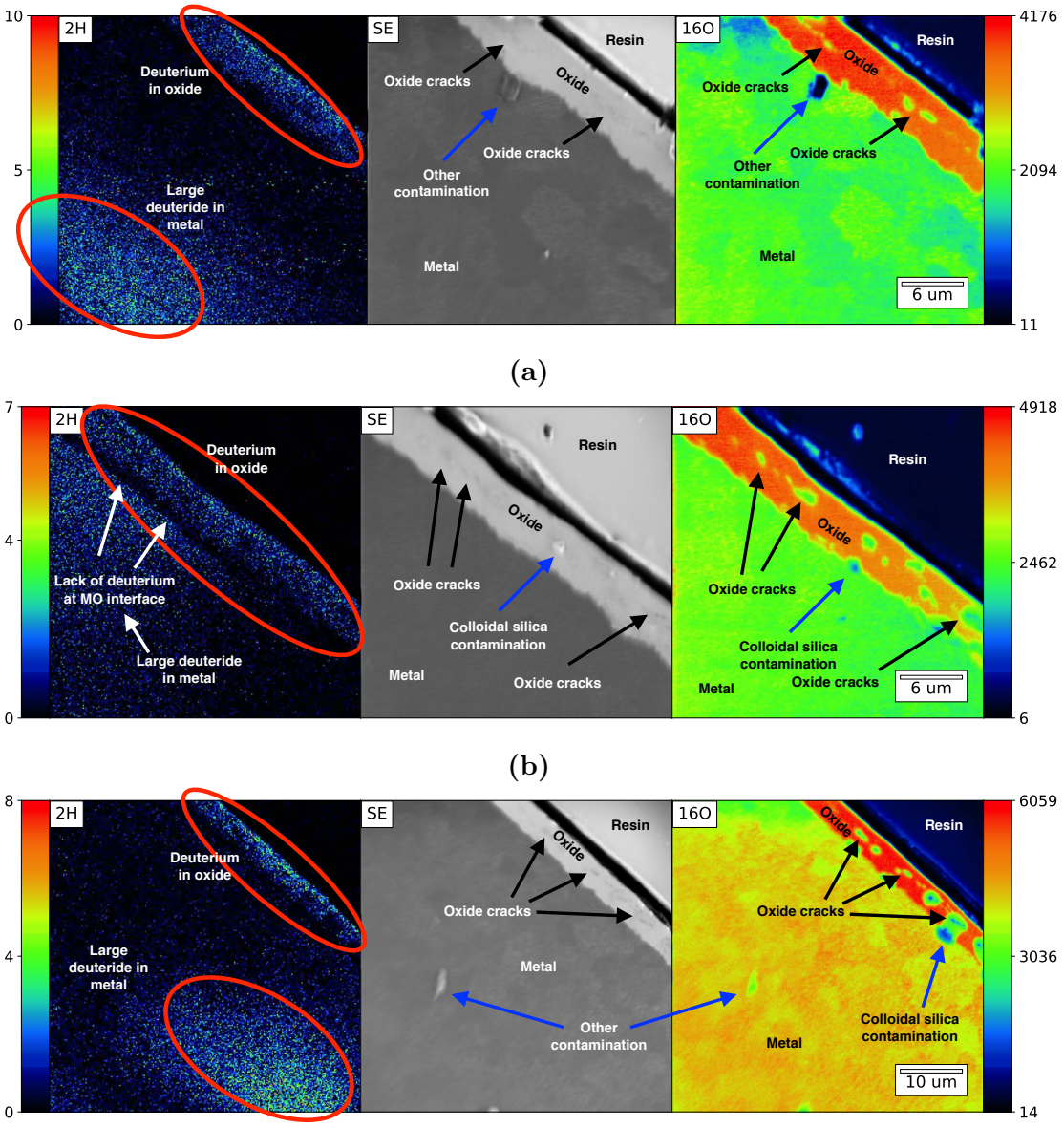


Figure 6.15: NanoSIMS results from several regions on a sample of post-transition 225-day ZIRLO. The red ovals indicate regions of high deuterium counts. Note that the image scale varies.

certainly contains cracks that are smaller than can be resolved here. Deuterium is overall much more intense in the first 1 µm of the oxide. Further into the oxide it decreases to almost zero in the thinner regions whilst the thicker oxide regions tend to have a more uniform distribution of deuterium.

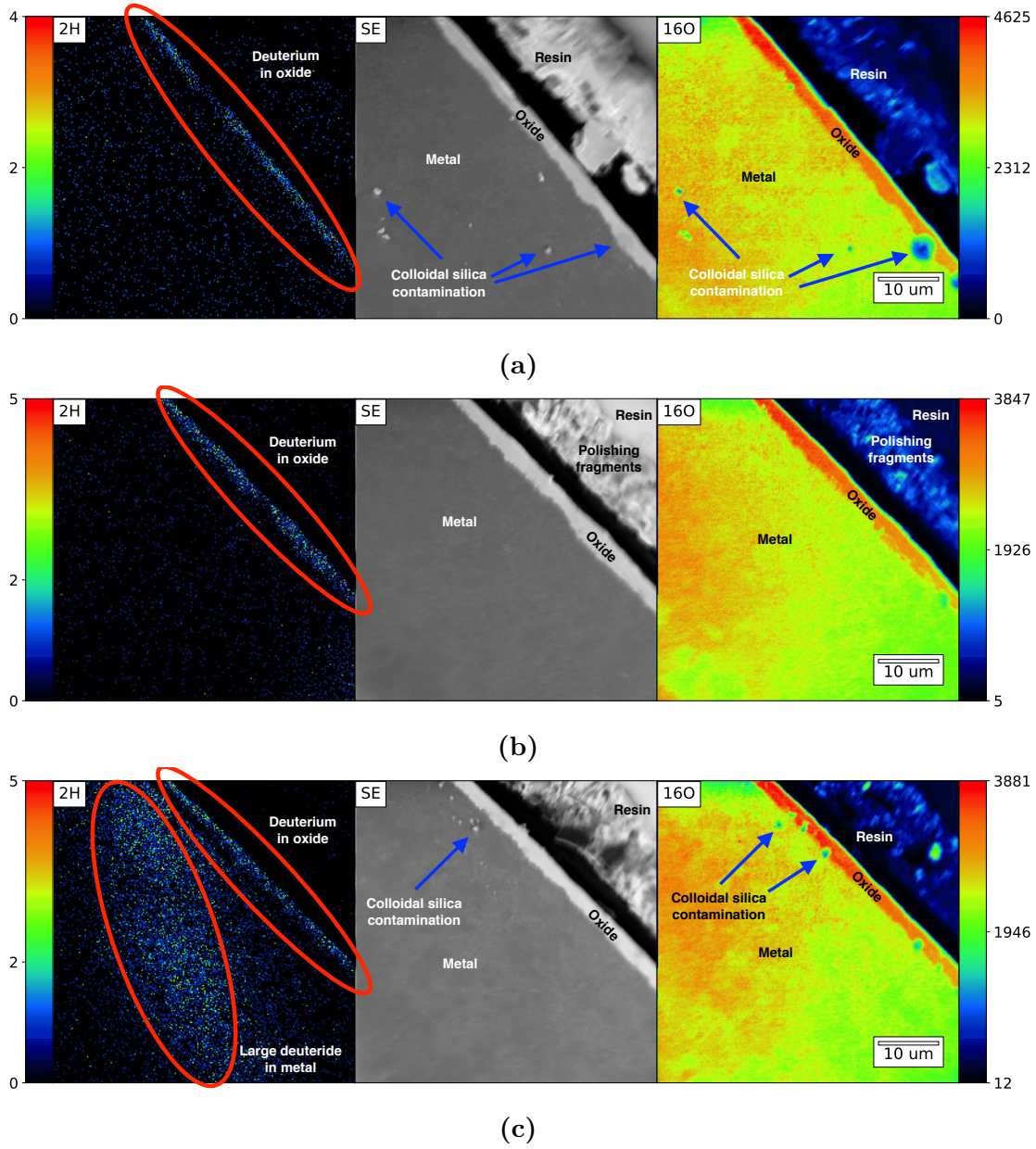


Figure 6.16: NanoSIMS results from several regions on a sample of pre-transition 225-day Zr-1Nb. The red ovals indicate regions of high deuterium counts.

6.4.4 585-day post-transition Zr-1Nb

Figure 6.17 shows typical low-magnification results for the 585-day post-transition Zr-1Nb sample. The oxide thickness is very uniform, and much thicker than for the other samples. The oxide ranges from 6.4 µm to 7.4 µm in thickness. Like when comparing the post-transition and pre-transition ZIRLO samples, the Zr-1Nb sample shows less variation in oxide thickness in post-transition than in pre-transition.

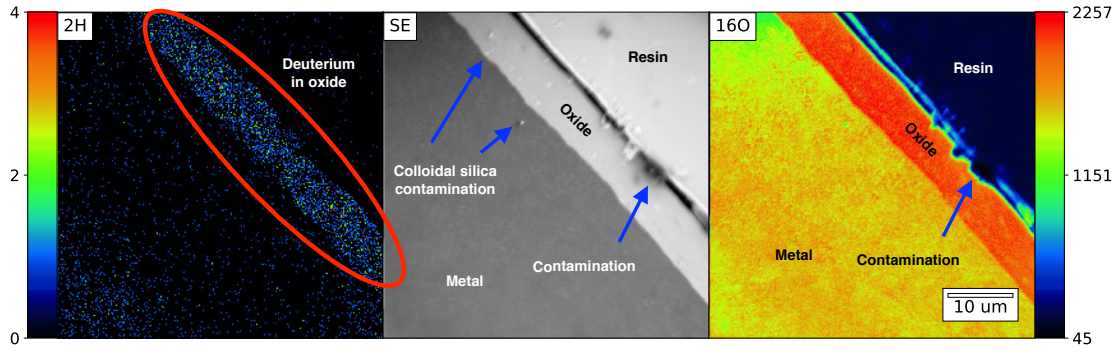
Cracks are visible in the SE images, particularly in figures 6.17b and 6.17c. The distribution of deuterium remains the same around the cracks as in the rest of the oxide. In the cracks however, the deuterium concentration decreases markedly. Unlike the pre-transition sample, the oxide appears entirely permeated by deuterium, with the exception of a narrow band just at the metal-oxide interface. It is difficult to say for certain whether the band lies in the metal or in the oxide, though it makes more sense for it to be due to a dense protective layer of oxide.

The sample contains deuterides that are similar in size and shape to the other samples. In the oxide, the deuterium is distributed evenly throughout, but a band of zero counts is again found at the metal-oxide interface.

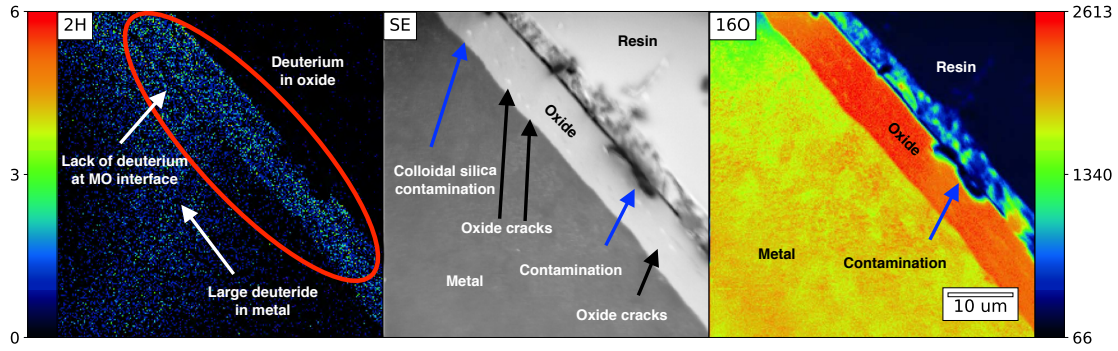
6.4.5 Hydrides compared between STEM and NanoSIMS

Hydrides are found to be a common feature on low-magnification NanoSIMS images. Comparing the ^{1}H and ^{2}H content found in the ZIRLO samples through NanoSIMS to the hydride results from EELS on ZIRLO, it is surprising to find relatively few counts in the metal near the metal-oxide interface. Hydrides were always present on the TEM foils, and often all the way into the metal-oxide interface. This could imply that the hydrides are artificially induced by sample preparation in the FIB, as is found for titanium alloys [142]. No TEM foils were extracted reaching deeper into the metal than ≈ 5 µm as it becomes very difficult to uniformly thin such a large sample if one intended to keep the oxide. It would be of interest to produce TEM foils from the regions of metal showing deuterides in the NanoSIMS.

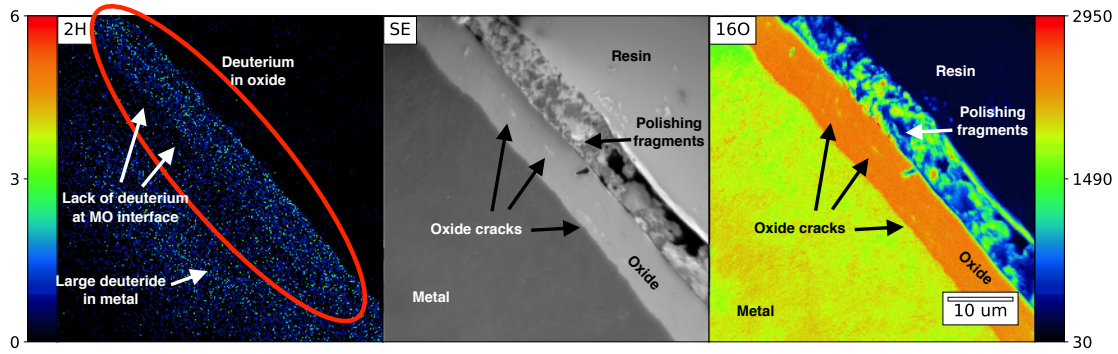
One NanoSIMS image showed a large deuteride present in the metal. The region strong in deuterium, shown in the ^{2}H image in figure 6.16c has an elongated shape.



(a)



(b)



(c)

Figure 6.17: NanoSIMS results from several regions on a sample of post-transition 585-day Zr-1Nb. The red ovals indicate regions of high deuterium counts.

It appears to start very close to the metal-oxide interface and carries over 30 µm into the metal, and at its widest is approximately 24 µm thick. In the same image, the distinct deuterium-free band in the oxide just above the metal-oxide interface is clearly present. This band features on all the samples studied by cross-sectional imaging, and is further discussed below.

6.5 High-resolution oxide analysis

In order to investigate the location of deuterium more accurately in the oxide, higher magnification images were acquired with a longer dwell time per pixel. Unless stated otherwise, the analysis was performed as a 256 px × 256 px raster. ROIs, drawn in red, indicate regions which have been magnified to emphasise features.

6.5.1 Peak of hydrogen in first part of the oxide

The position of hydrogen during corrosion has been visualised by using deuterium as a marker. Since the natural isotope abundance of ^{2}H relative to ^{1}H is 1.55×10^{-4} [217], deuterium measured at ratios higher than natural abundance must be from the D_2O-oxidation. By calculating the ratio of deuterium to hydrogen in each pixel and multiplying by 10^4, the concentration of ^{2}H in terms of number of times natural concentration can be plotted.

This ratio has been compared relative to the oxide using the SE image as a substitute for the ^{16}O image since the latter could not be detected due to detector limitations when simultaneously measuring for ^{1}H and ^{2}H. In some cases, as shown in figure 6.18, the secondary electron signal shows a strong peak indicating the angled surface of the oxide, and should not be mistaken for the start of the oxide in cross-section.

In the pre-transition samples, the $^{2}H/^{1}H$ ratio shows a clear inclination to peak strongly in the first 1 µm of the oxide, before falling sharply. In contrast, the post-transition samples show a fairly uniform high concentration up until the last 1 µm of oxide.

6.5.2 Pre-transition 125-day ZIRLO

The pre-transition 125-day ZIRLO sample, shown in figure 6.18 emphasises the presence of deuterium throughout the oxide. Here, cracks in the oxide are particularly visible on the ^{2}H image, where no deuterium is found. There is a clear band present in the oxide, close to the metal-oxide interface, where little to no ^{2}H is present. The ^{1}H image does not show such a region, suggesting that hydrogen may have permeated the oxide during the initial 80-day oxidation in pure water. During the following 45-day oxidation in deuterated water however, the deuterium had only begun to diffuse through the oxide.

On the left side of the SE image, a bright white band is present. This band is due to slight tilting of the sample, revealing the surface of the oxide to the beam, giving a bright edge effect. This has been emphasised on the images, and should not be taken as the beginning of the oxide layer.

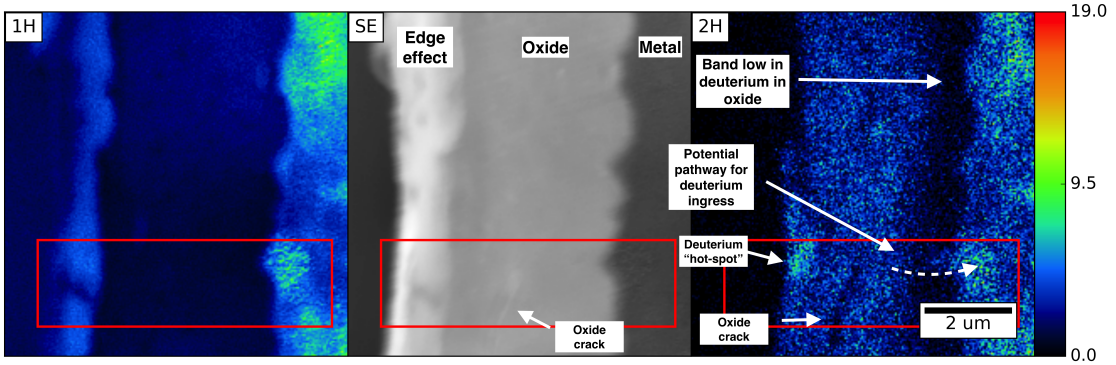


Figure 6.18: Hydrogen and deuterium shown in the oxide and metal-oxide interface on pre-transition 125-day ZIRLO. The red rectangles indicate the region shown in figure 6.19. The white dotted line indicates a possible pathway through the oxide for hydrogen, based on the shape of the ^{2}H signal present. The dwell time for the acquisition was 40 ms px^{-1}.

A deuterium "hot-spot", approximately 900 nm in diameter, showing increased counts relative to the rest of the oxide, was investigated by taking a ROI around it in the oxide. Plotting the $^{2}H/^{1}H$ ratio, seen in figure 6.19 shows us that the deuterium concentration is over 1800 times higher than background abundance of deuterium. The red ovals emphasise regions with high counts of ^{2}H. In particular, a region near the metal oxide interface (highlighted with a white arrow) could present a pathway

through the "barrier-oxide" which is normally devoid of ^{2}H. This hot-spot is about 200 nm in diameter, suggesting it could be an SPP. SPPs as pathways for hydrogen ingress has been suggested previously [90, 120]. In Chapter 5 I argued that the large distances between SPPs meant that it was unlikely that they could act as hydrogen pathways. Taking into account the fact that, except for a narrow band around the metal-oxide interface, deuterium is strongly present throughout most of the oxide, this means that SPPs could act as short circuits through this barrier layer after all.

Averaging along the metal-oxide interface, shown in figure 6.19b, the edge effect becomes particularly apparent. The oxide edge is just before the SE signal becomes flat. Here the hot-spot contributes to a peak in the ^{2}H/^{1}H signal in the outer region of the oxide. The concentration of deuterium remains high throughout the oxide, dropping off rapidly about 1 µm before the metal-oxide interface.

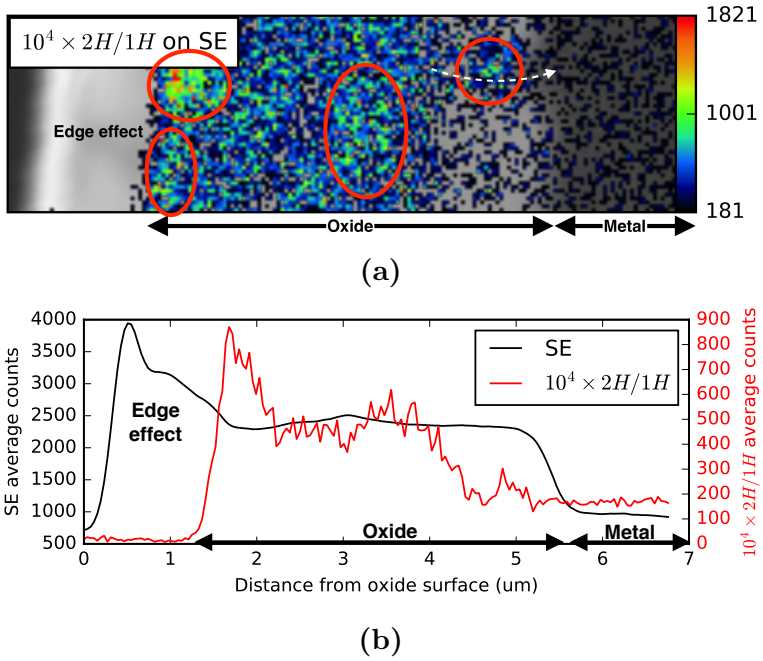


Figure 6.19: ^{2}H/^{1}H ratio shown in the oxide and metal-oxide interface on pre-transition 125-day ZIRLO. The red circles indicate regions of high ^{2}H/^{1}H ratio. The white dotted line indicates a possible pathway through the oxide for hydrogen, based on the shape of the ^{2}H signal present.

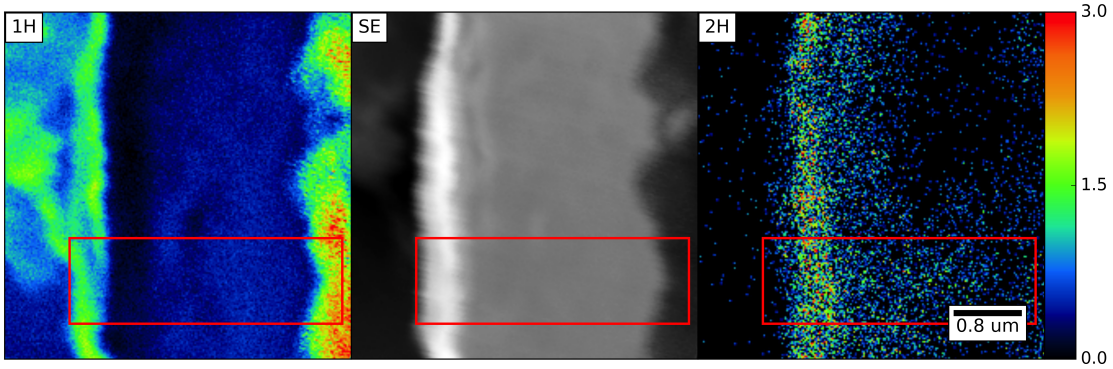


Figure 6.20: Hydrogen and deuterium shown in the oxide and metal-oxide interface on pre-transition 225-day Zr-1Nb. The red rectangles indicate the region shown in figure 6.21. The dwell time for the acquisition was $20\,\mathrm{ms\,px^{-1}}$.

6.5.3 Pre-transition 225-day Zr-1Nb

The pre-transition 225-day Zr-1Nb sample, shown in figure 6.20, stands in strong contrast to the pre-transition ZIRLO sample in figure 6.18. Its 2.1 µm thick oxide primarily only contains ^{2}H in the first 400 nm of the oxide.

In the ^{1}H image, one can see the hydrogen content of the resin on the left of the image. This emphasises the importance of using deuterium as a contrast agent when measuring for hydrogen. In the metal, it is likely the edge of a hydride that is visible giving a strong ^{1}H signal.

On this sample, deuterium is strongly present in the first 500 nm of oxide at 200 × natural abundance, before rapidly dropping off. Interestingly, in the top of the image, where the metal-oxide interface is particularly curved, the deuterium concentration is particularly low. The high concentration in the outer region of the oxide is again shown in the ROI image and plot in figure 6.21, where it peaks before rapidly dropping off. The pre-transition sample shows a wide, 2 µm barrier to deuterium. This contrasts strongly with the much more penetrated pre-transition ZIRLO oxide.

6.5.4 Pre-transition 61-days Zircaloy-4

Figure 6.22 shows the hydrogen and deuterium content on a sample of 61-day pre-transition sample of Zircaloy-4. The contrast of the oxide in the SE image is unusual and is likely to be an artefact due to bevelling of the edge from polishing.

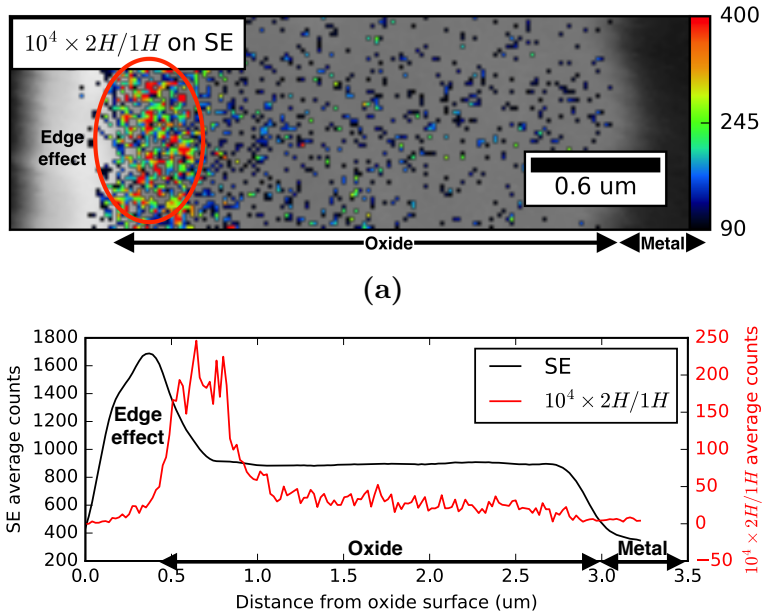


Figure 6.21: ^{2}H/^{1}H ratio shown in the oxide and metal-oxide interface on pre-transition 225-day Zr-1Nb. The red circle indicates a region of high concentration of deuterium.

Similar to the pre-transition 225-day Zr-1Nb sample, there is a wide region not penetrated by deuterium. There are high counts of hydrogen in the metal at the metal-oxide interface. These are likely to be hydrides, as seen in the same location on Zircaloy-4 TEM foils in Chapter 5.

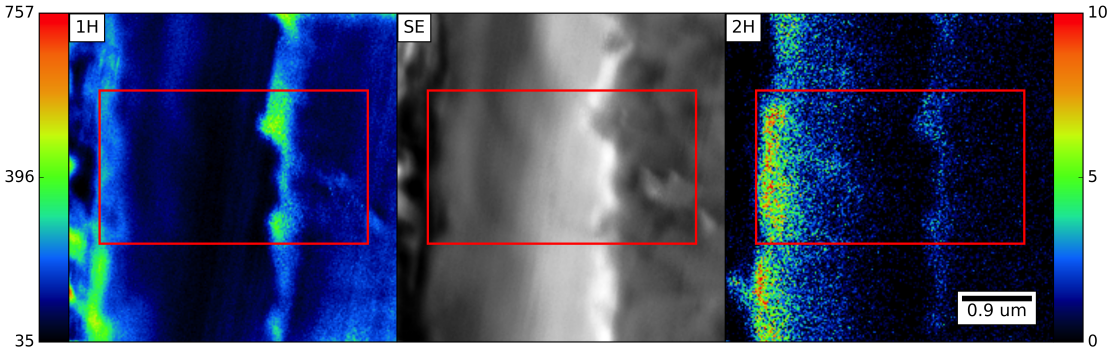


Figure 6.22: Hydrogen and deuterium shown in the oxide and metal-oxide interface on pre-transition 61-day Zircaloy-4. The red rectangles indicate the region shown in figure 6.23. The dwell time for the acquisition was 40 ms px^{-1}.

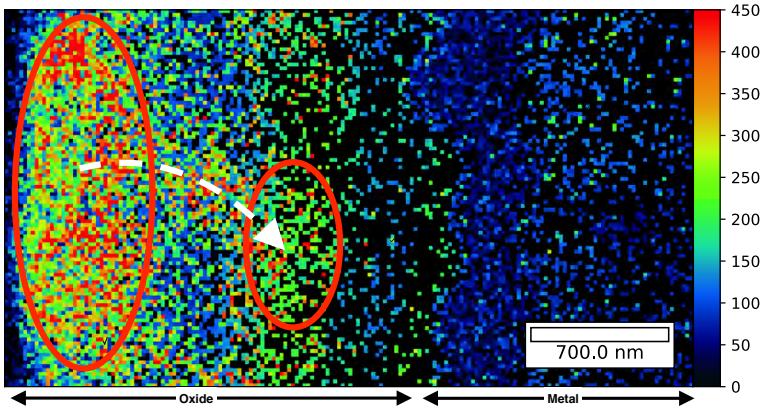
The ^{2}H/^{1}H ratio, shown in the ROI in figure 6.23 shows a region populated densely by deuterium 300 times above the natural abundance. In addition, a

potential pathway through part of the oxide is present, highlighted by a white arrow. As this is a 2-D type of imaging, one could hypothesise that an SPP could be present in the oxide even closer to the metal in a plane beneath the imaged plane, acting as a further pathway for deuterium into the metal. The SIMS result is compared to a TEM sample from the same material in figure 6.23c. Note that the TEM sample was taken from a region with a thinner oxide than the SIMS result. The very highly concentrated region shown on the line profile coincides with the oxide closest to the surface of the sample, which is leftmost on the HAADF image. Here the oxide appears quite porous and containing several cracks. This combined with the lack of a diffusion profile in this region suggests that the water is able to permeate the first 400 nm of oxide.

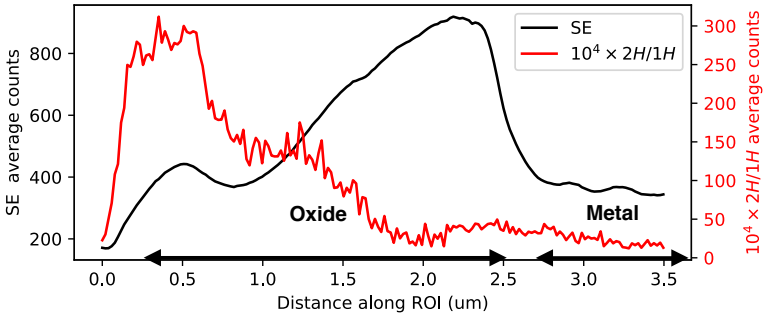
6.5.5 Post-transition 225-day ZIRLO

The post-transition 225-day ZIRLO sample, shown in figure 6.24, has several cracks present halfway through the oxide. It is difficult to see if they coincide with gaps in the ^{2}H image. In regions where the oxide thickness is at its thickest, the band of low-deuterium counts is at its widest. If the regions with thick oxide have recently grown, it could imply that freshly grown oxide acts as a better barrier than "older" oxide, but it could also mean that the deuterium has not had time to diffuse through it yet. This is the opposite behaviour of what I observe for the pre-transition 225-day Zr-1Nb, where the thicker oxide contains more deuterium throughout than on this sample.

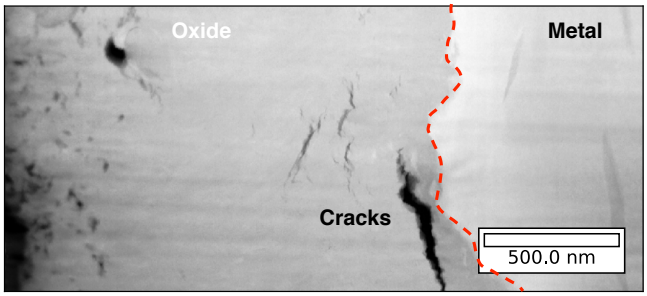
At the top right of the ^{2}H image, there is a region in the low-deuterium band containing two small "hot-spots" of deuterium emphasised by a dashed red circle. They sit halfway through the band, and could be SPPs containing deuterium. The hot-spots are approximately 300 nm to 400 nm in diameter, which is larger than the typical sizes of 100 nm to 200 nm that I have observed for $Zr(NbFe)_2$ Laves SPPs in ZIRLO (the largest type of SPPs), but taking into account broadening-effects due to focus and stigmatism, Laves SPPs are passable candidates to explain the



(a) $^{2}H/^{1}H$ ratio image.



(b) $^{2}H/^{1}H$ ratio averaged line profile.



(c) STEM HAADF image from the same sample.

Figure 6.23: (a) The $^{2}H/^{1}H$ ratio image from the ROI in figure 6.22 on pre-transition 61-day Zircaloy-4. The red circles indicate regions of high $^{2}H/^{1}H$ ratio. The unusual SE signal in averaged line profile (b) is likely to be an artefact due to bevelling of the edge from polishing the sample. (c) STEM HAADF image from the same sample, showing a similar region as in the NanoSIMS image.

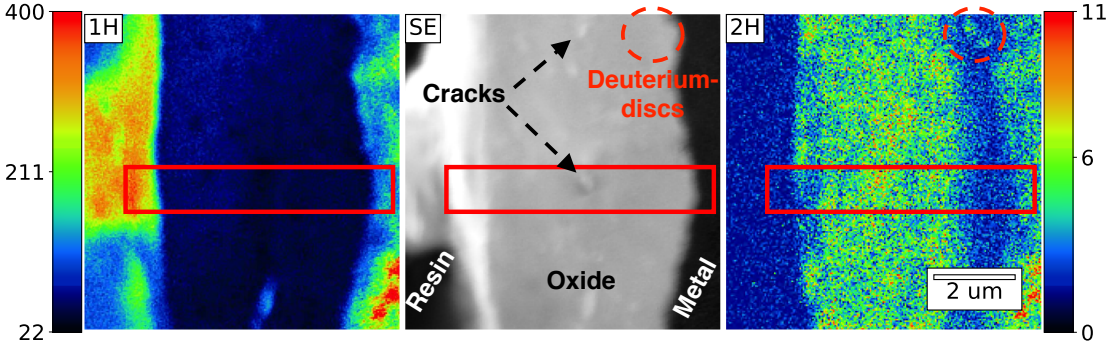
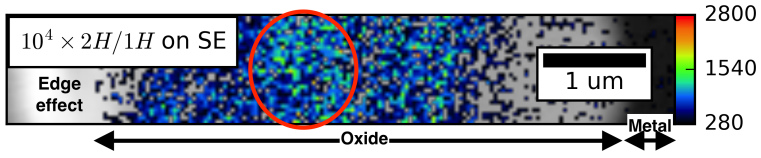
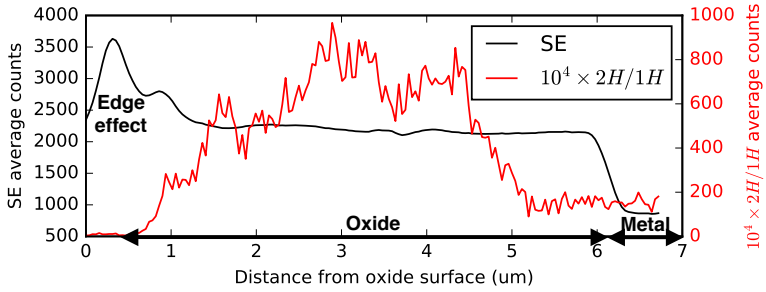


Figure 6.24: Hydrogen and deuterium shown in the oxide and metal-oxide interface on post-transition 225-day ZIRLO. The red rectangles indicate the region shown in figure 6.25. The dwell time for the acquisition was 30 ms px^{-1}.

presence of deuterium. However, even if SPPs do absorb hydrogen, it remains to be seen if they act as passageways for hydrogen, or simply hold it.



(a) $^2H/^1H$ ratio overlaid on SE.



(b) The $^2H/^1H$ image averaged along the y-axis.

Figure 6.25: $^2H/^1H$ ratio shown in the oxide and metal-oxide interface on post-transition 225-day ZIRLO. The red circle indicates the region of highest concentration.

A ROI was extracted, shown by the red rectangle, and plotted showing the $^2H/^1H$ ratio, in figure 6.25. Summing the counts along the y-axis of the image confirms that there is a large reduction in deuterium content in the last 1 µm of oxide, near the metal-oxide interface. The $^2H/^1H$ ratio is highest in the middle of the image. This is unexpected, as the surface of the oxide is closer to the source of deuterium (water), but may be due to large amounts of cracking and porosity

in the outer region of the oxide, giving a lower density of deuterium.

Using the newer NanoSIMS 50L at the Cameca headquarters, I acquired images using a beam current over three times higher than the Oxford instrument was capable of. The instrument was capable of higher resolution, and an image of post-transition 225-day ZIRLO can be seen in figure 6.26. Unfortunately, contamination from the resin covered a large part of the oxide, but in oxide in the lower region of the image, a deuterium hot-spot was found present two thirds through the oxide, just below a crack. A ROI in this area is shown in figure 6.27, showing the $^{2}H/^{1}H$ ratio. Here it can be seen that the hot-spot of deuterium is present approximately 1.3 µm from the metal-oxide interface at concentrations over 2000 times natural abundance. As with the other samples, there is a band very low in deuterium present.

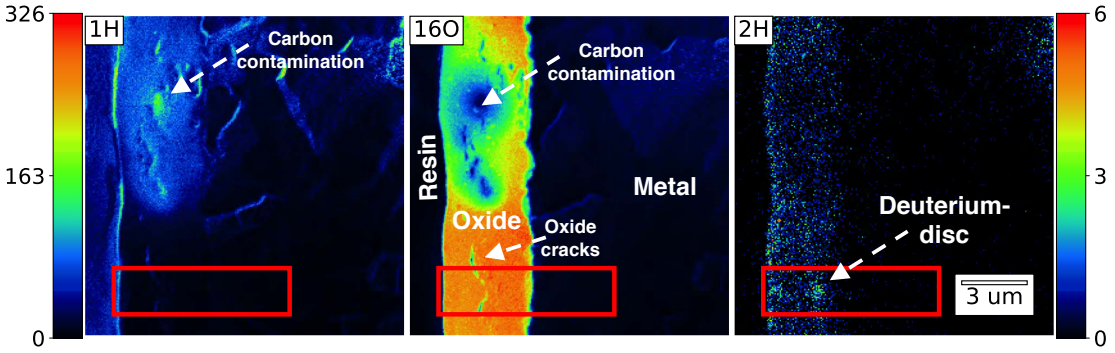
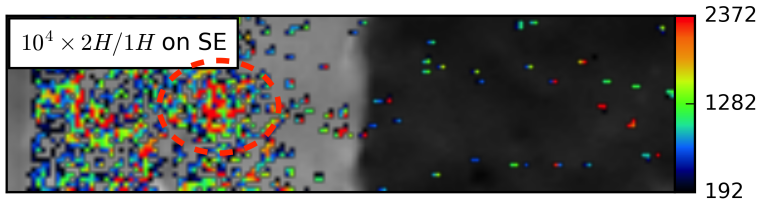


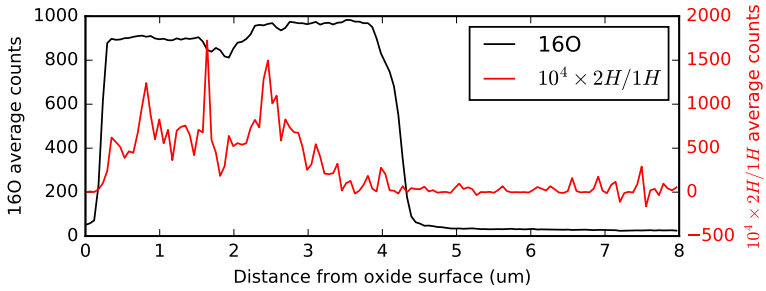
Figure 6.26: Hydrogen and deuterium shown in the oxide and metal-oxide interface on post-transition 225-day ZIRLO, acquired on a new-generation NanoSIMS 50L. The red rectangles indicate the region shown in figure 6.27. The primary beam current was 32 nA, over three times higher than that of the Oxford instrument normally used.

6.5.6 Post-transition 585-day Zr-1Nb

The post-transition 585-day Zr-1Nb sample shown in figure 6.28 shows overall very low transmission of deuterium through the oxide. Where ZIRLO oxides often have $^{2}H/^{1}H$ ratios above 600 times natural abundance, the post-transition Zr-1Nb has a much lower ratio throughout the entire oxide - barely peaking above 130 times natural abundance. This indicates that the Zr-1Nb alloy has much better resistance to hydrogen pickup than ZIRLO. Zr-1Nb was designed by Westinghouse to have



(a) ^{2}H/^{1}H ratio overlaid on SE.



(b) The ^{2}H/^{1}H image averaged along the y-axis.

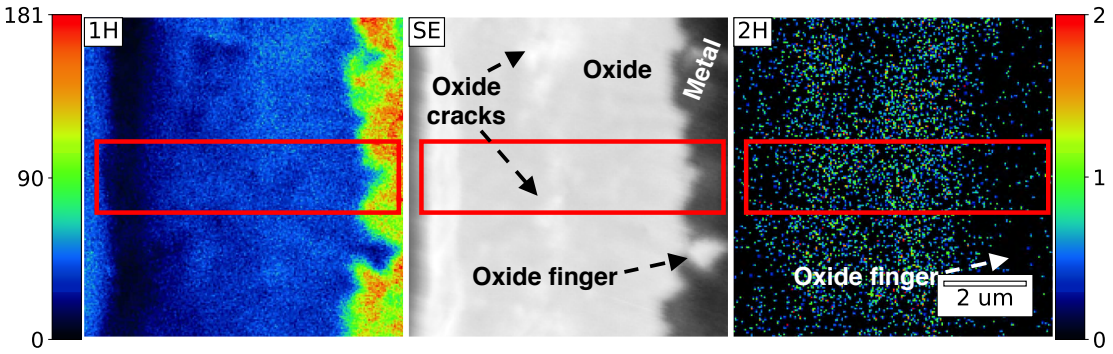
Figure 6.27: ^{2}H/^{1}H ratio shown in the oxide and metal-oxide interface on post-transition 225-day ZIRLO. The red circle indicates a hot-spot with deuterium content over 2000 times above natural abundance.

improved resistance to hydrogen-pickup, and hydrogen pickup measurements show that it succeeds at this. Therefore it is not surprising that such few counts are found.

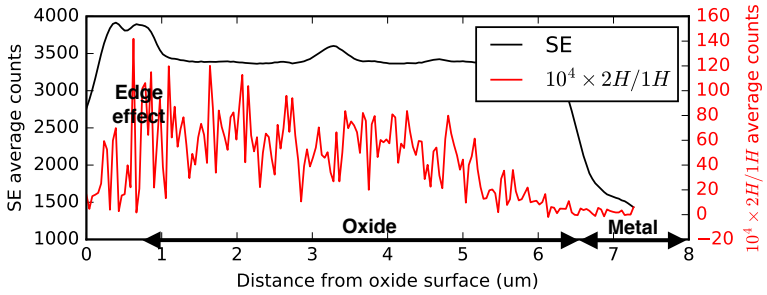
The distribution of deuterium, seen in figure 6.28, typically shows a noisy but even profile of deuterium through the oxide. However, looking at the deuterium image (2H) in figure 6.28a, there are two distinct layers running vertically down the image, parallel with the metal-oxide-interface. The white features in the middle of the oxide on the SE image are likely to be cracks, which might explain the gap between the deuterated regions. The lack of hydrogen in the top 1.5 µm of this thick oxide is unexpected, but can perhaps be explained due to a very porous outer region of the oxide being constantly "rinsed" with water, so that when the samples were removed from autoclave and dried, the hydrogen left with the water. The observation of a non-protective outermost region in the oxide agrees with the literature [69, 90, 218].

6.5.7 Barrier to hydrogen in oxide

On the sample of post-transition ZIRLO, shown in figure 6.29, there is a difference between the intensity of hydrogen and deuterium close to the metal-oxide interface.



(a) Overview image



(b) The above ROI averaged along the y-axis, showing the ^{2}H/^{1}H ratio overlaid on SE.

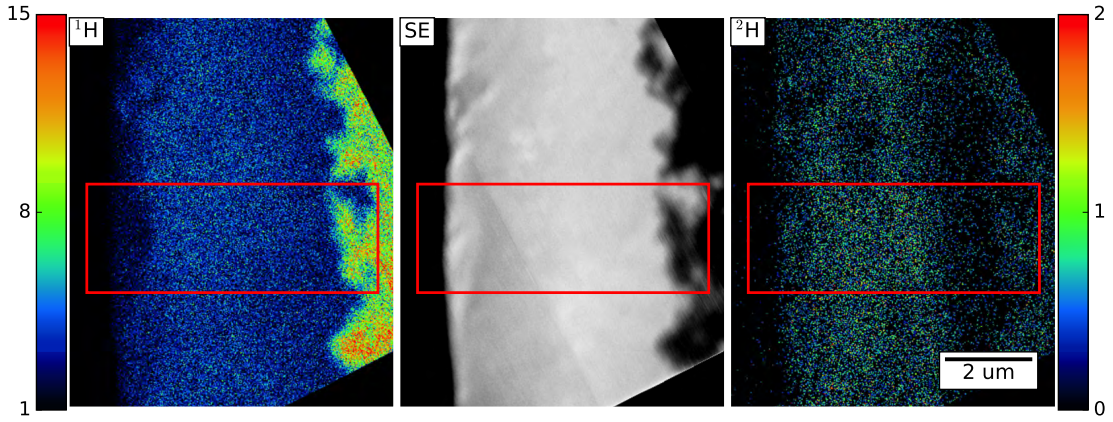
Figure 6.28: (a) Hydrogen and deuterium shown in the oxide and metal-oxide interface on post-transition 585-day Zr-1Nb. The red rectangles indicate the region shown summed in the line profile. The dwell time for the acquisition was 30 ms px^{-1}. (b) ^{2}H/^{1}H ratio shown in summed across the ROI in the red rectangle in (a).

The averaged line profile emphasises the drop in deuterium signal as it approaches the metal-oxide interface. Whilst the hydrogen is distributed relatively evenly throughout the oxide, the deuterium shows a marked depletion on the oxide side of the metal-oxide interface. This is very likely caused by the slow rate of diffusion of deuterium through the oxide combined with the fact that the samples were only exposed to deuterium for 45 days of the total oxidation duration.

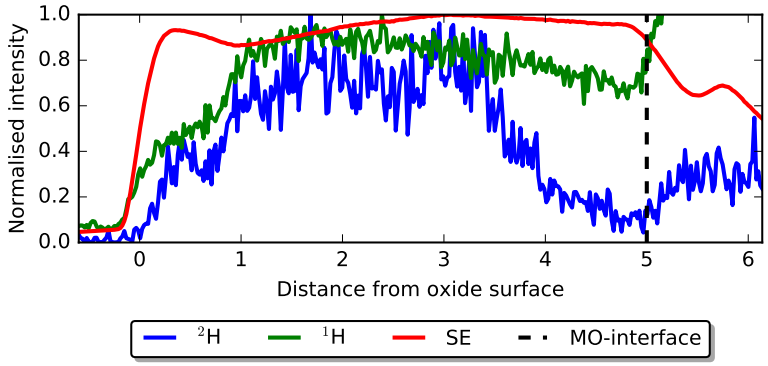
Diffusion profiles for deuterium through the oxide are discussed further in Chapter 7.

6.5.8 SEM imaging of post-SIMS areas

The NanoSIMS primary beam etching effect on the sample surface of these zirconium samples is significant. Figure 6.30 shows the result of imaging with the NanoSIMS after extensive surface cleaning using the caesium beam. The large hydride depicted



(a) NanoSIMS result from post-transition 225-day ZIRLO. The ROI indicates the location of the averaged line profile.



(b) Normalised profiles of ^{2}H(blue), ^{1}H (green) and SE (red) signals through the oxide and metal.

Figure 6.29: Maps and line profile showing decrease in ^{2}H compared to the ^{1}H signal near the metal-oxide interface.

strongly in the ^{2}H image overlaps several grains and is not visible directly on the SE image.

The ion etching damage was also clearly visible by FEGSEM imaging, particularly so in the metal, as shown in figure 6.31. On the SE images, the oxide appeared not to suffer particularly. However, in the weeks following measurements, the oxide on the surface of the cross-section samples spalled off the metal, which offered some frustration for samples that were yet to be imaged by EDS. Whether or not this was due to interaction with the caesium beam is unknown. To speculate, the rate of etching of the metal by the caesium beam appears to have been faster than the rate of etching of the oxide. The disappearance of the strained interface between

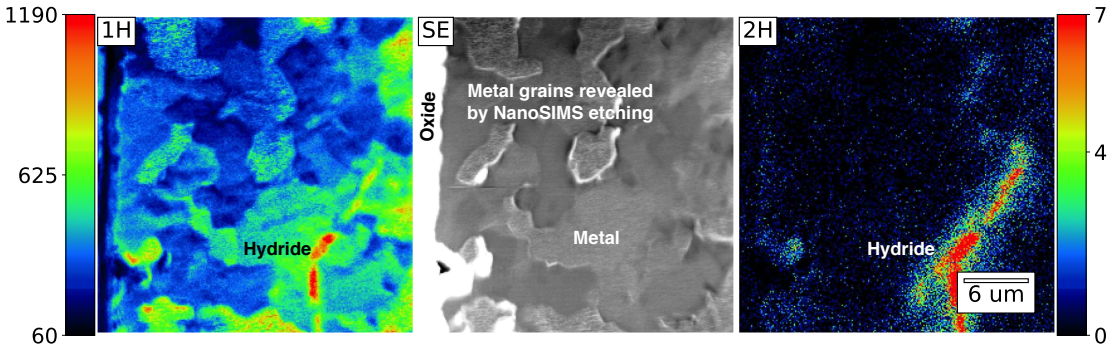


Figure 6.30: 125-day pre-transition ZIRLO NanoSIMS result. The oxide is on the far left, saturated in the SE image to enhance contrast in the metal. Metal grains are clearly visible due to etching due to the NanoSIMS caesium beam.

the oxide and metal could have relieved the oxide, making it expand and crack. These cracks could then have made the oxide spall from the metal.

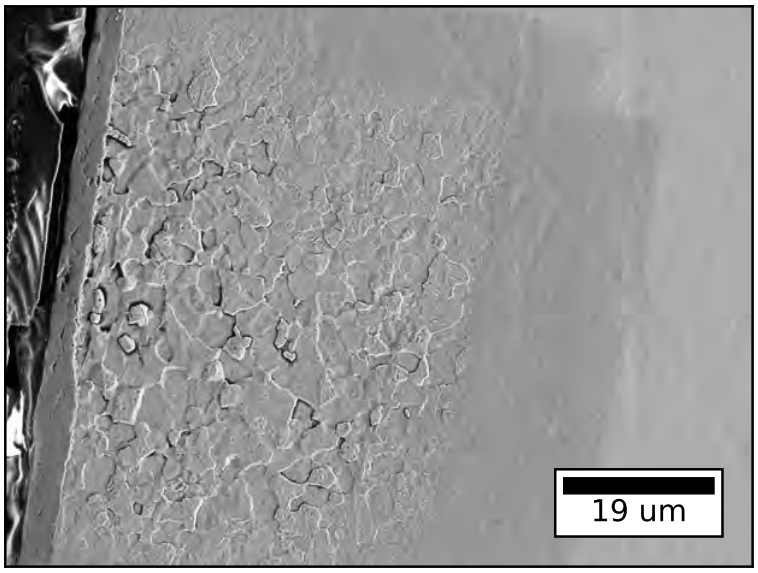


Figure 6.31: 225-day ZIRLO FEGSEM image after NanoSIMS analysis. The region analysed by NanoSIMS is clearly visible due to the metal grain etching from the caesium beam.

6.5.9 Deuterium hot-spots in the oxide

Of the many NanoSIMS results, some pixels in the oxide show much higher counts than the surrounding oxide. My hypothesis was that these "hot-spots" were second-phase particles rich in hydrogen. SPPs have been proposed as a short-circuit

mechanism for the ingress of deuterium, as has been argued by Elmoselhi [114] and Bossis [91]. In order to investigate this, EDS of the same area was performed using a FEGSEM. By locating the imaged regions using the SEM and cross-referencing the image features with the NanoSIMS SE image, EDS analysis could be performed. The biggest issue with this type of experiment is that the NanoSIMS technique is destructive. My hope was that the destructive primary ion beam from the NanoSIMS only destroyed the top section of SPPs, leaving enough material for EDS analysis.

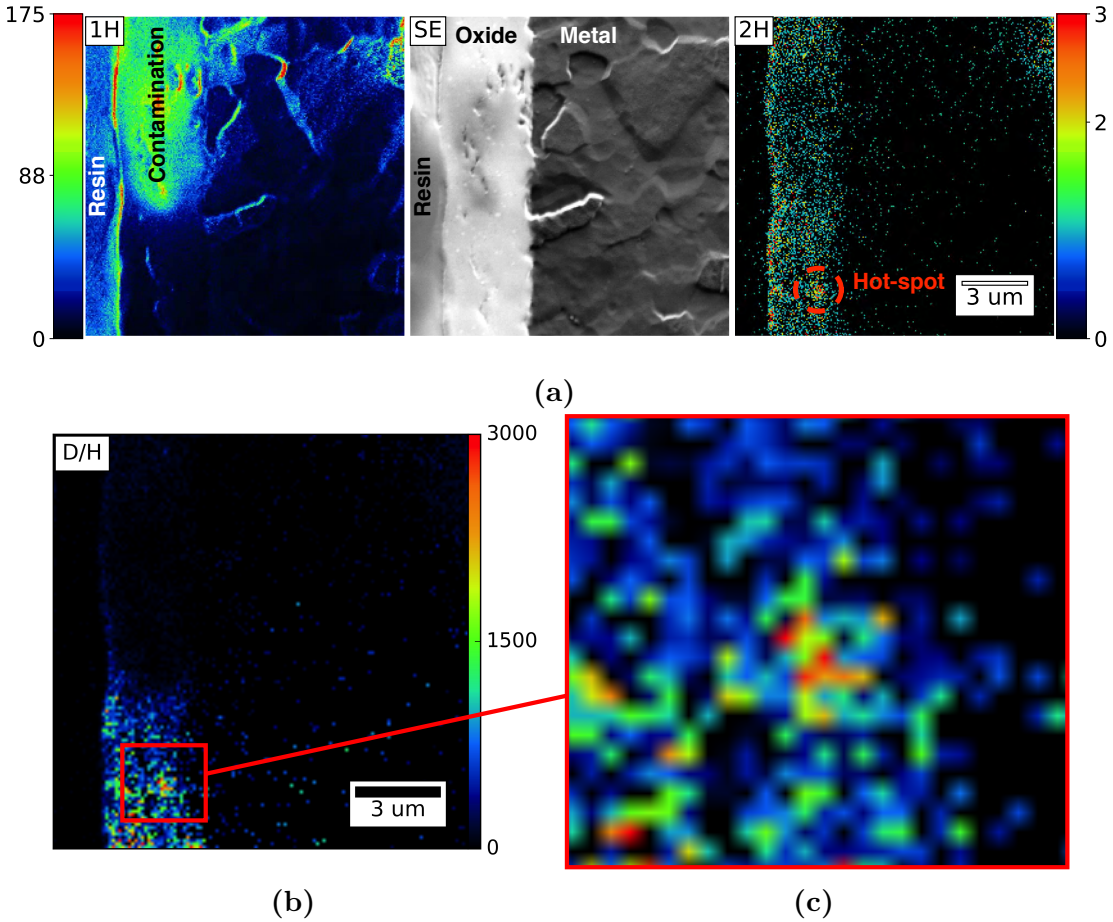


Figure 6.32: Post-transition 225-day ZIRLO sample (a) showing a deuterium hot-spot in the lower left of the ^{2}H image. The strong 1H signal in the upper left is due to carbon contamination. The $^{2}H/^{1}H$ ratio is shown in (b). The zoomed region (c) highlights a particularly strong spot, where the centre red region has a concentration 3,000 times the natural level of deuterium.

For post-transition 225-day ZIRLO, figure 6.32 shows the hydrogen/deuterium content and the ratio between deuterium and hydrogen ($\times 10^{4}$) respectively. Here the strongest signal in the zoomed region is a hot-spot 3000 times above natural

abundance. It would be very interesting to know what is causing this spike in deuterium.

Similarly, for pre-transition 225-day Zr-1Nb, a hot-spot of deuterium is visible half-way through the oxide in figure 6.33 - quite far away from the rest of the deuterium present near the surface of the oxide. The $^{2}H/^{1}H$ ratio image shows that the deuterium content is approximately 300 times above the natural concentration of the deuterium isotope in natural water.

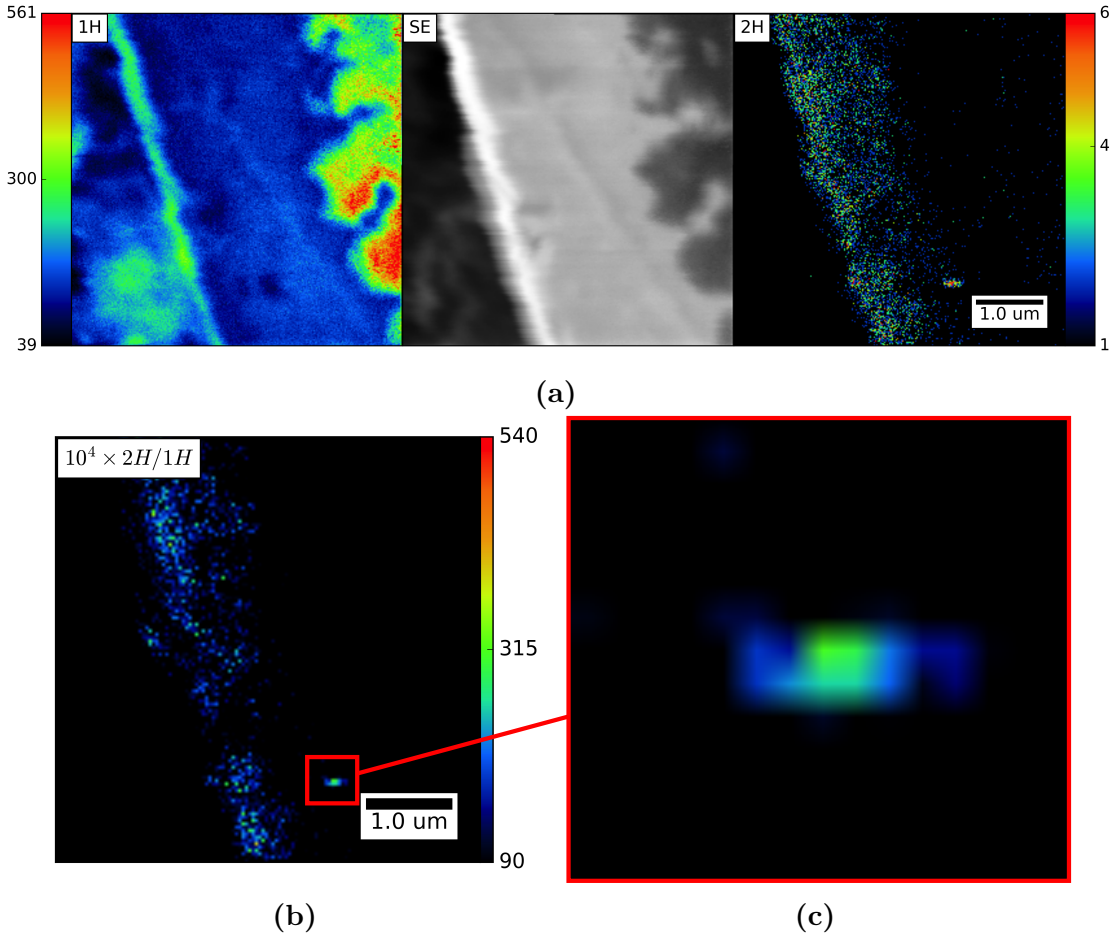


Figure 6.33: 225-day Zr-1Nb ratio image (b) of $^{2}H/^{1}H \times 10{,}000$ of the same area shown in figure 6.33a. The zoomed region (b) highlights a particularly strong spot, shown in (c), where the centre red region has a concentration 300 times the natural level of deuterium.

6.5.10 FEGSEM and EDS of hot-spot

A deuterium hot-spot found in the oxide of pre-transition 125-day ZIRLO contained deuterium 300 times above the natural abundance. This region was further analysed

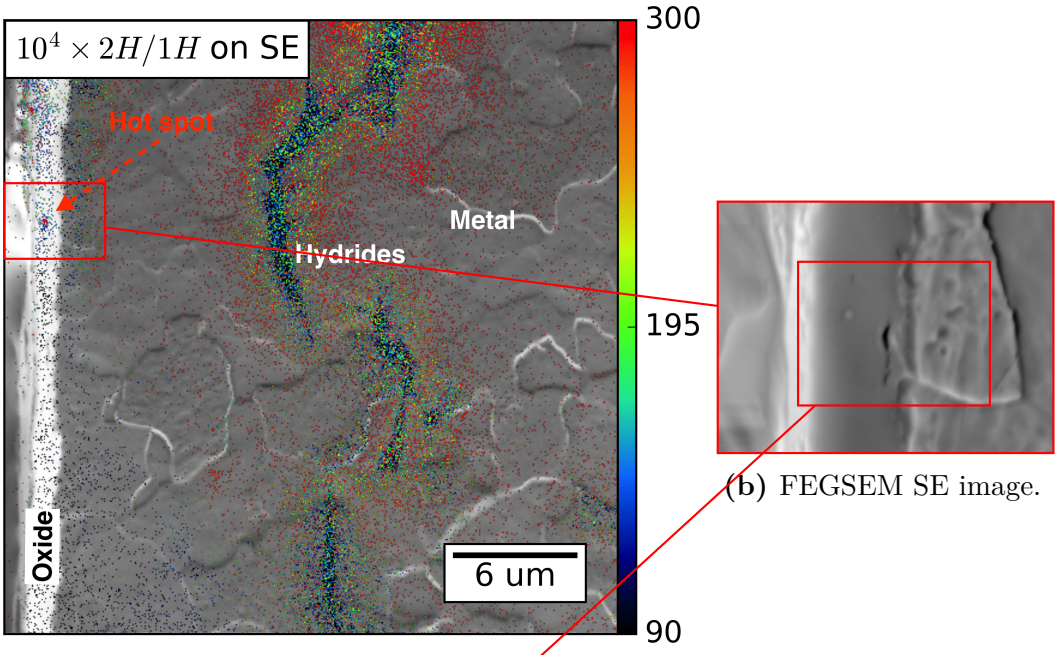
in a Zeiss Merlin FEGSEM using a high-performance EDS detector. The area was imaged at high magnification at 5 kV.

The NanoSIMS SE image was overlaid with the $^{2}H/^{1}H$ ratio, the FEGSEM SE image and the EDS map are all shown in figure 6.34. The EDS map in figure 6.34c contains a total of 7 SPPs, four of which are in the oxide. Only the SPP containing both Fe and Nb is overlaid with the hot-spot. The other three SPPs only contain Nb. This suggests that only $Zr(NbFe)_2$ SPPs contain deuterium (or hydrogen). On the other hand, the $Zr(NbFe)_2$ SPP is the closest SPP to the metal-oxide interface, making it more likely than the others to be unoxidised. This could mean that only metallic SPPs absorb hydrogen. One more $Zr(NbFe)_2$ SPP is present in the EDS map. It is in the metal and does not coincide with a peak in deuterium.

6.5.11 Deuterides in the metal

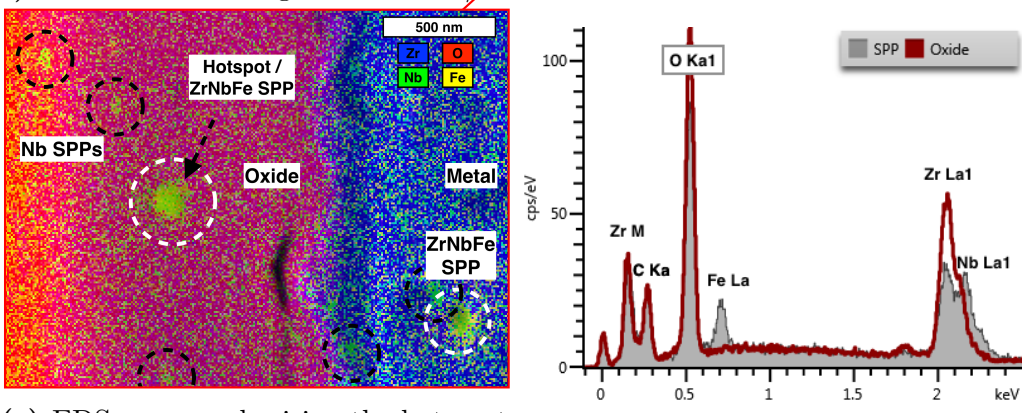
Once through the oxide, the hydrogen and deuterium form hydrides on cooling. These hydrides have a very characteristic shape when looked at through the NanoSIMS, and seem to differ significantly from what I have experienced from using EELS in the STEM to image them. A typical EELS result after separating the signals by ICA is shown in figure 6.35. Here the hydrides are 150 nm to 500 nm long.

By contrast, in NanoSIMS the hydrides are significantly larger and seem more connected than they do by STEM, shown in figure 6.36. The individual sections of the snaky hydrides range from 3000 nm to 6000 nm, more than ten times longer. This, combined with the fact that in EELS the hydrides are visible so close to the metal-oxide interface suggests to me that I am with STEM and EELS imaging a completely different "scale" of hydride than in NanoSIMS. Either the hydrides are clustered densely together, or exist individually but as far larger hydrides than the ones imaged near the metal-oxide interface by STEM. As previously discussed, is possible that the hydrides imaged in EELS are artificially induced by FIB-thinning. In contrast, the hydrides imaged here by NanoSIMS are likely to originate from the hydrogen ingress into the sample.



(a) NanoSIMS SE image with the $^2H/^1H$ ratio overlaid.

(b) FEGSEM SE image.



(c) EDS map emphasising the hot-spot in white.

(d) EDS spectra in and outside the SPP.

Figure 6.34: Deuterium hot-spot overlaid exactly with a $Zr(NbFe)_2$ SPP (white dashed circle). There is only one other $Zr(NbFe)_2$ SPP in the image, in the metal. In the oxide, three Nb-SPPs were found, which do not correspond to any other hot-spots.

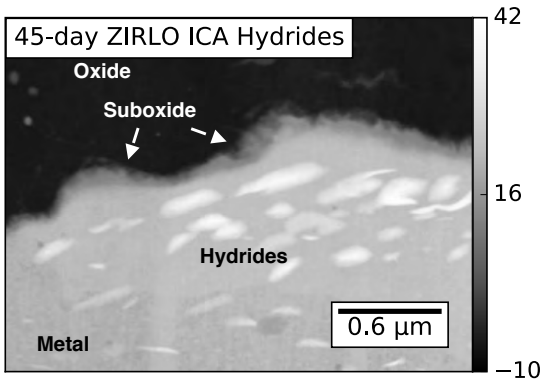


Figure 6.35: EELS ICA result showing the hydrides in TEM foil from a sample of 45-day ZIRLO. The oxide (dark) is at the top of the image whilst the metal (grey) is on the bottom, containing the hydrides in white.

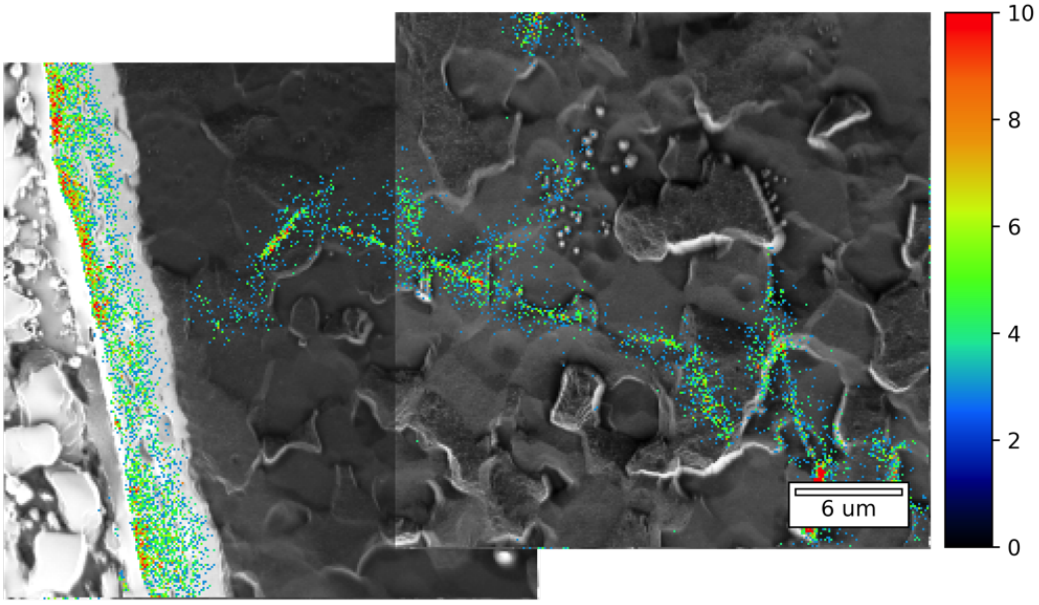


Figure 6.36: Aligned NanoSIMS SE images overlaid with the deuterium signal acquired on the Cameca NanoSIMS 50L in France. A long, winding hydride can be seen in the metal of 225-day post-transition ZIRLO. High counts are also visible in the oxide on the left.

6.6 Discussion

6.6.1 Comparison of alloys and impact of alloying additions on hydrogen pickup

At low magnification, NanoSIMS images provide a clear overview of a large part of the metal-oxide interface. The measured oxide thickness of the alloys from the SE images is in accordance with the trend expected from the overview in table 6.1 with the Zr-1Nb samples having a thicker oxide due to their longer oxidation time. For the pre-transition samples, the variation in oxide thickness on the samples appears higher for ZIRLO than Zr-1Nb. At post-transition the oxide thickness variations appear similar for ZIRLO and Zr-1Nb. The variations in thickness of the pre-transition ZIRLO oxide are likely to stem from the alloy being very close to transition according to its position on the graph in figure 6.1. Some local regions of the oxide are likely going through transition, as discussed previously in Chapters 4 and 5. While the oxide thickness is easily characterised at low magnification, there are no distinct differences in the hydrogen and deuterium content of the two alloys at this magnification.

At higher magnification, however, the differences become clearer. Firstly, the intensity of deuterium in the oxide on the ZIRLO samples is higher than on the Zr-1Nb samples. Particularly when looking from the outer oxide towards the metal-oxide interface there is a noticeable decrease in deuterium intensity. This change in intensity is not as obvious on the Zr-1Nb samples, both for pre- and post-transition. Instead, the concentration appears lower and more uniform throughout the oxide. The oxides of post-transition Zr-1Nb samples are found to contain substantially less deuterium compared to their ZIRLO counterparts. Whilst the ratio of ^{2}H / ^{1}H is typically 600 times natural abundance for pre- and post-transition ZIRLO, it rarely goes above 130 times natural abundance on the post-transition sample of Zr-1Nb. While direct comparison is difficult due to the Zr-1Nb samples being oxidised for longer in regular water, the lower deuterium ratio is expected due to the reported reduction in hydrogen pickup fraction of Zr-1Nb [90]. The main difference in composition between Zr-1Nb and ZIRLO is the reduction in Sn, as

shown in table 2.1 in Chapter 2 [15, 16]. The iron content in Zr-1Nb is also much reduced, with the Nb content remaining approximately constant. Hence, Sn is suggested to have the largest impact on corrosion resistance, as discussed in section 5.4.6 in Chapter 5. Although a reduction in Sn from 1.54% to 1.33% in Zircaloy-4 showed no noticeable change in the hydrogen pickup [127], it is likely that the large reduction is responsible for the vast improvement in Zr-1Nb over ZIRLO. Burr et al. [141, 219] showed through density functional theory (DFT) calculations that Zr-rich binaries such as Zr_3Fe and Zr_3Sn provide lower energy sites for hydrogen accommodation compared to α-Zr, and as such should function as hydrogen sinks in the metal. In the present work, the reason that no difference in deuterium concentration is found in the metal is due to the precipitation of hydrides. In the metal deuterium travelles much faster than in the oxide [115] (as described in Chapter 2), so it quickly spreads out and lowers the local concentration. Upon cooling, the hydrogen in the metal precipitates as hydrides, but a much larger region of the metal would need to be measured to compare the hydrogen content from the hydrides in the metal by NanoSIMS. Burr et al. [219] also show that β-Nb exhibits the same enthalpy of solution of hydrogen as α-Zr [219]. To my knowledge, no such studies exist calculating the solution enthalpies for the equivalent oxides, and would greatly improve the understanding of hydrogen in oxides. However, if a similar trend to the Zr-Sn binaries is found for oxides, this could explain the large increase in hydrogen content in the oxide for ZIRLO over Zr-1Nb. The improved hydrogen-pickup resistance seen in Zr-1Nb could have three explanations. Firstly, a significantly reduced deuterium diffusion coefficient in the Zr-1Nb oxide would cause deuterium to diffuse more slowly into the oxide. A second explanation could be that the oxide grew more slowly on Zr-1Nb than on ZIRLO in the 45 days of D_2O exposure, causing less free deuterium to be produced in the oxidation process. Thirdly, the HPUF of the alloy could be reduced by preventing hydrogen from entering the oxide. Looking ahead to the diffusion profiles measured in Chapter 7, it is seen that the measured diffusion coefficients of the Zr-1Nb and Zircaloy-4 oxides are very similar, even though the Zr-1Nb oxide is shown to contain much

less deuterium. This implies that the hydrogen pickup resistance cannot be due to a change in diffusion coefficient of the oxide. On the pre-transition samples, the ZIRLO and Zr-1Nb grew approximately the same amount in the D_2O oxidation step. This cannot explain the increased deuterium intensity seen on the pre-transition ZIRLO samples by NanoSIMS. Hence, this suggests that the third explanation must be correct. Garde et al. argues [127] that if one assumes that hydrogen diffuses into the alloy as a proton, then whether the proton reacts with an electron at the surface of the oxide or within the metal will affect whether the hydrogen atom is absorbed into the alloy or lost to the coolant. If the n-type semiconductor zirconia [220] has excess electrons available due to the replacement of a Zr^{4+} ion by a higher valence ion like Nb^{5+}, then replacement by a trivalent Sn^{3+} will increase the chance of hydrogen migration towards the metal. Hence, an increasing concentration of tin should increase the HPUF of the alloy. Therefore, the improvement in hydrogen pickup resistance seen by Zr-1Nb must be due to the reduction in HPUF, probably caused by the elimination of doping from Sn-substitution that occurs in ZIRLO!

6.6.2 Oxide barrier to hydrogen ingress

The distribution of deuterium in the oxide has been shown to vary substantially between alloys. For all alloys, a distinct diffusion profile is shown across the oxide close (within 1 µm) to the metal-oxide interface. In the outer oxide on nearly all samples, the deuterium is distributed uniformly in relatively high concentration, displaying no apparent diffusion-behaviour. This suggests that the outer oxide is completely penetrated by the autoclave water, and that only the oxide closest to the metal-oxide interface acts as a barrier. Whilst previously shown for individual depth profiles taken perpendicularly to the surface of the oxide, these novel cross-sectional results emphasise how the outer oxide is penetrated evenly on a large scale. The idea that only the innermost oxide functions as a protective barrier to hydrogen ingress is not new [114, 127]. Previously shown in figure 2.24 in Chapter 2, Elmoselhi et al. [114] showed depth profiling SIMS results showing deuterium concentration in two regimes - a flat region in the outer oxide, followed by a diffusion profile towards

the metal-oxide interface. This is the same that I observe. The high amount of deuterium in the outer oxide can be attributed to cracks and pores and oxide fully permeated by water. TEM images by Ni et al. [83], shown in figure 6.37 display many small cracks in the outer oxide. Closer to the metal-oxide interface, they report that the oxide appears much denser, with only a few cracks, parallel to, and isolated from the outside oxide surface. The protective layer aligns well with the region of denser and less porous oxide that I have observed near the metal-oxide interface by TEM in the previous Chapters. This denser protective oxide explains the diffusion behaviour and the deficiency in deuterium I see at the metal-oxide interface. Here it is shown by SIMS for regions much larger than is possible by TEM or conventional SIMS depth profiling.

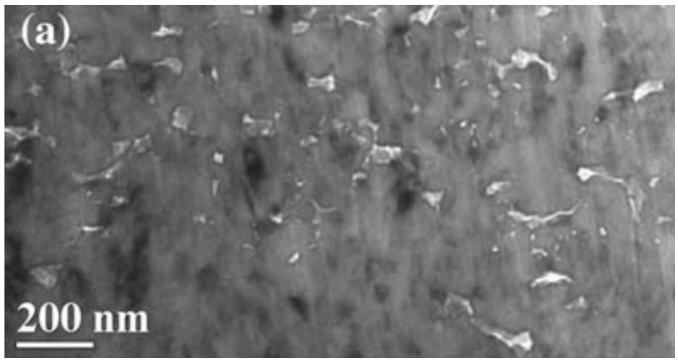


Figure 6.37: Bright-field TEM image of an area in the outer part of oxide containing cracks/pores associated with small equiaxed grain, on a sample of Zircaloy-4 after 90 days at 360 °C [83].

6.6.3 Hydrogen hot-spots in the oxide

Novel high-resolution NanoSIMS mapping has shown for the first time that high-intensity regions of deuterium exist in the oxides of ZIRLO and Zr-1Nb. They are found particularly frequently in the outer half of the oxide, though are sometimes found close to the metal-oxide interface. Their sizes, on the order of 100 nm, suggest that they are SPPs, which is in line with previous work done by Bossis et al. [91] where they found channels of deuterium matching the presence of Fe-containing SPPs. Through the combination of high-resolution EDS analysis with NanoSIMS analysis, a single hot-spot was found to perfectly coincide with a metallic ZrNbFe

SPP. The Fe-content further bolsters Bossis' work. The possibility of SPPs acting as pathways for hydrogen ingress has long been suspected [90, 120], and has been shown to be likely in high-Nb content ZrNbFe Laves phase SPPs [219]. However, while SPPs may contain hydrogen/deuterium, it is still unclear whether the hydrogen is able to escape from the SPP once it is absorbed. They could potentially function as hydrogen sinks rather than shortcuts. For the SPPs present in Zr-1Nb this is unclear, but it has been shown that partially metallic $Zr(Cr, Fe)_2$ SPPs [141] should aid hydrogen transport through the oxide, according to a model proposed by Hatano et al. [120]. As previously discussed, it seems likely that the outer oxide on all samples studied was permeated with water, meaning that hydrogen does not need to diffuse in order to permeate the outer oxide. Hence, SPPs should only function as shortcuts for hydrogen ingress if situated in the protective oxide, close to the metal-oxide interface. The possible migration of hydrogen-rich SPPs once the SPPs oxidise is also unclear. Due to the difficulty of detecting hydrogen by spectroscopy in STEM, DFT analysis similar to that done by Burr et al. [219] is perhaps best suited to this research.

6.7 Summary

In this Chapter, I have presented NanoSIMS results acquired on cross-sections of oxidised zirconium alloys. I have demonstrated the various difficulties associated with this type of analysis and shown ways of overcoming them in order to present the highest spatial-resolution SIMS analysis acquired on zirconium alloys to date. The following summarises the findings, with some discussion as to their context in the problem of hydrogen uptake of zirconium alloys in reactor.

- Samples of oxidised zirconium alloys cross-sectionally cut and polished have been successfully imaged on the NanoSIMS at both high and low magnification. Typical issues, including carbon contamination and silica particle contamination, have been identified. Methods of successfully handling these issues, such as changing sample medium, have been suggested.

- The deuterium distribution in the oxide has been shown to vary significantly between samples in pre- and post-transition. Pre-transition samples are shown to have a generally low concentration of deuterium, particularly concentrated at the top part of the oxide, while post-transition samples contain deuterium throughout. This indicates a breakdown of the protective behaviour against hydrogen ingress between pre- and post-transition. The protective behaviour has been shown to be due to the innermost oxide layer and is compared to previous measurements done on other alloys. The protective layer is shown to coincide with the denser and less porous oxide observed near the metal-oxide interface by TEM in the previous Chapters.

- The deuterium content of Zr-1Nb is significantly lower than that of ZIRLO and Zircaloy-4, in line with the expected improved corrosion-resistance of Zr-1Nb. The reduction of Sn is emphasised as playing the major role in the improved corrosion-resistance, and the role of Sn on hydrogen pickup is discussed with reference to DFT literature. Taking into account the diffusion coefficients reported in Chapter 7, a reduction in HPUF of the Zr-1Nb alloy is shown to be the cause of the improved hydrogen pickup resistance.

- Zirconium-hydrogen binaries called hydrides are shown in large numbers in the metal. These appear to be different from the hydrides shown by EELS analysis near the metal-oxide interface in previous Chapters, as they appear much further away from the interface, and are substantially larger (on the order of 10 µm and larger compared to 500 nm or smaller). Typical FIB liftouts will not reach deep enough to see these hydrides in the TEM. It is proposed that the hydrides typically visible on FIB samples are normally as a result of sample preparation.

- Hot-spots of deuterium found by NanoSIMS are shown to coincide with SPPs measured by EDS in SEM. The possible role of SPPs on the mechanism of hydrogen ingress is discussed. More experimental evidence as well as specific

theory-work on SPPs that show high hydrogen content is needed to further this understanding.

This concludes the discussion of the SIMS study of cross-sectioned Zirconium samples. In the next Chapter, samples are analysed in a perpendicular fashion, imaging through oxide into the metal.

7 Depth profiling

Contents

7.1 Introduction 231
7.2 Results 235
7.2.1 One-dimensional depth profiles 235
7.2.2 Three-dimensional depth profiles 238
7.3 Discussion 245
7.3.1 Hydrogen pathways through the metal-oxide interface . 245
7.3.2 Diffusion profiles 247
7.3.3 Hydrogen uptake hypothesis and relation to oxidation mechanism 252
7.4 Summary 253

7.1 Introduction

Seeing the difficulties arising from the sample preparation process in cross-sectioning the Zr-samples, an attempt was made to image the samples perpendicular to the previous method. By depth profiling with the NanoSIMS primary beam directly through the oxide towards the metal-oxide interface, no sample preparation (besides platinum-coating the oxide surface for electrical conductivity) was necessary. Whilst the surface is relatively rough, the small regions imaged were themselves comparatively flat. Depth profiling is subject to a number of limitations, in particular

the crater effect [221] and sample drift due to the long acquisition time. Active drift correction was not available on the NanoSIMS. Despite these limitations, I was able to extract useful preliminary data from the alloys.

Whilst the NanoSIMS returns accurate X-Y calibrated maps, it lacks a depth-calibration due to the material-dependency of the milling rate. However, the oxide thickness is known approximately from the weight gain of the alloy, and both the oxygen and SE signals show a large intensity difference between the metal and oxide (as reported in section 6.3.3). Therefore, for samples with oxide thin enough to mill through, an approximate depth distance calibration was possible. The metal-oxide interface is indicated on the images in this Chapter by a vertical line.

Several deuterated samples were imaged using this method, shown in table 7.1. Because only a few deuteration runs were planned in the MUZIC-2 project, none of these samples have had their weight gain measured at regular intervals during the autoclave oxidation, although the four samples with a regular H_2O pre-oxidation are taken from the materials processed by Westinghouse for the MUZIC-2 programme. The weight gain curves for Zircaloy-4 and high-temperature annealed Zr-1Nb are shown in figures 7.1 and 7.2. Since the temperature of oxidation for all samples was 350 °C to 360 °C, these weight-gain curves act as a guideline for the state of the samples relative to transition. For each of the three pairs of samples, the first was pre- or at-transition whilst the second was post-transition. The substantial difference in the weight gain of the two Zircaloy-4 alloys that had both been oxidised for 61 days, but in separate autoclaves ($22.1\,\mathrm{mg\,dm^{-2}}$ and $27.0\,\mathrm{mg\,dm^{-2}}$) may be attributed either to the temperature difference of 10 °C between the D_2O and H_2O oxidations (higher for H_2O), or more likely the possibility of slightly different chemistries in the autoclave water. Despite this, the size of the difference in weight gain is surprising.

In addition to the weight gain, measurements from the MUZIC-2 project of both the total hydrogen content of the alloy as well as the instantaneous hydrogen pickup fraction (IHPUF), are shown in figures 7.3 and 7.4. The additional D_2O oxidation should have placed the pre- and post-transition Zr-1Nb samples in states of high and low IHPUF respectively. For both Zircaloy-4 samples, it is very difficult

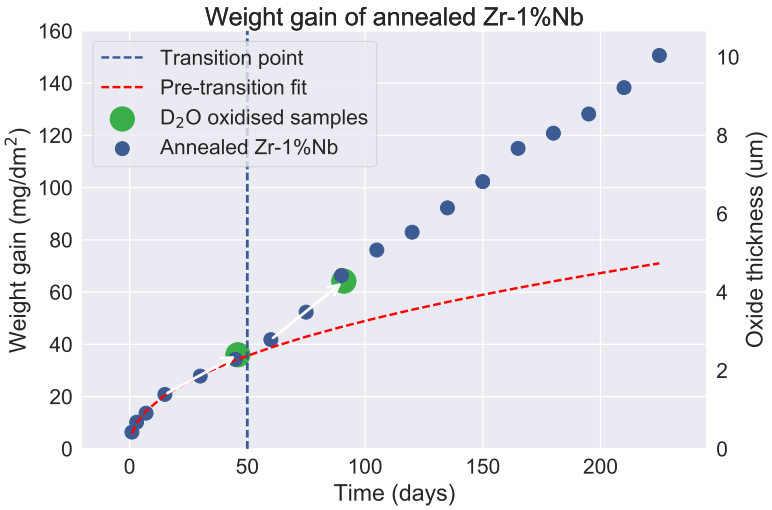


Figure 7.1: Weight gain of annealed Zr-1Nb at 360 °C. The green spots indicate the samples after D_2O oxidation. The white arrows indicate the D_2O oxidation period of 31 days. The fit (red dashed line) uses equation 2.4 where $k = 49$ and $n = 2.2$.

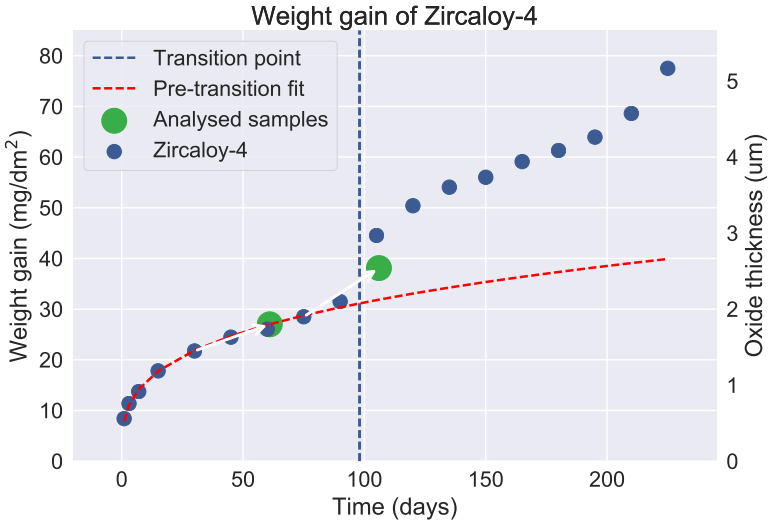


Figure 7.2: Weight gain of Zircaloy-4 at 360 °C. The green spots indicate the samples after D_2O oxidation. The white arrows indicate the D_2O oxidation period of 31 days. The fit (red dashed line) uses equation 2.4 where $k = 8.2\,\mathrm{mg\,dm^{-2}}$ and $n = 0.29$. The weight gain data and raw samples are the same as in Chapter 5.

Alloy	Oxidation (days) 100% H_2O	100% D_2O	50% D_2O	pH	Weight gain (mg dm^{-2})
Zircaloy-4			61	8.82	22.1
Zircaloy-4			147	8.82	44.0
Zircaloy-4	30	31		≈ 7	27.0
Zircaloy-4	75	31		≈ 7	38.1
Zr-1Nb**	15	31		≈ 7	36.0
Zr-1Nb**	60	31		≈ 7	64.2

Table 7.1: Alloys studied by depth profiling in this project.

*Other than the two Zircaloy-4 samples which were oxidised at pH 8.82, all other samples were oxidised in pH-neutral water, with a typical initial pH of about 6.8, with some day to day variation. The pH of the water increased to between 7.2 and 7.8 after oxidation. **Zr-1Nb annealed at 720 °C for 24 hours to increase SPP size.

to surmise the IHPUF condition after the second oxidation, although the total hydrogen content should have substantially increased. similar IHPUF data has previously been published [207]. The most notable takeaway from the paper is the distinct rise and fall in instantaneous hydrogen pickup in the days leading up to transition. This type of behaviour is clear on the Zr-1Nb sample in figure 7.3. Whilst not present on the Zircaloy-4 data from the MUZIC-2 program, it is a feature typically found for the rest of the alloys oxidised as part of the project. This increase in IHPUF is perhaps surprising, as it shows that the hydrogen pickup increases before the oxide loses its protective behaviour due to transition.

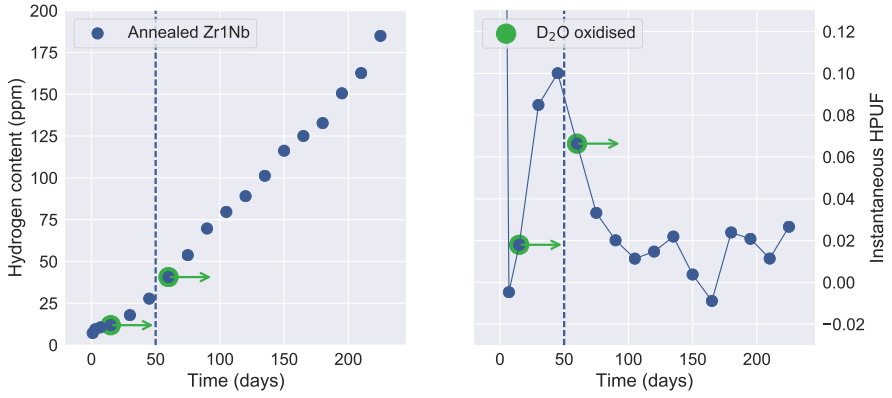


Figure 7.3: (Left) the total hydrogen content and (right) the IHPUF of the annealed Zr-1Nb MUZIC-2 samples. Hydrogen data was not available for the samples after D_2O oxidation. Instead, the green arrows show the x-axis position of the condition the samples should be in after 31 days of further (D_2O) oxidation.

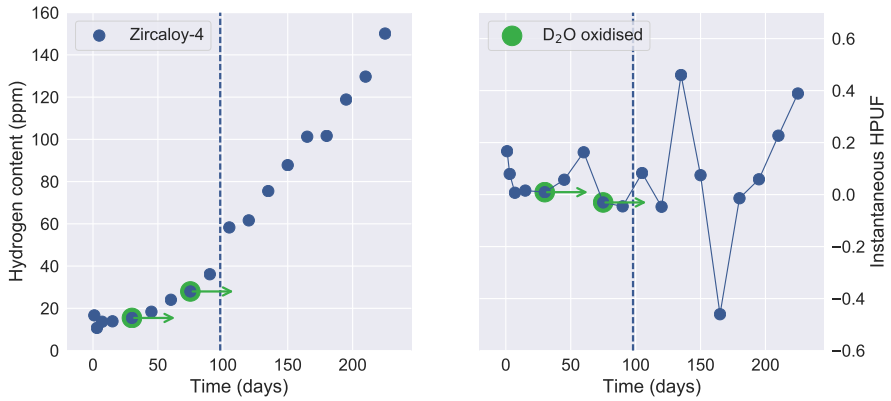


Figure 7.4: (Left) the total hydrogen content and (right) the IHPUF of the MUZIC-2 Zircaloy-4 samples. Hydrogen data was not available for the samples after D_2O oxidation. Instead, the green arrows show the x-axis position of the condition the samples should be in after 31 days of further (D_2O) oxidation.

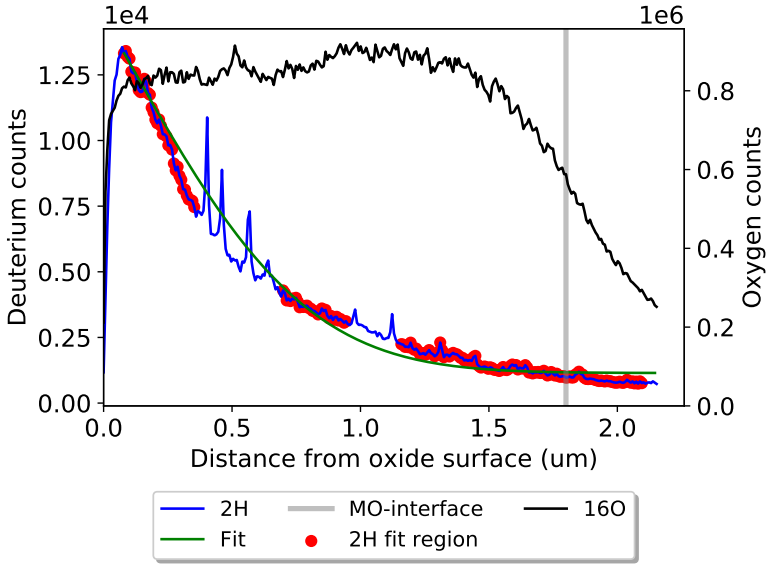
7.2 Results

7.2.1 One-dimensional depth profiles

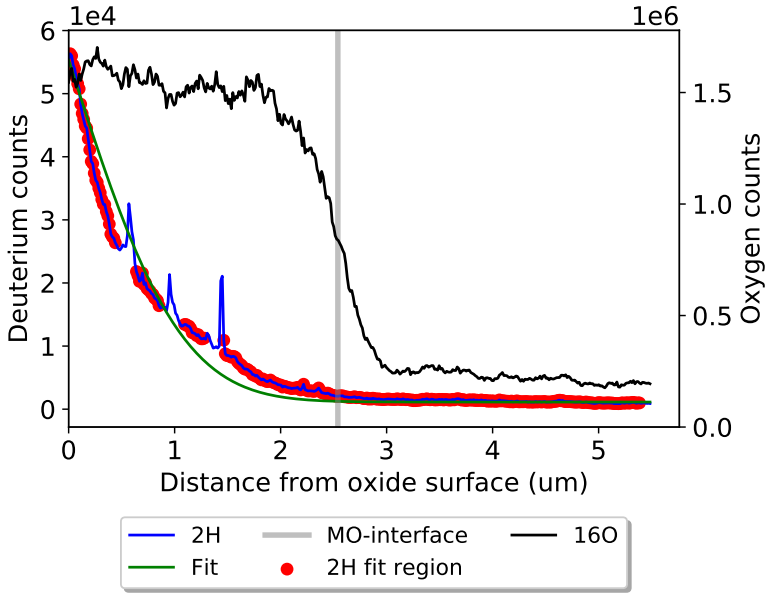
Figures 7.5 and 7.6 show typical one-dimensional depth profiles for the four samples oxidised at neutral pH. The one-dimensional depth profiles were acquired by Dr. Haibo Jiang, a fellow DPhil student. The 61-day pre-transition and 106-day post-transition Zircaloy-4 samples show convincing diffusion profiles throughout the oxide. Whilst both samples were oxidised for 31 days in the same deuterated water, the post-transition contained 2.3 times more deuterium than the pre-transition sample after normalising by oxygen counts. In addition to the deuterium profile, spikes in the deuterium content are seen on the gradually decreasing deuterium profile.

Fitting equation 3.8 yields diffusion coefficients of $5.8 \times 10^{-20}\,\mathrm{m^2\,s^{-1}}$ and $1.3 \times 10^{-19}\,\mathrm{m^2\,s^{-1}}$ for the pre- and post-transition samples respectively. The oxide thickness is converted from the weight gain data, and is assumed to be correct, despite the evidence of varying oxide thickness from Chapters 4 and 5.

In contrast to the Zircaloy-4 samples, the annealed Zr-1Nb samples shown in figure 7.6 show a very different deuterium profile through the oxide. The 46-day pre-transition annealed Zr-1Nb shows a sharp decline in deuterium content in the first 300 nm of oxide, before settling to a nearly linear deuterium profile in through the oxide. In the final 1 µm of oxide before the metal-oxide interface there

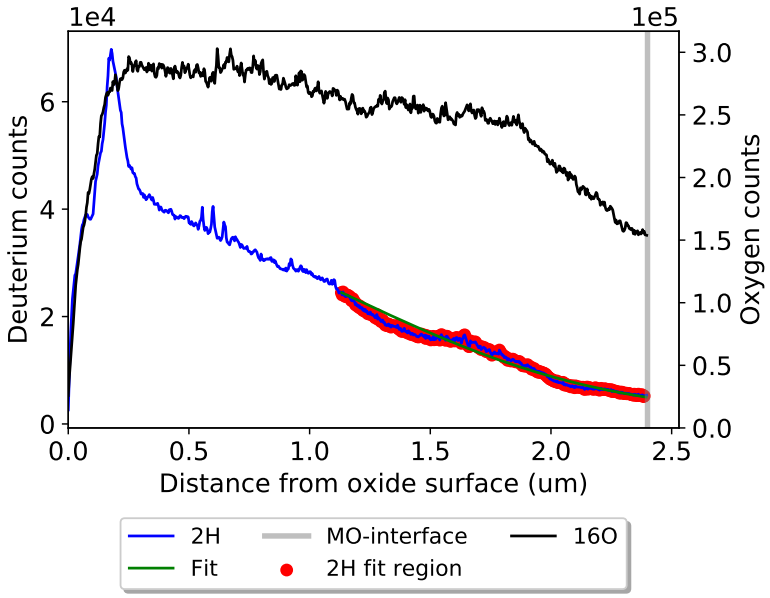


(a) 61-day pre-transition Zircaloy-4.

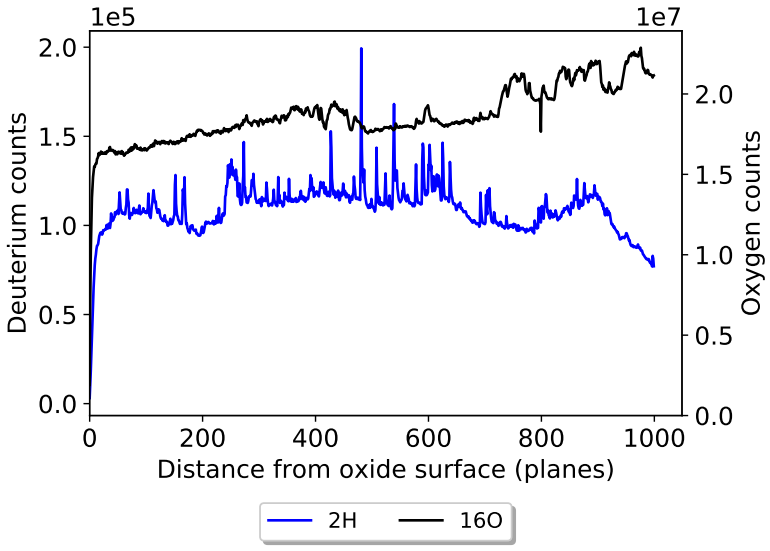


(b) 106-day post-transition Zircaloy-4.

Figure 7.5: (a) 1D depth profile acquired on 61-day pre-transition Zircaloy-4. (b) 1D depth profile acquired on 106-day post-transition Zircaloy-4. Both were oxidised at neutral pH and the 61-day sample is fitted by equation 3.8. The one-dimensional depth profiles were acquired and are reproduced with permission by Dr. Haibo Jiang.



(a) 46-day pre-transition annealed Zr-1Nb.



(b) 91-day post-transition annealed Zr-1Nb.

Figure 7.6: (a) 1D depth profile acquired on 46-day pre-transition annealed Zr-1Nb. (b) integrated 3D depth profile acquired on 91-day post-transition annealed Zr-1Nb. Both were oxidised at neutral pH and are fitted by equation 3.8. Since the metal-oxide on the 91-day was not reached the sample meant that the depth could not be calibrated. The average oxide thickness of the 91-day sample was 4.28 µm. The one-dimensional depth profiles were acquired and are reproduced with permission by Dr. Haibo Jiang.

is a curve in the profile. A diffusion profile was fitted from this point until the metal, yielding a diffusion coefficient of $5.8 \times 10^{-20}\,\mathrm{m^2\,s^{-1}}$ This is about the same as the 61-day Zircaloy-4 sample. For the 91-day annealed Zr-1Nb sample, no one-dimensional depth profile was acquired. Instead, as is described in section 7.2.2, a three-dimensional depth profile was taken. For completeness, it was summed across the X and Y axes and presented in figure 7.6. The oxide thickness calculated from the weight gain of the 91-day sample was 4.28 µm, nearly 1.7 times thicker than the 2.54 µm oxide on the 106-day Zircaloy-4 post-transition sample. As it was so thick, the NanoSIMS was unable to mill through the oxide before hitting a memory limit. Since the metal-oxide interface was not reached, the depth calibration could not be performed. Instead the x-axis is measured in image planes.

7.2.2 Three-dimensional depth profiles

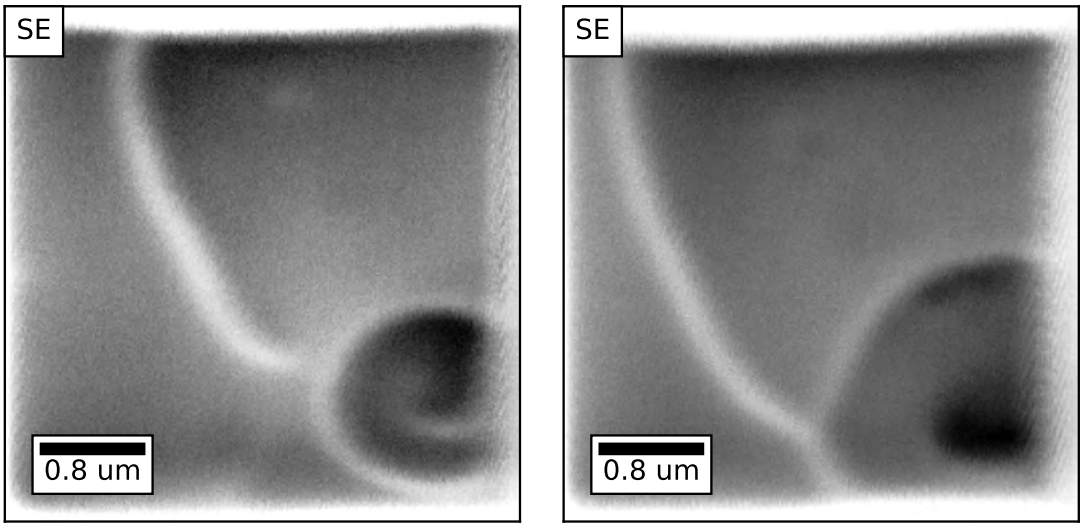
After acquiring the depth profile for the 46-day pre-transition annealed Zr-1Nb sample, shown in figure 7.6a, concerns were raised of the possibility of sample drift interfering with the results. I was able to minimise the problems by recording a data cube by repeated imaging of the same location, milling into the sample. Later alignment and cropping of the data cube helped remove edge effects, providing reasonably accurate data of the extracted volume. Conventional depth profiling would instead record the whole area, including all edge effects, into a single profile.

As it is quite difficult to present a 3D figure, I have chosen to sum the 3D volume parallel to the X axis, and present this as an image with the oxide on the left and the metal on the right, as was done in Chapter 6. The images tell more of a story than the depth profiles do on their own, as will be shown for the deuterium peaks along the diffusion profiles seen previously in section 7.2.1.

Drift correction

I attempted to compensate for the drift through post-processing. Unfortunately, the SE images - which had the highest amount of surface detail - did not always contain sharp enough features and rendered automatic image alignment unstable.

The images would sometimes be out of focus, and often the variable rate of milling - for instance due to horizontal cracks in the oxide - made it difficult for typical drift-correction software to predict the movement. An example of a crater causing a faster milling rate can be seen in figure 7.7.



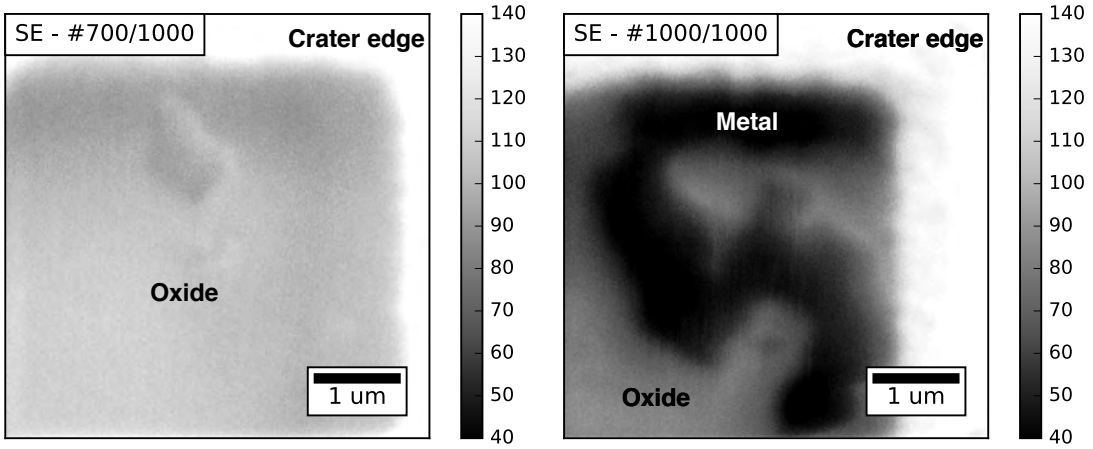
(a) Slice 490 of 1000 total. **(b)** Slice 668 of 1000 total.

Figure 7.7: SE images extracted from a 3D data cube from post-transition annealed Zr-1Nb. The crack in the bottom right of the image becomes wider due to different milling rates.

Often the post-processing drift correction would measure significant drift where, by stepping through the image slices by eye, it was clear that there was minimal drift present. Drift correction was attempted using the AutoTrack feature in the OpenMIMS plugin [222] for ImageJ/Fiji [223–225], as well as the `Signal2D.align2D()` method in Hyperspy[148]. As drift correction proved unreliable, it was decided that where automatic drift correction failed, the best approach was to crop the width and depth of the volume to select a region that was evenly milled. Regardless of drift correction, all volumes were cropped to remove edge features whilst maximising signal. As such, the final volumes vary somewhat in width and height.

Locating the metal-oxide interface

The oxygen signal varied significantly for some samples as the beam milled through the oxide. In some cases it was found that qualitative visual inspection of the 3D data was necessary to ascertain where the metal-oxide interface was. In other cases the oxygen signal would saturate its detector, forcing the NanoSIMS to switch off the detector for the remainder of the run. Thankfully, the secondary electron yield of the metal was significantly lower than that of the oxide, and never saturated, so as the metal-oxide interface came into view whilst milling, the SE image provided a strong contrast, as seen in figure 7.8.



(a) Slice 700 of 1000 total. **(b)** Slice 1000 of 1000 total.

Figure 7.8: The SE signal in the final slices of the 1000-slice volume reveals metal with a very dark contrast due to low secondary-electron yield. Due to oxygen-saturation in the metal, the equivalent oxygen images show less contrast.

Pre-transition Zircaloy-4

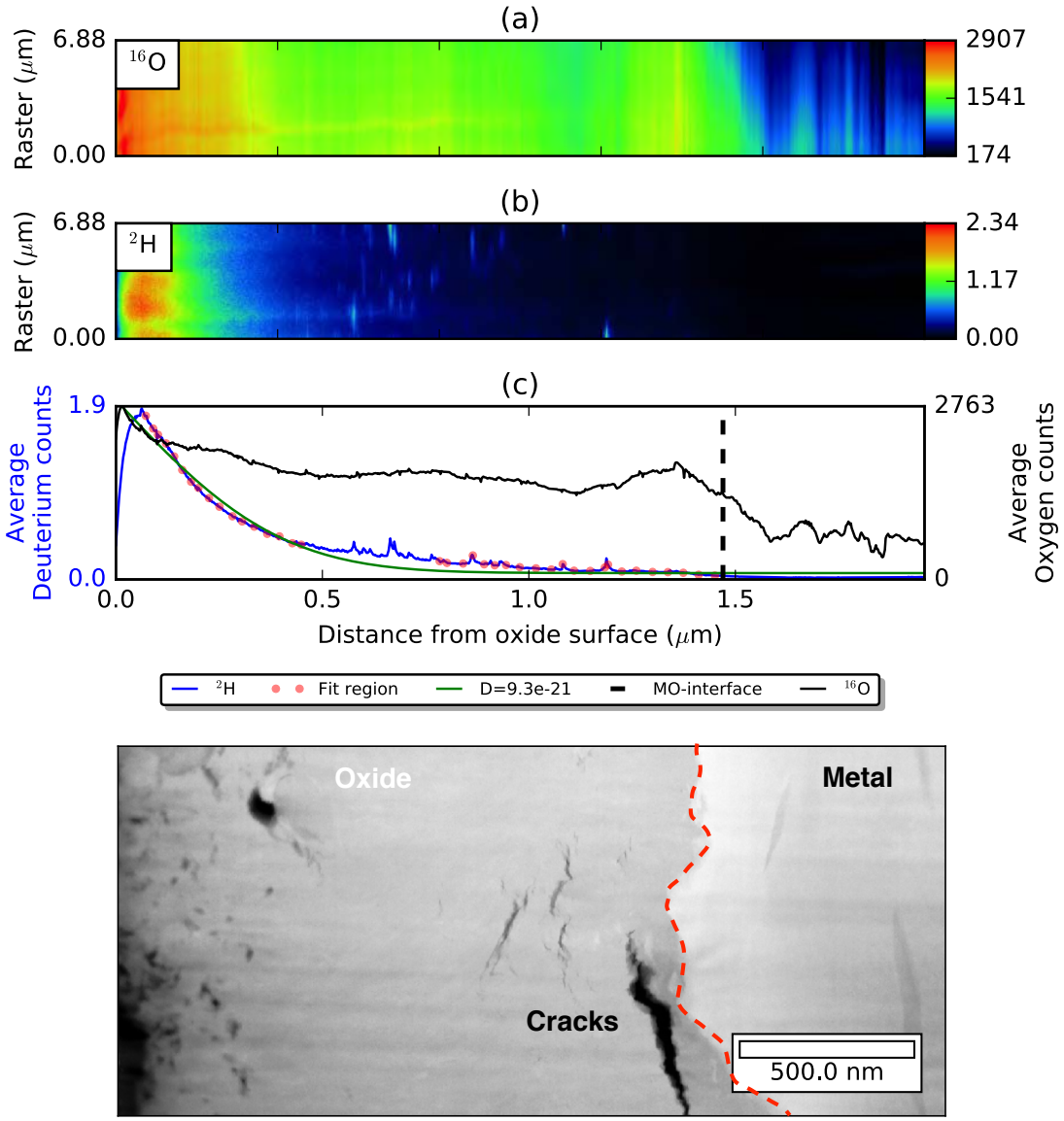
Figure 7.9 shows the volume depth profile for a sample of high-pH 61-day pre-transition Zircaloy-4. The deuterium content follows a smooth diffusion profile down the oxide. This shows that the oxide functions as a protective barrier only penetrable through diffusion. Halfway through the oxide some spikes in the deuterium profile can be seen. The STEM HAADF image from the same material in figure 7.9d shows that the spikes overlay cracks relatively well. It seems likely that deuterium is preferentially concentrating on the surface of the cracks. Whilst the HAADF

image is not taken directly from this region (impossible, as the NanoSIMS is a destructive technique) and it is possible that this region did not contain any large cracks, it seems likely that even horizontal cracks as large as the one imaged do not contain water during the oxidation process. The possibility of cracks causing transition was dismissed by Ni [69] as cracks were found to be forming continuously during the oxidation process rather than abruptly. It is possible, however, that it is only when the cracks link up properly that water can fill the cracks and accelerate corrosion, causing the transition. This could explain the undulation-behaviour found in Chapters 4 and 5 where a crack appears to slow oxidation. If these cracks are not filled with water, the void within them would act as a barrier to oxygen ingress.

The diffusion profile is fitted using the red dotted region in figure 7.9c, avoiding the deuterium spikes. The fit suggests a diffusion coefficient of $9.3 \times 10^{-21}\,\mathrm{m^2\,s^{-1}}$ for deuterium through ZrO_2 at 360 °C. This is slightly lower than the one-dimensional result for the neutral pH 61-day Zircaloy-4 result.

In some cases the sample would drift extensively during acquisition. In the case of the 3D dataset in figure 7.10, the entire initial image drifted out of the field of view after 200 planes of imaging. Despite the drift, cropping around the non-drifted area still allowed for the diffusion coefficient to be calculated. Observing the movement of the SE and O images, it was found that about 300 image slices in, the drift abruptly slowed significantly. Therefore this was chosen as the beginning of the oxide surface in order to calibrate the sample according to its 1.47 µm thickness. As the sample was almost entirely still for the remainder of the analysis, the fit matches the deuterium signal particularly well.

The dip in oxygen signal preceding the defined 0.0 µm starting point can be explained as the NanoSIMS requiring time to mill through the platinum layer coating the surface of the oxide (to ensure surface electrical conductivity). From here onwards there are large spikes in deuterium content, indicating a lot of cracks, more so than in figure 7.9, taken on the same sample. The diffusion profile is fitted with a diffusion coefficient of $1.0 \times 10^{-19}\,\mathrm{m^2\,s^{-1}}$, which is over an order of magnitude higher than the case for the other three-dimensional depth profile done on the same sample.



(d) STEM HAADF image taken from the same sample shown at the same scale.

Figure 7.9: High-pH pre-transition 61-day Zircaloy-4 volume data showing (a) ^{16}O and (b) ^{2}H projected through the x-axis. (c) shows the averaged profile along the depth axis, showing a smooth diffusion profile for deuterium through the oxide. Fick's law is fitted using the red region, and the fit suggests a diffusion coefficient of $9.3 \times 10^{-21}\,\mathrm{m^2\,s^{-1}}$ for deuterium through ZrO_2 at 360 °C. The deuterium spikes match the cracks in the HAADF image (d). The metal-oxide interface is indicated by a red dashed line on the HAADF image and a black dashed line on the depth profile.

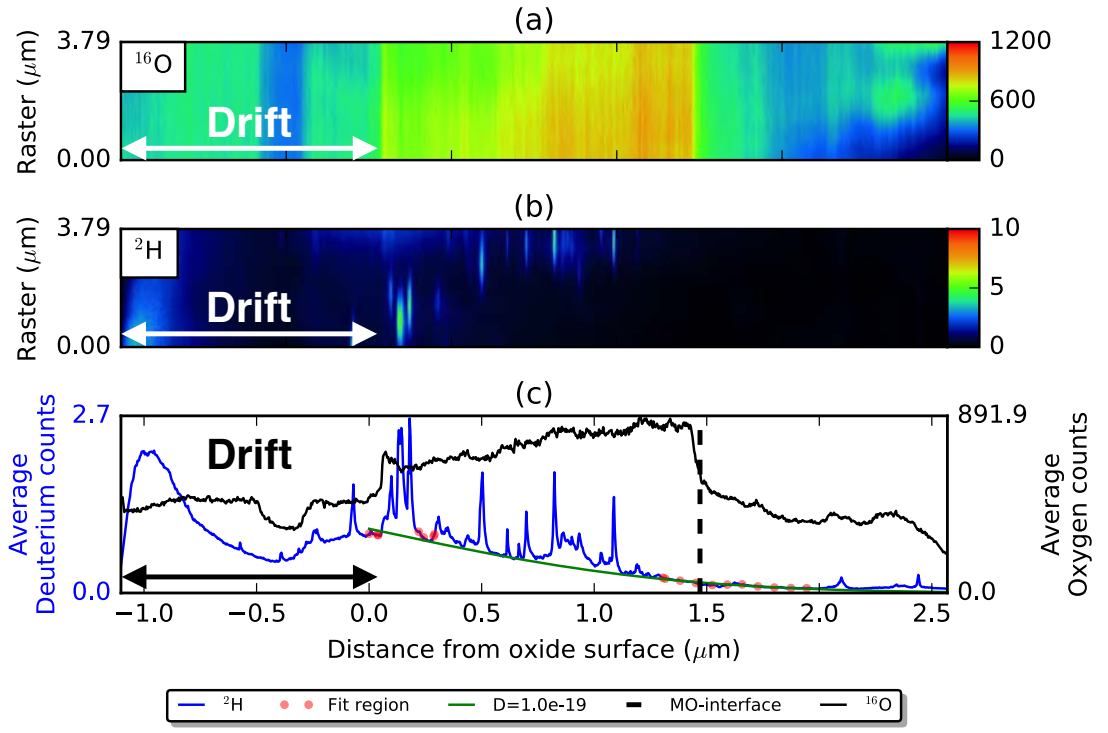


Figure 7.10: High-pH pre-transition 61-day Zircaloy-4 volume data showing (a) ^{16}O and (b) ^{2}H projected through the x-axis. (c) shows the averaged profile along the depth axis, showing a smooth diffusion profile for deuterium through the oxide. Large amounts of drift were detected for the first 200 planes of imaging. Fick's law is fitted using the red region, and the fit suggests a diffusion coefficient of $1.0 \times 10^{-19}\,m^2\,s^{-1}$ for deuterium through ZrO_2 at 360 °C. The metal-oxide interface is indicated by a black dashed line.

Figure 7.11 shows another case of drift on pre-transition 61-day Zircaloy-4, although less so than in the previous case. The ^{16}O image in 7.11b is especially revealing, showing particular drift at approximately 0.6 µm depth. The diffusion profile is a reasonable fit, resulting in a diffusion coefficient of $3.7 \times 10^{-20}\,m^2\,s^{-1}$.

Post-transition annealed Zr-1Nb

The NanoSIMS is limited to 1000 slices of image analysis before stopping analysis. As such, for samples with very thick oxides, I was sometimes unable to break through the oxide. Figure 7.12 shows the oxygen and deuterium 3D data set for a sample of post-transition 91-day annealed Zr-1Nb. The deuterium signal remains roughly constant throughout the thick oxide, but with many spikes throughout.

Using the weight-gain as an indicator, the oxide thickness should be 4.28 µm.

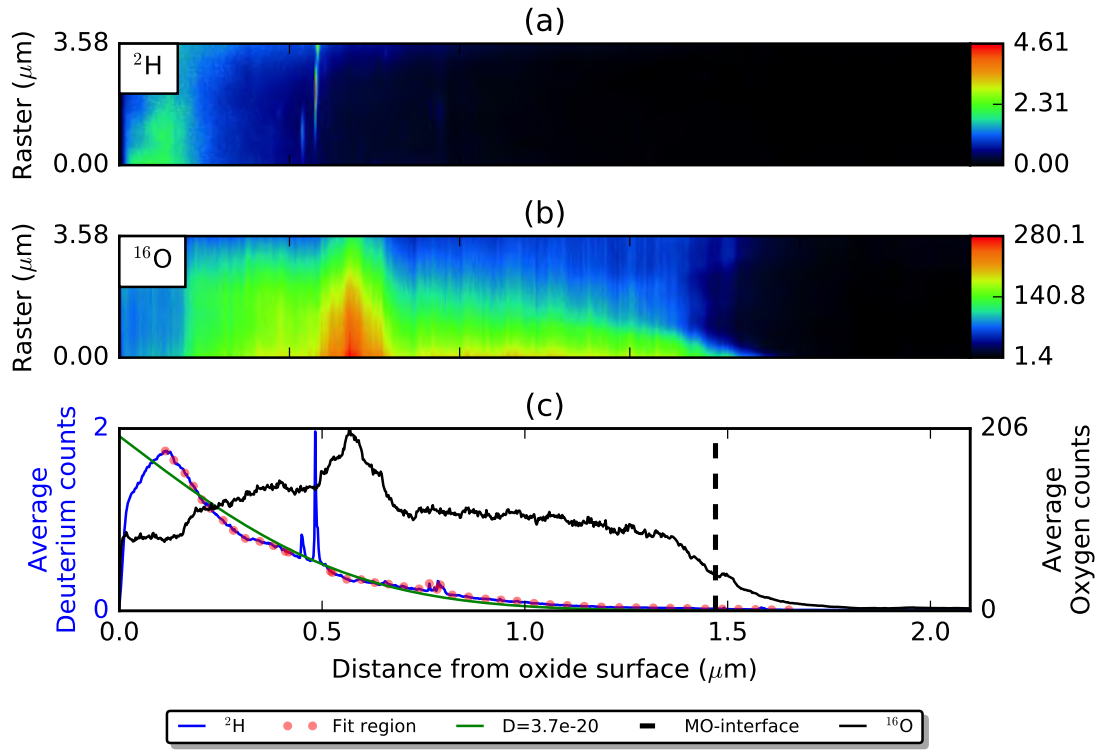


Figure 7.11: Pre-transition 61-day Zircaloy-4 volume data showing (a) ^{16}O and (b) ^{2}H projected through the x-axis. (c) shows the averaged profile along the depth axis, showing a smooth diffusion profile for deuterium through the oxide. Drift can be seen at a depth of 0.6 µm through the oxide. Fick's law is fitted using the red region, and the fit suggests a diffusion coefficient of $3.7 \times 10^{-20}\,\mathrm{m^2\,s^{-1}}$ for deuterium through ZrO_2 at 360 °C. The metal-oxide interface is indicated by a black dashed line.

This provided an upper limit on what the NanoSIMS was able to mill through at the beam current and dwell time used.

A second run of the same sample, shown in figure 7.13 saw the deuterium start to decline in the fashion associated with the diffusion profile. This was likely in a thinner part of the oxide, and more deuterium spikes are present.

Across all samples, nothing particularly indicative of the SPP hotspots seen in the previous Chapter are found. Deuterium spikes seem associated with cracks, but it is possible that SPPs can give the same signature, although one would expect them to be visible in several planes as they are milled through. Cracks and β-Nb SPPs often have similar depth thicknesses, but the EDS-analysed hotspot seen in the cross-sectional NanoSIMS data in figure 6.34 in Chapter 6 was a Laves phase $Zr(NbFe)_2$ SPP. They tend to be on the order of several hundred

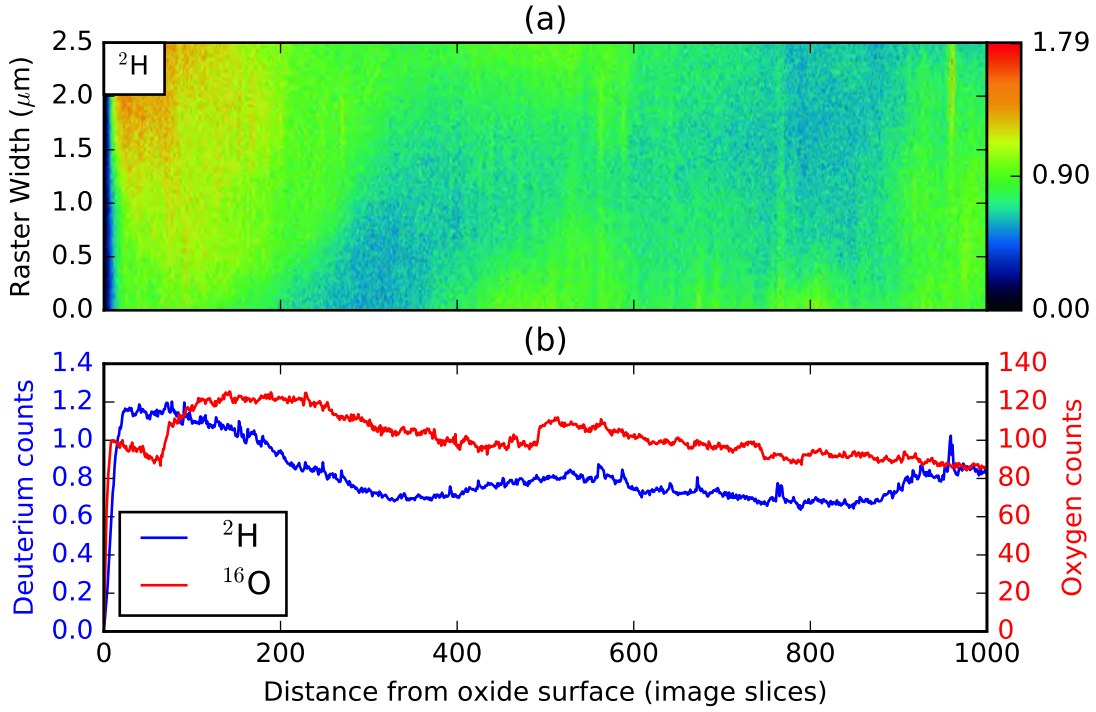


Figure 7.12: Post-transition 91-day annealed Zr-1Nb volume data showing the (a) ^{2}H projected through the x-axis. (b) shows the averaged profile along the depth axis. The oxide was too thick to penetrate. The deuterium shows a high nearly constant concentration through the oxide, showing only occasional peaks.

nanometre, larger than the width of the spikes on the ^{2}H profile. This implies that the hydrogen present in the spikes is primarily from surface-decoration of the cracks in the oxide. Next generation NanoSIMS instruments are likely to be able to image a larger mass dispersion. Imaging the metal content of SPPs simultaneously with hydrogen or deuterium content will hopefully reveal the role SPPs play with regards to hydrogen pickup.

7.3 Discussion

7.3.1 Hydrogen pathways through the metal-oxide interface

As mentioned at the beginning of section 7.2.2, it is difficult to present a three-dimensional object on a two-dimensional image. Since most pixels in the object have at least 1 count in them, any projection of the object will often simply be

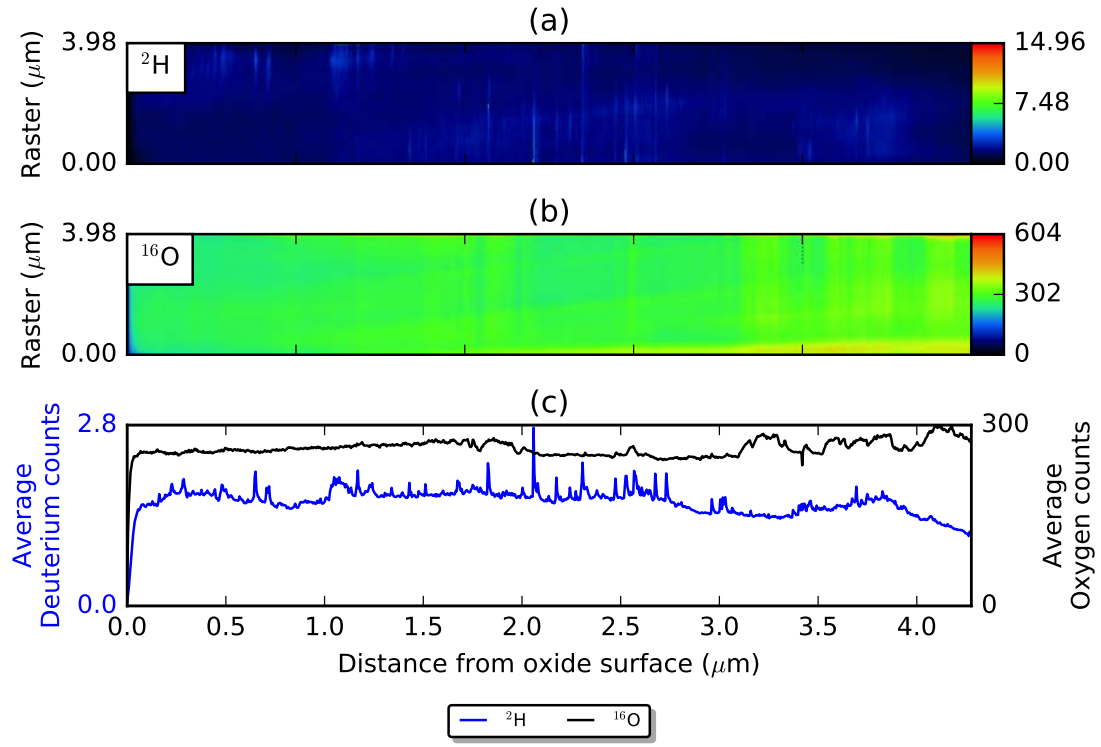


Figure 7.13: Post-transition 91-day annealed Zr-1Nb volume data showing the (a) ^{2}H and (b) ^{16}O projected through the x-axis. (c) shows the averaged profile along the depth axis. The oxide was too thick to penetrate. The deuterium shows a high nearly constant concentration through the oxide, showing only occasional peaks.

presented as a solid block. However, by separating pixels with low counts generally associated with the diffusion profile from the high counts associated with the cracks in the oxide, a better image can be presented of how the deuterium may be penetrating the oxide layer.

Figure 7.14 and 7.15 shows this approach for the 106-day post-transition Zircaloy-4 sample. This volume was acquired and is reproduced with permission by Dr. Kexue Li, a post-doc working on a similar project. Both volumes used a 5 µm raster size, but the first approach used a high number (512x512) of pixels for imaging, resulting in less depth penetrated. The second volume imaged using a lower number (256x256) resulting in penetration to the metal-oxide interface. In the first case, deuterium can be seen passing between large cracks using pathways indicated in red dashed lines. These are likely to be either vertical cracking or interconnected porosity. The formation of a network of pathways is seen - most of the features seen

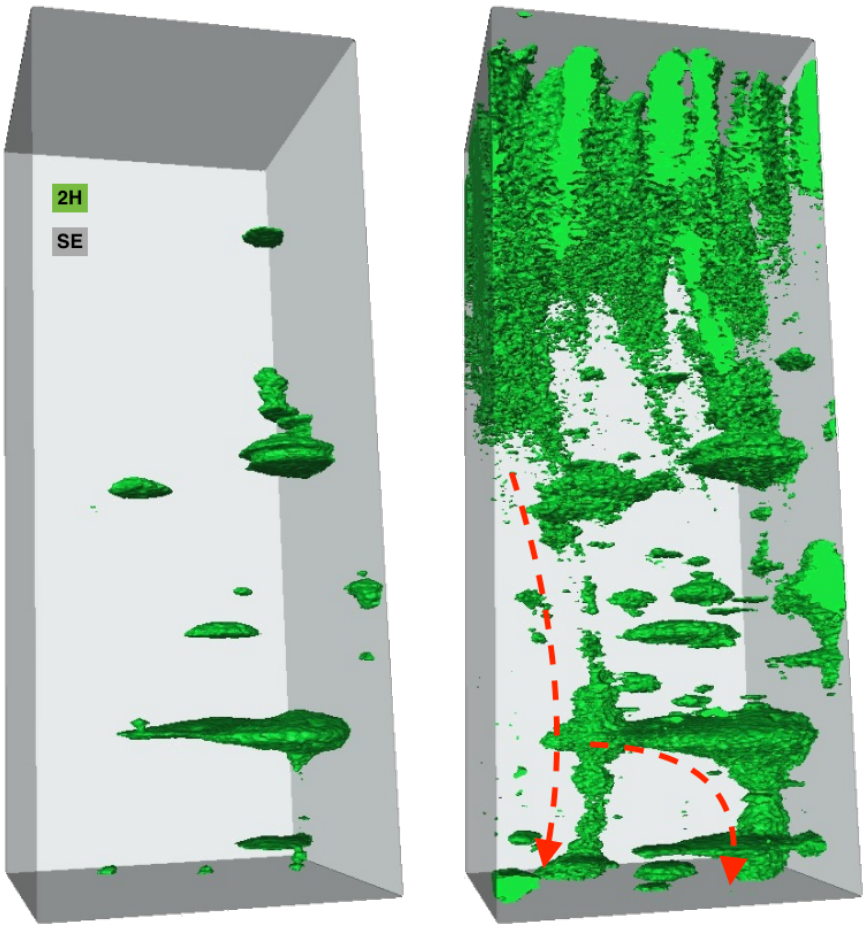
in the volume are linked. The larger features are almost certainly horizontal cracks, although the smaller features could be porosity or grain boundaries, the latter of which has previously been found to be enriched with hydrogen through APT [226].

In the second volume, the deuterium is shown to be following a path from the metal-oxide interface and further into the metal in a diagonal fashion, emphasised by red dashed lines. These lines are likely to be hydrides, formed on cooling from the 360 °C oxidation temperature. This makes it difficult to be certain of what is happening, but the fact that the deuterium signal is continuous from the oxide through to the metal in this region is certainly worthy of further attention. The difference in deuterium intensity between the two datasets is clear. In the first dataset deuterium is clearly only travelling along preferable pathways - probably porosity. In the second, deuterium permeates the entire oxide up until just before the metal-oxide interface. This further emphasises the argument of the inaccuracy of using pre- and post-transition terms to describe a local area of a sample, as previously discussed in Chapters 4 and 5.

The hypothesis of hydrogen ingress through porosity was presented in Chapter 2 on the basis of research by Elmohselhi [114] and Cox and Wong [7]. This work confirms the suggestion by Elmoselhi that most of the deuterium resides on accessible sites on surfaces and intergranular porosity. Together with the porosity work shown in Chapter 4 and previous research [83, 200], this work also confirms that hydrogen ingress occurs via porosity, although it remains unclear exactly how the transport occurs.

7.3.2 Diffusion profiles

The diffusion coefficients measured from the depth profiles on the various samples are shown in table 7.2. The values range between $10^{-21}\,m^2\,s^{-1}$ and $10^{-19}\,m^2\,s^{-1}$. This is close to the range of experimentally measured values for tritium diffusion by Kunz et al. [227] on Zircaloy-2 ($3 \times 10^{-20}\,m^2\,s^{-1}$), and hydrogen diffusion in Zircaloy-2 ($6 \times 10^{-19}\,m^2\,s^{-1}$) and Zr-20Nb ($6 \times 10^{-18}\,m^2\,s^{-1}$) by Khatamian et al. [228] all at 350 °C. Kato et al. [229] measured the average diffusion coefficient of



(a) **(b)**

Figure 7.14: 3D visualisation of deuterium showing pixels containing (a) more than four and (b) four and less counts on a 3D dataset of 106-day post-transition Zircaloy-4. All of the volume is in the oxide. The 3D visualisation was done by and is reproduced with permission Dr Kexue Li.

Alloy	Oxidation time	Diffusion Coefficient / m2/s	Comment
Pre-transition Zr-1Nb	46	5.8E-20	1D
Pre-transition Zircaloy-4	61	5.8E-20	1D
Pre-transition Zircaloy-4	61	9.3E-21	3D, High-pH
Pre-transition Zircaloy-4	61	1.0E-19	3D, High-pH
Pre-transition Zircaloy-4	61	3.7E-20	3D
Post-transition Zircaloy-4	106	1.3E-19	1D

Table 7.2: Diffusion coefficients measured on several alloys at 360 °C.

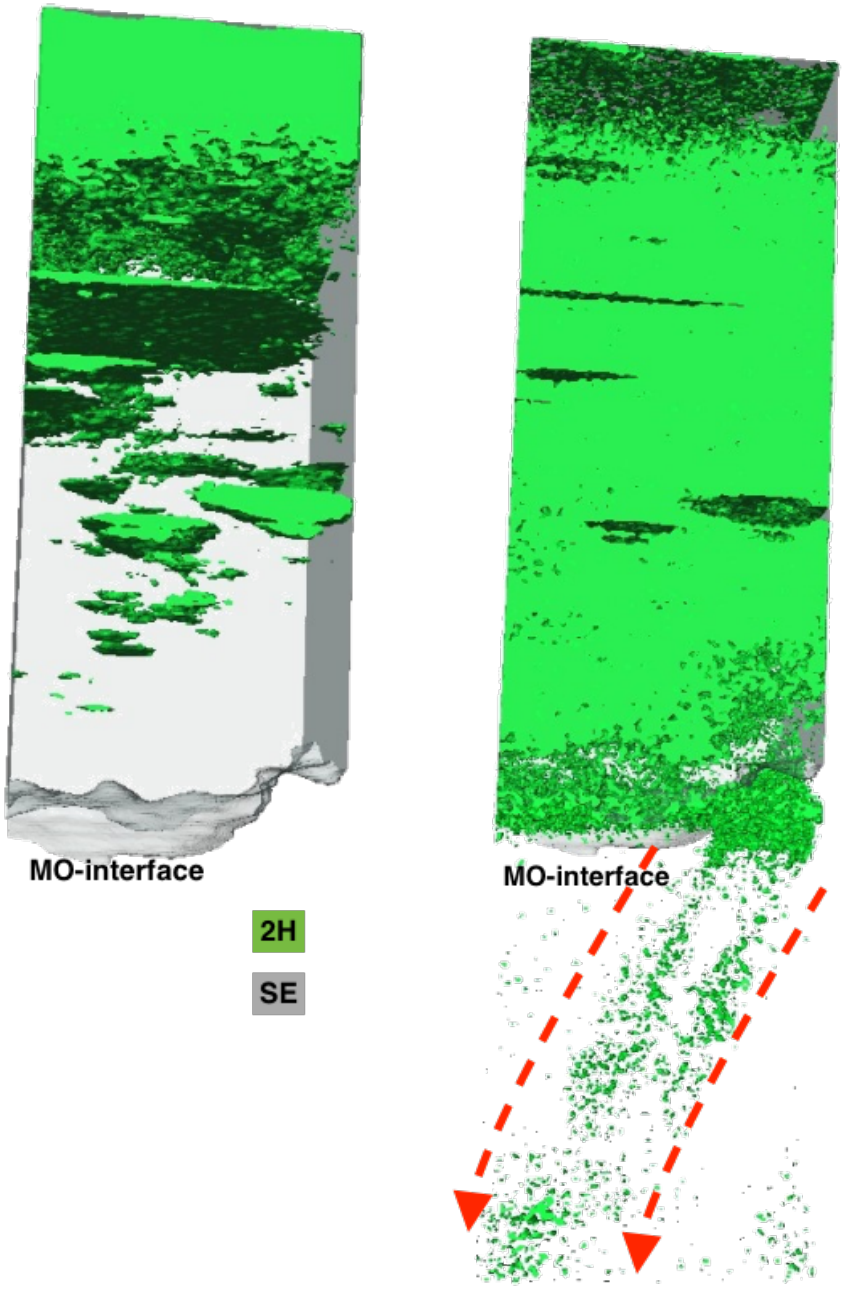


Figure 7.15: 3D visualisation of deuterium showing pixels containing (a) more than four and (b) four and less counts on a 3D dataset of 106-day post-transition Zircaloy-4. The grey layer indicates the oxide visualised using the SE signal. The acquisition of data and 3D visualisation of this dataset was done by Dr. Kexue Li.

deuterium in the protective part of the oxide on high iron-content Zircaloy-2 to be $2.3 \times 10^{-19}\,m^2\,s^{-1}$, in D_2O steam at 400 °C. They also showed that in the outer parts of the oxide, the diffusion coefficient is increased by between one and two orders of magnitude. This was measured by calculating the diffusion coefficients on separate depth ranges of the diffusion profiles. Their samples were oxidised for only up to four days (albeit at slightly elevated temperature compared to this project's samples), with the oxidation only going through early pre-transition, yet showed differences in the inner and outer oxides. While the typical characteristic of the non-protective oxide is a flat domain of deuterium concentration, Kato et al. do not observe this, but refer to the steeper slope of the initial diffusion profile as non-protective. This is in agreement with my own observations: Since I measured the diffusion coefficient by fitting to the entire diffusion range, this explains the poor fitting that is found at certain ranges of the diffusion profile. An example of this can be seen in figure 7.5 where the deuterium profiles are steeper than expected by the fit in the first micron of oxide, and shallower than expected by the fit closer to the metal-oxide interface. These results therefore support the idea that the outer oxide on pre-transition samples has a higher deuterium diffusion coefficient.

The characteristics of the "diffusing" protective and "flat-plateu" non-protective oxide have been described by Une et al. [230]. The non-protective oxide shown by Une is very similar to that measured on the post-transition samples of Zr-1Nb shown in this Chapter, where the autoclave water appears to penetrate the outer layers, leading to saturation of deuterium. No attempt was made to separate "steep" and "shallow" oxide diffusion coefficients on the results presented in this thesis. A possible explanation for the reduced diffusion coefficient near the metal-oxide interface could have been the increased tetragonal oxide fraction [45, 47, 87] found near the metal-oxide interface. Muta et al. [115] calculated the diffusion coefficient for monoclinic and tetragonal oxides by ab initio methods. However, they found that at 350 °C the coefficients are approximately $7 \times 10^{-24}\,m^2\,s^{-1}$ and $3 \times 10^{-17}\,m^2\,s^{-1}$, for monoclinic and tetragonal oxides respectively. The large difference between the tetragonal and monoclinic oxide diffusion coefficients explains some of the

variation between measurements on zirconium alloys. My measured values, in the range $10^{-21}\,m^2\,s^{-1}$ to $10^{-19}\,m^2\,s^{-1}$ lie between them. Since the oxides contain some fraction of tetragonal phase, this will raise the measured diffusion coefficient compared to the theoretical value for monoclinic oxide. The high diffusion coefficient for tetragonal oxide does not, however, explain the reduction in measured diffusion coefficient towards the metal-oxide interface. Therefore, it is more likely that the diffusion coefficient is lower due to less porous and less cracked oxide close to the metal-oxide interface. The work done by Muta does provide further evidence of tetragonal grain content having a significant effect on hydrogen ingress, alongside other research [85, 87, 210]. If the fraction of tetragonal oxide in an alloy is high, the hydrogen ingress should be faster than for alloys with a lower fraction of tetragonal oxide. An interesting prospect for further work could be to measure the diffusion coefficient for the 3D-datasets presented in figures 7.14 and 7.15, in order to remove effects such as possible fast-pathways and cracks which can result in artefacts when fitting a diffusion profile, as well as attempt to laterally as well as depth-wise spatially resolve the possibility of protective and non-protective oxides and differences in diffusion coefficient.

A correlation between average hydrogen pickup rate and diffusion coefficient of hydrogen in zirconium oxide has been shown by Une et al. [104] at 290 °C. Zr-2.5Nb and Zircaloy-2 showed diffusion coefficients of $1.1 \times 10^{-18}\,m^2\,s^{-1}$ and $1.2 \times 10^{-17}\,m^2\,s^{-1}$ and hydrogen pickup rates of $0.4\,ppm\,h^{-1}$ and $4.5\,ppm\,h^{-1}$ respectively. These diffusion coefficients are at least an order of magnitude higher than the values shown in this thesis. The diffusion coefficient was not successfully measured enough times for enough alloys in this thesis to test the relationship between hydrogen pickup rate and diffusion coefficient value, but Zr-1Nb has been shown to have much reduced hydrogen pickup compared to Zircaloy-4. However, this is not reflected in the diffusion coefficents calculated, which are identical for the first two measurements on Zr-1Nb and Zircaloy-4. More depth profile measurements with a more stable instrument (i.e. no drift) and an oxidation in purely deuterated water to improve counting statistics would improve the reliability of these values.

Here I have confirmed that the deuterium diffusion coefficients of Zircaloy-4 and Zr-1Nb lie in the ranges found in the literature for deuterium diffusion in ZrO_2. Further, analysis of the diffusion profiles have provided evidence in favour of two domains of diffusion behaviour, even in the pre-transition oxide.

7.3.3 Hydrogen uptake hypothesis and relation to oxidation mechanism

The snapshot in time provided by the three-dimensional NanoSIMS analysis together with the STEM analysis and literature review allows us to form a hypothesis for the hydrogen uptake mechanism, which is strongly connected to the oxidation mechanism. After oxide has formed on a fresh sample of a zirconium alloy, hydrogen initially diffuses through oxide grain boundaries [180] and porosity present in the outer oxide. The surface of any cracks present in the pre-transition oxide are covered in hydrogen (as shown by the NanoSIMS 3D analysis). As the hydrogen approaches the metal-oxide interface, its path can be aided if the oxide is in a state of slow oxide growth immediately before transition. The hydrogen ingress is aided by the presence of a network of porosity, caused by the stress present in the oxide at this stage, and transformation of tetragonal to monoclinic oxide grains [40, 85]. SPPs may also aid the hydrogen ingress [90], although whether this behaviour is linked to transition is unknown at this time. As the oxide ages towards transition, more porosity forms [47], increasing the rate of hydrogen uptake. Once transition occurs, the newly-grown oxide close to the metal-oxide interface again acts protectively (by a lack of porosity), reducing the rate of hydrogen ingress. At the same time, as major cracks have formed due to transition, water is allowed entry into the non-protective oxide, permeating the outer oxide with hydrogen. This effectively removes the diffusion behaviour of the outer oxide completely, and the diffusion profile now begins from the oxide depth at which the fast oxide growth began at the last transition (as shown in Chapters 6 and 7). An increase in porosity of the protective oxide would explain the increase in IHPUF [207] experienced by the alloys as they approach transition. The fall in IHPUF, which is shown to occur

immediately before transition, could be explained by transition having begun in some places (as the transition is argued to be happening out-of-phase in section 5.4.1) and non-porous protective oxide is forming. This would prevent fast hydrogen ingress into the metal in some areas, reducing the overall IHPUF.

7.4 Summary

- Chapters 6 and 7 have provided the first high resolution work on the ingress of hydrogen through the oxides of zirconium alloys. Before transition hydrogen is found at high intensity in the outer portion of the oxide, and after transition it is found in fairly even concentrations throughout most of it. There is a clear diffusion profile through the protective oxide on all alloys, resulting in diffusion coefficients for deuterium with values between $10^{-21}\,m^2\,s^{-1}$ and $10^{-19}\,m^2\,s^{-1}$, which is in the range of literature values.

- Three domains of hydrogen ingress in the oxide are found. On post-transition samples the outer oxide is clearly permeated by water. The part of the oxide that shows a diffusion profile can be divided into two - a region of fast diffusion further away from the interface and slow diffusion closer to the interface. The fast diffusion is suggested to be promoted by porosity in the oxide, and not due to tetragonal phase-fraction.

- Deuterium rich areas, shown as peaks in the one-dimensional depth profiles and as plates in the three-dimensional profiling, are determined to be cracks in the oxide decorated with deuterium. These larger volumes are interconnected either by vertical cracks, porosity or, possibly, SPPs.

- Oxide close to the metal-oxide interface clearly acts protectively against major hydrogen ingress. However, by 3D SIMS measurements, even within the protective oxide, pathways in the form of porosity are shown to exist.

- Sample drift is shown to be a major issue when doing one-dimensional depth profiling. Drift is shown to be compensated through three-dimensional depth profiling when combined with drift correction and cropping.

- A hydrogen uptake hypothesis is proposed based on the three-dimensional NanoSIMS results. Hydrogen is argued to diffuse through the protective oxide but ingress is accelerated by the presence of porosity. With transition the protective oxide formed reduces hydrogen uptake, consistent with hydrogen pickup measurements.

- While no SPPs were clearly identified in this work, next generation SIMS instruments are likely to be able to measure the metal content in SPPs simultaneously with deuterium pickup. Future work should focus on understanding the role on the SPPs present in the oxide just ahead of the metal-oxide interface.

8

Summary and suggestions for future work

Contents

8.1 Oxide microstructure and oxidation behaviour 255
8.2 EELS results 256
8.3 Hydrogen pickup results 258
8.4 Future work 260

8.1 Oxide microstructure and oxidation behaviour

- The oxide thickness can vary substantially from region to region. Using 3D-FIB to measure the oxide thickness within areas of 20 µm × 20 µm on each sample, I found variation in the thickness of the oxide of up to 1.5 µm. Taking into account the conversion of weight gain to average oxide thickness, the spread should be substantially more. For instance, the average oxide thickness for the 3-day Zircaloy-4 sample is 760 nm, but oxides over 77 % thicker were found.

- Like previous researchers, I find that the columnar oxide is much more frequently present at the metal-oxide interface than equiaxed oxide. Equiaxed

oxide is very common in the outer region of the oxide, and as is evident in the literature, I find that the equiaxed and columnar oxide tends to form in bands in the oxide.

- The weight gain rises much more sharply at transition for Zircaloy-4 than for ZIRLO.
- The 3-day samples of Zircaloy-4 contain far more cracks than the 3-day samples of ZIRLO. Rapid occurrence of cracking can explain the sharp point of transition on Zircaloy-4. There is no significant difference in the crack content on the alloys oxidised for longer periods of time.
- The oxide microstructure of Zircaloy-4 and ZIRLO appears generally similar by STEM ADF and HAADF observations.
- Throughout the oxide, including near the metal-oxide interface, interconnected porosity is found. It is argued that the porosity plays a major role in the hydrogen pickup of an alloy.
- The alloying additions Fe, Cr, Sn and Nb are discussed with respect to their impact on corrosion resistance. The elimination of Sn is shown to be the most important with regards to oxidation resistance, and arguments with regards to space charge formation in the oxide are discussed.

8.2 EELS results

- The thickness of the oxygen-saturated metal region varies between 0 and 300 nm for the analysed samples of ZIRLO and Zircaloy-4. In particular for the Zircaloy-4 sample, it appears that there is a trend towards a thin region for the 3- and 105-day samples and a thick region for the 45-day sample. Since the first two samples have recently oxidised quickly, it is likely that they have "used up" the oxygen present to form oxide. A less clear trend is seen for ZIRLO, but since the ZIRLO weight gain curve shows a more out-of-phase oxide growth than the Zircaloy-4 does, the samples are probably more out of

phase with one another. A better approach may have been to compare the oxide thickness to the oxygen-saturated metal thickness directly below it. That is currently beyond the capabilities of microscope speed and computing power, but these are quickly reaching the stage where low-magnification high-pixel count spectrum imaging is possible.

- Novel use of independent component analysis on EELS low-loss spectrum images allows for excellent separation of phases.

- The oxygen-saturated metal region is found to be reduced for alloys immediately after transition, suggesting that it has been consumed in the formation of fresh oxide.

- Suboxide has been identified as a complex, stress-stabilised layer at the metal-oxide interface. It is found particularly at regions of undulating metal-oxide interface, where there is high tensile stress. Mechanisms of its formation are discussed with reference to the literature. Suboxide is found to form on all zirconium alloys, including pure zirconium, suggesting that it is a general mechanism of zirconium oxidation!

- The combined suboxide and oxygen-saturated metal thickness is on average larger for ZIRLO than for Zircaloy-4. It is argued that a larger average combined thickness is correlated with a slow rate of oxidation.

- The oxygen content of the suboxide at the metal-oxide interface has been characterised for ZIRLO and Zircaloy-4 to be approximately 50 %. The value can vary, however, which makes it an interesting opportunity for future work.

- The oxidation state of Zr can be inferred from the position and ratio of the white lines on the L_3 and L_2 EELS edges, measured by curve fitting. As the oxidations state increases, both white lines move to higher energy loss, and the area of the L_3 white line increases relative to the L_2 white line. Due to this property, mapping of the oxidation state of Zirconium could be accelerated by

only acquiring the Zr L edges rather than two separate acquisitions of both the Zr and O edges in order to quantify the oxygen concentration.

- It was not possible to measure the oxidation state of Nb by measuring the Nb L edges on samples prepared from standards by FIB. Despite careful standard sample preparation the EEL spectra appear identical. Why this may be is uncertain, although stress relaxation of the FIB liftout or interaction with the FIB gallium beam are possibilities.

- Hydrides are in some cases seen by STEM in vast numbers in the metal. Concerns are raised on whether these are FIB-induced. It is still unclear why they tend to form close to the metal-oxide interface on autoclaved samples.

8.3 Hydrogen pickup results

- A novel first attempt at deuterium spiking the corrosion process of zirconium alloys to study the hydrogen pickup mechanisms by three-dimensional SIMS has been successful. Deuterium has been shown to act as a clear contrast agent for hydrogen, making clear what is "real" hydrogen and what is contamination.

- Post-transition Zr-1Nb samples are found to contain substantially less deuterium compared to their ZIRLO counterparts. Whilst the ratio of ^{2}H / ^{1}H is typically 600×10^{4} for pre- and post-transition ZIRLO, it rarely goes above 130×10^{4} on the post-transition sample of Zr-1Nb. Whilst direct comparison is difficult due to the Zr-1Nb samples being oxidised for longer in regular water, the lower deuterium ratio is expected due to Zr-1Nb's reported reduction in hydrogen pickup fraction.

- The outer region of the oxide of deuterated alloys has been found to be filled with deuterium on both pre- and post-transition samples. For the post-transition samples the outer oxide has a roughly constant intensity of deuterium. For all samples the oxide closest to the metal-oxide interface acts as a protective barrier to fast transport of deuterium.

- Deuterium is able to diffuse through the protective oxide barrier, with a diffusion coefficient on the order of $10^{-21}\,m^2\,s^{-1}$ to $10^{-19}\,m^2\,s^{-1}$, which fits well with the literature values of between $10^{-23}\,m^2\,s^{-1}$ to $10^{-16}\,m^2\,s^{-1}$.

- When the oxide displays diffusion behaviour, a range of fast and slow diffusion confirms what has been reported in the literature.

- The SE signal on the NanoSIMS is an excellent substitute for the oxygen signal, allowing for qualitative separation of the oxide and metal.

- SPPs are found near the metal-oxide interface, and preliminary NanoSIMS work combined with FEGSEM EDS suggests that they could act as a short-circuit for hydrogen ingress through the protective barrier.

- Sharp peaks on the deuterium diffusion profiles coincide with cracks in the oxide. It is suggested that deuterium decorates the surface of these cracks and escapes when hit by the NanoSIMS caesium beam. In depth profile, the hydrogen content of SPPs is yet to be measured.

- The deuterium content of Zr-1Nb is significantly lower than that of ZIRLO and Zircaloy-4, in line with the expected improved corrosion-resistance of Zr-1Nb. The reduction of Sn is emphasised as playing the major role in the improved corrosion-resistance, and the role of Sn on hydrogen pickup is discussed with reference to DFT literature. As the diffusion coefficients were extremely similar, a reduction in HPUF of the Zr-1Nb alloy is suggested to be the cause of the improved hydrogen pickup resistance.

- Based on TEM studies of porosity and the network of deuterium found near the metal-oxide interface by three-dimensional SIMS, a hydrogen pickup mechanism hypothesis is proposed that fits the result of current research and measurements.

8.4 Future work

- This work has examined a series of zirconium alloys oxidised for different amounts of time. In most cases the samples have been comparable, although it is not always clear whether the base for comparison should be similar weight gain, same number of days oxidised or hydrogen content. The advent of 3D-FIB, has made doing routine measurements on a large number of samples easier, but it is really the automation of the analysis routine that will make this technique blossom. Applied to zirconium alloys, I foresee that it will allow a better understanding of why some regions have thicker oxides than others, and correlate cracks and (with 3D-EDS and 3D-electron back-scatter diffraction (3D-EBSD)) second phase particles and grain orientations with one another. Even the stress exposed by the oxide to the metal can be imaged under the right detector conditions. The real benefit will be looking at a larger region on a larger number of samples whilst maintaining the high resolution that has enabled these measurements (albeit on few samples and in small areas) in the first place.

- Further study of the porosity present near the metal-oxide interface is necessary to fully validate the hydrogen pickup mechanism hypothesis. A TEM comparison between alloys with poor and superior resistance to hydrogen pickup, for instance with Zircaloy-4 and Zr-1Nb would help confirm the hyothesis.

- The hydrogen content of SPPs in the oxide being non-significant has been hinted at with the cross-sectional NanoSIMS work in this project. More work combining NanoSIMS with EDS could confirm the hypothesis of SPPs acting as short-circuits through the protective oxide.

- The two main limiting factors of the NanoSIMS depth profile analysis were sample drift and the acquisition limit of 1000 image planes. The technique could benefit much from improvements to these two problems, allowing for

more accurate study of the deuterium channels observed through the protective oxide in the final section of the depth profile Chapter. In an ideal case, performing a depth profile with a window size of 10 µm and comparing it to a neighbouring region imaged by 3D-FIB would make it clearer if second-phase particles can be seen in the depth profile images and help with the understanding of what gives the protective oxide its beneficial properties.

- SPPs in Zircaloy-4 were observed to be apparently dissolving in the oxide close to the surface. An in-depth study of SPPs over time (in oxidation) for both ZIRLO and Zircaloy-4 could reveal important differences in their oxidation mechanism.

- Low-loss EELS was particularly useful due to its high speed of acquisition. It could potentially be used to study whether SPPs are oxidised or not by observing peak shifts in the plasmon peaks. Whether or not the different types of SPPs have different plasmon signals is also yet to be revealed, and may dramatically speed up the characterisation of SPPs.

- The possibility of formation of "artificial" hydrides in FIB-thinned liftouts has been raised. A study into whether FIB fine-thinning correlates with an increase in hydrides present in the material would be useful.

9 Removal of cosmic rays in EELS spectrum images

Contents

9.1 Cosmic rays 263

9.1 Cosmic rays

Cosmic rays are very high-energy photons and particles that strike the planet from space. If a cosmic ray strikes the EELS CCD, a high-energy "spike" will be detected, as seen in the figure below. The very strong intensity of these peaks can appear to statistical multivariate analysis to be very significant, and can be a detriment to the noise-reduction step of the EELS analysis. To combat this, I have developed a Python function to compliment the data analysis package HyperSpy. Whilst HyperSpy has a spikes removal tool function for removing spikes, it was too slow for large datasets. My function only works on spectrum images (an accumulation of spectra acquired along a line spectrum or map) as it steps through the energy loss dimension whilst looking at the surrounding pixels to find outliers above a certain threshold. Instead of looking at the intensity of the raw spectrum, it looks at the

difference between one value and the next. The threshold is calculated as a multiple of the Median Absolute Deviation of the data. This deviation is more robust to outliers in the data than standard deviation, so is more applicable here.

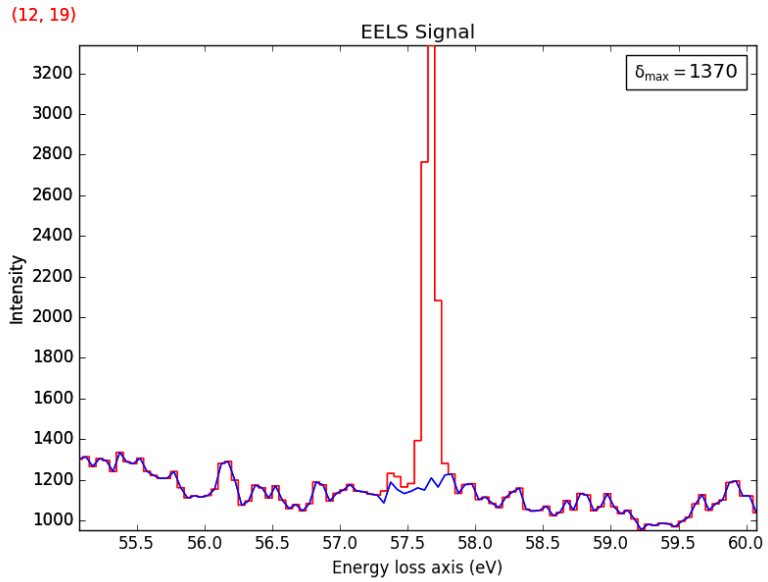


Figure 9.1: X-ray spike from a cosmic ray shown in red. The blue line shows the result after correcting for the spike using HyperSpy.

```
def median_from_neighbors(energy_slice, x, y=""):
    """Takes the median of the value of the list neighbors"""
    import numpy as np
    return(np.median(find_cell_neighbors(energy_slice, x,y)))

def find_cell_neighbors(data, X, Y, r=1):
    """Finds value of neighbors of a index in the SI, excluding the
       centre and any values outside the edges of the SI"""
    adjacent = []

    if Y == "":
        # Line spectrum
        for x in range(X-r, X+r+1):
            if (x == X): # Do not include the spike itself
                pass
            elif (x < 0) or (x >= data.shape[0]): # Do not include
                indices outside the edges
                pass
            else:
                adjacent.append(data[x])
    else:
        # map
        for x in range(X-r, X+r+1):
```

```
            for y in range(Y-r, Y+r+1):
                if (x == X) and (y == Y): # Do not include the spike
                    itself
                    pass
                elif (x < 0) or (x >= data.shape[0]): # Do not include
                    indices outside the edges
                    pass
                elif (y < 0) or (y >= data.shape[1]): # Do not include
                    indices outside the edges
                    pass
                else:
                    adjacent.append(data[x,y])
    return(adjacent)

def plot_spike_histogram(diff, diff_after):
    """Plots a single plot of the histogram of data differential before
       and after spikes removal"""
    import matplotlib.pyplot as plt
    import numpy as np

    hist_before, bins_before = np.histogram(diff, bins="auto")
    hist_after, bins_after = np.histogram(diff_after, bins="auto")
    center_before = (bins_before[:-1] + bins_before[1:]) / 2
    center_after = (bins_after[:-1] + bins_after[1:]) / 2
    width = 5.0 # Width of column

    plt.bar(center_before, hist_before, width=width, color = "red",
       label='before', log=True)
    plt.bar(center_after, hist_after, width=width, color = "blue",
       label='after', log=True)

    ax = plt.gca()
    (ymin, ymax) = ax.get_ylim()
    ax.set_ylim([1e-1,ymax])
    plt.legend()
    plt.title("Histogram of signal derivative")
    plt.xlabel("Derivative Magnitude")
    plt.ylabel("Counts")
    return

def remove_spikes(s=None, nMAD = 8, plot_difference=False):
    """Removes spikes outside nMad Median Absolute Deviations of the
       median of the differential of the spectrum"""
    from statsmodels.robust import scale
    import numpy as np

    shape = s.data.shape
    if len(shape) == 1:
```

```
        # Case single spectrum
        raise AttributeError("Remove spikes requires a Spectrum Image
            with non-zero navigation dimension")

    elif len(shape) == 2:
        # Case Line profile
        print("Recognised as Line Profile")
        diff = np.diff(s.data, axis=0)
        threshold = nMAD * scale.mad(diff.flatten()) # MAD - nMad is the
            number of deviations away from the median are included
        print("Gradient threshold is " + str(threshold))

        spike_positions = []

        positive = diff > threshold # Position of any inclining spikes
        (x,e) = np.nonzero(positive) # Get index of spikes
        x += 1 # Position of spike is the array index ahead of the
            gradient
        for i in range(len(x)):
            spike_positions.append([x[i], e[i]])

        negative = diff < -threshold # Position of any declining spikes
        (x,e) = np.nonzero(negative) # Get index of spikes
        for i in range(len(x)):
            spike_positions.append([x[i], e[i]])

        print("Found " + str(len(spike_positions)) + " spikes!")

        for (x,e) in spike_positions:
            s.data[x,e] = median_from_neighbors(s.data[:,e], x)

        if plot_difference == True:
            diff_after = np.diff(s.data, axis=0)
            plot_spike_histogram(diff, diff_after)

    elif len(shape) == 3:
        # Case EELS Map
        print("Recognised as 2D Spectrum Image")
        diff = np.diff(s.data, axis=1) # Get differential across data
        threshold = nMAD * scale.mad(diff.flatten()) # MAD
        print("Gradient threshold is " + str(threshold))

        positive = diff > threshold # Position of any inclining spikes
        negative = diff < -threshold # Position of any declining spikes

        spike_positions = []

        (x,y,e) = np.nonzero(positive) # Get index of spikes
```

```
        y += 1 # Position of spike is the array index ahead of the
            gradient
        for i in range(len(x)):
            spike_positions.append([x[i], y[i], e[i]])

        (x,y,e) = np.nonzero(negative) # Get index of spikes
        for i in range(len(x)):
            spike_positions.append([x[i], y[i], e[i]])

        print("Found " + str(len(spike_positions)) + " spikes!")

        for (x,y,e) in spike_positions:
            # Spike intensity replaced by median of neighbors
            s.data[x,y,e] = median_from_neighbors(s.data[:,:,e], x,y)

        if plot_difference == True:
            diff_after = np.diff(s.data, axis=1)
            plot_spike_histogram(diff, diff_after)
    else:
        print("The signal shape does not match an expected value (X, S or
            X, Y, S). Signal data shape is " + str(s.data.shape))

    return s
```

10 HyperSpy scripting notebook

Contents

10.1 Load and decompose the data using my own decomposition-interface 269
10.2 Fit Core loss EELS with Zr L edges, white lines and the O K edge. 279

This is a Python Jupyter notebook to analyse a set of EDS and EELS spectrum images acquired on the same region. Please see www.hyperspy.org for details on HyperSpy. Scripts written by me, Thomas Aarholt, 2014-2017. Functions used throughout the notebook will be available online with the digital version of the thesis.

10.1 Load and decompose the data using my own decomposition-interface

The function presents the user with an interactive tool for selecting PCA components in order to apply ICA

```
In [1]: %matplotlib inline
        import hyperspy.api as hs
        # This is my own collection of scripts.
        from tools import eels, aar, tools
```

```
import matplotlib.pyplot as plt
import numpy as np

# Specify file extension:
extension=".dm3"
# Specify expected elements in analysis
elements = ["Zr", "O"]

temp_path = input("Paste path here: ")
if temp_path == "":
    pass
else:
    path = temp_path
    signals = aar.analyse(path,
                          extension,
                          crop_zlp=False,
                          elements=elements,
                          decompose=True,
                          eds_log=False)
```

```
Paste path here: /G-8_Z3_EDX/EELS/Sawtooth/A/
Found these relevant files
EDS Spectrum Image.dm3
EELS Spectrum Image 0eV.dm3
EELS Spectrum Image 150eV.dm3
EELS Spectrum Image 2100eV.dm3
EELS Spectrum Image 510eV.dm3
GATAN BF-DF.dm3
SI Survey Image.dm3

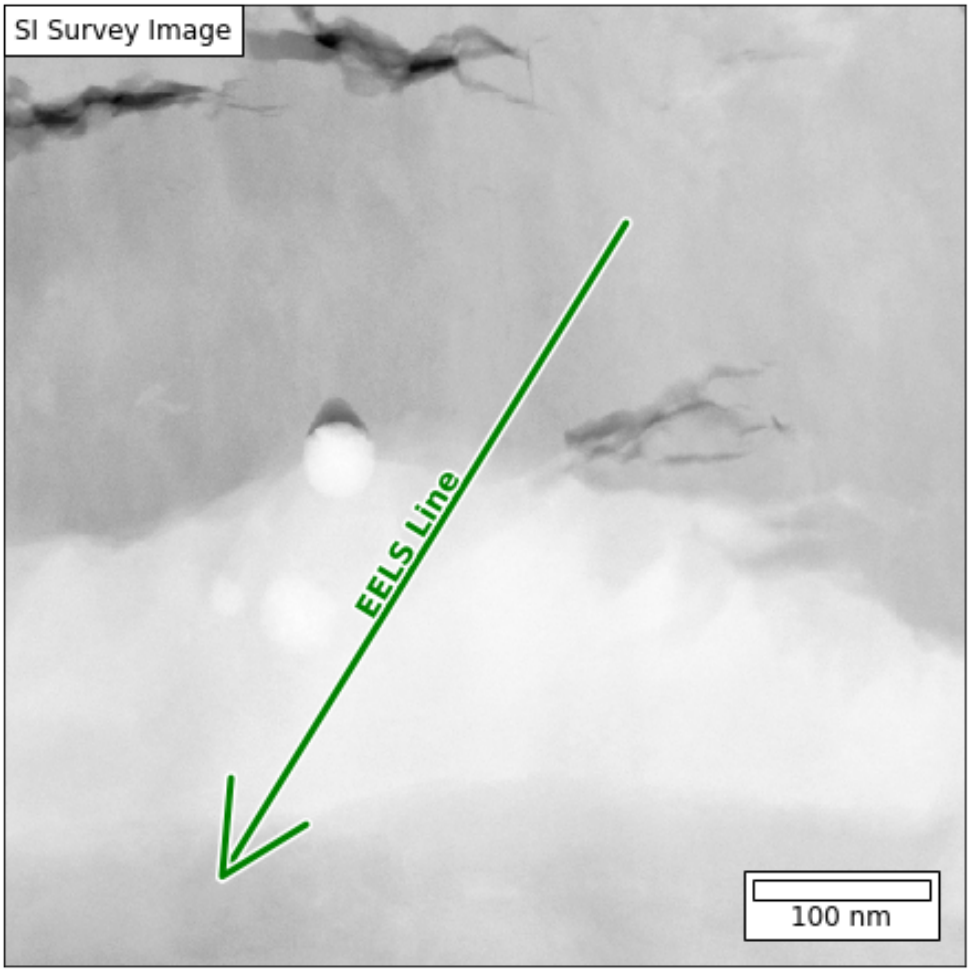
[<EDSTEMSpectrum, title: EDS Spectrum Image,
dimensions: (500|2048)>,
 <EELSSpectrum, title: EELS Spectrum Image 0eV,
 dimensions: (500|2048)>,
 <EELSSpectrum, title: EELS Spectrum Image 150eV,
 dimensions: (500|2048)>,
 <EELSSpectrum, title: EELS Spectrum Image 2100eV,
 dimensions: (500|2048)>,
 <EELSSpectrum, title: EELS Spectrum Image 510eV,
 dimensions: (500|2048)>,
 <Signal1D, title: GATAN BF-DF, dimensions: (|500)>,
 <Signal2D, title: SI Survey Image, dimensions: (|1024, 1024)>]
Aligning line using the zlp in EELS Line -50-461eV

Initial ZLP position statistics
```

```
--------------------------------
Summary statistics
------------------
mean:         0.021
std:          0.176

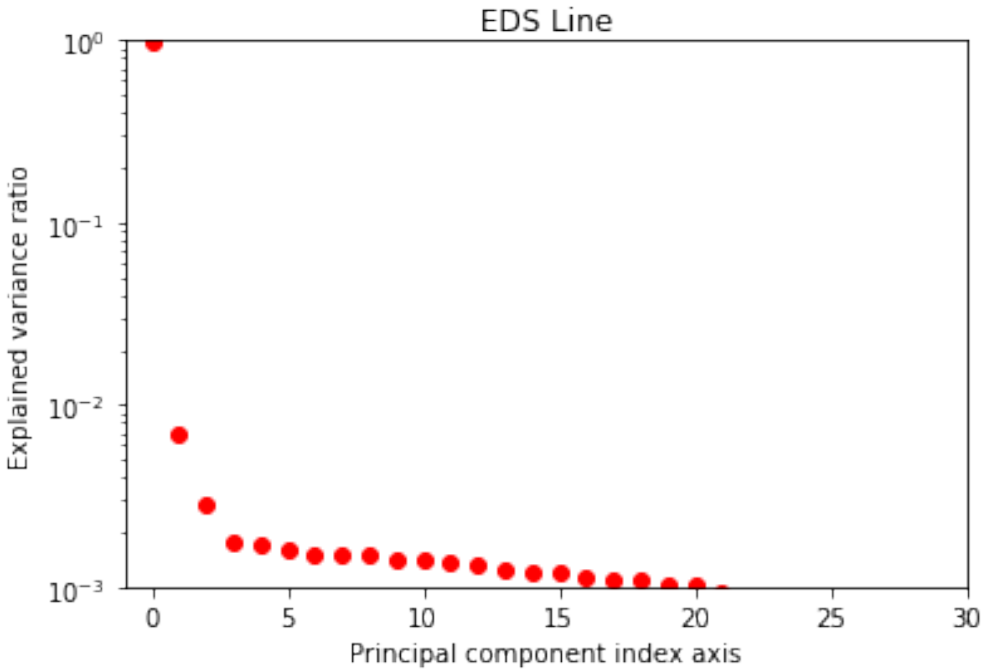
min:          -0.250
Q1:          0.000
median:          0.000
Q3:          0.250
max:          0.250


EELS Line -50-461eV
Warning: The signal has negative counts(Minimum: -58.2973).
This shouldn't happen, and may give an
error when doing decomposition
Subtract by the negative counts to make signal positive? (y/[n]): n
```

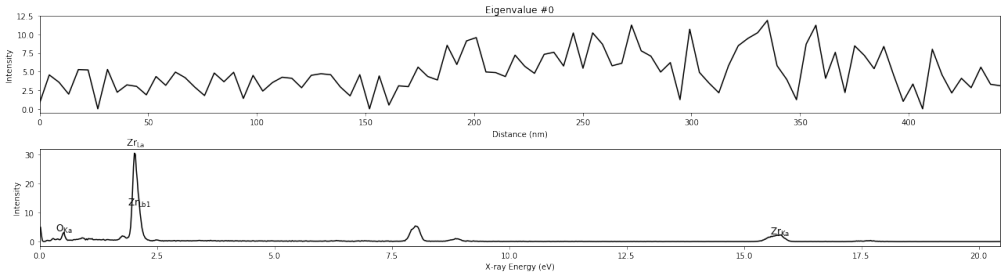


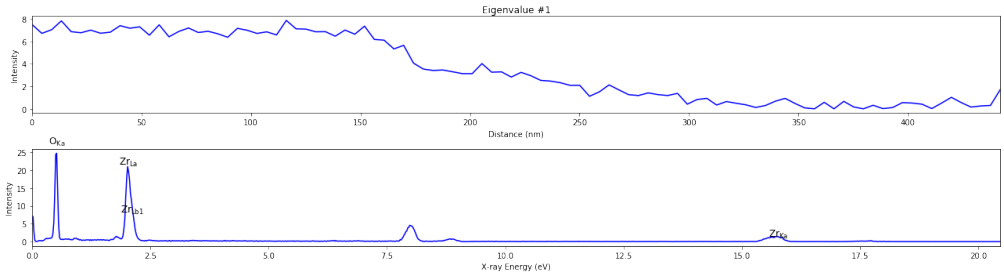
```
EDS Line
This is a rather large signal, with dimensions (500|2048).
Please enter factors to bin the signal by, separated by a space.
Bin factors [blank to pass] : 5 2

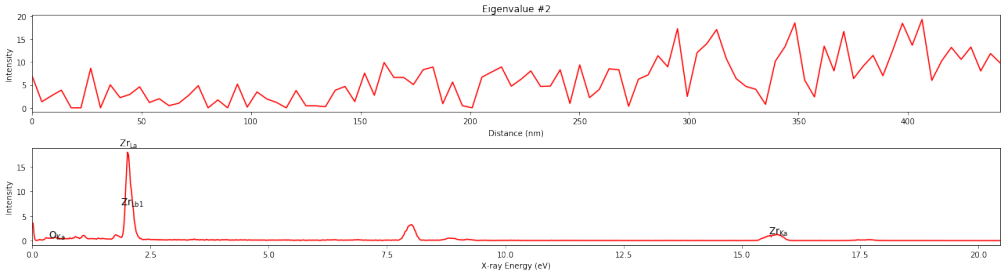

Binning EDS Line by (5 | 2).
New shape: (100|1024)
Estimated eigenvalues: 3
Performing NMF on EDS Line
```




```
Chosen eigenvalues: 3
```



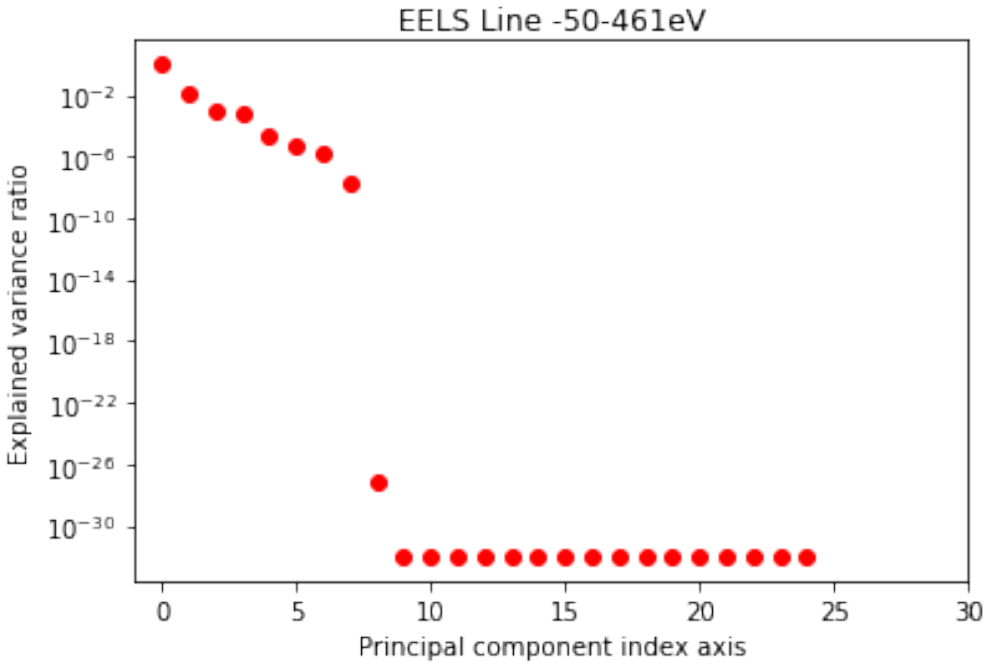





```
Try new eigenvalue?(Chose 3) Blank = Done.

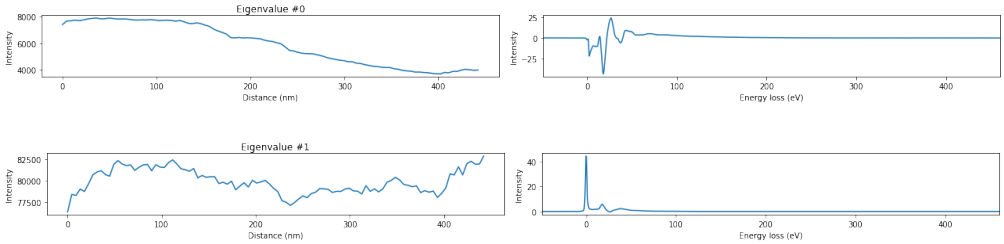
EELS Line -50-461eV
This is a rather large signal, with dimensions (500|2043).
Please enter factors to bin the signal by, separated by a space.
Bin factors [blank to pass] : 5 2
```

```
Binning EELS Line -50-461eV by (5 | 2).
New shape: (100|1021)
Estimated eigenvalues: 2
Perfoming BSS on EELS Line -50-461eV
```



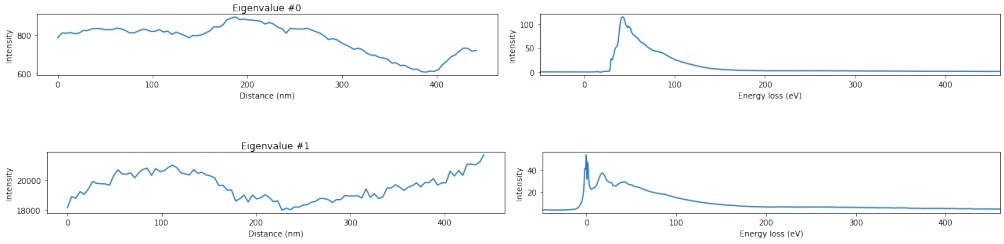

```
EELS Line -50-461eV

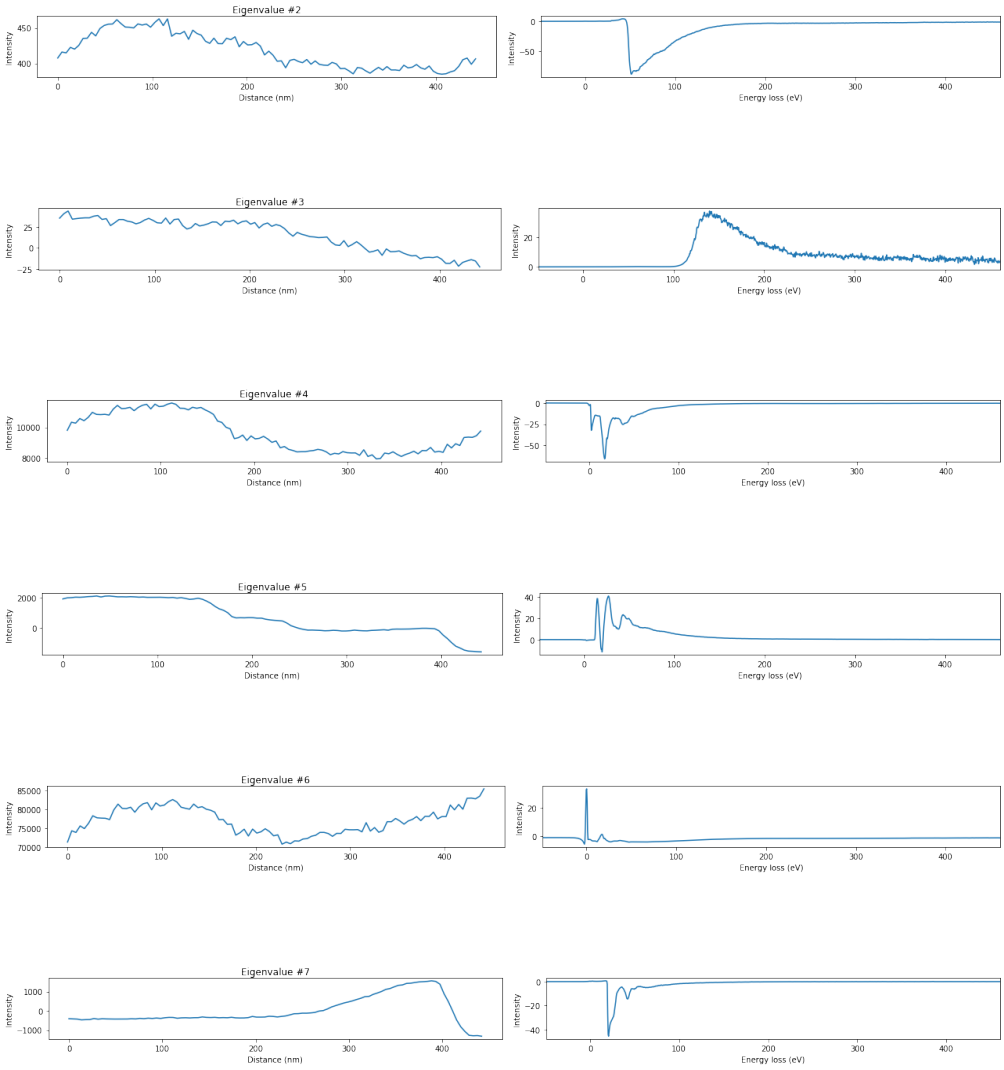
Chosen eigenvalues: 2
```




```
Try new eigenvalue?(Chose 2) Blank = Done.
8
EELS Line -50-461eV

Chosen eigenvalues: 8
```



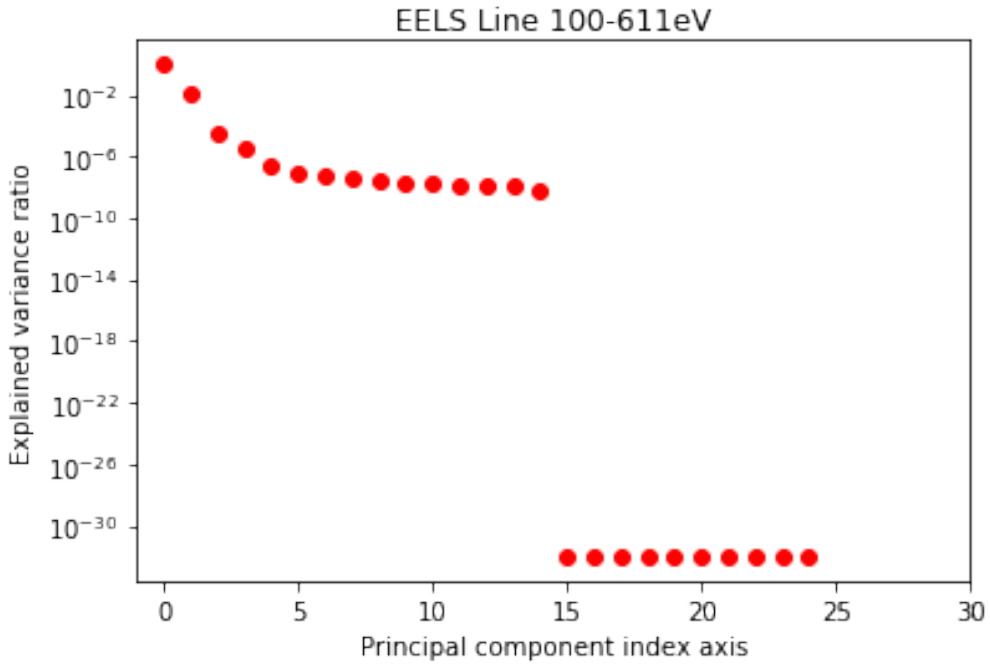



```
Try new eigenvalue?(Chose 8) Blank = Done.

EELS Line 100-611eV
This is a rather large signal, with dimensions (500|2043).
Please enter factors to bin the signal by, separated by a space.
Bin factors [blank to pass] : 5 2

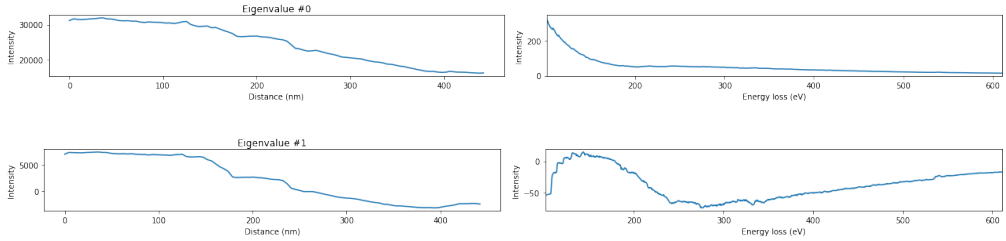


Binning EELS Line 100-611eV by (5 | 2).
New shape: (100|1021)
Estimated eigenvalues: 2
Perfoming BSS on EELS Line 100-611eV
```




```
EELS Line 100-611eV

Chosen eigenvalues: 2
```

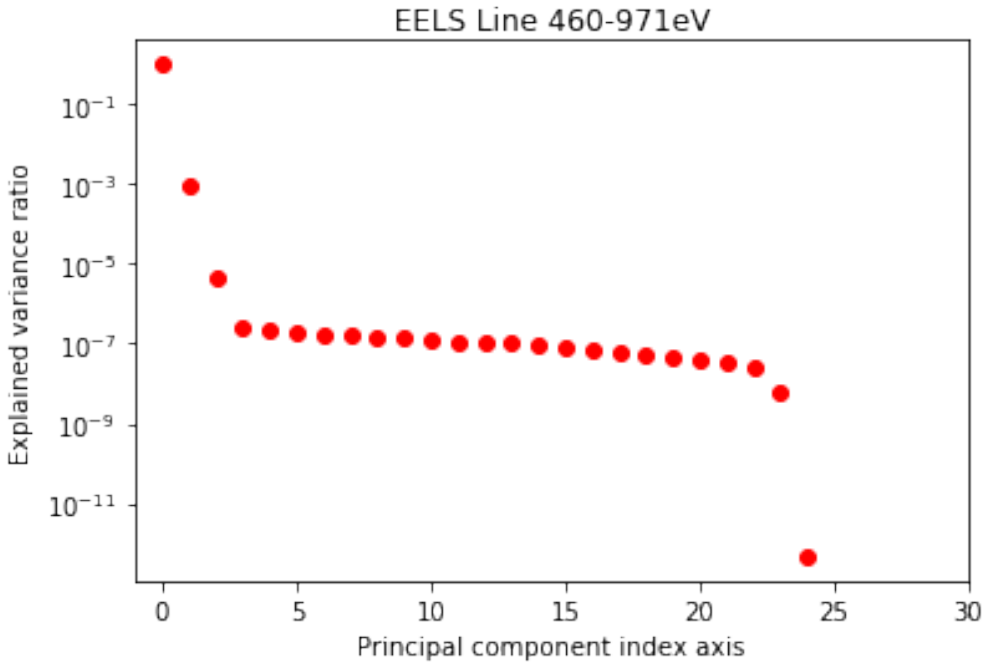



```
Try new eigenvalue?(Chose 2) Blank = Done.

EELS Line 460-971eV
This is a rather large signal, with dimensions (500|2043).
Please enter factors to bin the signal by, separated by a space.
Bin factors [blank to pass] : 5 2

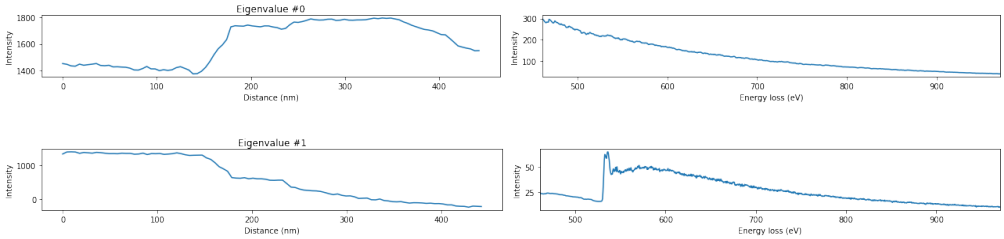


Binning EELS Line 460-971eV by (5 | 2).
New shape: (100|1021)
Estimated eigenvalues: 2
Perfoming BSS on EELS Line 460-971eV
```




```
EELS Line 460-971eV

Chosen eigenvalues: 2
```

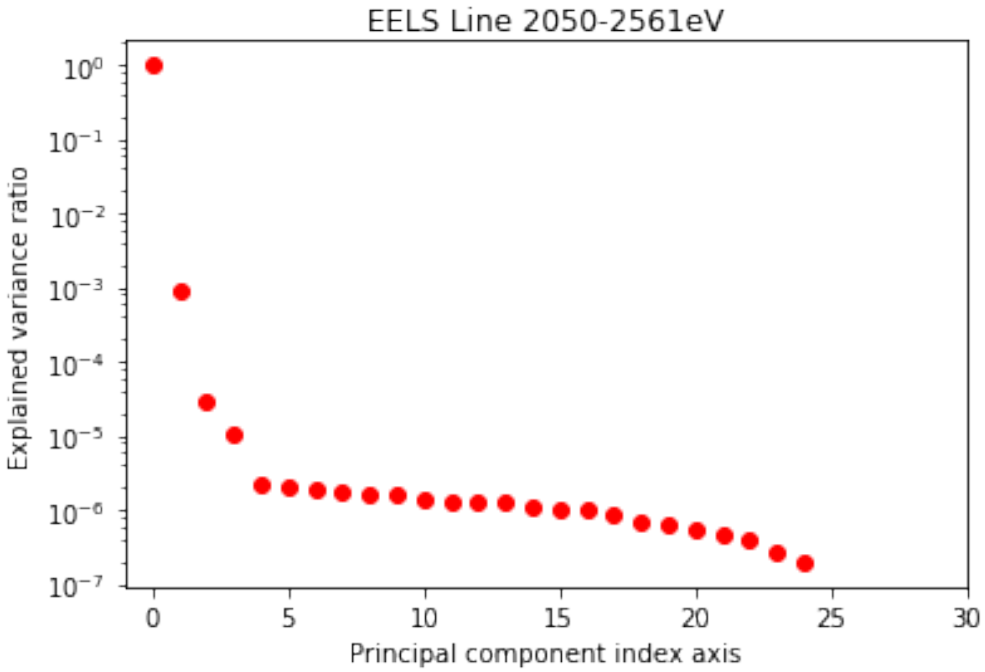



```
Try new eigenvalue?(Chose 2) Blank = Done.

EELS Line 2050-2561eV
This is a rather large signal, with dimensions (500|2043).
Please enter factors to bin the signal by, separated by a space.
Bin factors [blank to pass] : 5 2

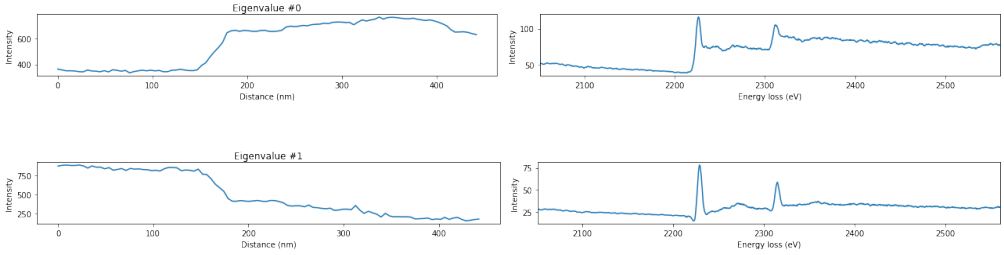


Binning EELS Line 2050-2561eV by (5 | 2).
New shape: (100|1021)
Estimated eigenvalues: 2
Perfoming BSS on EELS Line 2050-2561eV
```




```
EELS Line 2050-2561eV

Chosen eigenvalues: 2
```




```
Try new eigenvalue?(Chose 2) Blank = Done.

Find the factors and loadings in signal.metadata.Sample
Done!
```

```
In [3]: bss_signals = [signals[0].get_decomposition_model()]
        + [s.get_bss_model() for s in signals[1:-2]]
```

```
In [4]: bss_signals
```

```
Out[4]: [
<EDSTEMSpectrum, title: EDS Line, dimensions: (100|1024)>,
<EELSSpectrum, title: EELS Line -50-461eV, dimensions: (100|1021)>,
<EELSSpectrum, title: EELS Line 100-611eV, dimensions: (100|1021)>,
<EELSSpectrum, title: EELS Line 460-971eV, dimensions: (100|1021)>,
<EELSSpectrum, title: EELS Line 2050-2561eV, dimensions: (100|1021)>]
```

10.2 Fit Core loss EELS with Zr L edges, white lines and the O K edge.

```
In [7]: mZr_L = eels.fit_Zr_L(bss_signals[4], ll=bss_signals[1])
        mO_K = eels.fit_O_K(bss_signals[3], ll=bss_signals[1])
```

```
Finished fitting Zirconium
Finished fitting Oxygen
```

```
In [15]: mZr_L.components
```

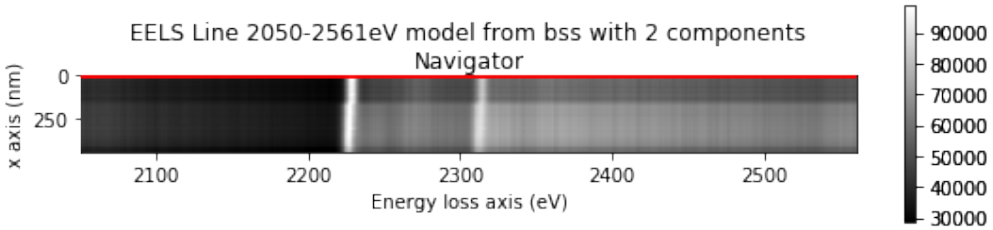
```
Out[15]:    # |      Component Name |      Component Type
          ---- | ------------------- | --------------------
             0 |            PowerLaw |            PowerLaw
             1 |    Zr_L3 White Line |            Gaussian
             2 |               Zr_L3 |          EELSCLEdge
             3 |    Zr_L2 White Line |            Gaussian
             4 |               Zr_L2 |          EELSCLEdge
```

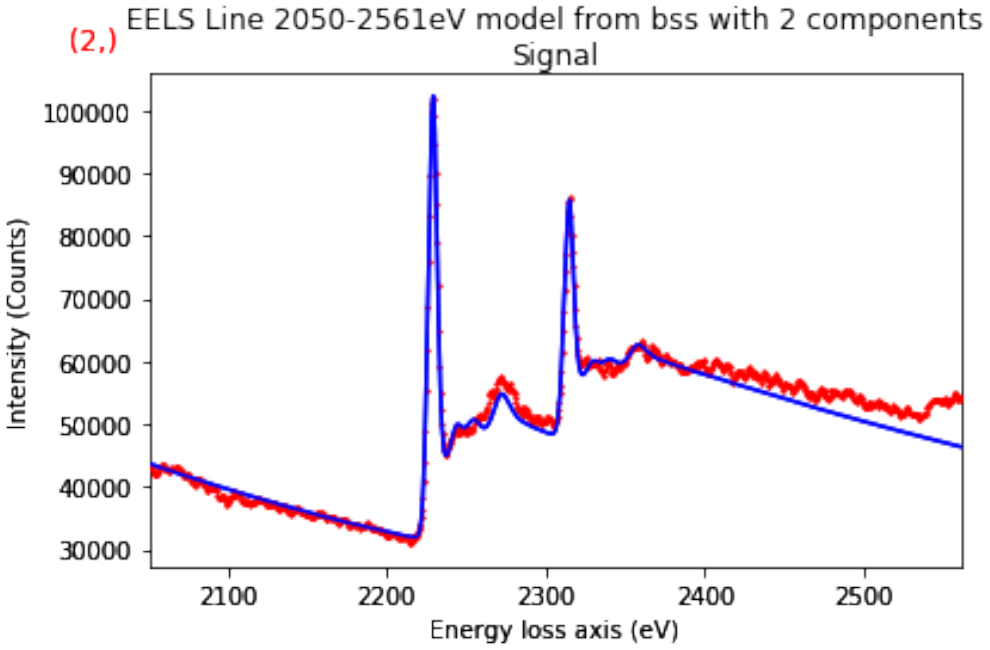
```
In [16]: mO_K.components
```

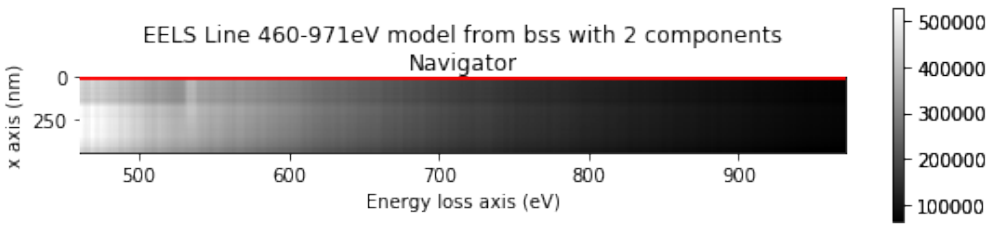
```
Out[16]:    # |      Component Name |      Component Type
          ---- | ------------------- | --------------------
             0 |            PowerLaw |            PowerLaw
             1 |      O_K White Line |            Gaussian
             2 |                 O_K |          EELSCLEdge
```

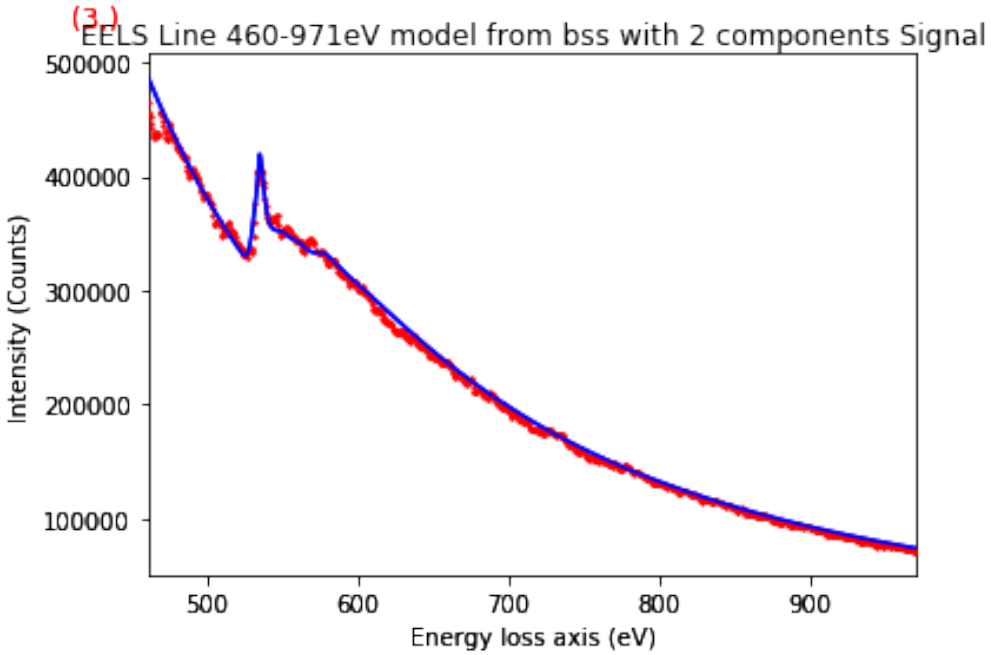
Visualise fit

```
In [13]: mZr_L.plot()
         mO_K.plot()
```


EELS Line 2050-2561eV model from bss with 2 components
Navigator
x axis (nm)
0
250
2100
2200
2300
2400
2500
Energy loss axis (eV)
90000
80000
70000
60000
50000
40000
30000


(2,)
EELS Line 2050-2561eV model from bss with 2 components
Signal
Intensity (Counts)
100000
90000
80000
70000
60000
50000
40000
30000
2100
2200
2300
2400
2500
Energy loss axis (eV)


EELS Line 460-971eV model from bss with 2 components
Navigator
x axis (nm)
0
250
500
600
700
800
900
Energy loss axis (eV)
500000
400000
300000
200000
100000

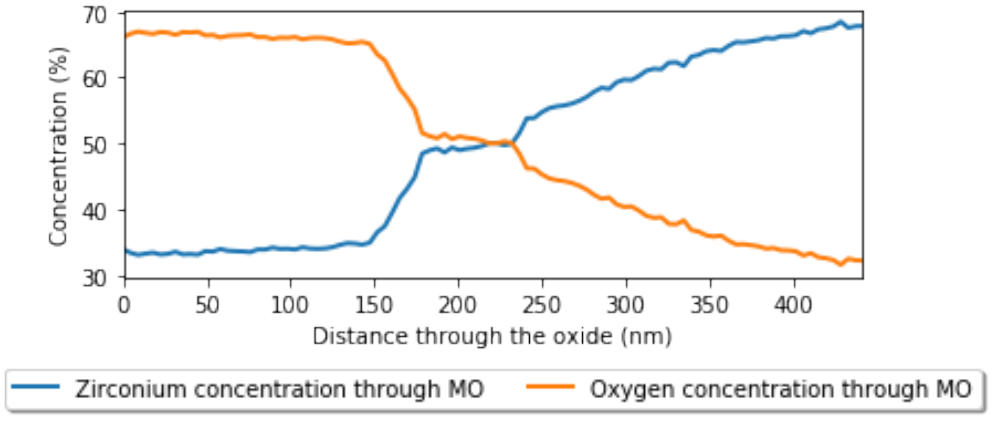


Calculate Zr:O ratio through the metal-oxide interface

In [18]:
```
Zr_intensity = mZr_L["Zr_L3"].intensity.as_signal()
O_intensity = mO_K["O_K"].intensity.as_signal()

k = eels.k_factor(Zr_intensity, O_intensity, ZrO2startstop=(0,10))
ZrO = eels.ZrO_Ratio(Zr_intensity, O_intensity, k)
tools.plot_spectra(ZrO, xlabel="Distance through the oxide (nm)",
ylabel="Concentration (%)");
```

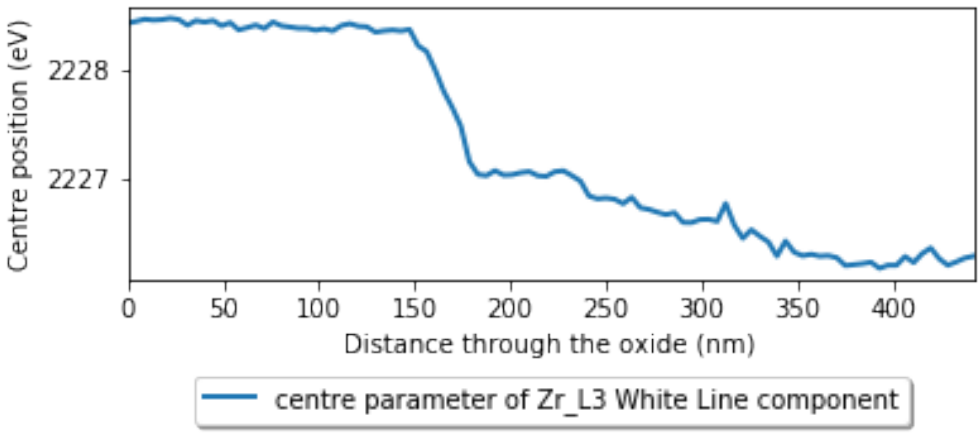
```
Recognised as Line profile
```



Plot the white line Gaussian centre through the metal-oxide interface

In [27]:
```
Zr_L3_centre = mZr_L["Zr_L3 White Line"].centre.as_signal()
tools.plot_spectrum(Zr_L3_centre, label=False,
xlabel="Distance through the oxide (nm)", ylabel="Centre position (eV)")
```

Out[27]:
```
((<matplotlib.figure.Figure at 0x1189de0b8>,
  <matplotlib.axes._subplots.AxesSubplot at 0x11c7684a8>),
 [<matplotlib.lines.Line2D at 0x1181a8940>])
```



References

[1] G. L. Miller. *Zirconium*. London: Butterworths Scientific Publications, 1954, p. 382.

[2] B. Lustman and F. Kerze. *The Metallurgy of Zirconium*. 1st Editio. Michigan: McGraw-Hill Book Company, 1955.

[3] W. E. Company. *Nuclear Fuel / Fuel Engineering, Optimized ZIRLO High-performance Fuel Cladding Material*. 2016. URL: http://www.westinghousenuclear.com/Portals/0/operating%20plant%20services/fuel/fuel%20products/NF-FE-0046%20Optimized%20ZIRLO%20HP%20Fuel%20Clad%20Mtl.pdf (visited on 09/30/2017).

[4] H. L. Yakel. *Oak Ridge National Laboratory Annual Progress Report for period ending September 1*. Tech. rep. Oak Ridge: Oak Ridge National Laboratory, 1958, p. 51.

[5] T. Sato and Y. Kojima. "Variations of a passive safety containment for a bwr with active and passive safety systems." In: *Nuclear Engineering and Design* 237.1 (2007), p. 74.

[6] H. I. Yoo, B. J. Koo, J. O. Hong, I. S. Hwang, and Y. H. Jeong. "A working hypothesis on oxidation kinetics of Zircaloy". In: *Journal of Nuclear Materials* 299.3 (2001), pp. 235–241.

[7] B. Cox and Y.-M. Wong. "A hydrogen uptake micro-mechanism for Zr alloys". In: *Journal of Nuclear Materials* 270.1–2 (1999), pp. 134–146. URL: http://linkinghub.elsevier.com/retrieve/pii/S0022311598008988.

[8] D. O. Pickman. "Zirconium alloy performance in light water reactors: A review of UK and Scandinavian experience". In: *Zirconium in the Nuclear Industry: Tenth International Symposium, ASTM STP 1245*. 1994, pp. 19–32.

[9] B. Cox. "Some thoughts on the mechanisms of in-reactor corrosion of zirconium alloys". In: *Journal of Nuclear Materials* 336.2-3 (Feb. 2005), pp. 331–368. URL: http://linkinghub.elsevier.com/retrieve/pii/S002231150400875X.

[10] G. P. Sabol. "ZIRLO (TM) - An alloy development success". In: *Zirconium in the Nuclear Industry: 14th International Symposium*. 2005, pp. 3–24.

[11] B. Cox. "Oxidation of Zirconium and its Alloys". In: *Advances in Corrosion Science and Technology* 5 (1976), p. 173.

[12] B. Cox, K. Alcock, and F. W. Derrick. "The Oxidation and Corrosion of Zirconium and Its Alloys VI: The Mechanism of Fission Fragment Induced Corrosion of Zircaloy-2". In: *Journal of The Electrochemical Society* 108.2 (1961), p. 129. URL: http://jes.ecsdl.org/cgi/doi/10.1149/1.2428027.

[13] W. Yeniscavich, R. Wolfe, and R. Lieberman. “Hydrogen absorption by nickel enriched zircaloy-2”. In: *Journal of Nuclear Materials* 3 (1959), pp. 271–280. URL: http://www.sciencedirect.com/science/article/pii/0022311559900236.

[14] B. A. Cheadle, C. E. Coleman, and H. Licht. “CANDU-PHW Pressure Tubes: Their Manufacture, Inspection, and Properties”. In: *Nuclear Technology* 57.3 (1982), pp. 413–425.

[15] C. Lemaignan. *Corrosion of Zirconium Alloy Components in Light Water Reactors*. Vol. 13C. 2006, pp. 415–420.

[16] A. V. Nikulina. “Zirconium-Niobium Alloys for Core Elements of Pressurized Water Reactors”. In: *Metal Science and Heat Treatment* 45.7 (2003), pp. 287–292. URL: http://dx.doi.org/10.1023/A:1027388503837.

[17] A. D. Schwope. *A General Comparison of the Metallurgy of Zirconium with that of Better Known Commercial Metals, in: Zirconium and Zirconium alloys.* Tech. rep. Cleverland: American Society for Metals, 1953, pp. 162–180.

[18] D. L. Douglass and D. D. L. “Corrosion mechanism of zirconium and its alloys-III. Solute distribution between corrosion films and zirconium alloy substrates.” In: *Corrosion Science* 5 (1965), p. 225.

[19] D. Taylor. “An oxide-semiconductance model of nodular corrosion and its application to Zirconium alloy development”. In: *Journal of Nuclear Materials* 184.1 (Aug. 1991), pp. 65–77. URL: http://linkinghub.elsevier.com/retrieve/pii/002231159190534E.

[20] J. Harding. “The effect of alloying elements on Zircaloy corrosion”. In: *Journal of Nuclear Materials* 202.3 (July 1993), pp. 216–221. URL: http://linkinghub.elsevier.com/retrieve/pii/002231159390390K.

[21] P. Tejland, C. Langhammer, and H.-O. Andrén. “On the black oxide colour of zirconium alloys”. In: *Journal of Nuclear Materials* 400.1 (Apr. 2010), pp. 79–83. URL: http://linkinghub.elsevier.com/retrieve/pii/S0022311510000528.

[22] G. Sundell, M. Thuvander, and H.-O. Andrén. “Enrichment of Fe and Ni at metal and oxide grain boundaries in corroded Zircaloy-2”. In: *Corrosion Science* 65 (Dec. 2012), pp. 10–12. URL: http://linkinghub.elsevier.com/retrieve/pii/S0010938X12004246.

[23] M. B. Elmoselhi. “Hydrogen uptake by oxidized zirconium alloys”. In: *Journal of Alloys and Compounds* 231 (1995), pp. 716–721.

[24] S. Kass. “The Development of the Zircaloys in Corrosion of Zirconium Alloys”. In: *ASTM STP* 368 (1964), pp. 3–27.

[25] C. Withmarsh. “Review of Zircaloy-2 and Zircaloy-4 Properties Relevant to N.S. Savannah Reactor Design”. In: *(No. ORNL-3281). Oak Ridge National Lab., Tenn..* 4500 (1962), p. 70.

[26] W. Gong, H. Zhang, Y. Qiao, H. Tian, X. Ni, Z. Li, and X. Wang. “Grain morphology and crystal structure of pre-transition oxides formed on Zircaloy-4”. In: *Corrosion Science* 74 (Sept. 2013), pp. 323–331. URL: http://linkinghub.elsevier.com/retrieve/pii/S0010938X13001972.

[27] K. T. Erwin, O. Delaire, A. T. Motta, Y. S. Chu, D. C. Mancini, and R. C. Birtcher. "Observation of second-phase particles in bulk zirconium alloys using synchrotron radiation". In: *Journal of Nuclear Materials* 294.3 (2001), pp. 299–304.

[28] J. E. LeSurf, P. E. C. Bryant, and M. C. Tanner. *AECL 2562*. Tech. rep. Atomic Energy of Canada, 1967.

[29] V. Urbanic, P. K. Chan, D. Khatamian, and O. T. Woo. "Growth and Characterization of Oxide Films on Zirconium-Niobium Alloys". In: *Zirconium in the Nuclear Industry: Tenth International Symposium, ASTM STP 1245*. West Conshohocken, 1994, pp. 116–132.

[30] K. Choo, Y. Kang, S. Pyun, and V. Urbanic. "Effect of composition and heat treatment on the microstructure and corrosion behavior of Zr-Nb alloys". In: *Journal of Nuclear Materials* 209.3 (May 1994), pp. 226–235. URL: http://linkinghub.elsevier.com/retrieve/pii/0022311594902569.

[31] B. Cox, F. Garzarolli, and P. Rudling. *ZIRAT-9 SPECIAL TOPICS REPORT Corrosion of Zr-Nb Alloys*. Tech. rep. Surahammar, Sweden: Advanced Nuclear Technology International, 2004.

[32] B. Cox and A. Strasser. *ZIRAT-10 SPECIAL TOPICS REPORT Structural Behavior of Fuel and Fuel Channel Components*. Tech. rep. Surahammar, Sweden: Advanced Nuclear Technology International, 2005, p. 46.

[33] P. Bossis, D. Pecheur, K. Hanifi, J. Thomazet, and M. Blat. "Comparison of the high burn-up corrosion on M5 and low tin Zircaloy-4". In: *Zirconium in the Nuclear Industry: Fourteenth International Symposium*. Stockholm, Sweden, 2005, pp. 494–524.

[34] B. Cox and J. P. Pemsler. "Diffusion of oxygen in growing zirconia films". In: *Journal of Nuclear Materials* 28 (1968), pp. 73–78.

[35] B. Cox. "Processes occurring during the breakdown of oxide films on zirconium alloys". In: *Journal of Nuclear Materials* 29 (1969), pp. 50–66.

[36] B. Cox. "Effects of irradiation on the oxidation of zirconium alloys in high temperature aqueous environments". In: *Journal of Nuclear Materials* 28 (1968), pp. 1–47.

[37] IAEA. *Corrosion of zirconium alloys in nuclear power plants*. Tech. rep. Vienna: International Atomic Energy Agency, 1993.

[38] IAEA. *Waterside corrosion of zirconium alloys in nuclear power plants - IAEA TECDOC 996*. Tech. rep. January. Vienna: International Atomic Energy Agency, 1998.

[39] P. Barberis. "Zirconia powders and Zircaloy oxide films: tetragonal phase evolution during 400°C autoclave tests". In: *Journal of Nuclear Materials* 226 (1995).

[40] A. Yilmazbayhan, A. T. Motta, R. J. Comstock, G. P. Sabol, B. Lai, and Z. Cai. "Structure of zirconium alloy oxides formed in pure water studied with synchrotron radiation and optical microscopy: relation to corrosion rate". In: *Journal of Nuclear Materials* 324.1 (Jan. 2004), pp. 6–22. URL: http://linkinghub.elsevier.com/retrieve/pii/S0022311503004240.

[41] S. Forsberg. *SKI Report 2004 : 54 Studies of Corrosion of Cladding Materials in Simulated BWR-environment Using Impedance Measurements Part II : Measurements in the Post-transition Region*. Tech. rep. September. Studsvik: Swedish Nuclear Power Inspectorate, 2004, pp. 1–74.

[42] E. M. Levin, H. F. McMurdie, and M. K. Reser. *Phase Diagram for Ceramists (1975 Supplement)*. The American Ceramic Society, 1975, p. 513.

[43] G. Lelièvre, D. Fruchart, P. Convert, and F. Lefèvre-Joud. "Characterisation by neutron diffraction in high temperature pressurised water of the surface corrosion and hydrogen embrittlement of zircaloy-4". In: *Journal of Alloys and Compounds* 347.1-2 (2002), pp. 288–294.

[44] J. Godlewski, J. P. Gros, M. Lambertin, J. F. Wadier, and H. Weidinger. "Raman Spectroscopy Study of the Tetragonal-to-monoclinic Transition in Zirconium Oxide Scales and Determination of Overall Oxygen Diffusion by Nuclear Microanalysis of O18". In: *Zirconium in the Nuclear Industry: Ninth International Symposium*. {ASTM} International, 1991, pp. 416–421. URL: http://dx.doi.org/10.1520/STP25520S.

[45] J. Wei, P. Frankel, E. Polatidis, M. Blat, A. Ambard, R. J. Comstock, L. Hallstadius, D. Hudson, G. D. W. Smith, C. R. M. Grovenor, M. Klaus, R. A. Cottis, S. Lyon, and M. Preuss. "The effect of Sn on autoclave corrosion performance and corrosion mechanisms in Zr–Sn–Nb alloys". In: *Acta Materialia* 61.11 (2013), pp. 4200–4214.

[46] M. Preuss, P. Frankel, E. Polatidis, J. Wei, J. Smith, C. E. F. Wang, R. Cottis, S. Lyon, S. Lozano-Perez, D. Hudson, et al. "Towards a mechanistic understanding of corrosion mechanisms in zirconium alloys". In: *ASTM STP1529: Zirconium in the Nuclear Industry-16th International Symposium*. ASTM International. 2011.

[47] N. Ni, D. Hudson, C. Grovenor, J. Wei, and P. Wang. "How the crystallography and nano-scale chemistry of the metal/oxide interface develops during the aqueous oxidation of zirconium cladding alloys". In: *Acta Materialia* 60 (2012), pp. 7132–7149.

[48] V. Bouineau, A. Ambard, G. Bénier, D. Pêcheur, J. Godlewski, L. Fayette, and T. Duverneix. "A New Model to Predict the Oxidation Kinetics of Zirconium Alloys in a Pressurized Water Reactor BT - A New Model to Predict the Oxidation Kinetics of Zirconium Alloys in a Pressurized Water Reactor". In: *Zirconium in the Nuclear Industry: 15th International Symposium, ASTM STP 1505*. 2009, pp. 405–429.

[49] G. A. Eloff, C. J. Greyling, and P. E. Viljoen. "The role of space charge in the oxidation of Zircaloy-4 between 350 and 450°C in air". In: *Journal of Nuclear Materials* 199.3 (1993), pp. 285–288. URL: http://www.sciencedirect.com/science/article/pii/002231159390149S.

[50] A. Couet, A. T. Motta, and A. Ambard. "The coupled current charge compensation model for zirconium alloy fuel cladding oxidation: I. Parabolic oxidation of zirconium alloys". In: *Corrosion Science* 100 (2015), pp. 73–84. URL: http://dx.doi.org/10.1016/j.corsci.2015.07.003.

[51] K. Hauffe. *Oxidation of metals*. New York: Plenum press, 1965, p. 113.

[52] G. P. Sabol. "The Origin of the Cubic Rate Law in Zirconium Alloy Oxidation". In: *Journal of The Electrochemical Society* 122.2 (1975), p. 316. URL: http://jes.ecsdl.org/cgi/doi/10.1149/1.2134204.

[53] E. Hillner, D. Franklin, and J. Smee. "Long-term corrosion of Zircaloy before and after irradiation". In: *Journal of Nuclear Materials* 278.2-3 (Apr. 2000), pp. 334–345. URL: http://linkinghub.elsevier.com/retrieve/pii/S0022311599002305.

[54] T. R. Allen, R. J. M. Konings, and A. T. Motta. *Corrosion of Zirconium Alloys*. 1st ed. Vol. 5. Elsevier, 2012, pp. 49–68. URL: http://dx.doi.org/10.1016/B978-0-08-056033-5.00063-X.

[55] M. Howlader, K. Shiiyama, C. Kinoshita, M. Kutsuwada, and M. Inagaki. "The electrical conductivity of zircaloy oxide films". In: *Journal of Nuclear Materials* 253.1-3 (Mar. 1998), pp. 149–155. URL: http://linkinghub.elsevier.com/retrieve/pii/S0022311597003097.

[56] C. Proff, S. Abolhassani, and C. Lemaignan. "Oxidation behaviour of binary zirconium alloys containing intermetallic precipitates". In: *Journal of Nuclear Materials* 416.1-2 (Sept. 2011), pp. 125–134. URL: http://linkinghub.elsevier.com/retrieve/pii/S0022311510008275.

[57] J. Wei. "Effect of Hydrogen on the Corrosion Performance of Zirconium Alloys". PhD. University of Manchester, 2012, p. 137.

[58] N. Ramasubramanian. "Localised electron transport in corroding zirconium alloys". In: *Journal of Nuclear Materials* 5 (1975), pp. 134–154.

[59] B. Griggs, H. P. Maffei, and D. W. Shannon. "Multiple rate transitions in the aqueous corrosion of zircaloy". In: *Journal of The Electrochemical Society* 109.8 (1962), p. 665. URL: http://jes.ecsdl.org/cgi/doi/10.1149/1.2425526.

[60] B. Cox. "Some effects of pressure on the oxidation of Zircaloy-2 in steam and oxygen". In: *Journal of the Less Common Metals* 5 (1963), pp. 325–336.

[61] M. Oskarsson, E. Ahlberg, U. Andersson, and K. Pettersson. "Characterisation of pre-transition oxides on Zircaloys". In: *Journal of Nuclear Materials* 297 (2001), pp. 77–88.

[62] B. Cox. "The Oxidation and Corrosion of Zirconium and its Alloys V: Mechanism of Oxide Film Growth and Breakdown on Zirconium and Zircaloy-2". In: *Journal of The Electrochemical Society* 108.1 (1961), pp. 24–30. URL: http://jes.ecsdl.org/cgi/doi/10.1149/1.2428005.

[63] J. Dawson, G. Long, W. Seddon, and J. White. "The kinetics and mechanism of the oxidation of zircaloy-2 at 350–500 °C". In: *Journal of Nuclear Materials* 25 (1968). URL: http://www.sciencedirect.com/science/article/pii/0022311568900445.

[64] B. Cox. "Environmentally-induced cracking of zirconium alloys — A review". In: *Journal of Nuclear Materials* 170.1 (1990), pp. 1–23.

[65] A. Yilmazbayhan, E. Breval, A. T. Motta, and R. J. Comstock. "Transmission electron microscopy examination of oxide layers formed on Zr alloys". In: *Journal of Nuclear Materials* 349.3 (Mar. 2006), pp. 265–281. URL: http://linkinghub.elsevier.com/retrieve/pii/S0022311505005106.

[66] Y. H. Jeong, J. H. Baek, S. J. Kim, H. G. Kim, and H. Ruhmann. "Corrosion characteristics and oxide microstructures of Zircaloy-4 in aqueous alkali hydroxide solutions". In: *Journal of Nuclear Materials* 270.3 (1999), pp. 322–333.

[67] W. Hsieh, J. Kai, C. Tsai, and X. Guo. "The kinetics of uniform oxide formation and its relationship to radiation effects on Zircaloy-2". In: *Materials Chemistry and Physics* 50.1 (1997), pp. 37–44. URL: http://www.sciencedirect.com/science/article/pii/S0254058497801812.

[68] M. Y. Yao, B. X. Zhou, Q. Li, W. Q. Liu, X. Geng, and Y. P. Lu. "A superior corrosion behavior of Zircaloy-4 in lithiated water at 360C/18.6 MPa by Beta-quenching". In: *Journal of Nuclear Materials* 374.1-2 (2008), pp. 197–203.

[69] N. Ni. "Study of Oxidation Mechanisms of Zirconium Alloys by Electron Microscopy". DPhil. University of Oxford, 2011.

[70] V. Likhanskii, T. Aliev, M. Y. Kolesnik, I. Evdokimov, and V. Zborovskii. "Method of elastic energy minimization for evaluation of transition parameters in oxidation kinetics of Zr alloys". In: *Corrosion Science* 61 (Aug. 2012), pp. 143–147. URL: http://linkinghub.elsevier.com/retrieve/pii/S0010938X12002119.

[71] N. Ni, S. Lozano-Perez, J. Sykes, and C. Grovenor. "Quantitative EELS analysis of zirconium alloy metal/oxide interfaces." In: *Ultramicroscopy* 111.2 (Jan. 2011), pp. 123–30. URL: http://www.ncbi.nlm.nih.gov/pubmed/21185456.

[72] N. Ni, S. Lozano-Perez, J. Sykes, G. Smith, and C. Grovenor. "Focussed ion beam sectioning for the 3D characterisation of cracking in oxide scales formed on commercial ZIRLO™ alloys during corrosion in high temperature pressurised water". In: *Corrosion Science* 53.12 (Dec. 2011), pp. 4073–4083. URL: http://linkinghub.elsevier.com/retrieve/pii/S0010938X11004264.

[73] H. G. Kim, S. Y. Park, M. H. Lee, Y. H. Jeong, and S. D. Kim. "Corrosion and microstructural characteristics of Zr–Nb alloys with different Nb contents". In: *Journal of Nuclear Materials* 373.1-3 (Feb. 2008), pp. 429–432. URL: http://linkinghub.elsevier.com/retrieve/pii/S0022311507008021.

[74] A. Couet. "Hydrogen pick-up behaviour in zirconium alloys". PhD. The Pennsylvania State University, 2011.

[75] J. Partezana, A. M. T., A. Yilmazbayhan, R. C. J., and G. S. P. "Microstructure and growth mechanism of oxide layers formed on zr alloys studied with micro-beam synchrotron radiation." In: *Technical Report ASTM STP 1467*. 2005.

[76] J. S. Bryner. "The cyclic nature of corrosion of zircaloy-4 in 633 k water." In: *Journal of Nuclear Materials* 82.1 (1979), p. 84.

[77] V. Bounieau. "A new model to predict the oxidation kinetics of zr alloys in pwr." In: *15th ASTM Internat. Symp. On Zr in the Nucl. Industry*. 2007.

[78] E. Hillner. "Corrosion of zirconium base alloys, an overview". In: *Technical Report ASTM STP 633*. 1977.

[79] H. J. Beie, A. Mitwalsky, F. Garzarolli, H. Ruhmann, and H. J. Sell. "Examinations of the corrosion mechanism of zirconium alloys." In: *Zirconium in the Nuclear Industry: Tenth International Symposium*. Ed. by A. M. Garde and E. R. Bradley. Philadelphia, PA: ASTM International, 1994, pp. 615–643.

[80] O. Gebhardt, A. Hermann, G. Bart, H. Blank, F. Garzarolli, and L. Ray. "Investigation of In-Pile Grown Corrosion Films on Zirconium-Based Alloys". In: *Zirconium in the Nuclear Industry: 11th International Symposium, ASTM STP 1295*. Ed. by E. Bradley and G. Sabol. West Conshohocken: American Society for Testing and Materials, 1996, pp. 218–241.

[81] P. Tejland and H.-O. Andrén. "Origin and effect of lateral cracks in oxide scales formed on zirconium alloys". In: *Journal of Nuclear Materials* 430.1-3 (Nov. 2012), pp. 64–71. URL: http://linkinghub.elsevier.com/retrieve/pii/S0022311512003467.

[82] S. S. Yardley, K. L. Moore, N. Ni, J. F. Wei, S. Lyon, M. Preuss, S. Lozano-Perez, and C. R. Grovenor. "An investigation of the oxidation behaviour of zirconium alloys using isotopic tracers and high resolution SIMS". In: *Journal of Nuclear Materials* 443.1-3 (Nov. 2013), pp. 436–443. URL: http://linkinghub.elsevier.com/retrieve/pii/S0022311513009410.

[83] N. Ni, S. Lozano-Perez, M. Jenkins, C. English, G. Smith, J. Sykes, and C. Grovenor. "Porosity in oxides on zirconium fuel cladding alloys, and its importance in controlling oxidation rates". In: *Scripta Materialia* 62.8 (Apr. 2010), pp. 564–567. URL: http://linkinghub.elsevier.com/retrieve/pii/S1359646209008070.

[84] J. Godlewski. "How the Tetragonal Zirconia is Stabilized in the Oxide Scale that is Formed on a Zirconium Alloy Corroded at 400C in Steam". In: *Zirconium in the Nuclear Industry: Tenth International Symposium*. {ASTM} International, 1994, pp. 621–663. URL: http://dx.doi.org/10.1520/stp15214s.

[85] E. Polatidis, P. Frankel, J. Wei, M. Klaus, R. Comstock, a. Ambard, S. Lyon, R. Cottis, and M. Preuss. "Residual stresses and tetragonal phase fraction characterisation of corrosion tested Zircaloy-4 using energy dispersive synchrotron X-ray diffraction". In: *Journal of Nuclear Materials* 432.1-3 (Jan. 2013), pp. 102–112. URL: http://linkinghub.elsevier.com/retrieve/pii/S0022311512003844.

[86] A. Heuer and M. Rühle. "Overview no. 45: On the nucleation of the martensitic transformation in zirconia (ZrO2)". In: *Acta metallurgica* 33.12 (1985), pp. 2101–2112. URL: http://www.sciencedirect.com/science/article/pii/0001616085901713.

[87] A. Garner, A. Gholinia, P. Frankel, M. Gass, I. Maclaren, and M. Preuss. "The microstructure and microtexture of zirconium oxide films studied by transmission electron backscatter diffraction and automated crystal orientation mapping with transmission electron microscopy". In: *Acta Materialia* 80 (2014), pp. 159–171. URL: http://dx.doi.org/10.1016/j.actamat.2014.07.062.

[88] M. Oskarsson. "Study on the Mechanisms for Corrosion and Hydriding of Zircaloy". PhD. Royal Institute of Technology, 2000.

[89] G. Sundell, M. Thuvander, P. Tejland, M. Dahlbäck, L. Hallstadius, and H. O. Andrén. "Redistribution of alloying elements in Zircaloy-2 after in-reactor exposure". In: *Journal of Nuclear Materials* 454.1-3 (2014), pp. 178–185.

[90] F. Garzarolli, B. Cox, and P. Rudling. *Corrosion and Hydriding*. Tech. rep. January. Mölnlycke: ANT International, 2012.

[91] P. Bossis, G. Lelièvre, P. Barberis, X. Iltis, F. Lefebvre, L. Thomas, and M. P. Maguire. "Multi-Scale Characterization of the Metal-Oxide Interface of Zirconium Alloys". In: *Zirconium in the Nuclear Industry: 12th International Symposium, ASTM STP 1354*. Toronto, Canada: American Society for Testing and Materials, 2000, pp. 918–945.

[92] N. Schönberg. "The Structure of the Metallic Quaternary Phase ZrTaNO." In: *Acta Chemica Scandinavica* 8 (1954), pp. 627–629. URL: http://actachemscand.org/doi/10.3891/acta.chem.scand.08-0627.

[93] R. W. G. Wyckoff. *Crystal Structures - Volume 1*. English. New York: John Wiley, 1963, p. 467.

[94] R. J. Nicholls, N. Ni, S. Lozano-Perez, A. London, D. W. McComb, P. D. Nellist, C. R. Grovenor, C. J. Pickard, and J. R. Yates. "Crystal Structure of the ZrO Phase at Zirconium/Zirconium Oxide Interfaces". In: *Advanced Engineering Materials* 17.2 (2015), pp. 211–215.

[95] J. Hu, A. Garner, N. Ni, A. Gholinia, R. J. Nicholls, S. Lozano-Perez, P. Frankel, M. Preuss, and C. R. M. Grovenor. "Identifying suboxide grains at the metal-oxide interface of a corroded Zr-1.0%Nb alloy using (S)TEM, transmission-EBSD and EELS." In: *Micron* 69 (2015), pp. 35–42.

[96] V. Perovic, G. C. Weatherly, and C. J. Simpson. "Hydride precipitation in alpha/beta zirconium alloys". In: *Acta Metallurgica* 31.9 (1983), pp. 1381–1391.

[97] A. Zieliński and S. Sobieszczyk. "Hydrogen-enhanced degradation and oxide effects in zirconium alloys for nuclear applications". In: *International Journal of Hydrogen Energy* 36.14 (2011), pp. 8619–8629. URL: http://linkinghub.elsevier.com/retrieve/pii/S0360319911008330.

[98] T. B. Massalski, H. Okamoto, P. R. Subramanian, and L. Kacprzak. *Binary Alloy Phase Diagrams*. Ed. by T. B. Massalski. Ohio: 2nd, 1990, p. 3589.

[99] E. Perryman. "Picketing Pressure Tube Cracking Experience". In: *Nuclear Energy* 17 (1978), pp. 95–105.

[100] K. Edsinger, J. H. Davies, and R. Adamson. "Degraded fuel cladding fractography and fracture behaviour". In: *Zirconium in the Nuclear Industry: 12th International Symposium, ASTM STP 1354*. Ed. by G. P. Sabol and G. Moan. Toronto, Canada: American Society for Testing and Materials, 2000, pp. 316–339.

[101] IAEA. *Delayed hydride cracking of zirconium alloy fuel cladding - IAEA TECDOC 1649*. Tech. rep. Vienna: International Atomic Energy Agency, 2010, pp. 1–77.

[102] IAEA. *Delayed hydride cracking in zirconium alloys in pressure tube nuclear reactors - IAEA TECDOC 1410*. Tech. rep. October. Vienna: International Atomic Energy Agency, 2004.

[103] S. Yamanaka and K. Higuchi. "Hydrogen solubility in zirconium alloys". In: *Journal of Alloys and Compounds* 231 (1995), pp. 503–507.

[104] K. Une, K. Sakamoto, J. Matsunaga, Y. Etoh, M. Aomi, I. Takagi, K. Sawada, H. Watanabe, and K. Matsunaga. "Controlling factors in hydrogen absorption of zirconium alloys". In: *TopFuel 2012*. 2012, p. 40.

[105] F. J. Gomez, M. A. Martin-Rengel, J. Ruiz-Hervias, and E. Torres. "New method to obtain the fracture energy of hydrogen-charged nuclear fuel cladding from ring compression tests". In: *Topfuel 2012*. 2012, pp. 51–55.

[106] N. A. P. K. Kumar. "Hydride formation in zirconium alloys". PhD. McGill University, 2011, p. 236.

[107] N. Vermaak, G. Parry, R. Estevez, and Y. Bréchet. "New insight into crack formation during corrosion of zirconium-based metal-oxide systems". In: *Acta Materialia* 61.12 (July 2013), pp. 4374–4383. URL: http://linkinghub.elsevier.com/retrieve/pii/S1359645413002814.

[108] Y. S. Kim and S. S. Park. "Stage I and II behaviors of delayed hydride cracking velocity in zirconium alloys". In: *Journal of Alloys and Compounds* 453.1-2 (Apr. 2008), pp. 210–214. URL: http://linkinghub.elsevier.com/retrieve/pii/S0925838806020081.

[109] S. K. Ghosal, G. C. Palit, and P. De. "Corrosion of Zirconium Alloys in Nuclear Applications – A Review". In: *Mineral Processing and Extractive Metallurgy Review* 22.4-6 (Jan. 2002), pp. 519–546. URL: http://www.tandfonline.com/doi/abs/10.1080/08827500208547428.

[110] K. Sadian, R. Johansson, and C. Alex. *Consequences of hydrogen pick-up in fuel cladding*. Tech. rep. Uppsala: Uppsala University, 2010, p. 18.

[111] T. Kubo and Y. Kobayashi. "Effects of d-hydride precipitation at a crack tip on crack propagation in delayed hydride cracking of Zircaloy-2". In: *Journal of Nuclear Materials* 439 (2013), pp. 202–211.

[112] L. Ponzoni, J. Mieza, E. De Las Heras, and G. Domizzi. "Comparison of delayed hydride cracking behavior of two zirconium alloys". In: *Journal of Nuclear Materials* 439.1-3 (Aug. 2013), pp. 238–242. URL: http://linkinghub.elsevier.com/retrieve/pii/S0022311512004539.

[113] G. A. McRae, C. E. Coleman, and B. W. Leitch. "The first step for delayed hydride cracking in zirconium alloys". In: *Journal of Nuclear Materials* 396 (2010), pp. 130–143.

[114] M. B. Elmoselhi, B. D. Warr, and S. McIntyre. "A study of the hydrogen uptake mechanism in zirconium alloys". In: *Zirconium in the Nuclear Industry: Tenth International Symposium, ASTM STP 1245*. Ed. by A. M. Garde and E. R. Bradley. Baltimore, MD, USA, 1994, pp. 62–79.

[115] H. Muta, Y. Etoh, Y. Ohishi, K. Kurosaki, and S. Yamanaka. "Ab initio study of hydrogen diffusion in zirconium oxide". In: *Journal of Nuclear Science and Technology* 49.5 (2012), pp. 544–550. URL: http://www.tandfonline.com/doi/abs/10.1080/00223131.2012.676820.

[116] M. Harada and R. Wakamatsu. "The Effect of Hydrogen on the Transition Kinetics of Corrosion Rate of Zirconium Alloys". In: *15th ASTM Internat. Symp. On Zr in the Nucl. Industry*. Sunriver, OR, 2007.

[117] K. Kakiuchi, N. Itagaki, T. Furuya, A. Miyazaki, Y. Ishii, S. Suzuki, T. Terai, and M. Yamawaki. "Effect of iron on hydrogen absorption properties of zirconium alloys". In: *Journal of Physics and Chemistry of Solids* 66.2-4 (2005), pp. 308–311. URL: http://linkinghub.elsevier.com/retrieve/pii/S0022369704003130.

[118] M. Miyake, M. Uno, and S. Yamanaka. "On the zirconium-oxygen-hydrogen ternary system". In: *Journal of Nuclear Materials* 270 (1999), pp. 233–241.

[119] R. A. Ploc. "Hydrogen Uptake Mechanism for Zr 2.5Nb". In: *Proc. 4th Int. Conf. on Microscopy of Oxidation*. Cambridge, 1999, pp. 29–33.

[120] Y. Hatano, R. Hitaka, M. Sugisaki, and M. Hayashi. "Influence of size distribution of Zr(Fe,Cr)2 precipitates on hydrogen transport through oxide film of Zircaloy-4". In: *Journal of Nuclear Materials* 248 (1997), pp. 311–314.

[121] R. J. Comstock. *MUZIC-2 Hydrogen Pickup Mechanism in Zirconium-Based Alloys – A Collaborative University Study*. Tech. rep. Pittsburgh, PA: Westinghouse Electric Company LLC, 2012, p. 33.

[122] W. E. Berry, D. A. Vaughan, and E. L. White. "Hydrogen pickup during Aqueous Corrosion of Zirconium Alloys". In: *Corrosion* 17 (1961), p. 109.

[123] G. Schanz, B. Adroguer, and A. Volchek. "Advanced treatment of zircaloy cladding high-temperature oxidation in severe accident code calculations". In: *Nuclear Engineering and Design* 232.1 (July 2004), pp. 75–84. URL: http://linkinghub.elsevier.com/retrieve/pii/S0029549304001542.

[124] H. Okamoto. "O-Zr (Oxygen-Zirconium)". In: *Journal of Phase Equilibria and Diffusion* 28.5 (Sept. 2007), pp. 498–498. URL: http://link.springer.com/10.1007/s11669-007-9154-2.

[125] J. P. Abriata, J. C. Bolcich, and D. Arias. "The Sn-Zr (Tin-Zirconium) Phase System". In: *Bulletin of Alloy Phase Diagrams* 4 (1983), p. 147.

[126] Y.-U. Kwon and J. D. Corbett. "Sn-Zr Phase Diagram". In: *Chemistry of Metals* 2 (1990), pp. 27–33.

[127] A. M. Garde, S. R. Pati, M. A. Krammen, G. P. Smith, and R. K. Endter. "Corrosion behaviour of zircaloy-4 cladding with varying tin content in high-temperature pressurized water reactors". In: *Zirconium in the Nuclear Industry: Tenth International Symposium, ASTM STP 1245*. Ed. by A. M. Garde and E. R. Bradley. Philadelphia, PA: ASTM International, 1994, pp. 760–778.

[128] P. Bossis, D. Pecheur, K. Hanifi, J. Thomazet, and M. Blat. "Zirconium in the Nuclear Industry: Fourteenth International Symposium, ASTM International". In: *Zirconium in the Nuclear Industry: Fourteenth International Symposium*. Sweden, Stockholm: Rudling, P.; Kammenzind, B.; 2005, pp. 494–525.

[129] M. Harada, M. Kimpara, and K. Abe. "Effect of Alloying Elements on Uniform corrosion resistance of zirconium-based alloys". In: *Zirconium in the Nuclear Industry: Ninth International Symposium, ASTM STP 1132*. Ed. by C. M. Eucken and A. M. Garde. Philadelphia: American Society for Testing and Materials, 1991, pp. 368–391.

[130] V. S. Emel'ianov, I. G. Godin, and A. I. Evstiukhin. "Study of the zirconium apex op the Zr-Ta-Nb phase diagram". In: *The Soviet Journal of Atomic Energy* 4.2 (1958), pp. 211–220. URL: http://dx.doi.org/10.1007/BF02207344.

[131] S. Oh, C. Jang, J. H. Kim, and Y. H. Jeong. "Effect of Nb on hydride embrittlement of Zr–xNb alloys". In: *Materials Science and Engineering: A* 527.6 (Mar. 2010), pp. 1306–1313. URL: http://linkinghub.elsevier.com/retrieve/pii/S0921509309012258.

[132] A. A. Kiselev, V. A. Myshkin, A. V. Kozhevnikov, S. I. Korolev, and E. G. Shorina. "Research on the Corrosion of Zirconium Alloys in Water and Steam at High Temperature and Pressure." In: *Corrosion of Reactor Materials* 2 (1962), p. 67.

[133] Z. M. Alekseeva and N. V. Korotkova. "The Zr-Fe Phase Diagram". In: *Russian Metallurgy (Metally)* 4 (1989), pp. 202–208.

[134] D. Arias and J. P. Abriata. "The Fe-Zr (Iron-Zirconium) System". In: *Bulletin of Alloy Phase Diagrams* 9 (1988), pp. 597–604.

[135] N. Itagaki, K. Kakiuchi, Y. Mozumi, T. Furuya, and O. Kubota. "Development of New High Corrosion Resistance Zr Alloy HiFi for High Burn-up BWR Fuel". In: *Proceedings European Nuclear Society TOPFUEL*. Würtzburg, 2003.

[136] D. Arias and J. P. Abriata. "The Cr-Zr (Chromium-Zirconium) System". In: *Bulletin of Alloy Phase Diagrams* 7.3 (1986), pp. 237–244.

[137] J.-Y. Park, S. J. Yoo, B.-K. Choi, and Y. H. Jeong. "Oxide microstructures of advanced Zr alloys corroded in 360°C water loop". In: *Journal of Alloys and Compounds* 437.1-2 (June 2007), pp. 274–279. URL: http://linkinghub.elsevier.com/retrieve/pii/S0925838806009741.

[138] D. Peng, X. Bai, R. Yu, X. Chen, Q. Zhou, X. Liu, and P. Deng. "Role of chromium ion implantation on the corrosion behavior of zircaloy-4 in 0.5M H2SO4". In: *Electrochimica Acta* 49.9-10 (Apr. 2004), pp. 1403–1408. URL: http://linkinghub.elsevier.com/retrieve/pii/S0013468603009010.

[139] L. Bsenko. "The Hf-Ni and Zr-Ni Systems in the Region 65-90 At. % Ni." In: *Journal of the Less Common Metals* 63.2 (1979), pp. 171–179.

[140] S.-J. Luo, C.-H. Wang, and S.-W. Chen. "Phase equilibria of the ternary Ni-Cr-Zr system and interfacial reactions in the Ni-Cr/Zr couples". In: *Metallurgical and Materials Transactions A* 33.4 (2002), pp. 995–1002. URL: http://dx.doi.org/10.1007/s11661-002-0200-8.

[141] P. A. Burr, S. T. Murphy, S. C. Lumley, M. R. Wenman, and R. W. Grimes. "Hydrogen accommodation in Zr second phase particles: Implications for H pick-up and hydriding of Zircaloy-2 and Zircaloy-4". In: *Corrosion Science* 69 (2013), pp. 1–4. arXiv: 1307.7617. URL: http://dx.doi.org/10.1016/j.corsci.2012.11.036.

[142] R. Ding and I. P. Jones. "In situ hydride formation in titanium during focused ion milling". In: *Journal of Electron Microscopy* 60.1 (2011), pp. 1–9.

[143] Wikipedia. *Scanning electron microscope*. 2016. URL: https://en.wikipedia.org/wiki/Scanning%7B%5C_%7Delectron%7B%5C_%7Dmicroscope (visited on 01/01/2016).

[144] P. Hovington, D. Drouin, and R. Gauvin. "CASINO: A new monte carlo code in C language for electron beam interaction —part I: Description of the program". In: *Scanning* 19 (1997), pp. 1–14.

[145] L. A. Giannuzzi and F. A. Stevie. *Introduction to focused ion beams: Instrumentation, theory, techniques and practice*. Ed. by L. A. Giannuzzi. Springer US, 2005, pp. 1–357.

[146] J. Orloff, M. Utlaut, L. Swanson, and A. Wagner. "High Resolution Focused Ion Beams: FIB and Its Applications". In: *Physics Today* 57.1 (2004), p. 54. URL: http://link.aip.org/link/PHTOAD/v57/i1/p54/s1%7B%5C&%7DAgg=doi.

[147] D. B. Williams and C. B. Carter. *Transmission Electron Microscopy: A Textbook for Materials Science*. Cambridge library collection Volume 2. Springer, 2009, p. 820. URL: https://books.google.co.uk/books?id=dXdrG39VtUoC.

[148] F. de la Peña, V. T. Fauske, P. Burdet, T. Ostasevicius, M. Sarahan, M. Nord, J. A. Taillon, D. Johnstone, K. E. MacArthur, A. Eljarrat, S. Mazzucco, J. Caron, T. Furnival, M. Walls, E. Prestat, G. Donval, B. Martineau, L. F. Zagonel, P. Jokubauskas, T. Aarholt, and Andreas Garmannslund, and I. Iyengar. *hyperspy: HyperSpy 0.8.5*. June 2016. URL: http://dx.doi.org/10.5281/zenodo.54004.

[149] F. de la Peña, M. H. Berger, J. F. Hochepied, F. Dynys, O. Stephan, and M. Walls. "Mapping titanium and tin oxide phases using EELS: An application of independent component analysis". In: *Ultramicroscopy* 111.2 (2011), pp. 169–176.

[150] G. H. Golub and C. F. Van Loan. *Matrix Computations*. 3rd. The Johns Hopkins University Press, 1996. arXiv: arXiv:1011.1669v3.

[151] I. T. Jolliffe. *Principal Component Analysis*. Springer Series in Statistics. Springer, 2002. URL: https://books.google.co.uk/books?id=%7B%5C_%7DolByCrhjwIC.

[152] A. Hyvärinen and E. Oja. "Independent component analysis: algorithms and applications". In: *Neural Networks* 13.4-5 (2000), pp. 411–430. URL: http://www.sciencedirect.com/science/article/pii/S0893608000000265%7B%5C%%7D5Cnhttp://www.ncbi.nlm.nih.gov/pubmed/10946390.

[153] P. Cueva, R. Hovden, J. A. Mundy, H. L. Xin, and D. A. Muller. "Data processing for atomic resolution electron energy loss spectroscopy". In: *Microscopy and Microanalysis* 18.04 (2012), pp. 667–675.

[154] R. Egerton. *Electron Energy-Loss Spectroscopy in the Electron Microscope*. 3rd. Springer US, 2011, p. 491. URL: http://link.springer.com/10.1007/978-1-4419-9583-4%7B%5C%%7D5Cnhttp://www.springerlink.com/index/10.1007/978-1-4419-9583-4.

[155] N. Ni, S. Lozano-Perez, J. Sykes, and C. Grovenor. "Transmission EELS Quantification Study of Oxygen Content at Zirconium Alloy Metal/Oxide Interface". In: *Microscopy and Microanalysis* 16.S2 (Aug. 2010), pp. 1614–1615. URL: http://www.journals.cambridge.org/abstract%7B%5C_%7DS1431927610054000.

[156] K. J. Annand, I. Maclaren, and M. Gass. "Utilising DualEELS to probe the nanoscale mechanisms of the corrosion of Zircaloy-4 in 350°C pressurised water". In: *Journal of Nuclear Materials* 465 (2015), pp. 390–399. URL: http://dx.doi.org/10.1016/j.jnucmat.2015.06.022.

[157] T. Manoubi, M. Tencé, and C. Colliex. "Quantification of white lines in electron energy loss spectroscopy (EELS)". In: *Ultramicroscopy* 28 (1989), pp. 49–55.

[158] J. H. Rask, B. A. Miner, and P. R. Buseck. "Determination of manganese oxidation states in solids by electron energy-loss spectroscopy". In: *Ultramicroscopy* 21.4 (1987), pp. 321–326.

[159] M. T. Otten, B. Miner, J. H. Rask, and P. R. Buseck. "The determination of Ti, Mn and Fe oxidation states in minerals by electron energy-loss spectroscopy". In: *Ultramicroscopy* 18.1-4 (1985), pp. 285–289.

[160] A. Benninghoven, F. G. Rudenauer, and H. Werner. "Secondary ion mass spectrometry–basic concepts, instrumental aspects, applications and trends." In: *Surface and Interface Analysis* 10.8 (1987), p. 435. URL: http://dx.doi.org/10.1002/sia.740100811.

[161] J. C. Vickerman, A. Brown, and N. M. Reed. *International Series of Monographs on Chemistry, 17: Secondary Ion Mass Spectrometry. Principles and Applications.* Oxford University Press, 1989, p. 341.

[162] B. de Gabory, Y. Dong, A. T. Motta, and E. A. Marquis. "EELS and atom probe tomography study of the evolution of the metal/oxide interface during zirconium alloy oxidation". In: *Journal of Nuclear Materials* 462 (2015), pp. 304–309. URL: http://www.sciencedirect.com/science/article/pii/S0022311515001907.

[163] B. De Gabory, A. T. Motta, and K. Wang. "Transmission electron microscopy characterization of Zircaloy-4 and ZIRLO oxide layers". In: *Journal of Nuclear Materials* 456 (2015), pp. 272–280.

[164] J. Huang, M.-y. Yao, C.-y. Gao, X. Liang, J.-c. Peng, J.-l. Zhang, and B.-x. Zhou. "The Influence of Second Phase Particles on the Crack Formation in Oxide Films Formed on Zirconium Alloys". In: *Corrosion Science* 99 (2015), pp. 172–177. URL: http://www.sciencedirect.com/science/article/pii/S0010938X15003182.

[165] E. M. Francis, A. Harte, P. Frankel, S. J. Haigh, D. Jädernäs, J. Romero, L. Hallstadius, and M. Preuss. "Iron redistribution in a zirconium alloy after neutron and proton irradiation studied by energy-dispersive X-ray spectroscopy (EDX) using an aberration-corrected (scanning) transmission electron microscope". In: *Journal of Nuclear Materials* 454.1 (2014), pp. 387–397. URL: http://dx.doi.org/10.1016/j.jnucmat.2014.08.034.

[166] M. Griffiths, R. W. Gilbert, and G. J. C. Carpenter. "Phase instability, decomposition and redistribution of intermetallic precipitates in Zircaloy-2 and -4 during neutron irradiation". In: *Journal of Nuclear Materials* 150.1 (1987), pp. 53–66.

[167] W. J. S. Yang, R. P. Tucker, B. Cheng, and R. B. Adamson. "Precipitates in zircaloy: Identification and the effects of irradiation and thermal treatment". In: *Journal of Nuclear Materials* 138.2-3 (1986), pp. 185–195.

[168] Y. Matsukawa, H. L. Yang, K. Saito, Y. Murakami, T. Maruyama, T. Iwai, K. Murakami, Y. Shinohara, T. Kido, T. Toyama, Z. Zhao, Y. F. Li, S. Kano, Y. Satoh, Y. Nagai, and H. Abe. "The effect of crystallographic mismatch on the obstacle strength of second phase precipitate particles in dispersion strengthening: Bcc Nb particles and nanometric Nb clusters embedded in hcp Zr". In: *Acta Materialia* 102 (2016), pp. 323–332.

[169] G. Choudhuri, M. Kiran Kumar, V. Kain, D. Srivastava, S. Basu, B. Shah, N. Saibaba, and G. Dey. "Influence of Fe content on corrosion and hydrogen pick up behavior of Zr–2.5Nb pressure tube material". In: *Journal of Nuclear Materials* 441.1-3 (Oct. 2013), pp. 178–189.

[170] P. Prieto, F. Yubero, E. Elizalde, and J. M. Sanz. "Dielectric properties of Zr, ZrN, Zr3N4, and ZrO2 determined by quantitative analysis of electron energy loss spectra". In: *Journal of Vacuum Science & Technology A: Vacuum, Surfaces, and Films* 14.6 (1996), pp. 3181–3188. URL: http://dx.doi.org/10.1116/1.580210.

[171] C. Palacio, J. Sanz, and J. Martinez-Duart. "Low energy electron emission and EELS of clean and oxidised zirconium". In: *Surface Science* 191.3 (Nov. 1987), pp. 385–394. URL: http://linkinghub.elsevier.com/retrieve/pii/S0039602887811858.

[172] K.-O. Axelsson, K.-E. Keck, and B. Kasemo. "AES and EEL spectra from Zr, Zr+O2 and ZrO2; peak energy shifts and intensity variations at various stages of oxidation in the pressure range 10-6-103 Torr". In: *Surface Science* 164.1 (Dec. 1985), pp. 109–126. URL: http://linkinghub.elsevier.com/retrieve/pii/0039602885907022.

[173] J. Frandon, B. Brousseau, and F. Pradal. "Electronic Excitations in Some Transition Metals and Their Oxides. Characteristic Energy Loss Measurements up to 50 eV". In: *physica status solidi (b)* 98.1 (1980), pp. 379–385. URL: http://dx.doi.org/10.1002/pssb.2220980140.

[174] J. Hu, S. B. Setiadinata, T. Aarholt, A. Garner, A. Vilalta-Clemente, J. M. Partezana, P. Frankel, P. A. J. Bagot, S. Lozano-Perez, A. Wilkinson, M. Preuss, M. Moody, and C. R. Grovenor. "Understanding Corrosion and Hydrogen Pickup of Zirconium Fuel Cladding Alloys: The Role of Oxide Microstructure, Porosity, Suboxides, and Second-Phase Particles". In: *Zirconium in the Nuclear Industry: 18th International Symposium*. Ed. by R. J. Comstock and A. T. Motta. West Conchohocken, PA: ASTM International, 2018, pp. 93–127.

[175] L. Yedra, E. Xuriguera, M. Estrader, A. López-Ortega, M. D. Baró, J. Nogués, M. Roldan, M. Varela, S. Estradé, and F. Peiró. "Oxide Wizard: An EELS Application to Characterize the White Lines of Transition Metal Edges". In: *Microscopy and Microanalysis* 20.03 (2014), pp. 698–705. URL: http://www.ncbi.nlm.nih.gov/pubmed/24750576%7B%5C%%7D5Cnhttp://www.journals.cambridge.org/abstract%7B%5C_%7DS1431927614000440.

[176] T. Manoubi, C. Colliex, and P. Rez. "Quantitative electron energy loss spectroscopy on M45 edges in rare earth oxides". In: *Journal of Electron Spectroscopy and Related Phenomena* 50.1 (1990), pp. 1–18.

[177] T. L. Daulton and B. J. Little. "Determination of chromium valence over the range Cr(0)-Cr(VI) by electron energy loss spectroscopy". In: *Ultramicroscopy* 106.7 (2006), pp. 561–573.

[178] K. Annand, M. Nord, I. MacLaren, and M. Gass. "The Corrosion of Zr(Fe, Cr) 2 and Zr 2 Fe Secondary Phase Particles in Zircaloy-4 under 350 °C pressurised water conditions". In: *Corrosion Science* January (2017), pp. 1–11. URL: http://linkinghub.elsevier.com/retrieve/pii/S0010938X17300173.

[179] I. Takagi, K. Une, S. Miyamura, and T. Kobayashi. "Deuterium diffusion in steam-corroded oxide layer of zirconium alloys". In: *Journal of Nuclear Materials* 419.1-3 (2011), pp. 339–346. URL: http://dx.doi.org/10.1016/j.jnucmat.2011.06.001%20http://linkinghub.elsevier.com/retrieve/pii/S0022311511005320.

[180] G. Sundell, M. Thuvander, and H. O. Andrén. "Tin clustering and precipitation in the oxide during autoclave corrosion of Zircaloy-2". In: *Journal of Nuclear Materials* 456 (2015), pp. 409–414. URL: http://dx.doi.org/10.1016/j.jnucmat.2014.10.003.

[181] E. R. Bradley and G. P. Sabol. "Zirconium in the Nuclear Industry: Eleventh International Symposium". In: *ASTM Special Technical Publication 1295*. Vol. 1295. 1996, p. 907. URL: https://www.scopus.com/inward/record.uri?eid=2-s2.0-0030289361%7B%5C&%7DpartnerID=40%7B%5C&%7Dmd5=.

[182] W. J. S. Yang and R. B. Adamson. "Zirconium in the Nuclear Industry". In: *Zirconium in the Nuclear Industry: 8th International Symposium, ASTM STP 1023* (1989), pp. 451–477.

[183] C. Roy and G. David. "X-ray diffraction analyses of zirconia films on zirconium and zircaloy-2". In: *Journal of Nuclear Materials* 37.1 (1970), pp. 71–81.

[184] V. Busser, J. Desquines, S. Fouguet, M. Bauetto, and J. Mardon. "Modelling of Corrosion Induced Stresses during Zircaloy-4 Oxidation in Air". In: *Materials Science Forum* 595 (2008), pp. 419–427.

[185] L. Kurpaska, J. Favergeon, J.-L. Grosseau-Poussard, L. Lahoche, and G. Moulin. "In-situ stress analysis of the Zr/ZrO2 system as studied by Raman spectroscopy and deflection test in monofacial oxidation techniques". In: *Applied Surface Science* 385 (2016), pp. 106–112.

[186] A. J. G. Maroto, R. Bordoni, M. Villegas, A. M. Olmedo, M. A. Blesa, A. Iglesias, and P. Koenig. "Growth and characterization of oxide layers on zirconium alloys". In: *Journal of Nuclear Materials* 229 (1996), pp. 79–92.

[187] N. Pétigny, P. Barberis, C. Lemaignan, C. Valot, and M. Lallemant. "In situ XRD analysis of the oxide layers formed by oxidation at 743 K on Zircaloy 4 and Zr–1NbO". In: *Journal of Nuclear Materials* 280.3 (2000), pp. 318–330.

[188] H. Anada and K. Takeda. "Microstructure of Oxides on Zircaloy-4, 1.0Nb Zircaloy-4, and Zircaloy-2 Formed in 10.3-MPa Steam at 673 K". In: *Zirconium in the Nuclear Industry: 11th International Symposium, ASTM STP 1295* (1996), pp. 35–54.

[189] H. El Kadiri, Z. N. Utegulov, M. Khafizov, M. Asle Zaeem, M. Mamivand, A. L. Oppedal, K. Enakoutsa, M. Cherkaoui, R. H. Graham, and A. Arockiasamy. "Transformations and cracks in zirconia films leading to breakaway oxidation of Zircaloy". In: *Acta Materialia* 61.11 (2013), pp. 3923–3935. URL: http://dx.doi.org/10.1016/j.actamat.2013.02.052.

[190] M. Preuss, P. Frankel, S. Lozano-Perez, D. Hudson, E. Polatidis, N. Ni, J. Wei, C. English, S. Storer, K. B. Chong, M. Fitzpatrick, P. Wang, J. Smith, C. Grovenor, G. Smith, J. Sykes, B. Cottis, S. Lyon, L. Hallstadius, B. Comstock, A. Ambard, M. Blat-Yrieix, P. Barberis, and S. W. Dean. "Studies Regarding Corrosion Mechanisms in Zirconium Alloys". In: *Journal of ASTM International* 8.9 (2011), p. 103246. URL: http://www.astm.org/doiLink.cgi?JAI103246.

[191] D. J. Spengler, A. T. Motta, R. Bajaj, J. R. Seidensticker, and Z. Cai. "Characterization of Zircaloy-4 corrosion films using microbeam synchrotron radiation". In: *Journal of Nuclear Materials* 464 (2015), pp. 107–118. URL: http://dx.doi.org/10.1016/j.jnucmat.2015.04.006.

[192] P. Bossis, F. Lefebvre, P. Barbéris, and A. Galerie. "Corrosion of Zirconium Alloys: Link between the Metal/Oxide Interface Roughness, the Degradation of the Protective Oxide Layer and the Corrosion Kinetics". In: *High Temperature Corrosion and Protection of Materials 5*. Vol. 369. Materials Science Forum. Trans Tech Publications, 2001, pp. 255–262.

[193] E. Polatidis, P. Frankel, J. Wei, M. Klaus, R. Comstock, A. Ambard, S. Lyon, R. Cottis, and M. Preuss. "Residual stresses and tetragonal phase fraction characterisation of corrosion tested Zircaloy-4 using energy dispersive synchrotron X-ray diffraction". In: *Journal of Nuclear Materials* 432.1-3 (Jan. 2013), pp. 102–112. URL: https://www.sciencedirect.com/science/article/pii/S0022311512003844?via%7B%5C%%7D3Dihub.

[194] Y. Dong, A. T. Motta, and E. a. Marquis. "Atom probe tomography study of alloying element distributions in Zr alloys and their oxides". In: *Journal of Nuclear Materials* 442.1-3 (2013), pp. 270–281.

[195] P. Rudling, R. Adamson, B. Cox, F. Garzarolli, A. Strasser, and C. Patterson. *Impact of manufacturing changes on Zr alloy in-pile performance Authors*. Tech. rep. September. Skultuna, Sweden: Advanced Nuclear Technology International, 2009.

[196] H. S. Hong, S. J. Kim, and K. S. Lee. "Influence of dilute silicon addition on the oxidation resistance and tensile properties of modified Zircaloy-4". In: *Journal of Nuclear Materials* 304.1 (2002), pp. 8–14.

[197] A. Motta, A. Yilmazbayhan, R. Comstock, J. Partezana, G. Sabol, B. Lai, and Z. Cai. "Microstructure and Growth Mechanism of Oxide Layers Formed on Zr Alloys Studied with Micro-Beam Synchrotron Radiation BT - Microstructure and Growth Mechanism of Oxide Layers Formed on Zr Alloys Studied with Micro-Beam Synchrotron Radiation". In: *Journal of ASTM International* 2.5 (2005).

[198] B. Wadman, Z. Lai, H.-O. Andren, A. .-.-L. Rudling, and H. Pettersson. "Microstructure of Oxide Layers Formed During Autoclave Testing of Zirconium Alloys". In: *Zirconium in the Nuclear Industry: 10th International Symposium ASTM STP 1245*. 1994, pp. 579–598.

[199] P. Tejland, M. Thuvander, H.-O. Andrén, S. Ciurea, T. Andersson, M. Dahlbäck, L. Hallstadius, P. Barberis, and S. W. Dean. "Detailed Analysis of the Microstructure of the Metal/Oxide Interface Region in Zircaloy-2 after Autoclave Corrosion Testing". In: *Journal of ASTM International* 8.6 (2011), p. 102956. URL: http://www.astm.org/doiLink.cgi?JAI102956.

[200] J. Hu, B. Setiadinata, T. Aarholt, A. Garner, J. Partezana, P. Bagot, S. Lozano-Perez, M. Preuss, M. Moody, and C. Grovenor. "High-resolution characterization of Zr nuclear fuel cladding alloys". In: *Zirconium in the nuclear industry: Eighteenth international symposium*. Hilton Head Island, SC: American Society of Testing Materials, 2016.

[201] W. M. Rumball. "The effect of chromium, oxygen and microstructure on the hardness of zirconium-chromium alloys". In: *Journal of The Less-Common Metals* 39.1 (1975), pp. 35–42.

[202] Z. Zhao, J. Morniroli, A. Legris, L. Thuinet, Y. Kihn, and A. Ambard. "Characterization of Zirconium Hydrides and Phase Field Approach to a Mesoscopic-Scale Modeling of Their". In: *Journal of ASTM* 5.3 (2011), pp. 1–20.

[203] G. J. C. Carpenter. "The precipitation of γ-zirconium hydride in zirconium". In: *Acta Metallurgica* 26.8 (1978), pp. 1225–1235. URL: http://www.sciencedirect.com/science/article/pii/0001616078900068.

[204] K. J. Annand and T. Aarholt. personal communication. Apr. 10, 2018.

[205] B. Puchala and A. Van Der Ven. "Thermodynamics of the Zr-O system from first-principles calculations". In: *Physical Review B - Condensed Matter and Materials Physics* 88.9 (2013).

[206] G. P. Sabol, G. R. Kilp, M. Balfour, and E. Roberts. "Development of a Cladding Alloy for High Burnup". In: *Zirconium in the Nuclear Industry - 8th International Symposium. ASTM STP 1023.* (1989), pp. 227–244.

[207] A. Couet, A. T. Motta, and R. J. Comstock. "Hydrogen pickup measurements in zirconium alloys: Relation to oxidation kinetics". In: *Journal of Nuclear Materials* 451.1-3 (2014), pp. 1–13. URL: http://dx.doi.org/10.1016/j.jnucmat.2014.03.001.

[208] U. Otgonbaatar, W. Ma, M. Youssef, and B. Yildiz. "Effect of niobium on the defect chemistry and oxidation kinetics of tetragonal ZrO2". In: *Journal of Physical Chemistry C* 118.35 (2014), pp. 20122–20131.

[209] B. D. Bell, S. T. Murphy, R. W. Grimes, and M. R. Wenman. "The effect of Nb on the corrosion and hydrogen pick-up of Zr alloys". In: *Acta Materialia* 132 (2017), pp. 425–431. URL: http://dx.doi.org/10.1016/j.actamat.2017.04.063.

[210] B. D. Bell, S. T. Murphy, P. A. Burr, R. W. Grimes, and M. R. Wenman. "Accommodation of tin in tetragonal ZrO2". In: *Journal of Applied Physics* 117.8 (2015). arXiv: 1502.06883.

[211] J. P. Foster, H. Ken Yueh, and R. J. Comstock. "ZIRLO Cladding Improvement". In: *Zirconium in the Nuclear Industry: 15th International Symposium, ASTM STP 1505*. Ed. by B. Kammerzind and M. Limbäck. West Conchohocken, PA: ASTM International, 2007, pp. 457–470.

[212] S. C. Lumley, S. T. Murphy, P. A. Burr, R. W. Grimes, P. R. Chard-Tuckey, and M. R. Wenman. "The stability of alloying additions in Zirconium". In: *Journal of Nuclear Materials* 437.1-3 (2013), pp. 122–129. URL: http://dx.doi.org/10.1016/j.jnucmat.2013.01.335.

[213] B. Kyriacou, K. L. Moore, D. Paterson, M. D. De Jonge, D. L. Howard, J. Stangoulis, M. Tester, E. Lombi, and A. A. T. Johnson. "Localization of iron in rice grain using synchrotron X-ray fluorescence microscopy and high resolution secondary ion mass spectrometry". In: *Journal of Cereal Science* 59.2 (2014), pp. 173–180. URL: http://dx.doi.org/10.1016/j.jcs.2013.12.006.

[214] P. Kontis, H. A. M. Yusof, S. Pedrazzini, M. Danaie, K. L. Moore, P. A. J. Bagot, M. P. Moody, C. R. M. Grovenor, and R. C. Reed. "On the effect of boron on grain boundary character in a new polycrystalline superalloy". In: *Acta Materialia* 103 (2016), pp. 688–699. URL: http://dx.doi.org/10.1016/j.actamat.2015.10.006.

[215] S. Yamanaka. "Study on the hydrogen solubility in zirconium alloys". In: *Journal of Nuclear Materials* 247 (1997), pp. 315–321. URL: http://linkinghub.elsevier.com/retrieve/pii/S0022311597001013.

[216] C. E. Coleman and J. F. R. Ambler. "Solubility of hydrogen isotopes in stressed hydride-forming metals". In: *Scripta Metallurgica* 17.1 (1983), pp. 77–82.

[217] P. Lesot and O. Lafon. "Natural Abundance Deuterium NMR Spectroscopy A2 - Lindon, John C." In: *Encyclopedia of Spectroscopy and Spectrometry (Third Edition)*. Ed. by G. E. Tranter, D. W. B. T. .-.-. E. o. S. Koppenaal, and S. (Edition). Oxford: Academic Press, 2017, pp. 1–14. URL: file://www.sciencedirect.com/science/article/pii/B9780124095472121109.

[218] G. Wikmark, P. Rudling, B. Lehtinen, B. Hutchinson, A. Oscarsson, and E. Ahlberg. "The importance of oxide morphology for the oxidation rate of zirconium alloys." In: *Zirconium in the Nuclear Industry: 11th International Symposium, ASTM STP 1295*. West Conshohocken, PA, 1996, pp. 55–73.

[219] P. A. Burr, S. T. Murphy, S. C. Lumley, M. R. Wenman, and R. W. Grimes. "Hydrogen solubility in zirconium intermetallic second phase particles". In: *Journal of Nuclear Materials* 443.1-3 (2013), pp. 502–506. arXiv: 1307.7617. URL: http://dx.doi.org/10.1016/j.jnucmat.2013.07.060.

[220] M. W. Mallett and W. M. Albrecht. "High Temperature Oxidation of Two Zirconium-Tin Alloys". In: *Journal of The Electrochemical Society* 102.7 (July 1955), pp. 407–414. URL: http://jes.ecsdl.org/content/102/7/407.abstract.

[221] Magee C.W. and R. Honig. "Depth Profiling by SIMS-Depth Resolution, Dynamic Range and Sensitivity". In: *Surface and Interface Analysis* 4.2 (1982), pp. 35–41.

[222] P. Gormanns, S. Reckow, J. C. Poczatek, C. W. Turck, and C. Lechene. "Segmentation of Multi-Isotope Imaging Mass Spectrometry Data for Semi-Automatic Detection of Regions of Interest". In: *PLoS ONE* 7.2 (Feb. 2012), e30576. URL: http://dx.doi.org/10.1371%7B%5C%%7D2Fjournal.pone.0030576.

[223] C. A. Schneider, W. S. Rasband, and K. W. Eliceiri. "NIH Image to ImageJ: 25 years of image analysis". In: *Nature methods* 9.7 (2012), pp. 671–675.

[224] J. Schindelin, C. T. Rueden, and M. C. Hiner. "The ImageJ ecosystem: An open platform for biomedical image analysis". In: *Molecular Reproduction and Development* 82.7-8 (2015), pp. 518–529.

[225] J. Schindelin, I. Arganda-Carreras, and E. Frise. "Fiji: an open-source platform for biological-image analysis". In: *Nature methods* 9.7 (2012), pp. 676–682.

[226] G. Sundell, M. Thuvander, and H.-O. Andrén. "Barrier oxide chemistry and hydrogen pick-up mechanisms in zirconium alloys". In: *Corrosion Science* 102 (2016), pp. 490–502. URL: http://linkinghub.elsevier.com/retrieve/pii/S0010938X15301438.

[227] W. Kunz, H. Münzel, and U. Kunz. "Tritium release from Zircaloy-2: Dependence on temperature, surface conditions and composition of surrounding medium". In: *Journal of Nuclear Materials* 136.1 (1985), pp. 6–15.

[228] D. Khatamian. "Hydrogen diffusion in oxides formed on surfaces of zirconium alloys". In: *Journal of Alloys and Compounds* 253-254 (May 1997), pp. 471–474. URL: https://www.sciencedirect.com/science/article/pii/S092583889603068X.

[229] T. Kato, I. Takagi, K. Sakamoto, and M. Aomi. "Hydrogen diffusivity in oxide layers formed in Zr alloy in air or steam". In: *Journal of Nuclear Materials* 494 (2017), pp. 79–86. URL: http://dx.doi.org/10.1016/j.jnucmat.2017.07.010.

[230] K. Une, K. Sakamoto, M. Aomi, J. Matsunaga, Y. Etoh, I. Takagi, S. Miyamura, T. Kobayashi, and K. Ito. "Hydrogen absorption mechanism of zirconium alloys based on characterization of oxide layer". In: *Zirconium in the Nuclear Industry: 16th International Symposium*. Ed. by P. Barbéris and M. Limbäck. ASTM International. West Conshohocken, PA: ASTM International, 2011, pp. 401–432.